Lehrstuhl für Leichtbau
der Technischen Universität München

An Adaptive Feed-Forward Controller for Active Wing Bending Vibration Alleviation on Large Transport Aircraft

Andreas Wildschek

Vollständiger Abdruck der von der Fakultät für Maschinenwesen der Technischen Universität München zur Erlangung des akademischen Grades eines

Doktor-Ingenieurs

genehmigten Dissertation.

Vorsitzender: Univ.-Prof. Dr.-Ing. habil. B. Lohmann

Prüfer der Dissertation:

1. Univ.-Prof. Dr.-Ing. H. Baier

2. Univ.-Prof. Dr.-Ing. F. Holzapfel

Die Dissertation wurde am 04. Juni 2008 bei der Technischen Universität München eingereicht und durch die Fakultät für Maschinenwesen am 21. Januar 2009 angenommen.

Preface

This PhD thesis arose from almost four years of research on adaptive aeroelastic control at EADS Innovation Works in Ottobrunn, Germany.

I would like to thank Professor Horst Baier, head of the Institute for Lightweight Structures at Technische Universität München, Germany for his encouragement, supervision, and support. I am also grateful to Professor Florian Holzapfel, head of the Institute of Flight System Dynamics at Technische Universität München for his expertise and co-supervision.

Moreover, I would like to express my sincere gratitude to Dr. Rudolf Maier, with EADS Innovation Works for his exceptional support, and the fruitful technical discussions. My thanks also go to Dr.-Ing. Matthieu Jeanneau and Dipl.-Ing. Nicky Aversa, both with Airbus France, as well as to Dr.-Ing. Simon Hecker with the Institute of Robotics and Mechatronics at the German Aerospace Center (DLR) Oberpfaffenhofen, and to Professor Zbigniew Bartosiewicz, head of the Department of Mathematics at Bialystok Technical University, Republic of Poland, for their invaluable suggestions.

I would also like to thank Dr. Ravindra Jategaonkar and his colleagues at the Institute of Flight Systems at DLR Braunschweig for the fruitful discussions and their support, in particular for providing me with flight test data of their ATTAS research aircraft.

Many thanks go to Dr.-Ing. habil. Christian Breitsamter, with the Institute for Aerodynamics at Technische Universität München and his team for their exceptional support with the wind tunnel test. In this context I would also like to thank my colleagues at EADS Germany, particularly Dipl.-Ing. Falk Hoffmann, Josef Steigenberger, and Karl-Heinz Kaulfuss, as well as Dipl.-Ing. Theodoros Giannopoulos, with Airbus Deutschland GmbH, and Dr.-Ing. Athanasios Dafnis, with the Department of Aerospace and Lightweight Structures at the RWTH Aachen, Germany for their invaluable suggestions and support with the design of the wind tunnel test setup, and the realization of the wind tunnel test.

Last but not least, my family and friends, in particular my wife Marriah deserve my gratefulness for their loving support and continuous encouragement.

Ottobrunn
June 2008 Andreas Wildschek

Contents

Nomenclature

Symbols frequently used in this thesis are listed below alphabetically. In addition, the place of their first occurrence in the text is given in the very right column. The state space matrices **A**, **B**, **C**, and **D** are only used in Eq. 2-1, and are not noted here. Neither are the counting variables i, k, and m, or the discrete frequency domain auxiliary functions, such as $a_1(f_k)$, $a_\Delta(f_k)$, $b(f_k)$, $\bar{b}(f_k)$, $g_1(f_k)$, $g_\Delta(f_k)$, $v(\omega)$, $w(\omega)$ in this list.

Latin Symbols

Symbol	Meaning	First occurrence
$A\left(e^{j\omega T}\right)$	Fourier transform of the reference signal	Eq. (2-13)
$A(z)$	numerator of discrete transfer function of IIR controller	Eq. (6-2)
a_i	i^{th} coefficient of $A(z)$	Eq. (6-2)
$\overline{ab}$	distance between the points “a” and “b”	Eq. (2-14)
$B(z)$	denominator of discrete transfer function of IIR controller	Eq. (6-2)
b_k	k^{th} coefficient of $B(z)$	Eq. (6-2)
$B\left(e^{j\omega T}\right)$	multiplicative magnitude error	Eq. (4-5)
c	convergence coefficient for FIR controller update	Eq. (3-15)
c_1, c_2	convergence coefficients for IIR controller update	Eqs. (6-3), (6-4)
d, $D\left(e^{j\omega T}\right)$	disturbance signal and its Fourier transform	Figure 2-11
e, $E\left(e^{j\omega T}\right)$	error signal and its Fourier transform	Eq. (2-3)
$F(s)$	closed loop transfer function	Eq. (2-6)
$F_P(s)$	parasitic feedback transfer function, i.e. from u_{FF} to α	Eq. (2-19)
$F_\delta(s)$	aileron actuation mechanism’s transfer function	Eq. (2-2)
f	frequency	Eq. (2-14)
f_k	k^{th} discrete frequency	Eq. (3-16)
$G(z)$	plant transfer function seen by the digital controller $H(z)$	Figure 3-2
$G(f_k)$	estimated value of 2N-point DFT of plant impulse response	Eq. (3-37)
$\widetilde{G}(f_k)$	biased approximation of $G(f_k)$ by evaluating $G\left(e^{j\omega T}\right)$ at f_k	Eq. (4-19)
$\hat{G}(f_k)$	estimate or mean of $G(f_k)$ at the discrete frequency f_k	Eq. (3-18)
$G_c(s)$	continuous-time SCP transfer function	Eq. (2-4)
$H(s)$	transfer function of the (pseudo) feed-forward controller	Figure 2-11
$H(z)$	discrete-time transfer function of the FIR controller	Eq. (3-4)
$\vec{h}$	vector of FIR coefficients	Eq. (3-1)
I	order of numerator of IIR controller	Eq. (6-2)

Symbol	Meaning	First occurrence
j	$\sqrt{-1}$	Eq. (2-8)
K	order of denominator of IIR controller	Eq. (6-2)
$K(s)$	transfer function of feedback controller	Eq. (2-5)
$K_{5/6}(v), K_{11/6}(v)$	modified Bessel functions of the second kind for orders five sixths and eleven sixths, respectively	Eq. (2-14)
$\hat{K}_t(\omega, a)$	von Kármán power spectral density of v_z at point "a"	Eq. (2-14)
$\hat{K}_t(\omega, b)$	von Kármán power spectral density of v_z at point "b"	Eq. (2-14)
$\hat{K}_t(\omega, \overline{ab})$	von Kármán cross spectral density between "a" and "b"	Eq. (2-14)
L	integral scale length of the turbulence	Eq. (2-14)
l	number of Eigen modes in a state-space model	Eq. (2-1)
Ma	Mach number	page 10
Mx_{WR}	deviation of the vertical bending moment at the left wing root from the static value in trimmed 1-g flight	Eq. (2-1)
N	number of FIR coefficients	Eq. (3-3)
Nz	vertical acceleration	Eq. (2-1)
n	discrete time step	Eq. (3-1)
$P(s)$	transfer function of the PCP	Eq. (2-4)
q	pitch rate	Eq. (2-1)
$r,\ R(e^{j\omega T})$	SCP filtered reference signal and its Fourier transform	Eq. (3-5)
$\hat{r}$, $\hat{R}(e^{j\omega T})$	filtered reference signal and its Fourier transform	Eq. (3-15)
$S_{xy}(e^{j\omega T})$	cross spectral density between the signals x and y	Eq. (2-11)
$\widetilde{S}_{xy}(f_k)$	estimate of $S_{xy}(e^{j\omega T})$ over the last N samples at f_k	Eq. (3-25)
$\overline{S}_{xy}(f_k)$	average value of $\widetilde{S}_{xy}(e^{j\omega T})$ over the last Δ samples at f_k	Eq. (3-34)
s	Laplace variable	Eq. (2-4)
T	sample time in seconds	Eq. (2-11)
t	time	Eq. (4-18)
$u,\ U(e^{j\omega T})$	control input to the actuator and its Fourier transform	Eq. (2-2)
$\widetilde{u}$	IIR controller's output filtered by $\hat{G}(z)/B(z)$, or $\hat{G}(z)$	Eq. (6-4)
V_{TAS}	true airspeed of the aircraft	page 10
v_z	vertical flow rate	page 57
x	gust generator driving signal used as reference signal	Figure 5-1
$x_{chirp}, X_{chirp}(f_k)$	chirp signal for plant identification and its DFT	Eq. (5-1)
$y(n), Y(e^{j\omega T})$	output of $G(z)$ and the output's Fourier transform	Eq. (3-5)
z	z-transform variable	Eq. (6-1)

Greek Symbols

Symbol	Meaning	First occurrence
α	reference signal	Figure (2-12)
α_0	static angle of attack of the trimmed aircraft	Eq. (2-18)
α_{air}	alpha probe measurement	Eq. (2-18)
α_{ground}	aircraft movement and vibration induced angle of attack deviation from the static value α_0 at the alpha probe mounting position (measured in a ground reference system)	Eq. (2-1)
α_{sim}	reference signal used for the simulation	Eq. (4-3)
α_w	atmospheric turbulence induced angle of attack variation at the alpha probe mounting position	Eq. (2-1)
α_{wind}	measurable atmospheric turbulence induced angle of attack variation at the alpha probe mounting position	Eq. (2-18)
α_v	non-measurable atmospheric turbulence induced angle of attack variation at the alpha probe mounting position	Eq. (2-17)
$\Gamma(1/3)$	gamma function of $1/3$	Eq. (2-14)
$\gamma_{xy}{}^2(e^{j\omega T})$	quadratic coherence function between the signals x and y	Eq. (2-11)
Δ	maximum feedback delay in samples	Eq. (3-23)
$\Delta_{\max}$	maximum of $\Delta_G(\omega)$ rounded down to an integer value	Eq. (3-24)
ΔH	Deviation of the controller from its optimum	Eq. (3-19)
Δ_{overlap}	update delay due to an infrequently updated gradient estimate	Eq. (3-24)
$\Delta_G(\omega)$	plant delay over angular frequency	page 46
δ	deflection angle of the symmetrically driven ailerons	Eq. (2-1)
ε_{excess_n}	excess mean square control error for $\vec{h} = \vec{h}(n)$	Eq. (3-21)
ζ_i	damping of the i^{th} Eigen mode	Eq. (2-1)
λ	$\lambda = c/c_{\max}$ with $0 < \lambda < 1$	page 52
μ	number of modal states in a state-space model	Eq. (2-1)
$\Xi(e^{j\omega T})$	(frequency dependent) performance index for feed-forward control	Eq. (4-6)
ξ_i	i^{th} element of the modal state vector	Eq. (2-1)
$\phi(f_k), \phi(\omega)$	phase angle at discrete frequency f_k, at angular frequency ω	Eq. (3-37)
$\omega = 2\pi f$	angular frequency	Eq. (2-1)
ω_i	natural angular frequency of the i^{th} Eigen mode	Eq. (2-1)

Subscripts

Symbol	Meaning
CG	at the Center of Gravity
CL	Closed Loop Share
c	continuous-time
FB	FeedBack
FF	Feed-Forward
front	at the front of the aircraft fuselage (alpha probe mounting point)
G	for the plant
$\hat{G}$	for the plant model
HY	HYbrid control
IMC	Internal Model Control
LW	Left Wing
law	modal wing bending measurement
Minimum over frequency	minimum over frequency
max	maximum
min	minimum
n	at time step *n*
non-adaptive control	for a non-adaptive controller
OL	Open Loop Share
opt	optimum
RW	Right Wing
rear	at the rear of the aircraft fuselage
sim	simulation
WR	(left) Wing Root
∞	infinity

Transforms

Symbol	Meaning	First occurrence
$X(s) = \mathcal{L}\{x(t)\}$	Laplace transform of $x(t)$	Eq. (2-2)
$X(j\omega) = \mathcal{F}\{x(t)\}$	Fourier transform of $x(t)$	Eq. (G-2)
$x(t) = IFT\{X(j\omega)\}$	Inverse Fourier Transform of $X(j\omega)$	Eq. (G-3)
$X(e^{j\omega T}) = \mathcal{F}\{x(n)\}$	Fourier transform of $x(n)$	Eq. (2-12)
$x(n) = IFT\{X(e^{j\omega T})\}$	Inverse Fourier Transform of $X(e^{j\omega T})$	Eq. (3-15)
$X(f_k) = DFT\{x(n)\}$	Discrete Fourier Transform of $x(n)$	Eq. (3-16)
$x(n) = IDFT\{X(f_k)\}$	Inverse Discrete Fourier Transform of $X(f_k)$	Eq. (3-16)
$x(n) = IDFT\{...\}_+$	Only the *causal* share of the Inverse Fourier Transform of "…" is considered in $x(n)$, i.e. application of the *overlap-save method*.	Eq. (3-16)

Operators

Symbol	Meaning	First occurrence
$\partial\phi_G(\omega)/\partial\omega$	derivative of $\phi_G(\omega)$ with respect to ω	page 46
$Re\{\ldots\}$	real part of "…"	Eq. (3-10)
$Im\{\ldots\}$	imaginary part of "…"	Eq. (3-10)
$\max_{\omega}...$	maximum value of "…" over the angular frequency ω	Eq. (2-8)
z^{-1}	delay of a discrete signal by one sample	Figure (3-1)
$\dot{\xi}_i$	time derivative of ξ_i	Eq. (2-1)
$\|...\|_\infty$	H_∞ norm of "…"	Eq. (2-8)
$\|...\|_2$	H_2 norm of "…"	Eq. (2-9)
$...*$	complex conjugation of "…"	Eq. (2-12)
$\langle ... \rangle$	expectation value of "…"	Eq. (2-12)
$...^T$	transposition of "…"	Eq. (3-1)
$\|...\|$	magnitude of "…"	Eq. (2-13)

Abbreviations

Abbreviation	Meaning
ADC	Analogue to Digital Converter
AF	Anti-aliasing Filter
ANC	Active Noise Control
ASAC	Active Structural-Acoustic Control
ATTAS	Advanced Technologies Testing Aircraft System
AWIATOR	Aircraft WIng with Advanced Technology OpeRation
CFRP	Carbon Fiber Reinforced Plastic
CG	Center of Gravity
DAC	Digital to Analogue Converter
DFT	Discrete Fourier Transform
DLR	German Aerospace Center
DOF	Degree Of Freedom
DSP	Digital Signal Processor
FCS	Flight Control System
FIR	Finite Impulse Response
GFRP	Glass Fiber Reinforced Plastic
IDFT	Inverse Discrete Fourier Transform
IIR	Infinite Impulse Response
IM	Internal Model
IMC	Internal Model Control
LIDAR	LIght Detection And Ranging
LMS	Least Mean Square
MIMO	Multiple Input/Multiple Output
MRAC	Model Reference Approach Control
NN	Neural Network
PCP	Primary Control Path, i.e. transfer function from atmospheric turbulence induced angle of attack variation $\alpha_w(t)$ to error signal $e(t)$.
RF	Reconstruction Filter
SCP	Secondary Control Path, i.e. transfer function from symmetric aileron command $u(t)$ to error signal $e(t)$.
SISO	Single Input/Single Output

Abstract

This thesis provides the design and the validation of an adaptive feed-forward controller for the compensation of atmospheric turbulence excited symmetric wing bending vibrations on large transport aircraft. Thereby, it is shown that the adaptation increases the robustness of the feed-forward controller's performance against plant uncertainties. In order to allow for a certification of the proposed adaptive controller on a flying aircraft a detailed robust stability analysis is performed.

The performance of a feed-forward control system depends mainly on the availability of an appropriate reference signal. Investigations on the two-dimensional von Kármán turbulence spectrum show that a 50% reduction of the first symmetric vertical wing bending vibration magnitude can be obtained on a large four-engine example aircraft by pure feed-forward control when an alpha probe that responds quite directly to alpha variations up to 4 Hz is used as a reference sensor. Subsequent numeric simulations with state space models of said large four-engine transport aircraft confirm this performance estimate. Thereby, the highest alleviation of first symmetric vertical wing bending vibrations is naturally obtained with a hybrid controller, i.e. a combination between a robust feedback controller, and an adaptive feed-forward controller. The stable convergence of the adaptation of the feed-forward controller is in accordance with the previously derived mathematical analysis.

In order to demonstrate the implementation of the proposed adaptive feed-forward controller on a real plant, and also to investigate the real time behavior, a wind tunnel experiment is performed. Thereby, an elastic aircraft model which is mounted in the airflow with free rotational degrees of freedom serves as control plant. A gust generator is placed upstream in order to provide a locally correlated excitation. This gust generator is driven with a white noise signal, which is also used as reference signal for feed-forward wing bending vibration control. Symmetrically driven piezo-electric trailing edge flaps serve as actuators. As predicted by the previously performed robust stability analysis, the controller adaptation remains stable under the real-time conditions in the wind tunnel. Moreover, the reduction of the first symmetric vertical wing bending vibration is in accordance with the mathematical analysis, as well as with the numeric simulations.

It is concluded that the proposed adaptive wing bending vibration controller is a promising approach for the realization of feed-forward control of atmospheric turbulence excited structural vibrations on large transport aircraft. One important point

thereby is that the adaptation provides high performance robustness against plant uncertainties. In combination with robust feedback control the proposed adaptive feed-forward wing bending vibration controller offers a great chance for further reduction of dynamic structural loads, and an increase of passenger comfort and handling qualities on large transport aircraft.

Kurzfassung

Die vorliegende Arbeit beschäftigt sich mit dem Entwurf und mit der Validierung einer adaptiven Vorsteuerung zur Kompensation von turbulenzerregten symmetrischen Flügelbiegeschwingungen. Der Einsatz einer solchen Steuerung ist vor allem für sehr große Transportflugzeuge geeignet, deren Strukturmoden stark von atmosphärischer Turbulenz angeregt werden. Es kann gezeigt werden, daß die Adaption der Vorsteuerung zu einer Erhöhung der Robustheit der Regelgüte gegenüber Unsicherheiten in der Regelstrecke beiträgt. Um auch eine Flugzulassung zu ermöglichen, wird eine detaillierte Stabilitätsanalyse des vorgeschlagenen adaptiven Regelalgorithmus durchgeführt.

Die Regelgüte einer Vorsteuerung hängt stark von der Verfügbarkeit eines geeigneten Referenzsignals ab. Untersuchungen am zwei-dimensionalen von Kármán Turbulenzspektrum zeigen, daß die modalen Beschleunigungen der ersten symmetrischen Flügelbiegeschwingung bei einem großen vierstrahligen Beispielflugzeug um 50% reduziert werden können, sofern ein Anstellwinkelsensor verfügbar ist, der Änderungen des Anstellwinkels bis 4 Hz direkt wiedergibt. Diese Vorhersage kann schließlich durch numerische Simulationen mit Zustandsraummodellen dieses vierstrahligen Transportflugzeuges bestätigt werden. Die höchste Reduktion der ersten symmetrischen Flügelbiegeschwingung wird dabei natürlich mit einem Hybridregler, also einer Kombination aus robuster Rückführregelung und adaptiver Vorsteuerung erreicht. Das Stabilitätsverhalten der Adaption der Vorsteuerung stimmt in den Simulationen mit der zuvor durchgeführten mathematischen Analyse überein.

Um letztendlich auch die Implementierung der adaptiven Vorsteuerung anhand einer echten Regelstrecke zu demonstrieren, und das Echtzeitverhalten zu überprüfen, wird ein Windkanalversuch durchgeführt. Dabei dient ein, in der Strömung frei drehbar gelagertes elastisches Flugzeugmodell als Regelstrecke. Ein stromaufwärts montierter Böengenerator, der mit einem weißen Rauschsignal betrieben wird, erzeugt örtlich korrelierte Störungen. Besagtes Rauschsignal dient gleichzeitig als Referenzsignal für die Vorsteuerung. Als Aktoren werden symmetrisch betriebene piezoelektrische Hinterkantenklappen benutzt. Die Adaption der Vorsteuerung verläuft stabil, wie in der Stabilitätsanalyse vorhergesagt. Auch die Reduktion der ersten symmetrischen Flügelbiegeschwingung stimmt mit den Berechnungen, und den numerischen Simulationen überein.

Zusammenfassend kann gesagt werden, daß die vorgeschlagene adaptive Vorsteuerung einen vielversprechenden Ansatz zur Realisierung einer Kompensation von turbulenzerregten Strukturschwingungen bei großen Transportflugzeugen darstellt. Dabei ist ein wichtiger Punkt, daß die Robustheit der Regelgüte gegenüber Unsicherheiten in der Regelstrecke durch die Adaption entscheidend verbessert werden kann. In Kombination mit einem robusten Rückführstrukturregler ermöglicht die vorgeschlagene adaptive Vorsteuerung eine weitere Reduktion dynamischer Strukturlasten, sowie eine Verbesserung des Passagierkomforts und des Flugverhaltens.

1 Introduction

Economic aspects demand the design of large transport aircraft with high aspect ratio wings and fuselage at low structural weight/payload ratio. For such aircraft it can be shown by fairly simple calculations, that the frequencies of rigid body motions and aeroelastic vibrations have the tendency to get closer to each other, increasing the aeroelastic coupling between flight mechanics and structural dynamics, see HANEL [50]. Thus, turbulent atmosphere, gusts and maneuvers significantly excite structural vibrations. These vibrations cause dynamic structural loads and also influence the rigid body motions of the aircraft, decreasing handling qualities and passenger comfort.

In the last decades active control technology was found to be the appropriate means to overcome these problems and thus significantly improve the performance of aircraft [58]. According to HARRIS & RICKARD [53] an aircraft utilizing active controls can in general be identified as one in which significant inputs (over and above those of the pilot) are transmitted to the control surfaces for the purpose of augmenting vehicle performance. Although the use of control surfaces generally seems to be the most obvious approach, other actuator concepts such as piezo-electric or additional aerodynamic devices are possible, see for example BREITSAMTER [10]/[11], KRAG [70], RANEY ET AL. [93], or SHETA ET AL. [103].

An important field of active control technology is noise and *vibration control*. The idea of noise control dates back to the 1930's, when LUEG [76]/[77] patented a "process of silencing sound oscillations", as he called it. He suggested to eliminate a one-dimensional sound wave with a 180° phase shifted sound wave, which is the principle of Active Noise Control (ANC). In the 1950's this principle was used to develop headsets that actively reduced the noise in the instant adjacence of the ears [33]. The development of modern digital computers finally allowed for active noise and vibration control of much more complex systems and led to a boom of active noise and vibration control applications from the 1970's on.

Regarding a standard configuration aircraft, it is generally the vertical wing bending modes as well as fuselage bending modes which are responsible for high dynamic loads, and the decrease of ride comfort. Thereby, the highest dynamic structural loads are usually experienced at the wing roots and are due mainly to the first symmetric vertical wing bending vibration. Moreover, maneuvers, gust loads, the landing impact, and airdrops (e.g. water for fire fighting, bombs) cause static load peaks mainly at the wing roots. The reduction of static wing loads is generally achieved by lift distribution control systems as state of the art [63]. However, this thesis is concerned with the

alleviation of aircraft vibration, in particular with the *reduction of vertical wing bending vibrations*.

In the 1950's the problem of aircraft vibration was intensely investigated by SCANLAN & ROSENBAUM [99]. Active wing bending vibration control was applied on a commercial aircraft in the 1970's, when an active wing load alleviation system was developed to be able to increase the wing span of the L-1011 commercial transport aircraft without reinforcement of the wing structure, see JOHNSTON, J. F., ET AL. [66]. Said wing load alleviation system was based on robust feedback of structural accelerations to the aircraft's control surfaces. Even though a very large amount of new control techniques, such as *adaptive vibration compensation* (i.e. feed-forward controller that monitors its own performance and adjusts its parameters in the direction of better performance), has been developed and successfully applied to various application fields of active noise and vibration control in the last decades, control strategies for active wing load alleviation have not changed.

Thus, the objective of this thesis is to investigate if advanced control architectures can be used to increase the performance of active wing bending vibration alleviation on a standard configuration commercial transport aircraft.

1.1 State of the Art

Today active control is utilized to provide reduced trim drag and tail area through stability augmentation (i.e. active control of rigid body modes [111]), as well as to reduce structural fatigue (i.e. active control of structural modes, see [13], [22], [23], [63], [66], [70], [93]). Active control is also used for gust load (or gust response) alleviation [3], [22], [23], [48], [97], [106], [69], to reduce cabin noise [26], [89], [90], [104] as well as to improve ride comfort (e.g. reduction of weather cocking [22]). Another objective of active control, generally applied to modern fighter aircraft is the enhancement of agility and flight performance [10], [11], [16], [103].

Active control of wing bending and fuselage bending modes on transport aircraft today is still based on the same principle that was already used by JOHNSTON ET AL. [66] in the 1970's. On the Airbus A330/A340 and the Boeing 777 *feedback control* drives the control surfaces (i.e. rudder, elevator, ailerons) using measured structural accelerations to reduce oscillations by up to 50%, see DORNHEIM [22]. Thereby, the plant transfer functions vary mainly due to changing filling levels of the fuel tanks during flight operation, compare JEANNEAU ET AL. [63]. The active vibration control design must be robust against these plant variations and thus can only be regarded as a compromise over all flight and load conditions. Robust stability of the feedback controller is generally achieved by the choice of the error sensor positions and the controller transfer function. Advances were made on optimization techniques (especially regarding multi-objective control) rather than on finding new control strategies, see [38], [50], [64], [92], [101]. Current research activities are also dedicated to *gain scheduled control* to

reduce the performance degradation related to robust stability constraints, see [7], [39]. However, the idea of gain scheduled flight control originates from the late 1960s, see [6]. The technical challenge of gain scheduling lies in the transition between different operating points. A key problem in the design of gain scheduled control is to find suitable scheduling variables (e.g. the wing bending frequency for wing bending vibration control.)

Moreover, *feed-forward control* can provide an improved vibration reduction compared to feedback control if a proper reference signal is available [42], [52]. According to DORNHEIM [22] feed-forward control thus should be considered if aggressive efforts in vibration control on aircraft are sought. HAHN & KOENIG [48], and KOENIG ET AL. [69] for example present a gust load alleviation system for the DLR *Advanced Technologies Testing Aircraft System* (ATTAS) with a feedback system for the control of the first symmetric vertical wing bending mode and an additional feed-forward controller for gust load alleviation. A modified alpha probe thereby provided the reference signal for feed-forward control. RYNASKI ET AL. [98] present the design of a feed-forward gust alleviation system that compensates rigid and structural modes. However, RYNASKI ET AL. do not consider whether a suitable reference signal is available, which in fact is valued as the key problem of feed-forward control. SOREIDE ET AL. [106] and ROBINSON [97] suggest the use of a LIDAR (light detection and ranging) sensor for predictive control of static gust loads. For the control of atmospheric turbulence excited vibrations such LIDAR systems are not yet accurate enough to provide a proper lead-time reference signal [100]. However, an alpha probe mounted at the front fuselage can easily provide a lead-time reference for vertical winds and gusts as shown by SLEEPER [105]. SLEEPER used alpha probe sensors mounted on the nose and on the wing tips of the NASA B-57B test airplane to investigate the validity of the von Kármán atmospheric turbulence model [112], [113] in rough atmosphere. HECKER & HAHN [54] propose a sensor fusion algorithm in order to combine the accuracy of the alpha probe with the lead-time advantage of a LIDAR for dynamic feed-forward control of gust loads.

Moreover, advanced control concepts can often be found on military aircraft. The Northrop Grumman B-2 stealth bomber already uses a feed-forward control system for gust load alleviation, see [13], [23]. The reference signal is taken from differential pressure sensors on the leading edge of this flying wing aircraft. The Rockwell/Boeing B-1B strategic bomber is equipped with small canard-like control surfaces for active damping of vertical fuselage-bending, see [70]. It is notable that also for future supersonic civil transport aircraft additional control surfaces on the forward fuselage were suggested in RANEY ET AL. [93] in order to actively damp the fuselage bending modes. Moreover, several attempts were made to address vertical tail buffet alleviation of fighter aircraft at high angles of attack, see BREITSAMTER [10], [11] or SHETA ET AL. [103]. Thereby, advances were rather made on using new actuation concepts such as smart materials than on the introduction of new control algorithms. A large amount of research activities addressing active flutter suppression was done since the 1970's, see [1], [2], [25], [41], [73], [84], [85]. In the early 1980's an active flutter suppression

system was flight tested with a transonic drone vehicle. Unfortunately the drone was destroyed in a flutter incident due to an implementation error of the controller [25].

Regarding *adaptive control*, several useful algorithms have been developed and successfully implemented in active control applications. ASTRÖM [6] gives an interesting summary about the developments on adaptive feedback control from the 1960's to the 1990's. A suitable summary of stability Lemmas for adaptive systems can be found in NARENDRA & ANNASWAMY [86]. REW ET AL. [95] have successfully demonstrated an adaptive control algorithm for active damping of a cantilevered composite plate (i.e. idealized delta wing with external loads). They used an adaptive 2^{nd} order band pass controller for each mode to control (i.e. multi-narrowband controller.) Thereby, the center frequency of each band pass controller was continuously updated according to the online identified natural frequencies (i.e. scheduling variables) of the composite plate. The advantage of this adaptive (gain scheduled) control system over fixed feedback control is that optimum performance is maintained also when the natural frequencies of the investigated structure change due to variations of the external load configuration. However, the structure of an entire transport aircraft with pylon mounted engines generally shows a more complex transfer function, higher mode density and higher modal damping than the composite plate in [95]. Thus, on a real aircraft structure a 2^{nd} order band pass controller will probably show less performance than reported in REW ET AL.

A similar adaptive multi-narrowband algorithm, also described in [8], and in [47], was successfully flight tested on the Raytheon 1900D turboprop aircraft for the reduction of blade-passing noise inside the cabin, see PALUMBO ET AL. [89], [90]. The same approach was used for cabin noise reduction on helicopters by active vibration isolation of the rotor/gearbox from the cabin (see for example HOFFMANN ET AL. [57] or MILLOTT ET AL. [80]). In these applications narrowband or tonal noise related to the engine speed is controlled, which is generally easier than controlling broadband disturbances like atmospheric turbulence. However, in TEWES [110] cabin panel vibrations are successfully controlled to reduce tonal as well as random noise.

The technology, where a vibrating structure is controlled for noise reduction is called *Active Structural-Acoustic Control* (ASAC), and is closely related to active vibration control. The main difference is that ANC and ASAC, unlike vibration control seek to reduce noise. Note, that reducing vibration does not necessarily reduce noise (e.g. active vibration control of a robot arm [102]). Efforts in ANC were made in many application fields, see [51], such as reduction of tonal noise (e.g. blade passage frequency of turbofan) radiated by aircraft turbo engines, see MAIER ET AL. [79], and noise cancellation for vehicle [5], [20], helicopter [9] and aircraft cabins [26], [104], to mention only a few applications. However, ANC already is a standard feature in active headsets, in the cabins of the Honda Accord hybrid car and the Acura RL, as well as in the cabin of the Saab 340B-Plus turboprop aircraft [104].

The same (adaptive) algorithms used for ANC and ASAC applications can be used for active wing bending vibration control. Thus, the ANC and ASAC literature is fairly important for this thesis. One of the most popular adaptive algorithms used in many ANC and ASAC applications is the *Least-Mean-Square*-algorithm (LMS-algorithm) which was first described by WIDROW & STEARNS [116]. This adaptive control algorithm is counted to the *steepest descent algorithms* [28]. The LMS-algorithm's architecture is very simple which, regarding certification issues, is very important for implementation on flying vehicles. It also features high robustness against modeling errors. The convergence behavior of the LMS-algorithm is well understood, see [15], [42], [45], [94], [114]. For several simple applications stability proofs are available in the literature, see [8], [75], [82]. The LMS-algorithm like most algorithms for active vibration control requires a plant model, and is therefore counted to the *indirect adaptive control* algorithms.

However, KEWLEY ET AL. [68], as well as MAEDA & YOSHIDA [78] present adaptive ANC systems that do not require a plant model of any kind. These algorithms are likely to only work for alleviation of tonal, time-invariant disturbances (e.g. propeller noise) and to have long convergence time. They are not regarded as useful for broadband disturbance rejection with a time varying plant such as wing bending vibration control on a transport aircraft.

Another application field of active control is *adaptive flight control*, which can be used to optimize the control of the time-varying plant (e.g. adaptive inverse control, see WIDROW & WALACH [117]). Adaptive flight control was also used for the realization of fault tolerant control by PAGE ET AL. [88], who flight tested a *reconfigurable flight controller*, that would automatically re-trim an F/A-18C fighter aircraft in the case of a control surface failure. Another application field of adaptive flight control is the *reduction of pilot excited vibrations*. In general, pilot excited vibrations are alleviated by active damping systems, but it is also possible to add a dynamic signal to the pilot command to drive the actuators in a way, that the aircraft carries out the demanded maneuver at least possible structural vibration excitation. In this context CALISE ET AL. [16] propose *direct adaptive control* (i.e. adaptive control without a plant model, also known as MRAC or *Model Reference Approach Control*) based on a *Neural Network* (NN) controller for the compensation of the flexible dynamics. This approach provides the advantage that structural modes do not have to be filtered out of the flight control system's signals in order to avoid the interaction between flight controls and flexible modes, as it is state of the art [49], [81]. Moreover, the MRAC flight controller smoothly maneuvers the aircraft without excitation of flexible modes by using a model of desired aircraft response (i.e. reference model).

A NN MRAC was also proposed for flight control of a reusable launch vehicle by JOHNSON & CALISE [65]. KROGMANN [71] designed a NN controller for a missile to demonstrate neuronal control of a time-variant nonlinear plant. NN control was also applied to control fighter aircraft in highly non-linear flight conditions such as wing rock at high angles of attack, see CALISE ET AL. [17]. A NN-based direct adaptive flight

controller was flight tested by PRASAD ET AL. [91]. It can be summarized that MRAC (described in detail for example in LANDAU [72] or in KAUFMAN ET AL. [67]) is an excellent adaptive algorithm for the alleviation of pilot excited structural vibrations but does not offer anything new in regards to the reduction of atmospheric turbulence excited structural vibrations. Moreover, NN control architectures were shown to be powerful in controlling nonlinear plants, and can adapt to quickly changing plants (e.g. actuator failure). However, for vibration control of transport aircraft structures which in general behave almost linearly within their flight envelope NN control is not the best choice. Another problem with NN aircraft control is its certification. Procedures would have to be changed to allow for certification of NN controllers. This subject is discussed in detail by CORTELLESSA ET AL. [19].

Summarizing the literature, several ANC and ASAC applications advantageously make use of adaptive algorithms. In many cases tonal noise is reduced [57], [79], [80], [89], [90], etc., or structures with slightly damped modal peaks are controlled respectively (i.e. modal control, see [95]), which in general is easier than broadband control. Successful adaptive control of broadband disturbances in a commercial product is only known from active headsets [34]. Adaptive control methods have also been developed for flight control, see [16], [17], [65], [71], [88], [91], etc., but these algorithms do not seem to be useful for vibration control on a transport aircraft. However, several applications of active vibration alleviation on aircraft based on robust feedback control can be found in the literature [48], [63], [66], [69]. In [98] a feed-forward system for the control of rigid and structural modes is presented without considering the problem of providing an appropriate reference signal. In [54] however, a combination between alpha probe and LIDAR is proposed for the dynamic feed-forward compensation of atmospheric turbulence excited wing bending vibrations.

1.2 The Main Research Objective of this Thesis

As already shown in [119] the performance of wing bending vibration alleviation based on a feedback control system can be improved by the additional use of feed-forward control if a proper reference signal for the atmospheric turbulence excitation is available. The performance of feed-forward control however is more sensitive to modeling errors and plant variations than it is for feedback control. Thus, the main objective of this thesis is to investigate if an *online self-optimization* of *feed-forward wing bending vibration control* can make its performance more robust against plant uncertainties. Thereby, a model of a four-engine example aircraft in different fuel mass and Mach conditions is used for the design of an adaptive controller as well as for validation in numeric simulations.

Moreover, the two-dimensional von Kármán turbulence model is investigated in order to find out in how far an *alpha probe can provide a proper reference signal*. These results are used to obtain an estimate of the performance of feed-forward wing bending

vibration control, as well as for the correct modeling of the control problem for the subsequent numeric simulations.

In order to allow for certification on a flying aircraft another objective of this thesis is to provide a *detailed stability analysis* of the adaptation algorithm. Finally, the proposed adaptive wing bending vibration control system is tested in a wind tunnel experiment in order to demonstrate its implementation, as well as to *study the real-time behavior* of the adaptive wing bending vibration controller and above all, to validate the conditions for robust stability of the adaptation.

1.3 Organization of the Thesis

Following the introduction of Chapter 1, Chapter 2 provides an analysis of the control problem. At first the aircraft model used for the controller design and validation is introduced. Thereafter, the possibilities for wing bending vibration control are discussed. Based on the two-dimensional von Kármán turbulence model, Chapter 2 also features a performance estimation for active alleviation of atmospheric turbulence induced aircraft vibrations with feed-forward control. Said performance estimation is based on the assumption that an alpha probe with quite direct response to alpha variations up to 4 Hz is used for the generation of a proper feed-forward reference signal. Chapter 2 also shows how the required reference for atmospheric turbulence can be extracted from the alpha probe measurement. Finally, Chapter 2 concludes that a hybrid controller (i.e. combination of robust feedback and adaptive feed-forward wing bending vibration control) provides optimum wing bending vibration alleviation, as well as additional active damping of maneuver excited vibrations.

In Chapter 3, the proposed adaptive feed-forward wing bending vibration controller is derived including a detailed stability analysis. The designed controller is validated in numeric simulations in Chapter 4 with the aircraft model introduced in Chapter 2. It is shown that the adaptation algorithm remains stable, and converges to an estimate of the optimum feed-forward controller even in the presence of modeling errors and plant variations. The performances of a robust feedback controller, of the converged adaptive feed-forward controller, and of said hybrid controller are compared. In order to obtain a benchmark for adaptive feed-forward control, a formula for rough performance estimation of non-adaptive feed-forward control is derived. Therewith, Chapter 4 illustrates that an adaptive feed-forward wing bending vibration controller truly provides higher control performance in the presence of plant deviations from the nominal plant than a non-adaptive feed-forward controller. Moreover, it is shown that the proposed adaptive controller is able to track variations in the plant which are due to changing Mach and mass conditions. The converged feed-forward wing bending vibration controller can also compensate discrete gusts.

For the validation of the real-time performance of the proposed adaptive wing bending vibration controller, wind tunnel tests with an elastic aircraft model with a structural

Eigen mode distribution similar to the aircraft model used for the numeric simulations in Chapter 4, have been performed. The results of this test are shown in Chapter 5, proving that the wing bending vibration controller also works perfectly in a real-time environment. In order to provide a perspective, Chapter 6 introduces a recursive adaptive filter for feed-forward wing bending vibration control in order to significantly reduce the number of controller coefficients that have to be updated. However, no stability proof is available yet for this approach. Finally, Chapter 7 summarizes the conclusions of this thesis.

2 Analysis of the Control Problem

During flight, atmospheric turbulence, gusts and maneuvers can excite the structural Eigen modes significantly, especially on large transport aircraft. Thereby, vertical gusts are the most disruptive as they act on the large wing area, see DORNHEIM [22]. Particularly, the first symmetric vertical wing bending mode is responsible for dynamic loads, and the decrease of ride comfort. Therefore, the main control objective in this thesis is the active alleviation of first symmetric vertical wing bending vibrations on a large transport aircraft. Thus, a plant model of only the symmetric dynamics of a large four-engine example aircraft is used for control law design. Due to the changing fuel mass condition and Mach number during flight, an aircraft is generally exposed to variations of its dynamics. Thus, for the control law design and validation, aircraft models for various fuel load and Mach cases are used.

Chapter 2.1 shortly introduces the description and the properties of these models. It is shown that symmetrically driven ailerons represent a suitable actuator for the control of the first symmetric vertical wing bending mode. Chapter 2.2 contains a discussion about the available concepts for active wing bending vibration control. It is explained why the adaptation of feedback control does not provide any notable improvements regarding the trade-off between robust stability and control performance. The performance of feed-forward control in general is more sensitive to variations in the plant, and to modeling errors than feedback control. The adaptation of a feed-forward controller can make its performance more robust against such deviations from a nominal plant model. Moreover, unlike a feedback controller, a feed-forward controller cannot destabilize the plant. It is thus argued that introducing an adaptation algorithm to feed-forward wing bending vibration control truly makes sense.

In Chapter 2.3 the two-dimensional von Kármán turbulence spectrum is used to estimate of the achievable performance of feed-forward wing bending vibration control. It is concluded that a reduction of modal wing bending vibration accelerations of 50% is achievable, when an alpha probe mounted at the front fuselage is used as reference sensor. Chapter 2.4 deals with the modeling of the reference measurement. Finally, Chapter 2.5 concludes that using a hybrid controller (i.e. combination of robust feedback, and adaptive feed-forward wing bending vibration control) an optimum wing bending vibration alleviation, as well as additional active damping of maneuver excited vibrations can be achieved.

2.1 The Example Aircraft Model

The following problem analysis of wing bending vibration control on large transport aircraft is based on state-space models which have been generated in the European AWIATOR project for the design of a feedback control law for active wing load alleviation, compare [63]. Said models are also used for the validation of the adaptive feed-forward wing bending vibration controller designed in this thesis, see Chapter 4. They represent the symmetric aeroelastic dynamics of a large four-engine transport aircraft in trimmed cruise at three different Mach number/altitude combinations (denoted Ma=0.7 Ma=0.82 and Ma=0.86) in the four different fuel mass conditions, shown in Table 2-1. The linearization of the aeroelastic equations at a certain Mach number/altitude/fuel mass case is feasible because Mach number, altitude, and filling levels of the fuel tanks change only slowly compared to the system dynamics. The fuel tanks are located in the outer, the inner, and the centre wing box as well as in the horizontal tail plane.

Table 2-1. Representative fuel tank fillings

	Mass case A	Mass case B	Mass case C	Mass case D
Outer wing tanks	0%	100%	100%	100%
Inner wing tanks	21%	21%	100%	0%
Wing box tank	100%	100%	100%	0%
Trim tank in the horizontal tail plane	0%	0%	100%	100%

The separation of the symmetric structural Eigen modes is possible due to the modal representation of the state-space models. Moreover, under the assumption of quasi-steady state flight, also the longitudinal motion may be separated from the lateral motion, see BROCKHAUS [14].

The symmetric dynamics state-space models' original number of states of around 190 (depending on the mass and Mach case) has been reduced to 41, or to 42 respectively in order to reduce the computational effort for the performed time domain simulations. In this thesis the reduced modal state-space representation of the symmetric plant dynamics reads (with $\mathbf{B}_{ik}$, $\mathbf{C}_{ik}$, and $\mathbf{D}_{ik}$ denoting the elements of the matrices **B**, **C**, and **D**):

$$\begin{pmatrix} \dot{\xi}_1 \\ \dot{\xi}_2 \\ \dot{\xi}_3 \\ \dot{\xi}_4 \\ \dots \\ \dot{\xi}_{\mu-1} \\ \dot{\xi}_{\mu} \end{pmatrix} = \begin{pmatrix} -\zeta_1 \cdot \omega_1 & -\omega_1 \cdot \sqrt{(1-\zeta_1^2)} & 0 & 0 & \dots & 0 & 0 \\ \omega_1 \cdot \sqrt{(1-\zeta_1^2)} & -\zeta_1 \cdot \omega_1 & 0 & 0 & \dots & 0 & 0 \\ 0 & 0 & -\zeta_2 \cdot \omega_2 & -\omega_2 \cdot \sqrt{(1-\zeta_2^2)} & \dots & 0 & 0 \\ 0 & 0 & \omega_2 \cdot \sqrt{(1-\zeta_2^2)} & -\zeta_2 \cdot \omega_2 & \dots & 0 & 0 \\ \dots & \dots & \dots & \dots & \dots & \dots & \dots \\ 0 & 0 & 0 & 0 & \dots & -\zeta_l \cdot \omega_l & -\omega_l \cdot \sqrt{(1-\zeta_l^2)} \\ 0 & 0 & 0 & 0 & \dots & \omega_l \cdot \sqrt{(1-\zeta_l^2)} & -\zeta_l \cdot \omega_l \end{pmatrix} \cdot \begin{pmatrix} \xi_1 \\ \xi_2 \\ \xi_3 \\ \xi_4 \\ \dots \\ \xi_{\mu-1} \\ \xi_{\mu} \end{pmatrix} +$$

$$\begin{pmatrix} B_{11} & B_{12} \\ B_{21} & B_{22} \\ B_{31} & B_{32} \\ B_{41} & B_{42} \\ \dots & \dots \\ B_{(\mu-1)1} & B_{(\mu-1)2} \\ B_{\mu 1} & B_{\mu 2} \end{pmatrix} \cdot \begin{pmatrix} \alpha_w \\ \delta \end{pmatrix}$$

$$\begin{pmatrix} \alpha_{ground} \\ q_{CG} \\ Nz_{CG} \\ Nz_{LW} \\ Nz_{RW} \\ Nz_{front} \\ Nz_{rear} \\ Mx_{WR} \end{pmatrix} = \begin{pmatrix} C_{11} & C_{12} & C_{13} & C_{14} & \dots & C_{1\mu-1} & C_{1\mu} \\ C_{21} & C_{22} & C_{23} & C_{24} & \dots & C_{2\mu-1} & C_{2\mu} \\ \dots & \dots & \dots & \dots & \dots & \dots & \dots \\ C_{81} & C_{82} & C_{83} & C_{84} & \dots & C_{8\mu-1} & C_{8\mu} \end{pmatrix} \cdot \begin{pmatrix} \xi_1 \\ \xi_2 \\ \xi_3 \\ \xi_4 \\ \dots \\ \xi_{\mu-1} \\ \xi_{\mu} \end{pmatrix} + \begin{pmatrix} D_{11} & D_{12} \\ D_{21} & D_{22} \\ \dots & \dots \\ D_{81} & D_{82} \end{pmatrix} \cdot \begin{pmatrix} \alpha_w \\ \delta \end{pmatrix} \tag{2-1}$$

The first equation is called the state equation, and the second one is the measurement equation. The inputs of each model are the atmospheric turbulence induced (span-wise constant) angle of attack variation related to the alpha probe mounting position α_w (i.e. one-dimensional vertical turbulence), and the deflection angle of the symmetrically driven ailerons δ. Unless the ailerons' actuators are driven into saturation, or over rate limits, the actuation mechanism behavior may be approximated as transfer function $F_\delta(s)$. Thus, with $\mathcal{L}\{\delta\}$, and $\mathcal{L}\{u\}$ denoting the Laplace transforms of the symmetrically driven ailerons' deflection angle δ and the input command u, one gets:

$$\mathcal{L}\{\delta\} = F_\delta(s) \cdot \mathcal{L}\{u\} \tag{2-2}$$

With the assumption, that the actuation mechanism's natural frequencies lie high enough to be neglected, $F_\delta(s)$ is represented by a 2nd order low pass filter with a cut-off frequency at about 4 Hz in order to consider the mechanism's inertia. The symbol μ denotes the number of modal states, and l is the number of Eigen modes represented in

the state space model. The matrices **C** and **D** are chosen in order to obtain the following outputs:

- Angle of attack deviation from the static value α_0 at the alpha probe mounting position (measured in a ground reference system) α_{ground}. This angle of attack deviation from the static value is due to aircraft movements and structural vibrations.
- Pitch rate *q* at the CG, denoted q_{CG}.
- Vertical accelerations at the CG, denoted Nz_{CG}, and vertical accelerations at the left and at the right outer engine Nz_{LW}, Nz_{RW}, at the cockpit Nz_{front}, and at the rear fuselage Nz_{rear}.
- Deviation of the vertical wing bending moment at the (left) wing root $M_{x_{WR}}$ from the static value in trimmed 1-g level flight.

The diagonal elements of the **A**-matrix (i.e. $\mathbf{A}_{ii}$) are the real parts of the Eigen values, the secondary diagonal elements are the imaginary parts. For oscillatory Eigen modes both elements arise pair wise, so that a block of four elements of the **A**-matrix describe one imaginary Eigen value. For each mode *i*, ω_i denotes the natural frequency, and ζ_i denotes the damping. Non-oscillatory modes (i.e. real Eigen values) occupy only one element in the **A**-matrix. The advantage of this modal representation is, that one gets *l* independent linear differential equation systems, allowing direct access to the modes. The outputs are calculated by superposition of influences of the different modes. The generated state-space models describe the angle of attack mode as well as several symmetric structural Eigen modes.

For the computation of the example aircraft's aero-elastic dynamics, required for the state-space modeling, full FEM models consisting of beam and shell elements, as well as mass elements have been used. Thereby, the original models' degree of freedom of about $2.5*10^5$ has been reduced to about $2*10^3$ after node condensation. In the following, Figure 2-1 through Figure 2-6 illustrate the first 6 symmetric structural Eigen modes of the four-engine example aircraft. The red arrows illustrate the displacement of the according nodes (in blue color) of the respective Eigen mode:

- Figure 2-1: First symmetric vertical wing bending mode.
- Figure 2-2: Outer engines vertical mode.
- Figure 2-3: Inner engines lateral mode.
- Figure 2-4: First vertical fuselage bending mode.
- Figure 2-5: Outer engines lateral mode.
- Figure 2-6: First symmetric planar wing bending mode.

The dimensions are in meters. The origin is at the nose of the aircraft. The X-axis is positive rearward along the fuselage centerline, the Y-axis is positive to the right, and the Z-axis is positive upwards. In order to obtain the aerodynamic influence coefficients required for the state-space modeling, the Doublet Lattice Method was applied using around $1*10^3$ panels.

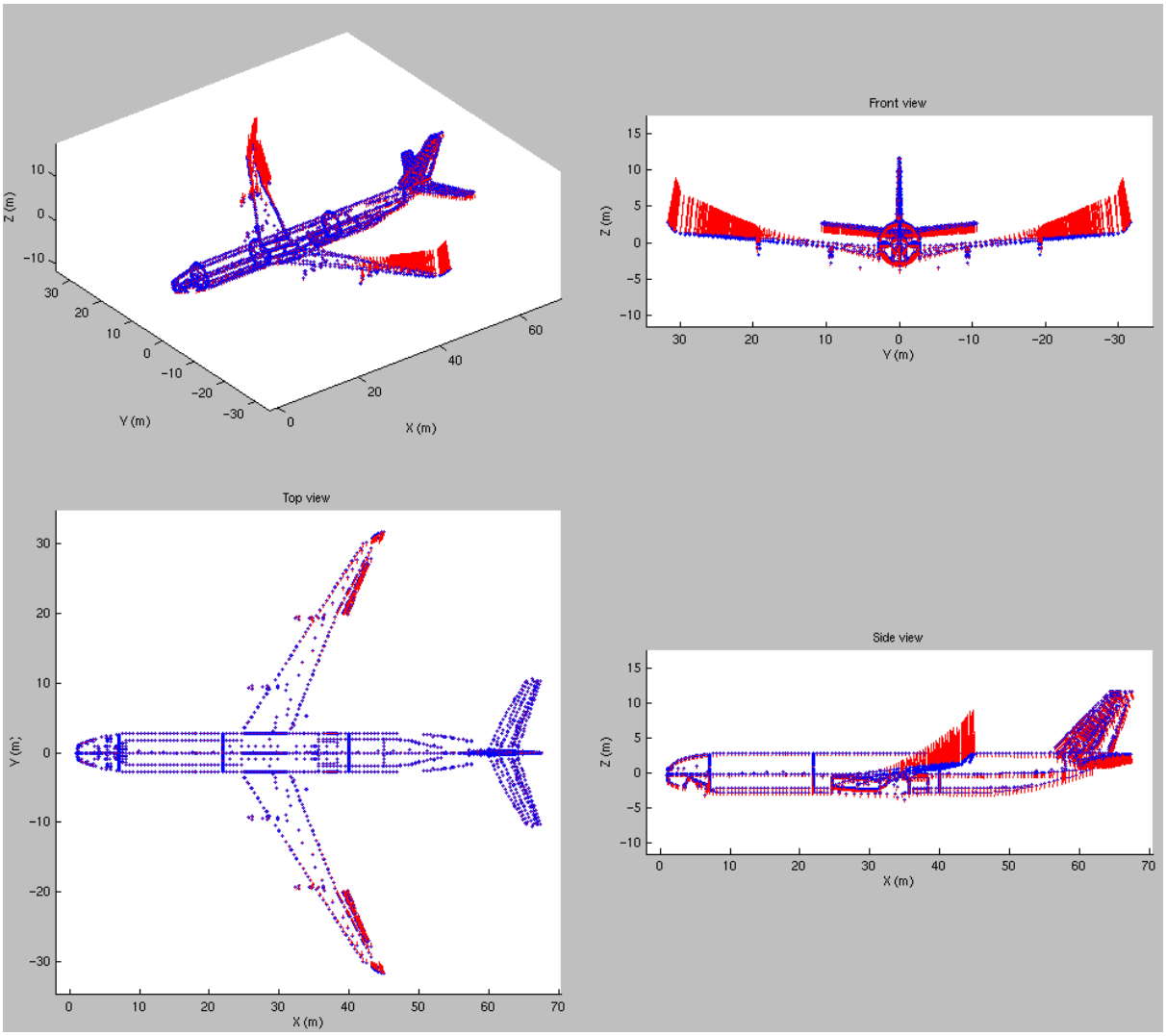

Figure 2-1. First symmetric vertical wing bending mode (internal source).

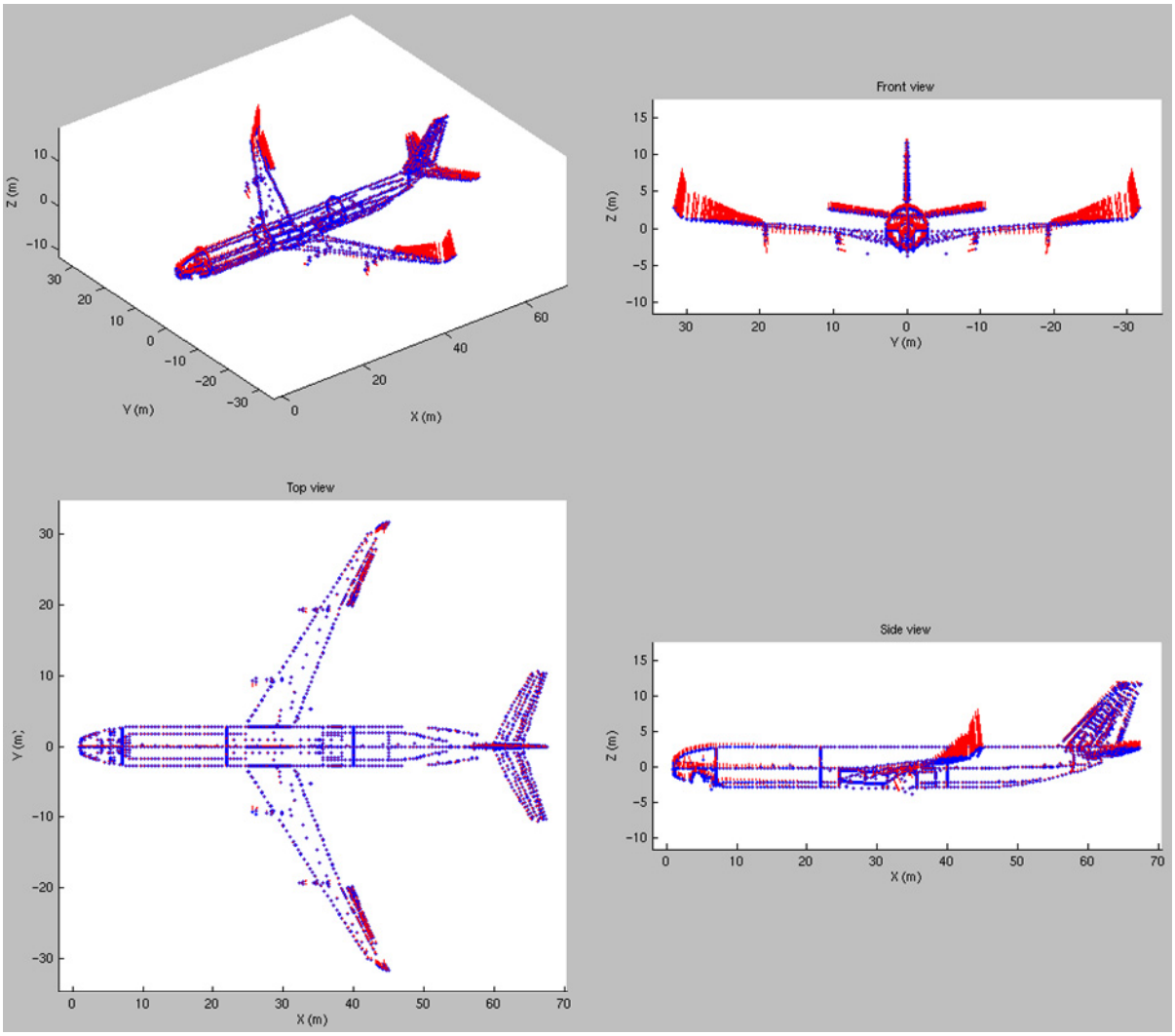

Figure 2-2. Outer engines vertical mode (internal source).

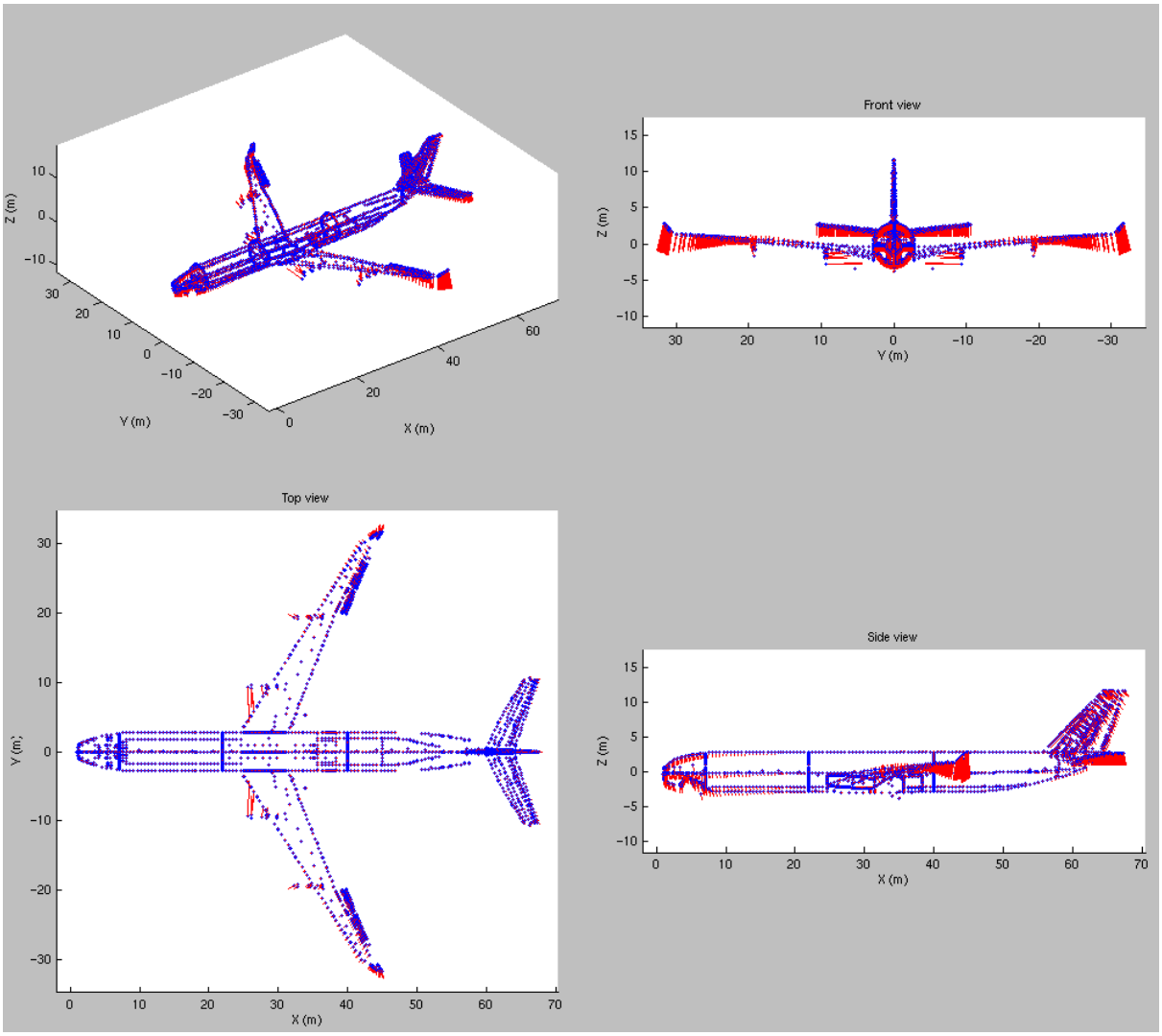

Figure 2-3. Inner engines lateral mode (internal source).

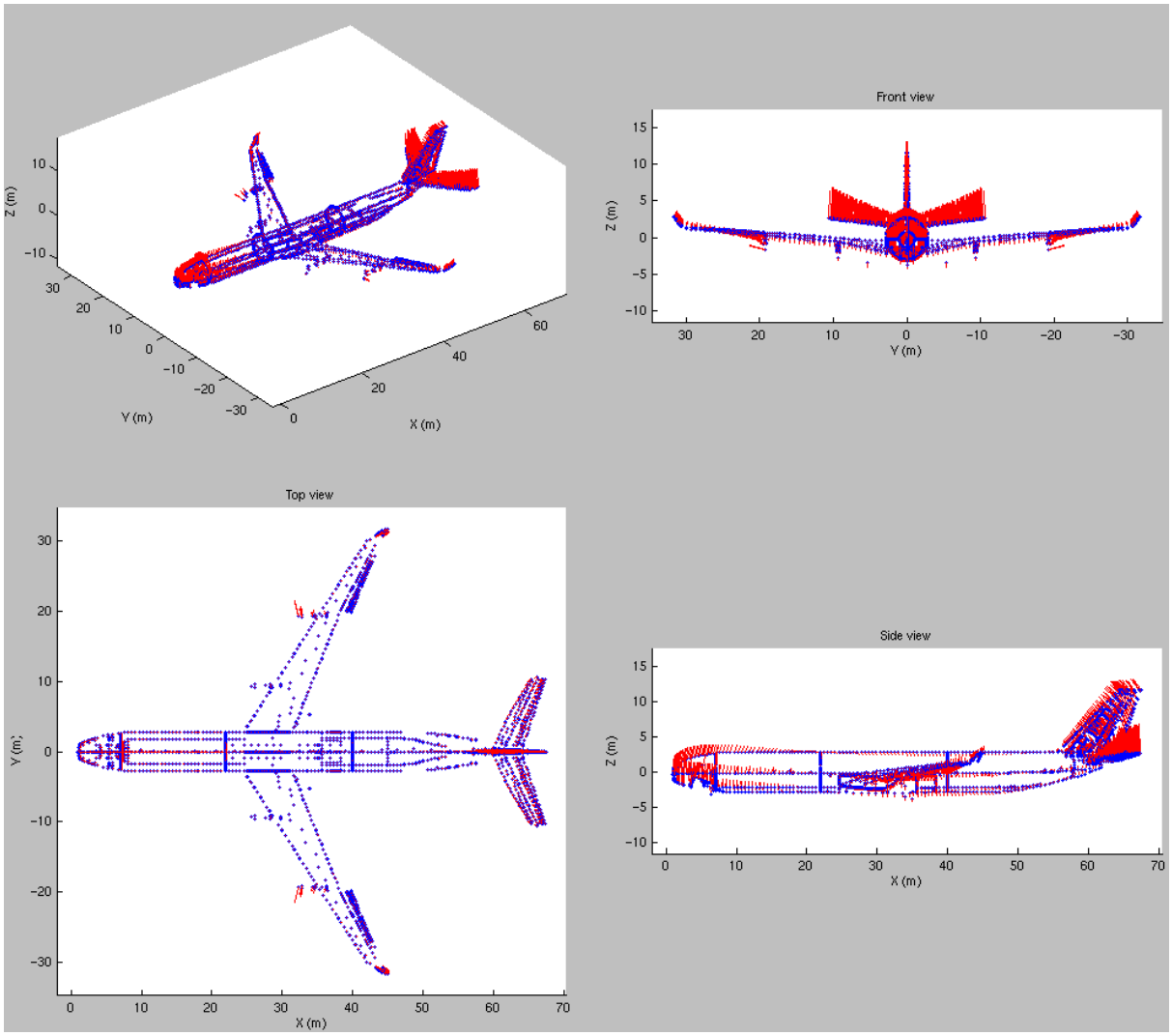

Figure 2-4. First vertical fuselage bending mode (internal source).

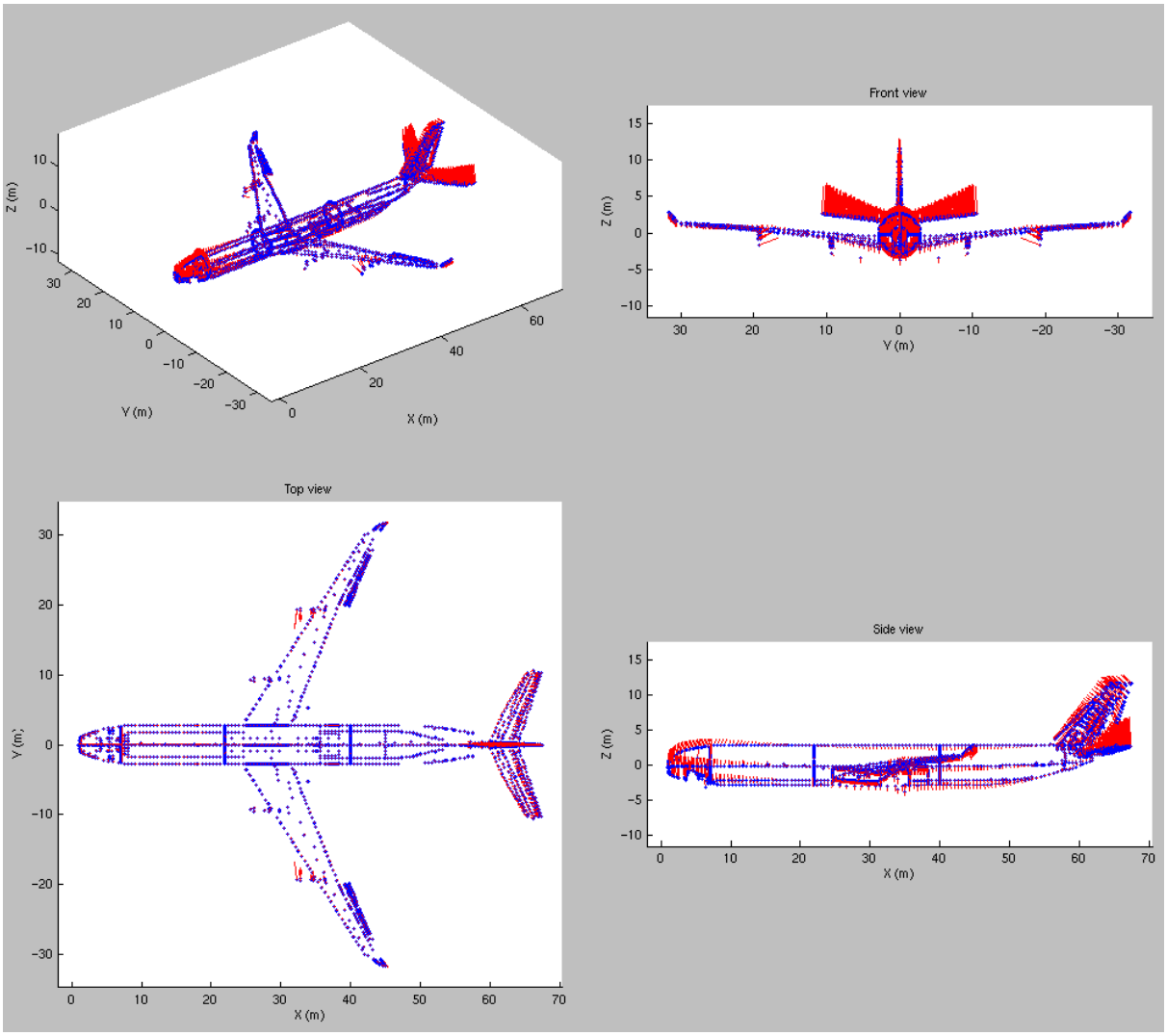

Figure 2-5. Outer engines lateral mode (internal source).

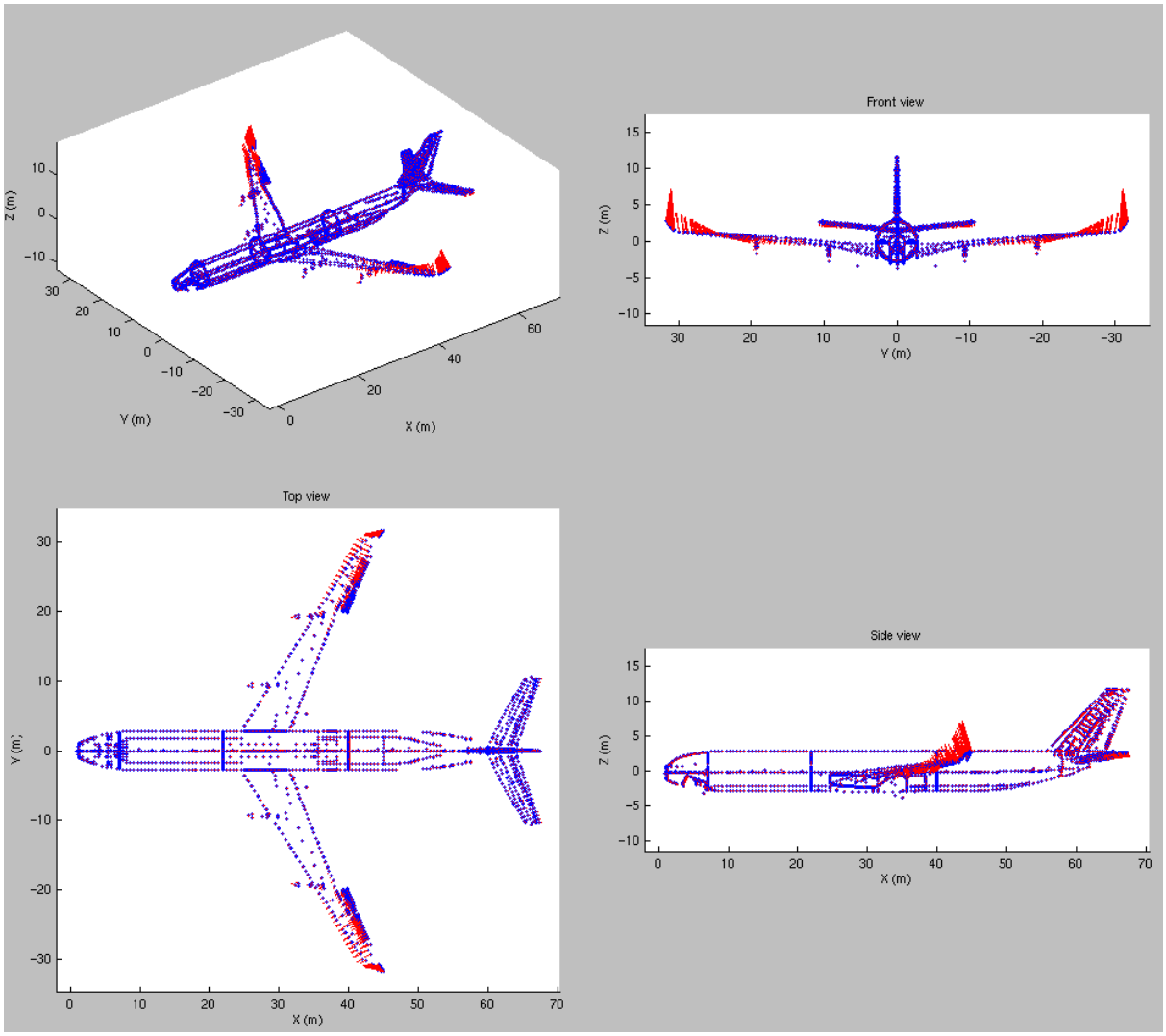

Figure 2-6. First symmetric planar wing bending mode (internal source).

Note, that on the example aircraft the engines are mounted on elastic pylons under the wings, which is generally done for easy maintenance, and to avoid engine excited vibrations, and noise in the fuselage. As illustrated in Figure 2-1 through Figure 2-6 this leads to a coupling between the engine mass/elastic pylon system and the wing and fuselage bending modes, increasing the mode-density of the plant. The aeroelastic behavior of this coupled wing/fuselage/pylon/engine mass system depends on the Mach number, altitude, and on the filling levels of the fuel tanks. The elastic aircraft structure therefore represents a time-variant plant.

If an active vibration controller was optimized for a certain Mach number, altitude, and fuel distribution, it generally will have decreased performance for another Mach number/altitude/fuel mass condition. An active vibration controller thus either must be robust against the expected variations in the plant, or track these variations.

In order to observe mainly vertical wing bending vibrations, a modal acceleration signal $Nz_{law}(t)$, also called error signal $e(t)$ is calculated, as illustrated in Eq. (2-3). As proposed in [63], the vertical accelerations on the two wings at the locations of the outer engines $Nz_{LW}(t)$, $Nz_{RW}(t)$ are added and the vertical acceleration at the *CG* $Nz_{CG}(t)$ is subtracted from half of this value, see Figure 2-7.

This allows for observation of mainly vertical wing bending, but inhibits the measurement of rigid body motions.

$$e(t) = Nz_{law}(t) = \left[\frac{\left(Nz_{LW}(t) + Nz_{RW}(t) \right)}{2} - Nz_{CG}(t) \right] \tag{2-3}$$

Assuming the sensor signals are sampled at 25 Hz for discrete time flight control, a 60 ms time delay was impinged on the error signal $e(t)$ for the sake of completeness. This delay considers a one period delay reserved for pre-filtering of the sensor signal plus an average delay of half a period because orders are executed at any time during the next period. This delay however has no influence on the feed-forward control design.

The green dot in Figure 2-7 marks the location of the example aircraft's alpha probe. Said alpha probe is mounted at the front fuselage, and will be used for feed-forward control in this thesis, compare Chapter 2.2, and all following chapters.

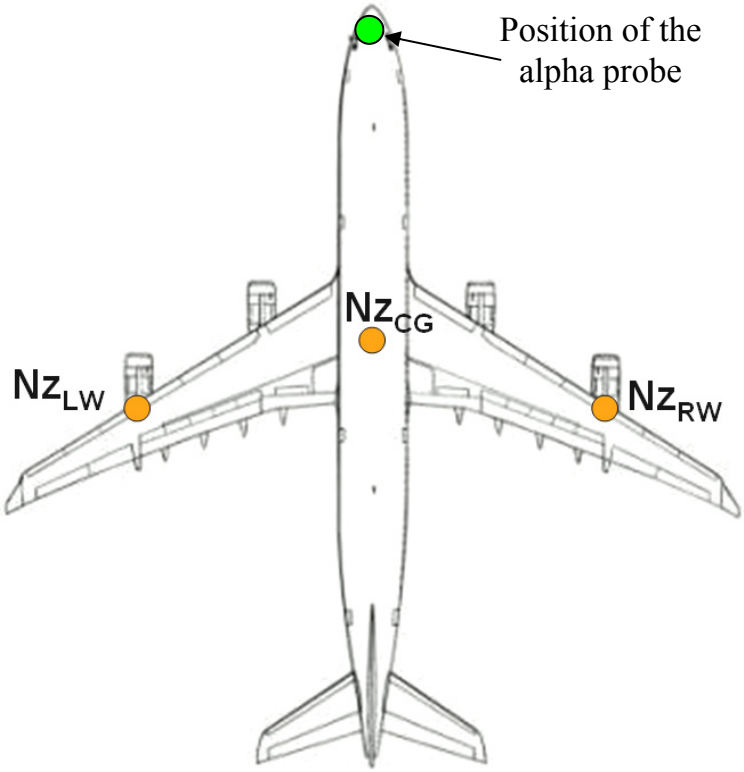

Figure 2-7. Positions of the reference sensor, and of the vertical acceleration sensors on the large four-engine example aircraft.

The control path from the atmospheric turbulence induced angle of attack variation at the alpha probe mounting position $\alpha_w(t)$ to the error signal $e(t)$ is called primary control path (*PCP*). Its transfer function will be denoted $P_c(s)$ in the following. The control path from symmetric aileron deflection command u to the error signal $e(t)$ is the secondary control path (*SCP*). Its transfer function will be denoted $G_c(s)$. Thereby, the subscript "c" denotes that these are the transfer functions of the continuous-time plant. Figure 2-8 illustrates the magnitudes over frequency of the transfer functions from $\alpha_w(t)$ to (from top to bottom):

- The vertical acceleration at the cockpit Nz_{front}.
- The vertical acceleration at the *CG* Nz_{CG}.
- The vertical acceleration at a node at the rear fuselage Nz_{rear}.
- The modal acceleration Nz_{law} (i.e. transfer function of the PCP $P_c(s)$.)

The transfer functions are plotted for the different Mach and mass cases shown in Table 2-1. It can be seen that the ride comfort (i.e. vertical accelerations of the fuselage due to $\alpha_w(t)$) is influenced by the first vertical wing bending vibration, and also by higher Eigen modes. The error sensor (plot at the very bottom) not only measures the first symmetric vertical wing bending vibration (*observability* of the first symmetric vertical

wing bending mode) but also measures higher modes. Thus, pure modal control of the first vertical wing bending vibration is still difficult with this error sensor.

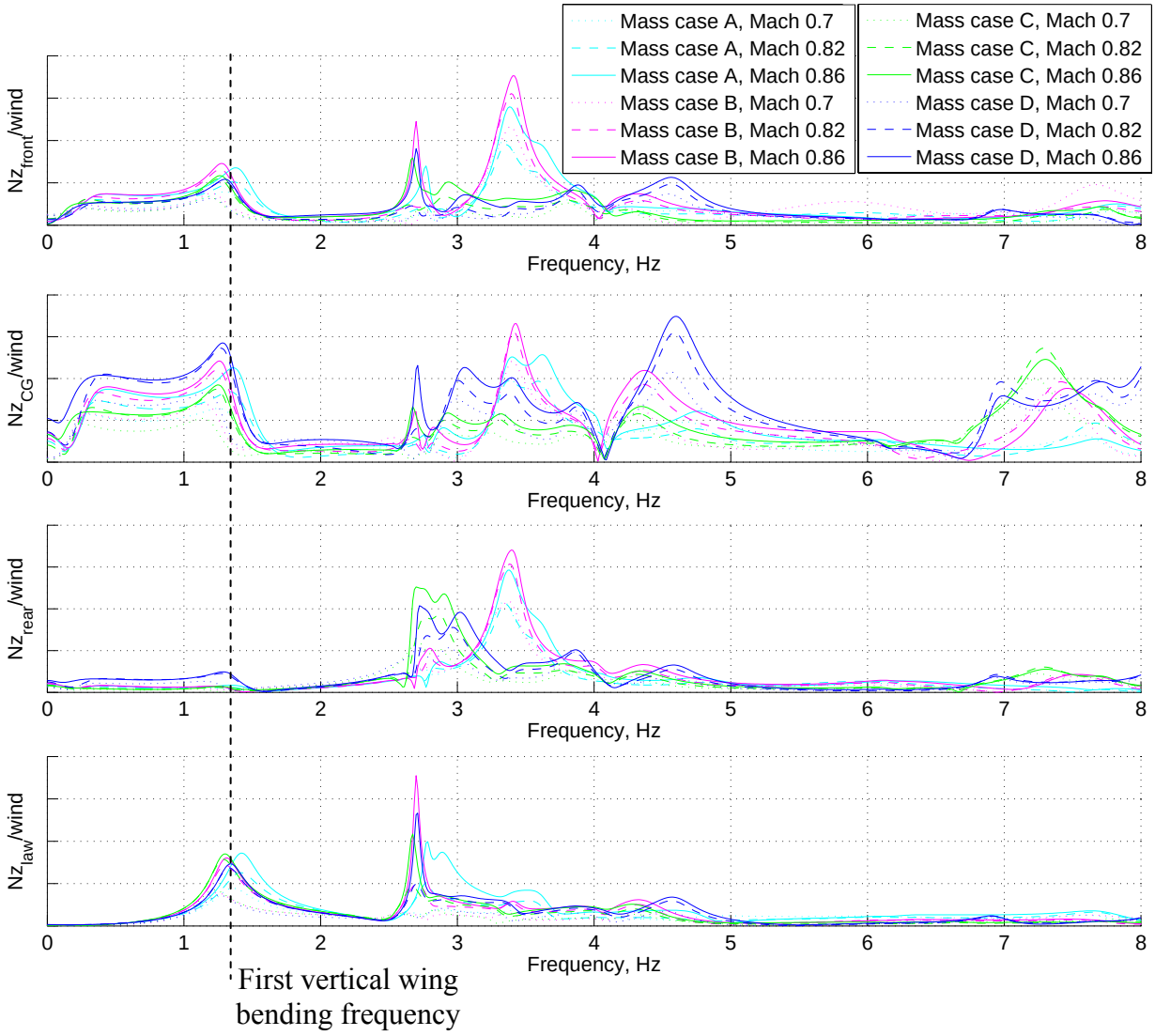

Figure 2-8. Magnitudes of the wind to Nz transfer functions of the four-engine aircraft model.

Figure 2-9 illustrates the magnitudes over frequency of the transfer functions from symmetric aileron deflection command $u(t)$ to (from top to bottom):

- The vertical acceleration at the cockpit Nz_{front}.
- The vertical acceleration at the CG Nz_{CG}.
- The vertical acceleration at a node at the rear fuselage Nz_{rear}.
- The modal acceleration Nz_{law} (i.e. transfer function of the SCP $G_c(s)$.)

Again the transfer functions are plotted for the different Mach and mass cases shown in Table 2-1. It can be seen, that the symmetrically commanded ailerons are indeed a suitable actuator for first symmetric vertical wing bending vibration control (*controllability* of the first symmetric vertical wing bending mode), and in addition can also be used for the control of several higher symmetric Eigen modes. Using the symmetrically commanded ailerons as actuator has the advantage that no additional components have to be implemented on the aircraft.

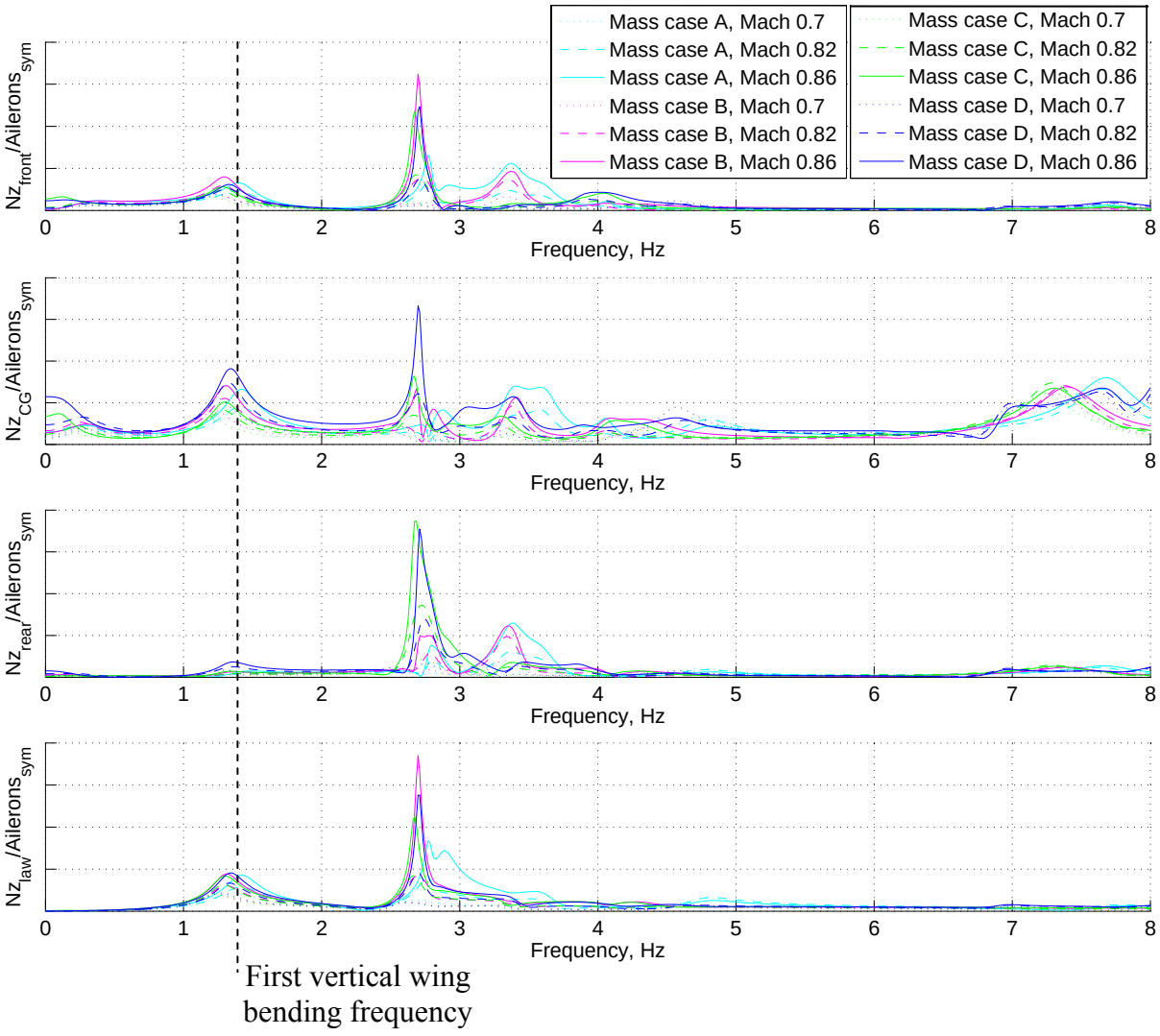

Figure 2-9. Magnitudes of the symmetric aileron command to Nz transfer functions of the four-engine aircraft model.

2.2 Concepts for Active Wing Bending Vibration Control

As will be shown in this section, there are basically two concepts for vibration control [18]. One is increasing the damping of the system by *feedback* control, see Figure 2-10, and the other is compensating the excitation of structural vibrations by *feed-forward* control, see Figure 2-12.

For a SISO (Single Input Single Output) controller, in both cases (feedback and feed-forward) an error signal $e(t)$ measures structural vibrations (or a plant state estimate for state feedback respectively). Regarding feedback control the error signal $e(t)$ is fed to a feedback controller *K(s)* which calculates a proper control input $u(t) = u_{FB}(t)$. The advantages of feedback control are that structural vibrations are alleviated regardless of the excitation (maneuvers, turbulence/gusts, airdrops, etc.), and that the performance is generally more robust against uncertainties in the plant model, than for feed-forward control.

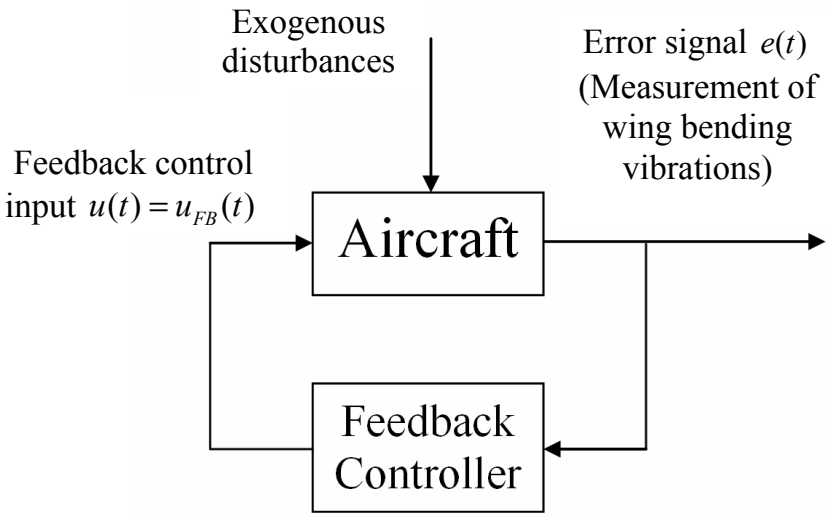

Figure 2-10. Active wing bending damping with a feedback controller.

The objective of the feedback controller in Figure 2-10 is the minimization of wing bending vibrations (i.e. minimization of the error signal $e(t)$) caused by exogenous disturbances (i.e. maneuvers, turbulence/gusts, airdrops, etc.) If said exogenous disturbance is just a span-wise constant angle of attack variation at the alpha probe mounting position $\alpha_w(t)$, the Laplace transform of the error signal $\mathcal{L}\{e(t)\}$ makes:

$$\mathcal{L}\{e(t)\} = \begin{bmatrix} P_c(s) & G_c(s) \end{bmatrix} \cdot \begin{bmatrix} \mathcal{L}\{\alpha_w(t)\} \\ \mathcal{L}\{u(t)\} \end{bmatrix} \tag{2-4}$$

with $\mathcal{L}\{\alpha_w(t)\}$ and $\mathcal{L}\{u(t)\}$ denoting the Laplace transforms of $\alpha_w(t)$ and $u(t)$, and s denoting the complex Laplace variable. In this case the control plant *aircraft* consists of a Primary Control Path (PCP) with transfer function $P_c(s)$, i.e. the transfer function from $\alpha_w(t)$ to the error signal $e(t)$, and a Secondary Control Path (SCP) with transfer function $G_c(s)$, i.e. the transfer function from the control input $u(t)$ (i.e. symmetric aileron command) to the error signal $e(t)$. With the feedback controller *K(s)* the control input $u(t) = u_{FB}(t)$ is calculated by:

$$\mathcal{L}\{u_{FB}(t)\} = K(s) \cdot \mathcal{L}\{e(t)\} \tag{2-5}$$

Thereby, $\mathcal{L}\{u_{FB}(t)\}$ denotes the Laplace transform of $u_{FB}(t)$. The closed-loop dependence of the error signal $e(t)$ on the atmospheric turbulence induced angle of attack variation $\alpha_w(t)$, can be expressed as:

$$\mathcal{L}\{e(t)\} = F(s) \cdot \mathcal{L}\{\alpha_w(t)\} \tag{2-6}$$

$$F(s) = \frac{P_c(s)}{1 - G_c(s) \cdot K(s)} \tag{2-7}$$

For $s = j\omega$ the Fourier transform is obtained with ω denoting the angular frequency, see Appendix G. The aim of the feedback vibration controller design is the minimization of some norm of the closed loop transfer function $F(j\omega)$. Two important norms are the H_∞ and the H_2 norm.

H_∞ norm:
$$\|F(j\omega)\|_\infty = \max_\omega |F(j\omega)| \tag{2-8}$$

H_2 norm:
$$\|F(j\omega)\|_2 = \left(\frac{1}{2\pi} \cdot \int_{-\infty}^{\infty} |F(j\omega)|^2 \, d\omega \right)^{1/2} \tag{2-9}$$

The minimization of the H_∞ norm corresponds to a minimization of the maximum value of the frequency response magnitude of $F(j\omega)$, while the H_2 norm minimization aims at minimizing the total energy of the magnitude of $F(j\omega)$.

Regarding Figure 2-8 and Figure 2-9, if only the first wing bending damping shall be increased, the H_∞ minimization can be used for controller design (i.e. H_∞ synthesis), as described in JEANNEAU ET AL. [63]. If the damping of all structural modes with frequencies e.g. < 4 Hz shall be increased (e.g. to reduce the total energy which the wing structure has to absorb), H_2 minimization will be more practical (i.e. H_2 optimal controller). According to ELLIOT [33] pure H_2 minimization of the closed loop transfer function $F(j\omega)$ leads to rather aggressive control with potentially poor robustness. Thus, it is recommended to include the additional constraints of robust stability in regards to modeling errors and plant variations, as well as the constraint of limited disturbance enhancement outside the frequency range of control.

In general a *robust* feedback controller must provide a robust stability margin for changes in the plant transfer functions and modeling errors [4]. Thus, every controller design poses a trade-off between robust stability margin and performance. An *adaptive* feedback control algorithm however would minimize the respective norm of $F(j\omega)$ in regards to the transfer functions of the PCP, and the SCP, as well as in regards to the actual excitation. Thus, the control design would not need a robust stability margin against plant uncertainties any more and thus can provide a better performance. However, there are 3 possible reasons for instability of adaptive feedback control:

1. Instability of the closed feedback loop
2. Instability of the adaptation
3. Instability of the adaptive feedback controller

It is quite difficult to formulate an optimization criteria for the minimization of a norm of $F(j\omega)$ explicitly considering plant and disturbance uncertainties, and at the same time to assure that none of the three possible instabilities occur. One possibility of realizing adaptive feedback wing bending vibration control would be to monitor the wing bending frequency, or other related parameters (i.e. fuel tank filling levels, Mach number,…), and switch or interpolate between different feedback controllers, as proposed by AYACHE ET AL. [7]. This concept, also known as gain scheduling, deems very promising. The technical challenge of gain scheduling mainly lies in the transition between different operating points. A simpler adaptive solution would be to move the center frequency of a band-pass feedback controller according to the online-identified wing bending frequency like proposed by REW ET AL. [95]. Such *parameter-adaptive* methods seem to be the only useful solutions for the realization of adaptive feedback wing bending vibration control. Parameter-adaptive feedback control, also proposed in [60] is not further investigated in this thesis.

Another common method (which was originally proposed by NEWTON ET AL. [87] for the analytical design of linear feedback control), which can be used for a fairly simple implementation of adaptive feedback control algorithms (see [35]), is the reorganization of the feedback control system in the form shown in Figure 2-11. This scheme is called *Internal Model Control* (IMC) formulation of the feedback control problem. Today this formulation is widely used for robust feedback controller design.

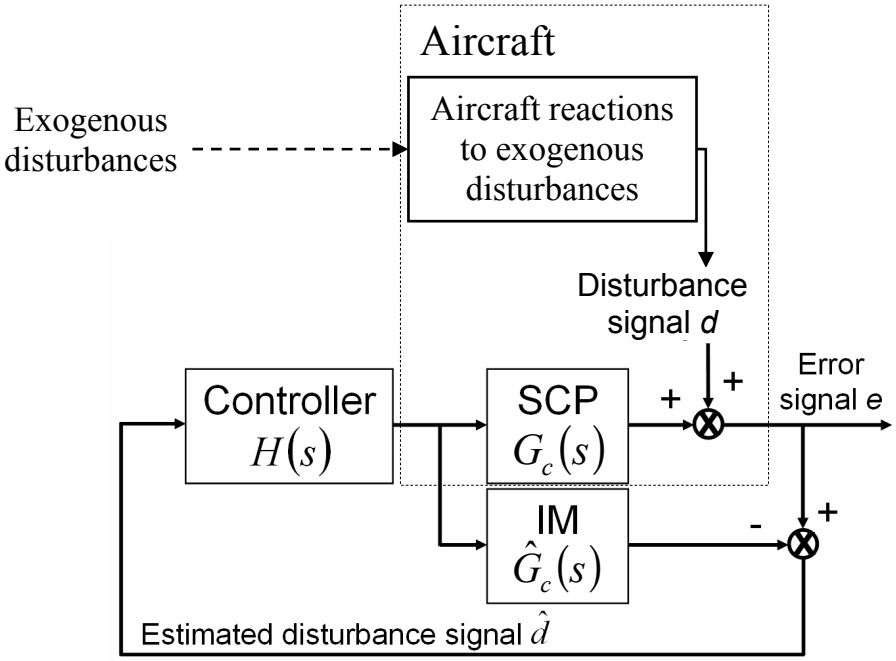

Figure 2-11. IMC-scheme.

The *effect* of exogenous disturbances on the error signal is thereby represented by the so-called disturbance signal $d(t)$. Said effect is not regarded as common signal (since the exogenous disturbances contain the spatial turbulence distribution) and is thus illustrated by a dashed arrow from exogenous disturbances to the according aircraft reactions. The Internal Model (IM) is a model of the SCP transfer function $G_c(s)$ with transfer function $\hat{G}_c(s)$. If $\hat{G}_c(s)$ was a perfect representation of $G_c(s)$, the IMC-scheme would be a perfect compensator like controller (i.e. estimated disturbance signal $\hat{d}(t) = d(t)$), though without any lead-time. Thus, the optimum (pseudo feed-forward) controller $H_{opt_{IMC}}(s)$ would be:

$$H_{opt_{IMC}}(s) = -\frac{1}{G_c(s)} \tag{2-10}$$

Thereby, $H_{opt_{IMC}}(s)$ is only realizable if the SCP transfer function $G_c(s)$ is minimum phase (i.e. $1/G_c(s)$ is stable), and if there was no delay in the SCP (i.e. $1/G_c(s)$ is causal). These constraints generally limit the performance of IMC. Moreover, *adaptive* IMC is suitable for control of non-steady state disturbances when $G_c(s)$ is very accurately known. However, if the SCP is not accurately known or exposed to variations during operation (i.e. $\hat{G}_c(s) \neq G_c(s)$) the adaptation even decreases the robust stability margins of the IMC, compare ELLIOT [35].

If a proper reference $\alpha(t)$ for the exogenous disturbances is available (in this thesis i.e. the measurement of atmospheric turbulence with e.g. an alpha probe mounted at the front fuselage, see Figure 2-7), the wing bending vibration excitation can be compensated by feed-forward control, avoiding said problems of IMC, see Figure 2-12. In order to get optimal performance with a causal feed-forward controller $H(s)$, the time interval it takes for the exogenous disturbances to affect the error signal $e(t)$ must be longer than the time it takes the feed-forward controller to affect the error signal, compare BURDISSO ET AL. [15]. This implies that the disturbance is measurable before it excites the plant. The performance advantage compared to feedback control is that a proper (feed-forward) control input $u(t) = u_{FF}(t)$ is already available when the disturbance excites the plant.

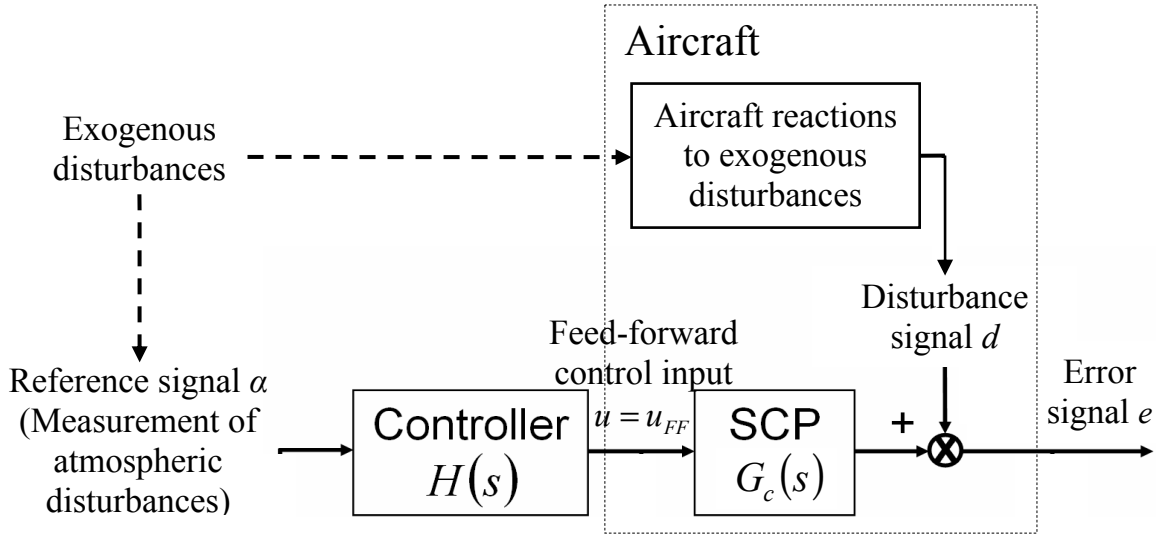

Figure 2-12. Alleviation of structural vibrations with a feed-forward control algorithm.

Moreover, FULLER ET AL. [42] argue that, since feed-forward control is more sensitive to magnitude and phase errors than feedback control, the need for an adaptive algorithm is greater for a feed-forward system than for a feedback one. Moreover, there are only 2 possible reasons for instability of adaptive feed-forward control:

1. Instability of the adaptation
2. Instability of the adaptive feed-forward controller, which can be avoided by monitoring $H(s)$ during adaptation

Assuming that the reference signal has at least the lead-time to compensate the computational delay of the controller plus the delay of the SCP minus the delay of the PCP, the optimum feed-forward controller is causal. Furthermore, a feed-forward controller cannot destabilize the plant, since the system dynamics remain untouched. Thus, adaptive feed-forward control in general may adapt more aggressively than adaptive feedback control. The design of the adaptive feed-forward wing bending vibration controller is discussed in Chapter 3.

2.3 Estimation of Expected Performance of Feed-Forward Control

The performance of the proposed feed-forward compensation of atmospheric turbulence excited wing bending vibrations depends mainly on the coherence between the reference signal α, and the disturbance signal d (i.e. the error signal when the feed-forward wing bending vibration controller is turned off), see [30], [43].

$$\frac{S_{ee_{\min}}\left(e^{j\omega T}\right)}{S_{dd}\left(e^{j\omega T}\right)} = 1 - \frac{\left|S_{\alpha d}\left(e^{j\omega T}\right)\right|^2}{S_{\alpha\alpha}\left(e^{j\omega T}\right) S_{dd}\left(e^{j\omega T}\right)} = 1 - \gamma_{\alpha d}{}^2\left(e^{j\omega T}\right) \tag{2-11}$$

The derivation of the term $\gamma_{\alpha d}{}^2\left(e^{j\omega T}\right)$, which is called the (quadratic) coherence function between the reference signal α, and the disturbance signal d, is shown in Chapter 3. $S_{dd}\left(e^{j\omega T}\right)$ is the power spectral density of the disturbance signal d, defined as:

$$S_{dd}\left(e^{j\omega T}\right) = \left\langle D^*\left(e^{j\omega T}\right) D\left(e^{j\omega T}\right)\right\rangle \tag{2-12}$$

Thereby, $D\left(e^{j\omega T}\right)$ is the Fourier transform of the *sampled* disturbance signal $d(n)$ with discrete time step n, angular frequency ω, sample period T and (non-dimensional) normalized angular frequency ωT, compare [27]. The superscript * denotes complex conjugation, and $\langle ... \rangle$ denotes the expectation value of the quantity inside the brackets. $S_{ee_{\min}}\left(e^{j\omega T}\right)$ is the minimum control error, i.e. the minimum attainable power spectral density of the error signal e. $S_{\alpha\alpha}\left(e^{j\omega T}\right)$ is the power spectral density of the reference signal α. The term $S_{\alpha d}\left(e^{j\omega T}\right)$ denotes the cross spectral density between the reference signal α and the disturbance signal d:

$$S_{\alpha d}\left(e^{j\omega T}\right) = \left\langle A^*\left(e^{j\omega T}\right) D\left(e^{j\omega T}\right)\right\rangle \tag{2-13}$$

with $A\left(e^{j\omega T}\right)$ denoting the Fourier transform of the *sampled* reference signal $\alpha(n)$. The higher the coherence function between α and the disturbance signal d, the smaller the remaining control error. For the theoretic value of $\gamma_{\alpha d}{}^2\left(e^{j\omega T}\right) = 1$ the minimum control error is zero, which means that the wing bending vibrations can be completely erased through feed-forward control. In this thesis the reference signal α is provided by an angle of attack measurement at the front fuselage, compare green dot in Figure 2-7. That means that atmospheric turbulence is measured at only one point of the generally span-wise turbulence distribution and thus, the coherence between the reference signal α and the disturbance signal d will be far from one.

One way to analytically formulate the span-wise turbulence distribution is by a two-dimensional von Kármán spectrum, compare [59]. This formulation is widely accepted and also validated by flight tests in rough atmosphere with the NASA B-57B test airplane, see [105]. The quadratic coherence function $\gamma_{ab}{}^2(\omega)$ of the vertical flow field variations between two span-wise separated points "a" and "b" can be expressed as:

$$\gamma_{ab}{}^2(\omega)=\frac{\left|\hat{K}_t(\omega,\overline{ab})\right|^2}{\hat{K}_t(\omega,a)\hat{K}_t(\omega,b)}=\frac{2^{\frac{4}{3}}\cdot 1.339^2\cdot\pi}{2\cdot[\Gamma(1/3)]^2}\cdot\left[\frac{\frac{8}{3}\cdot(w(\omega))^{\frac{5}{6}}\cdot K_{5/6}(v(\omega))-(w(\omega))^{\frac{11}{6}}\cdot K_{11/6}(v(\omega))}{\left[1+\frac{8}{3}\cdot\left(1.339\cdot L\cdot\frac{\omega}{V_{TAS}}\right)^2\right]\Big/\left[1+\left(1.339\cdot L\cdot\frac{\omega}{V_{TAS}}\right)^2\right]^{\frac{11}{6}}}\right]^2 \tag{2-14}$$

with:
$$w(\omega)=\frac{\overline{ab}}{1.339\cdot L}\cdot\frac{1}{\sqrt{1+\left(1.339\cdot L\cdot\frac{\omega}{V_{TAS}}\right)^2}} \tag{2-15}$$

and with:
$$v(\omega)=\frac{\overline{ab}}{1.339\cdot L}\cdot\sqrt{1+\left(1.339\cdot L\cdot\frac{\omega}{V_{TAS}}\right)^2} \tag{2-16}$$

Thereby, the same notation as in [59] has been used. $\hat{K}_t(\omega,\overline{ab})$ is the cross spectral density between the vertical flow field variations at two span-wise separated points "a" and "b", which depends on the distance between "a" and "b", i.e. $\overline{ab}$. $\hat{K}_t(\omega,a)$ and $\hat{K}_t(\omega,b)$ are the related power spectral densities of the vertical flow field variations at point "a" and point "b". So, the left equation of Eq. (2-14) is in accordance with the right equation of Eq. (2-11). For the right side of Eq. (2-14) it is assumed, that $\hat{K}_t(\omega,a)=\hat{K}_t(\omega,b)$, i.e. the power of the turbulence is constant over the wing-span, which is reasonable as long as phenomena such as wake vortex are excluded. $\Gamma(1/3)$ is the gamma function of $1/3$, and $K_{5/6}(v)$ and $K_{11/6}(v)$ are modified Bessel functions of the second kind for orders five sixths and eleven sixths, respectively. V_{TAS} is the true airspeed and L denotes the integral scale length of turbulence.

The quadratic coherence function $\gamma_{ab}{}^2(\omega)$ has been evaluated for various span-wise separation distances $\overline{ab}$, and for two different integral scale lengths L. Figure 2-13 shows $\gamma_{ab}{}^2(\omega)$ over frequency in Hz for V_{TAS}=260m/s, and for $\overline{ab}=10\,\text{m}$, $\overline{ab}=15\,\text{m}$, and $\overline{ab}=20\,\text{m}$. One can see, that $\gamma_{ab}{}^2(\omega)$ is degraded with increasing $\overline{ab}$, as well as with increasing frequency, and that above 1 Hz (i.e. in the frequency range of structural modes) the integral scale length L has almost no influence on $\gamma_{ab}{}^2(\omega)$, see also [55].

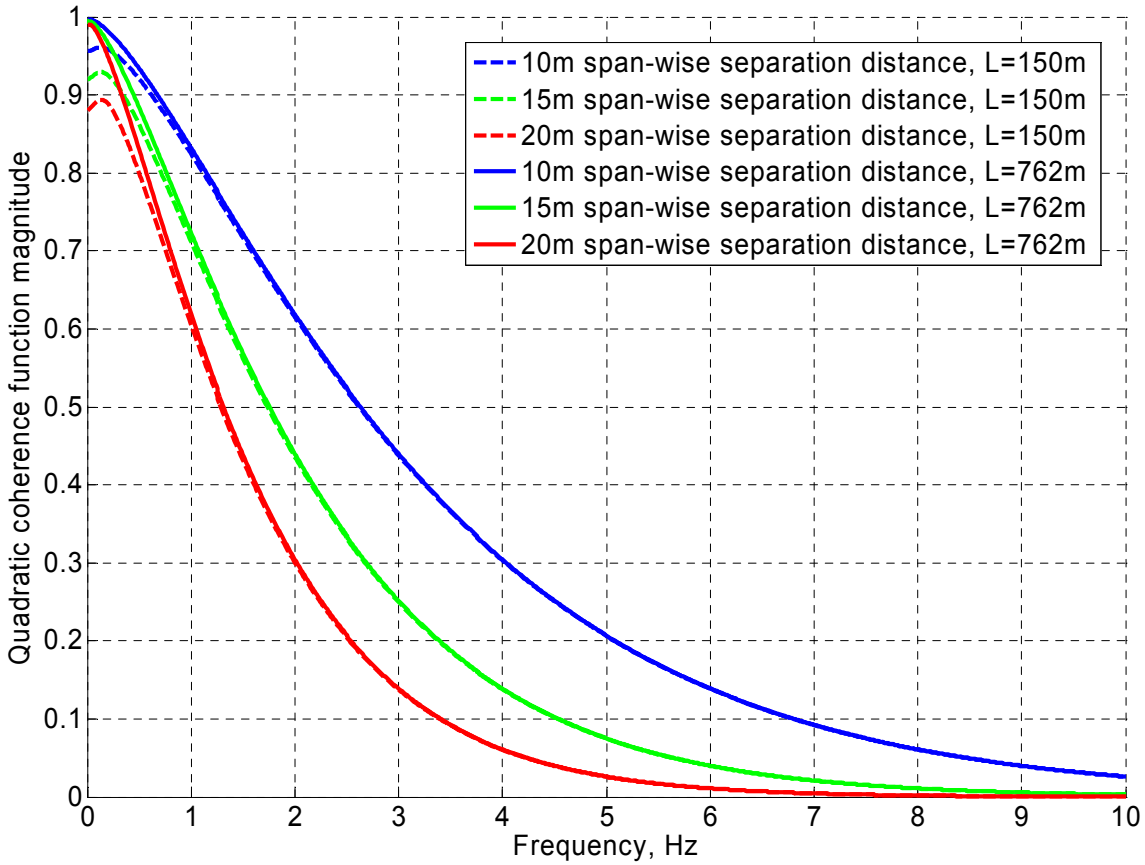

Figure 2-13. Von Kármán turbulence model computed quadratic coherence function between two span-wise separated points “a” and “b”.

A simplified view of the excitation of first symmetric vertical wing bending by span-wise distributed vertical turbulence is to consider a resultant vertical flow rate $v_z(t)$ acting on the aerodynamic center of the wing. The four-engine example aircraft wing’s aerodynamic center has an Y-coordinate of +/-10m to +/-15m. Assuming that the Y-coordinate of the alpha probe is zero, the relevant span-wise separation between reference measurement and wing excitation is between $\overline{ab} = 10\,\text{m}$, and $\overline{ab} = 15\,\text{m}$. Thus, an estimate for the quadratic coherence function between reference measurement and first symmetric vertical wing bending excitation can be read from Figure 2-13. Considering, that the first symmetric vertical wing bending frequency of the four-engine example aircraft is a bit above 1 Hz, an optimistic estimate is $\gamma_{\alpha d}{}^2\left(e^{j\omega T}\right) = 75\%$. The validity of this simple method for the estimation of the quadratic coherence function between the reference signal α, and the disturbance signal d is supported by flight tests results, see Appendix H.

The estimate can also be numerically validated by feeding the outputs of a two-dimensional von Kármán turbulence generator described in [59] to a full model of the four-engine example aircraft. Such a model, containing longitudinal and lateral motion, as well as symmetric, anti-symmetric and asymmetric structural Eigen modes was also used in the European AWIATOR project, compare [54].

Instead of just one gust input α_w as in Eq. (2-1), this full aircraft model has 13 gust inputs distributed over the wing span, which are fed by the 13 outputs of the two-dimensional von Kármán turbulence generator [59]. Figure 2-14 shows the magnitude of the quadratic coherence function $\gamma_{\alpha d}{}^2\left(e^{j\omega T}\right)$ between the reference signal α, and the disturbance signal d, which has been measured in a numeric simulation with two-dimensional von Kármán turbulence and full aircraft model, but without structural control. For this simulation, V_{TAS} =260m/s, and L = 762m, which is the recommended value for L for the determination of gust loads, see HOBLIT [55].

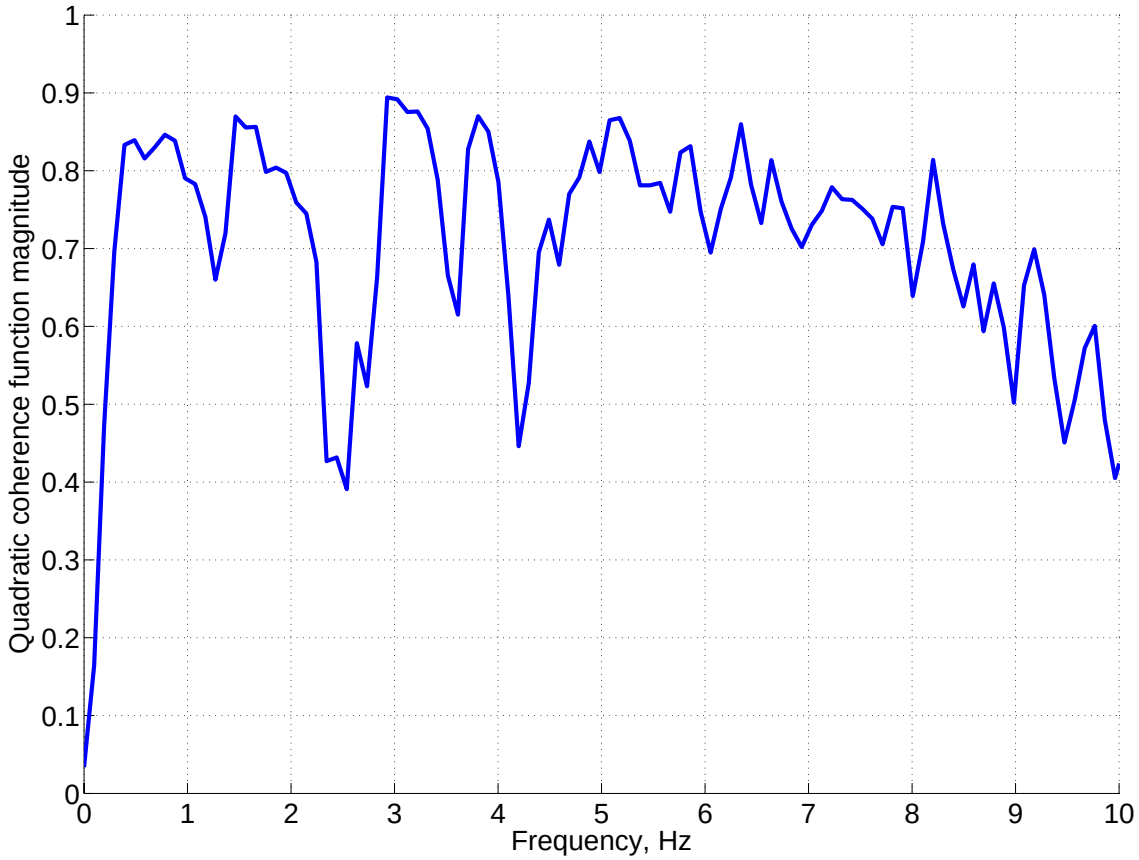

Figure 2-14. Magnitude of $\gamma_{\alpha d}{}^2$ obtained by numeric simulation of mass case D.

In Figure 2-14 the coherence function $\gamma_{\alpha d}{}^2\left(e^{j\omega T}\right)$ is approximately 75% in the frequency range of the first symmetric vertical wing bending mode of the four-engine example aircraft $\omega_{wingbending}$, which (according to Eq. 2-11) is sufficient for a 50% reduction of related vibration accelerations by feed-forward control alone:

$$\frac{\left|E_{\min}\left(e^{j\omega_{wingbending}T}\right)\right|}{\left|D\left(e^{j\omega_{wingbending}T}\right)\right|}=\left[\frac{S_{ee\min}\left(e^{j\omega_{wingbending}T}\right)}{S_{dd}\left(e^{j\omega_{wingbending}T}\right)}\right]^{1/2}\approx 0.5 \qquad (2\text{-}17)$$

2.4 Using the Alpha Probe as a Reference Sensor

It is assumed now, that an alpha probe is available that responds quite directly to angle of attack variations in the controlled frequency range (in this thesis up to 4 Hz), and that has no natural Eigen frequencies in said frequency range. This assumption is reasonable, since the NASA B-57B test airplane described in [105] has an alpha vane sensor with even harder constraints. Excluding flight situations with high span-wise gradients of the turbulence such as flight through a wake vortex, such an alpha probe can provide a proper reference for the turbulence. On the four-engine example aircraft used in this thesis, the delay from an atmospheric disturbance passing the alpha probe till the symmetric deflection of the ailerons (i.e. the overall delay of the feed-forward control system including the alpha probe dynamics, the controller, converters, filters, and the aileron actuation mechanism) must not be larger than about 100 ms in order ensure that the optimum feed-forward controller is causal for all Mach and mass cases.

An alpha probe not only measures gust, and turbulence (i.e. subscript wind), but also aircraft reactions to maneuvers, turbulence/gust, as well as aircraft reactions to the feed-forward control input u_{FF}. The measurable angle of attack at the alpha probe mounting position α_{air}, (i.e. the angle between the aircraft, and the velocity vector of the airflow) can be split up into:

$$\alpha_{air} = \alpha_{wind} + \alpha_0 + \alpha_{ground} = \alpha_{wind} + \alpha_0 + \alpha_{ground_{OL}} + \alpha_{ground_{CL}} \tag{2-18}$$

Thereby, α_0 denotes the static angle of attack of the trimmed aircraft in a ground reference system, (α_0 is a constant in each state-space model of the four-engine example aircraft.) The static angle of attack α_0 can easily be erased by a high-pass filter as shown in [48]. The alpha probe mounting node's angle of attack deviation from this static value α_0 in a ground reference system is denoted α_{ground}, (the term α_{ground} is modeled as an output of the four-engine example aircraft's state-space model.) The feed-forward controller however requires α_{wind} as reference signal. The signal α_{ground} can be split up into an *open loop share* $\alpha_{ground_{OL}}$, and into a *closed loop share* $\alpha_{ground_{CL}}$. The open loop share $\alpha_{ground_{OL}}$ is due to two effects, which are related to rigid body motions and structural vibrations:

I. Aircraft reactions to maneuvers: Aircraft reactions to maneuvers can affect the alpha probe measurement, but must not be interpreted as disturbance in order to prevent the adaptive feed-forward wing bending vibration controller from counteracting any pilot commands. Pilot inputs however are not considered in this thesis.

II. Aircraft reactions to turbulence/gust: The alpha probe measurement of aircraft reactions to turbulence does not contain any lead-time information about the turbulence, and thus can cause a non-causal share in the optimum feed-forward wing bending vibration controller. In the frequency range of structural Eigen modes this effect is negligibly small for the state-space models of the symmetric dynamics

of the four-engine example aircraft (i.e. less than one per cent of the alpha probe signal.)

The closed loop share $\alpha_{ground_{CL}}$, which is due to the coupling between the feed-forward control input u_{FF} and the alpha probe measurement, can even destabilize the system. The control path from u_{FF} to α_{air} is therefore called *parasitic feedback path* with $F_P(s)$ denoting its transfer function:

$$\mathcal{L}\{\alpha_{ground_{CL}}(t)\} = \mathcal{L}\{u_{FF}(t)\} \cdot F_P(s) \tag{2-19}$$

Any significant parasitic feedback has to be compensated. It has been shown in numeric simulations of the proposed adaptive feed-forward wing bending vibration controller that, at least for the example aircraft, parasitic feedback due to coupling via aircraft movements and vibrations is very small in the frequency range of structural modes, see *Appendix E*. Feed-forward control input induced local aerodynamic effects on α_{air} have not been investigated in this thesis, but are expected to be even smaller. Anyway, parasitic feedback is neglected in the derivation of the proposed adaptive feed-forward wing bending vibration control algorithm, as well as in the subsequent stability analysis.

An algorithm for the extraction of α_{wind} from the alpha probe measurement at least in the *frequency range of rigid body motions* is presented in HAHN & KOENIG [48], and in HECKER & HAHN [54]. In conclusion it is to say that the feed-forward vibration control system will work properly only if both the static angle of attack α_0 and α_{ground} are compensated in the frequency range of rigid body motions, and if:

$$\alpha_{wind} >> \alpha_{ground} \quad \text{in the frequency range of controlled structural modes} \tag{2-20}$$

The feed-forward vibration control system should be turned off in flight phases where Eq. (2-20) is not valid (i.e. rough maneuvers in calm atmosphere as worst case) in order to avoid malfunction. For the numeric simulations presented in Chapter 4 rigid body motions *due to turbulence* were *not* compensated. The effect II of the open loop share of α_{ground}, as well as the closed loop share due to structural coupling between u_{FF} and α_{air} have been fully considered without any loss of control performance.

2.5 Conclusions of Chapter 2 – The Hybrid Control Concept

In Chapter 2 the problem of wing bending vibration control has been illustrated. Thereby, state-space models of the linearized symmetric dynamics of a four-engine example aircraft in different Mach and mass conditions serve as plant. A modal sensor (i.e. error sensor) for mainly the observation of the first symmetric vertical wing bending vibration is defined. The symmetrically driven ailerons serve as actuator. The concepts of feedback and feed-forward control have been opposed. Thereby, feed-forward control theoretically can perfectly compensate atmospheric turbulence excited

wing bending vibrations. Essentially, the performance of such a feed-forward system mainly depends on the accuracy of the reference measurement.

It has been shown that using an alpha measurement at the front fuselage as reference sensor can be sufficient for 50% reduction of modal wing bending vibration accelerations by feed-forward control. Since the performance of feed-forward compensation is more sensitive to plant uncertainties than the performance of feedback control, it really makes sense to introduce an adaptive algorithm to feed-forward wing bending vibration control in order to track the generally present variations of the PCP and the SCP, and to compensate any modeling errors.

In order to achieve maximum wing bending vibration alleviation, and additionally actively damp maneuver (and airdrop) excited vibrations, a combination of robust feedback and adaptive feed-forward wing bending control (i.e. hybrid control [18]) is proposed in this thesis, see Figure 2-15. Thereby, the inner control loop increases the damping of the wing bending mode. The adaptive feed-forward controller $H(s)$ aims at the additional compensation of atmospheric turbulence excited wing bending vibrations. The outputs of the robust feedback controller $K(s)$ and the adaptive feed-forward controller $H(s)$ are added, in order to generate the combined signal u_{HY} for the symmetric aileron deflection command:

$$u = u_{HY} = u_{FF} + u_{FB} \tag{2-21}$$

In Figure 2-15 the (slow) adaptation loop from the error signal *e* to the feed-forward controller update is indicated as dashed line in order to illustrate the problem of stability of the controller adaptation. The properties of this (slow feedback) loop are discussed in detail in the following chapters.

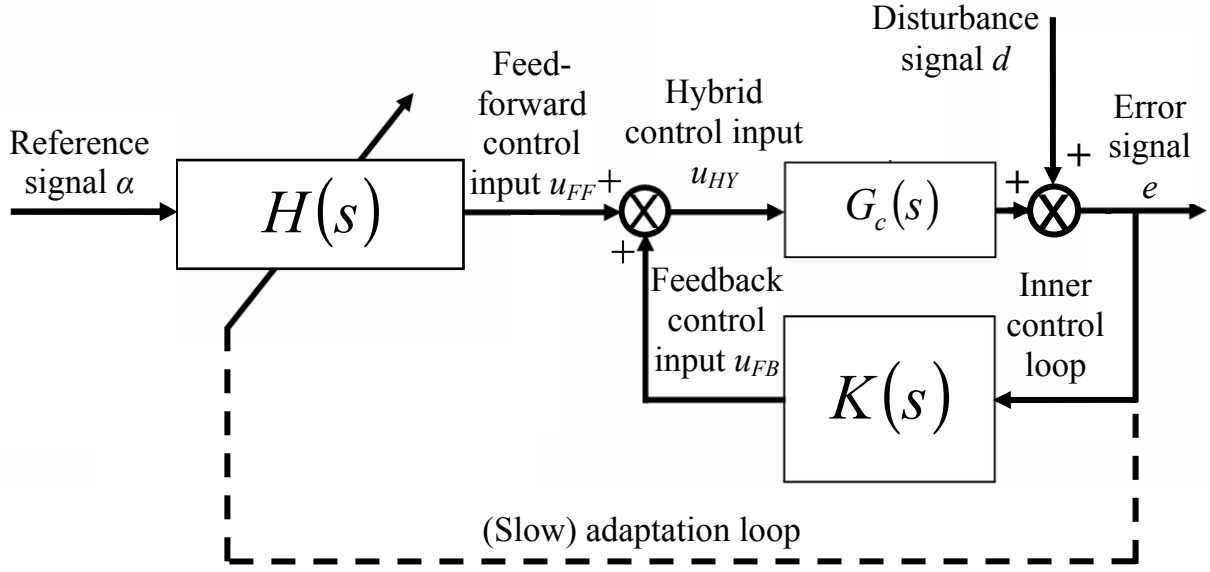

Figure 2-15. Hybrid wing bending vibration control.

3 Wing Bending Vibration Controller Synthesis

The proposed adaptive wing bending vibration control system is designed as shown in Chapter 2.5, see Figure 2-15. An inner control loop feeds the error signal back to the symmetrically driven ailerons in order to increase the damping of the wing bending mode. This robust feedback loop also acts on maneuver excited vibrations. In addition, an adaptive feed-forward control path alleviates the remaining share of the error signal *e* that is correlated with the alpha probe measured atmospheric turbulence.

As proposed by CLARK & BERNSTEIN [18] the design of feedback, and feed-forward controller are separated. The H_∞ optimal feedback controller designed in the European AWIATOR project [63] is used for the inner control loop. The subsequent design of the adaptive feed-forward controller regards the aircraft plus said inner control loop as the plant. The feed-forward controller shall adapt automatically to the changing aircraft dynamics, mainly dependent on the Mach and mass condition.

The proposed adaptive feed-forward control algorithm for the compensation of atmospheric turbulence excited wing bending vibrations is derived in Chapter 3.1. The stability analysis of this algorithm is performed in the frequency domain in Chapter 3.2. For said derivation it is assumed in Chapter 3 that the reference signal α is:

I. *persistently exciting* (i.e. the adaptive controller can be turned on only when a predefined threshold of turbulence strength is exceeded), and
II. *ergodic* (i.e. the ensemble average may be replaced by time average, compare [83].), and
III. has a *zero mean value* in order to avoid static symmetric aileron deflections. This can be ensured by high pass filtering of α_{air}, as also proposed in [48].
IV. The parasitic feedback from u_{FF} to the reference signal is assumed to be small enough to be neglected, i.e. $\alpha_{wind} >> \alpha_{ground_{CL}}$ (The validity of this assumption is supported by the results shown in *Appendix E*), or else $\alpha_{ground_{CL}}$ is compensated.
V. It is also assumed, that the reference signal has *enough lead time* to ensure the causality of the optimum feed-forward controller.
VI. The share in the reference signal that is due to aircraft vibrations excited by turbulence and maneuvers is assumed to be marginal, i.e. $\alpha_{wind} >> \alpha_{ground_{OL}}$ in the frequency range of controlled structural modes, and the influence of rigid body motions on the reference signal is assumed to be compensated.
VII. Sensor noise as well as any offset or measurement bias in the alpha probe are neglected in the following derivation. Neither are Eigen dynamics of the alpha sensor considered, i.e. in conclusion: $\alpha \approx \alpha_{wind}$.

3.1 Design of the Adaptive Feed-Forward Controller

The adaptive feed-forward controller is realized as a digital filter. Common digital controller structures with linear steady-state response (i.e. with linear behavior when not being adapted) are FIR (Finite Impulse Response), and IIR (Infinite Impulse Response) filters. An FIR controller generally needs more coefficients than an IIR controller for the same control task, compare Chapter 6.

On the other hand, since the poles and zeros of an IIR controller are both adaptive, an IIR controller can become unstable. An FIR controller however only has adaptive zeros (i.e. all poles of an FIR controller lie in the origin, see Eq. (3-4)), and therefore can never become unstable, which is in favor of an aspired certification on commercial aircraft. The adaptive feed-forward controller thus is realized as an FIR filter.

An FIR filter generates the discrete-time feed-forward control input $u_{FF}(n)$ from the discrete-time reference signal $\alpha(n)$ with the following vector equation:

$$u_{FF}(n) = \vec{h}^{T} \cdot \vec{\alpha}(n) = \vec{\alpha}^{T}(n) \cdot \vec{h} \tag{3-1}$$

with:

$$\vec{h} = \left[h_0, h_1, h_2 ..., h_{N-1}\right]^T \tag{3-2}$$

Thereby, $h_0, h_1, h_2 ..., h_{N-1}$ are the controller coefficients, and N denotes the filter length of the FIR filter. The superscript ^{T} denotes transposition, and $\vec{\alpha}(n)$ is the vector of the sampled reference signal at time step n.

$$\vec{\alpha}(n) = \left[\alpha(n), \alpha(n-1), ..., \alpha(n-N+1)\right]^T \tag{3-3}$$

Figure 3-1 illustrates the implementation of the FIR filter. The z-transform variable is z, and z^{-1} therefore denotes a one sample delay. So, the delayed versions of the sampled reference signal $\alpha(n)$ are multiplied with the according controller coefficients $h_0, h_1, ..., h_{N-1}$, and are then linearly combined in order to obtain the discrete-time feed-forward control input $u_{FF}(n)$. Thus, the FIR controller's transfer function, which relates the z-transform of the discrete control input sequence $U_{FF}(z)$ to the z-transform of the sampled reference signal sequence $A(z)$, can be written as [27]:

$$H(z) = \frac{U_{FF}(z)}{A(z)} = h_0 + h_1 \cdot z^{-1} + h_2 \cdot z^{-2} + \ldots + h_{N-1} \cdot z^{-N+1} \tag{3-4}$$

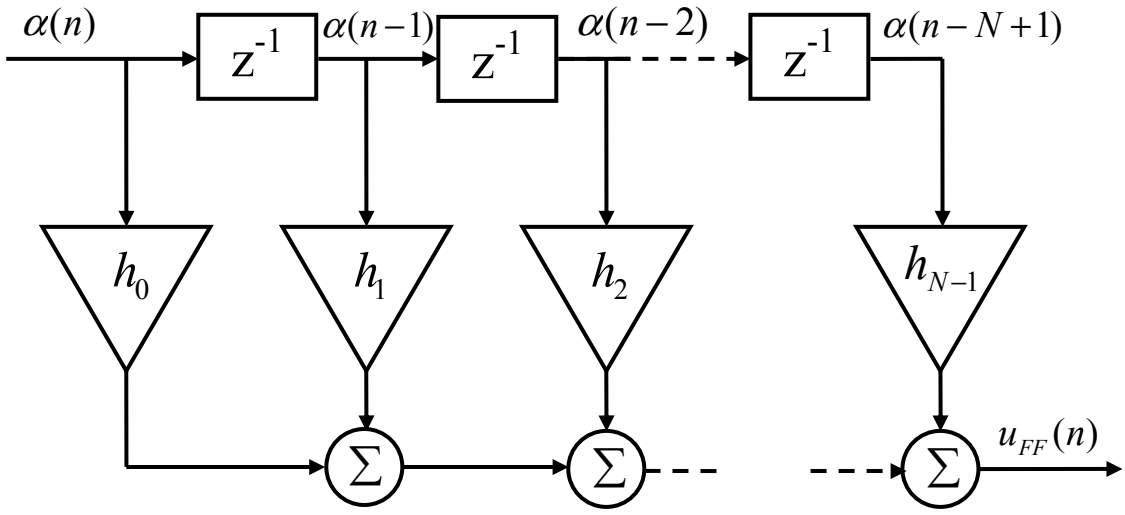

Figure 3-1. Implementation of the FIR controller.

In order to be able to introduce the digital feed-forward controller to the continuous-time plant, the wing bending vibration control system shown in Figure 2-15 is refined as illustrated in Figure 3-2. The sampled reference signal $\alpha(n)$ is fed forward to the adaptive FIR controller $H(z)$ in order to calculate a discrete-time feed-forward control input $u_{FF}(n)$ for the compensation of the continuous time disturbance signal $d_c(t)$. Thereby, $t = n \cdot T$ is the continuous time, with T denoting the sample period, and $Fs = 1/T$ denoting the sampling frequency.

As proposed in [31] the sampled plant transfer function $G(z)$, i.e. the transfer function which is seen by the digital feed-forward controller, is assumed to include not only the continuous-time SCP transfer function $G_c(s)$, but also the Digital to Analogue Converter (DAC) and the Reconstruction Filter (RF) required for the generation of a continuous-time control input that can be forwarded to the (continuous-time) plant, as well as the Anti-aliasing Filter (AF) and the Analogue to Digital Converter (ADC) required to obtain the discrete error signal $e(n)$.

For the sake of generalization it is also presumed in the following derivation that the inner feedback loop for additional active wing bending damping is already included in the transfer function $G(z)$. Moreover, the computational delay of the digital controller is counted to $G(z)$. For completeness it should be mentioned, that an additional AF cuts off frequencies $f > Fs/2$ in the continuous time reference signal $\alpha(t)$ before it is sampled.

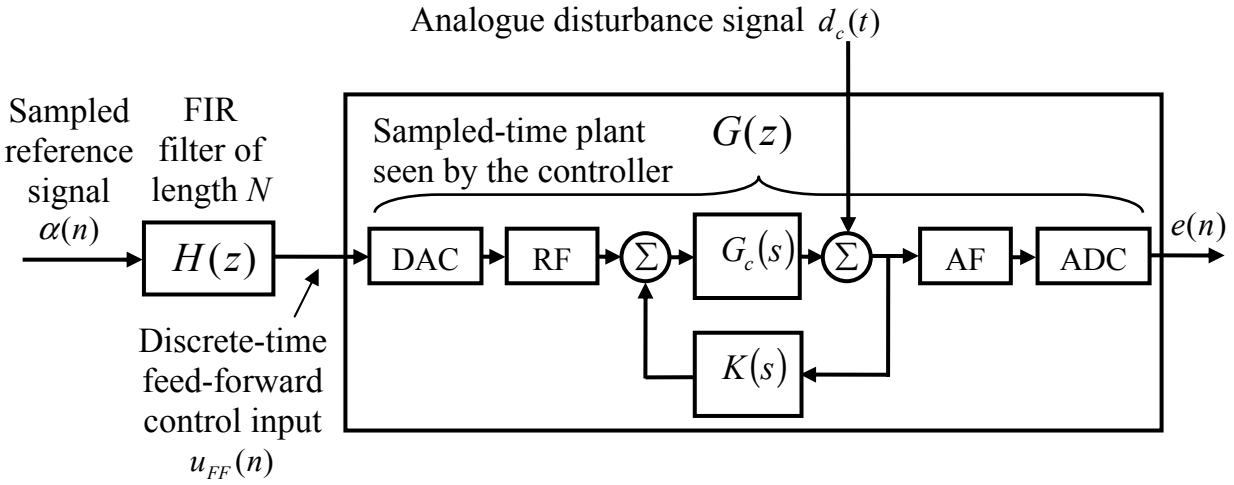

Figure 3-2. Digital feed-forward controller driving the continuous-time plant.

Finally, the sampled-time representation of the proposed wing bending vibration control system can be illustrated as shown in Figure 3-3. Thereby, it is already considered that the new sampled-time disturbance signal $d(n)$ is a sampled version of the analogue disturbance signal $d_c(t)$ filtered by the transfer function of the AF, as well as by $1/(1-G_c(s)\cdot K(s))$, i.e. consideration of the inner feedback loop.

The fact that this new sampled-time disturbance signal $d(n)$ differs from the original continuous-time signal $d_c(t)$ however does not have any consequences on the design of the adaptive control algorithm, and therefore will not be indicated in the notation in the following. The signal $y(n)$ denotes the share of feed-forward control (of the actively damped plant) in the error signal $e(n)$.

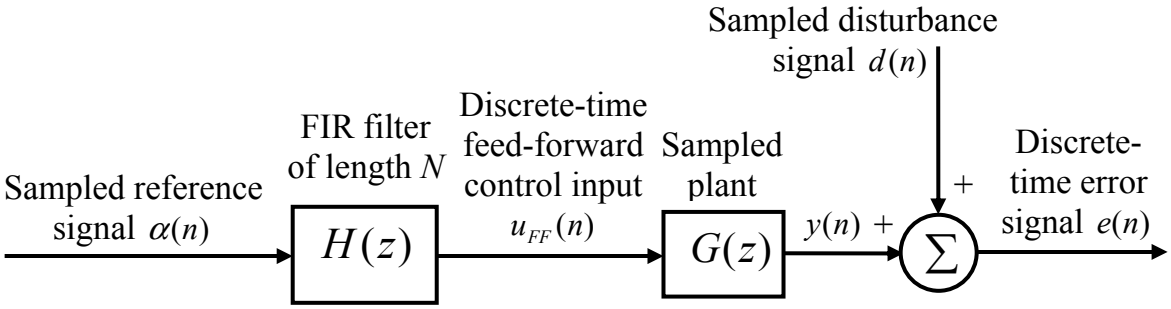

Figure 3-3. Sampled-time representation of hybrid wing bending vibration control.

It is assumed that all signals are steady state, allowing for a frequency domain representation. The applied Fourier transform is considered to be a special case of the z transform with $z = e^{j\omega T}$, where ωT is the (non-dimensional) normalized angular frequency [27]. For the derivation of a proper update law for the adaptive feed-forward

wing bending vibration controller $H(z)$ it is also presumed that the FIR coefficients and the Mach and fuel mass conditions of the aircraft change only very slowly. Under the assumption that $H(z)$ and $G(z)$ are linear quasi-steady state, $H(z)$ and $G(z)$ may be rearranged as shown in Figure 3-4.

For a large transport aircraft in trimmed flight the plant can certainly be regarded as linear quasi-steady state. In order to support the validity of the assumption that the adaptive controller $H(z)$ is quasi-steady state, *Appendix D* shows that the bias that is made by the rearrangement of $H(z)$ and $G(z)$ is marginal in the controlled frequency range.

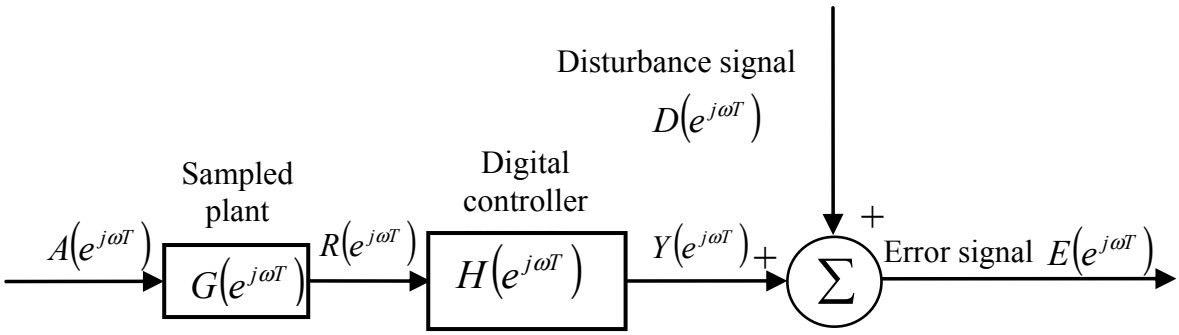

Figure 3-4. Rearranged controller $H(e^{j\omega T})$ and plant $G(e^{j\omega T})$.

The frequency domain reference signal $A(e^{j\omega T})$, filtered by $G(e^{j\omega T})$ is called filtered reference signal $R(e^{j\omega T})$, with $r(n)$ denoting its discrete time-domain representation. The Fourier transformed error signal $E(e^{j\omega T})$ makes:

$$E(e^{j\omega T}) = D(e^{j\omega T}) + Y(e^{j\omega T}) = D(e^{j\omega T}) + H(e^{j\omega T})R(e^{j\omega T}) \tag{3-5}$$

with $D(e^{j\omega T})$ and $Y(e^{j\omega T})$ denoting the Fourier transforms of the discrete-time signals $d(n)$ and $y(n)$, and $H(e^{j\omega T})$ denotes the frequency response of the adaptive FIR controller. The objective is to find the controller $H(e^{j\omega T})$ that minimizes the power spectral density of the error signal $S_{ee}(e^{j\omega T})$.

This optimization criteria assures that there is only one (global) optimum of the FIR filter (also called *Wiener filter*), and that the adaptation therefore cannot be trapped in a local optimum, see [27]. The power spectral density of the error signal $S_{ee}(e^{j\omega T})$ is:

$$S_{ee}(e^{j\omega T}) = \langle E^*(e^{j\omega T})E(e^{j\omega T})\rangle \tag{3-6}$$

Introducing Eq. (3-5) into Eq. (3-6), $S_{ee}\left(e^{j\omega T}\right)$ may be written as:

$$S_{ee}\left(e^{j\omega T}\right)=S_{dd}\left(e^{j\omega T}\right)+S_{rd}{}^{*}\left(e^{j\omega T}\right)H\left(e^{j\omega T}\right)+H^{*}\left(e^{j\omega T}\right)S_{rd}\left(e^{j\omega T}\right)+H^{*}\left(e^{j\omega T}\right)S_{rr}\left(e^{j\omega T}\right)H\left(e^{j\omega T}\right) \tag{3-7}$$

with $S_{dd}\left(e^{j\omega T}\right)$ denoting the power spectral density of the disturbance signal *d*, compare Eq. (2-12), and with the cross spectral density between filtered reference signal *r* and disturbance signal *d* being defined as:

$$S_{rd}\left(e^{j\omega T}\right)=\left\langle R^{*}\left(e^{j\omega T}\right)D\left(e^{j\omega T}\right)\right\rangle \tag{3-8}$$

The power spectral density of filtered reference signal *r* makes:

$$S_{rr}\left(e^{j\omega T}\right)=\left\langle R^{*}\left(e^{j\omega T}\right)R\left(e^{j\omega T}\right)\right\rangle=\left|G\left(e^{j\omega T}\right)\right|^{2}S_{\alpha\alpha}\left(e^{j\omega T}\right) \tag{3-9}$$

Thereby, $S_{\alpha\alpha}\left(e^{j\omega T}\right)$ is the power spectral density of the reference signal α. Eq. (3-7) is a standard Hermitian quadratic form [36]. The complex gradient of $S_{ee}\left(e^{j\omega T}\right)$ is obtained by differentiating the power spectral density $S_{ee}\left(e^{j\omega T}\right)$ with respect to real and imaginary part of the controller's frequency responses $\mathrm{Re}\left\{H\left(e^{j\omega T}\right)\right\}$ and $\mathrm{Im}\left\{H\left(e^{j\omega T}\right)\right\}$:

$$\frac{\partial S_{ee}\left(e^{j\omega T}\right)}{\partial\,\mathrm{Re}\left\{H\left(e^{j\omega T}\right)\right\}}+j\cdot\frac{\partial S_{ee}\left(e^{j\omega T}\right)}{\partial\,\mathrm{Im}\left\{H\left(e^{j\omega T}\right)\right\}}=$$

$$=2\cdot\left[S_{rr}\left(e^{j\omega T}\right)H\left(e^{j\omega T}\right)+S_{rd}\left(e^{j\omega T}\right)\right]=2\cdot\left\langle R^{*}\left(e^{j\omega T}\right)E\left(e^{j\omega T}\right)\right\rangle \tag{3-10}$$

The minimum of $S_{ee}\left(e^{j\omega T}\right)$ is obtained by setting the term $\left[S_{rr}\left(e^{j\omega T}\right)H\left(e^{j\omega T}\right)+S_{rd}\left(e^{j\omega T}\right)\right]$ to zero at each frequency. Under the assumption of a non-singular power spectral density $S_{rr}\left(e^{j\omega T}\right)$ the *unconstrained* optimum controller in the frequency domain thus finally makes:

$$H_{opt}\left(e^{j\omega T}\right)=-\frac{S_{rd}\left(e^{j\omega T}\right)}{S_{rr}\left(e^{j\omega T}\right)} \tag{3-11}$$

For frequencies where the magnitude of $G\left(e^{j\omega T}\right)$ is zero (i.e. non-controllability), no optimum controller exists. *Unconstrained* means, that it is presumed that the optimum controller is realizable [42], so that the time-domain representation of the optimum controller $H_{opt}(z)$ is causal.

The major requirement for the causality of the time-domain representation of the optimum controller is, that the lead-time of the reference signal is long enough, to compensate the delay of the SCP and the feed-forward controller minus the delay of the PCP. It has already been assumed at the beginning of Chapter 3, that this requirement is fulfilled.

Introducing Eq. (3-11) into Eq (3-7) gives the minimum control error $S_{ee_{\min}}\left(e^{j\omega T}\right)$, i.e. the remaining power spectral density of the error signal, when the optimum feed-forward controller is implemented:

$$S_{ee_{\min}}\left(e^{j\omega T}\right) = S_{dd}\left(e^{j\omega T}\right) - \frac{\left|S_{rd}\left(e^{j\omega T}\right)\right|^2}{S_{rr}\left(e^{j\omega T}\right)} \tag{3-12}$$

Normalizing the minimum control error by the power spectral density of the disturbance signal $S_{dd}\left(e^{j\omega T}\right)$ gives:

$$\frac{S_{ee_{\min}}\left(e^{j\omega T}\right)}{S_{dd}\left(e^{j\omega T}\right)} = 1 - \frac{\left|S_{rd}\left(e^{j\omega T}\right)\right|^2}{S_{rr}\left(e^{j\omega T}\right)S_{dd}\left(e^{j\omega T}\right)} = 1 - \frac{\left|S_{\alpha d}\left(e^{j\omega T}\right)\right|^2}{S_{\alpha\alpha}\left(e^{j\omega T}\right)S_{dd}\left(e^{j\omega T}\right)} = 1 - \gamma_{\alpha d}{}^2\left(e^{j\omega T}\right) \tag{3-13}$$

with $S_{\alpha d}\left(e^{j\omega T}\right)$ denoting the cross spectral density between the reference signal α and the disturbance signal d, where:

$$S_{rd}\left(e^{j\omega T}\right) = G^*\left(e^{j\omega T}\right)S_{\alpha d}\left(e^{j\omega T}\right) \tag{3-14}$$

and $\gamma_{\alpha d}{}^2\left(e^{j\omega T}\right)$ is the *quadratic coherence function* between the reference signal α and the disturbance signal d.

Thus, the better the coherence between the reference signal α and the disturbance signal d, the better the performance of the structural feed-forward control, compare Eq. (2-11).

For the convergence of the feed-forward wing bending vibration controller to its optimum, the controller coefficients are updated with the gradient of the power spectral density $S_{ee}\left(e^{j\omega T}\right)$. Defining a positive real convergence coefficient c (that already includes the factor 2 from Eq. (3-10)) the vector of the FIR controller coefficients $\vec{h}$ can be updated proportional to the negative local gradient of $S_{ee}\left(e^{j\omega T}\right)$, which depends on the actual controller $\vec{h} = \vec{h}(n-1)$, see Eq. (3-10). This frequency domain *steepest descent* algorithm then reads:

$$\vec{h}(n) = \vec{h}(n-1) - c \cdot IFT\left\{\left\langle \hat{R}^*\left(e^{j\omega T}\right) E_{\vec{h}=\vec{h}(n-1)}\left(e^{j\omega T}\right)\right\rangle\right\} \tag{3-15}$$

Thereby, IFT denotes the Inverse Fourier Transform of the quantity inside $\{...\}$, and $E_{\vec{h}=\vec{h}(n-1)}\left(e^{j\omega T}\right)$ is the Fourier transform of the error signal with quasi-steady state controller $\vec{h} = \vec{h}(n-1)$. Since the filtered reference signal r is not directly available, it has to be estimated online with the help of an (approximate) plant model of $G\left(e^{j\omega T}\right)$, compare [31]. This estimated filtered reference signal is denoted with $\hat{r}$. Its Fourier transform is $\hat{R}\left(e^{j\omega T}\right)$.

Note, that the frequency domain version of the steepest descent algorithm used for wing bending vibration controller adaptation in this thesis has the advantage to save computational costs compared to time domain algorithms such as the LMS algorithm, compare [28].

Furthermore the frequency domain steepest descent algorithm allows to manipulate the adaptation at certain frequencies (i.e. to set the quantity inside $\langle ... \rangle$ to zero at frequencies where the plant transfer function is not properly known, or exposed to huge variations between different mass and Mach cases, see Chapter 4.4. *Introduction of a Mean Plant Model*.)

The Calculation of the expectation value $\langle ... \rangle$ in the right term Eq. (3-15) requires averaging over an infinite, or at least very large data segment. Thus, the controller coefficients could only be updated rather infrequently. In order to be able to update the controller every time step n, an estimate of the gradient of $S_{ee}\left(e^{j\omega T}\right)$ over the last N samples is used. Then the frequency domain steepest descent algorithm may finally be written as:

$$\vec{h}(n) = \vec{h}(n-1) - c \cdot IDFT\left\{\hat{R}_n{}^*\left(f_k\right) E_n\left(f_k\right)\right\}_+ \tag{3-16}$$

Thereby, circular correlation effects are erased by the application of the *overlap-save method*, see [29] and [83], with $IDFT\{...\}_+$ denoting the causal part of the Inverse Discrete Fourier Transform (IDFT) of the quantity inside $\{...\}$.

The term $\hat{R}_n(f_k)$ denotes the Discrete Fourier Transform (DFT) of the latest $2N$ point segment of $\hat{r}(n)$, and $E_n(f_k)$ is the $2N$ point DFT of the latest N point segment of $e(n)$ padded with N zeros. For computational efficiency, $\hat{R}_n(f_k)$ and $E_n(f_k)$ are only updated every $\Delta_{overlap}{}^{\text{th}}$ sample.

In order to be able to update the controller every sample n, and thus assure a smooth convergence, the values for $\hat{R}_n(f_k)$ and $E_n(f_k)$ are held constant until new values are available. With the discrete frequency variable k=1,…,$2N$ the discrete frequencies f_k are:

$$f_k = \frac{Fs(k-1)}{2N} \tag{3-17}$$

For an efficient controller implementation, the $2N$ point DFT of the estimated filtered reference signal $\hat{R}_n(f_k)$ is approximated by multiplying the $2N$ point DFT of the reference signal $A_n(f_k)$ with the estimated plant response $\hat{G}(f_k)$ at each discrete frequency f_k, as also proposed in [28]:

$$\hat{R}_n(f_k) \approx A_n(f_k)\hat{G}(f_k) \tag{3-18}$$

This procedure however involves neglecting circular convolution effects. Since the conservative choice of the convergence coefficient c makes the adaptation robust to a biased estimate of the filtered reference signal, see Eq. (3-41), above approximation did hardly influence the performance of the adaptive wing bending vibration controller.

The resulting adaptive feed-forward control algorithm for wing bending alleviation is illustrated in Figure 3-5. The reference signal $\alpha(t)$ is passed through an AF, and the ADC. The sampled-time reference signal $\alpha(n)$ is split in order to be fed to the adaptive FIR controller, as well as to the frequency domain steepest descent algorithm defined in Eq. (3-16). The update algorithm also requires the sampled-time error signal $e(n)$ in order to calculate the new vector of controller coefficients $\vec{h}(n)$.

The adaptive FIR controller is implemented as defined in Eq. (3-1) in order to generate the feed-forward control input $u_{FF}(n)$. This feed-forward control input $u_{FF}(n)$ is passed through the DAC before being fed to the actuators of the ailerons to generate a symmetric aileron deflection $\delta(t)$.

As already mentioned the actuator transfer function $F_\delta(s)$ has low pass character, and thus already provides the required properties of a RF. So, in order to minimize the delay of the feed-forward path, no additional RF is used.

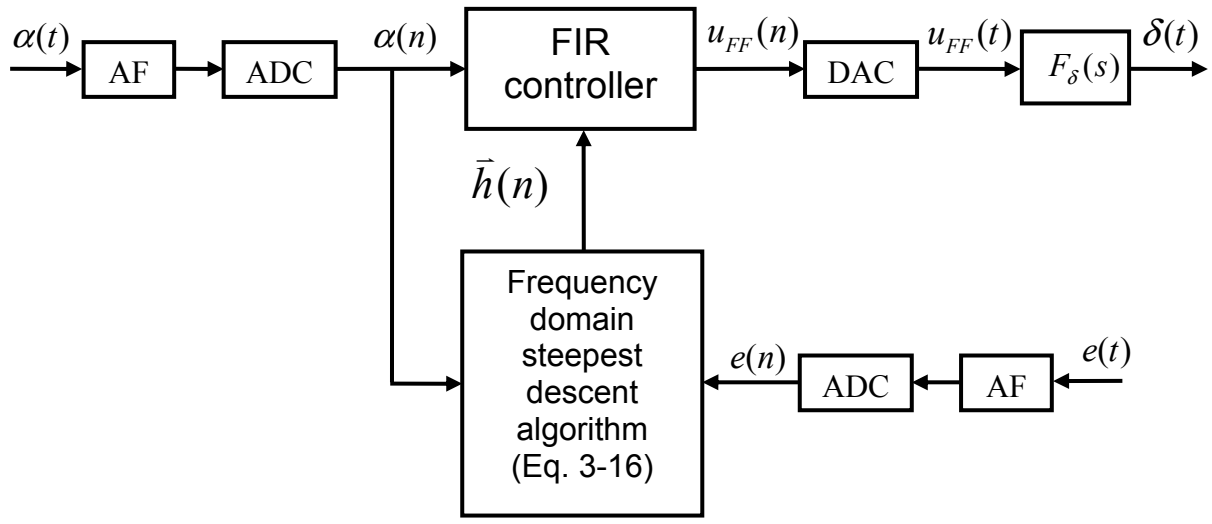

Figure 3-5. The adaptive feed-forward control algorithm.

3.2 Stability Analysis of the Adaptive Control Algorithm

For the derivation of a frequency domain stability analysis of the proposed adaptive control algorithm shown in Eq. (3-16) the deviation of the frequency response of the (regarded as *quasi-steady state*) controller $H_n\left(e^{j\omega T}\right)$ from the optimum causal controller $H_{opt}\left(e^{j\omega T}\right)$ is defined as:

$$\Delta H_n\left(e^{j\omega T}\right) = H_n\left(e^{j\omega T}\right) - H_{opt}\left(e^{j\omega T}\right) \tag{3-19}$$

Then Eq. (3-7) can be rewritten for $H\left(e^{j\omega T}\right) = H_n\left(e^{j\omega T}\right)$ as:

$$S_{ee_n}\left(e^{j\omega T}\right) = \left\langle E_{\vec{h}=\vec{h}(n)}{}^{*}\left(e^{j\omega T}\right) E_{\vec{h}=\vec{h}(n)}\left(e^{j\omega T}\right)\right\rangle =$$

$$= S_{dd}\left(e^{j\omega T}\right) + S_{rd}^{*}\left(e^{j\omega T}\right) H_{opt}\left(e^{j\omega T}\right) + \Delta H_n{}^{*}\left(e^{j\omega T}\right) S_{rr}\left(e^{j\omega T}\right) \Delta H_n\left(e^{j\omega T}\right) \tag{3-20}$$

Thereby, $S_{ee_n}\left(e^{j\omega T}\right)$ denotes the power spectral density of the error signal obtained with the controller $\vec{h} = \vec{h}(n)$, and $E_{\vec{h}=\vec{h}(n)}\left(e^{j\omega T}\right)$ is the Fourier transform of said error signal. The first and the second term of Eq. (3-20) are independent of the actual controller, and again denoted the minimum control error $S_{ee_{\min}}\left(e^{j\omega T}\right)$, see Eq. (3-12).

The term on the very right of Eq. (3-20) depends on $\Delta H_n\left(e^{j\omega T}\right)$, and is denoted the *excess square control error* for the quasi-steady state controller $H_n\left(e^{j\omega T}\right)$, i.e.:

$$\varepsilon_{excess_n}(e^{j\omega T}) = \Delta H_n{}^*\left(e^{j\omega T}\right) S_{rr}\left(e^{j\omega T}\right) \Delta H_n\left(e^{j\omega T}\right) \tag{3-21}$$

In order to get an estimate of the boundaries for the convergence coefficient c for stable convergence of the controller update algorithm, the expected progression of this excess square control error against c is investigated in the following. Said progression has a fundamental effect on the stability and on the performance of the adaptation algorithm. If the adaptation of the feed-forward controller works properly, $\left\langle \varepsilon_{excess_n}(e^{j\omega T}) \right\rangle$ will decrease with increasing n. If $\left\langle \varepsilon_{excess_n}(e^{j\omega T}) \right\rangle$ goes to infinity the adaptation is unstable.

Thus, a necessary constraint for stable adaptation of the feed-forward wing bending vibration controller is the existence of a *finite steady-state* of $\left\langle \varepsilon_{excess_n}(e^{j\omega T}) \right\rangle$. In the following sufficient conditions for the existence of a finite steady-state excess square control error are derived.

Assuming the controller update defined in Eq. (3-16) is completely performed in the frequency domain before $IDFT\left\{...\right\}_+$ is computed in order to obtain $\vec{h}(n)$, one can write:

$$\vec{h}(n) = IDFT\left\{H_n\left(f_k\right)\right\}_+ = IDFT\left\{H_{n-1}\left(f_k\right) - c \cdot \hat{R}_n{}^*\left(f_k\right) E_n\left(f_k\right)\right\}_+ \tag{3-22}$$

Thereby, $H_n\left(f_k\right)$ is the frequency response of the controller at time step n that still contains circular correlation effects from the multiplication of $\hat{R}_n\left(f_k\right)$ with $E_n\left(f_k\right)$.

The $2N$ point DFT of the zero padded error signal that is actually used for controller update is considered to depend on the controller Δ+1 samples ago in the worst case. With the assumption of a *quasi-steady state* controller $\vec{h}(n-\Delta-1)$, and neglecting circular convolution effects one can thus write:

$$E_n\left(f_k\right) \approx D_n\left(f_k\right) + H_{n-\Delta-1}\left(f_k\right) R_n\left(f_k\right) \tag{3-23}$$

Thereby, $D_n\left(f_k\right)$, and $R_n\left(f_k\right)$ denote the $2N$ point DFTs of $d(n)$ and $r(n)$ evaluated at the discrete frequency f_k, and $H_{n-\Delta-1}\left(f_k\right)$ is the frequency response of the controller at time step n-Δ-1.

The one sample delay represents the fact that the computation of a new set of filter coefficients $\bar{h}(n)$ is based on the error signal obtained with the set of filter coefficients of at least one sample ago $\bar{h}(n-1)$. As already shown in [118], the additional delay of Δ samples originates from two effects:

- Firstly, the plant introduces a (*frequency dependent*) group delay $\Delta_G(\omega) = -\partial\phi_G(\omega)/\partial\omega$ between the sampled-time symmetric aileron command *u(n)* and the sampled-time error signal *e(n)*. Thereby, $\phi_G(\omega)$ denotes phase angle of the transfer function $G(e^{j\omega T})$ in radians. The *maximum* of this group delay in the controlled frequency range is rounded *down* to an integer value. This integer value corresponds to a delay of $\Delta_{\max}$ samples in addition to the minimum one sample delay.

- Secondly, although the controller is updated every time step *n* for smooth convergence of its coefficients, the quantity inside $IDFT\{...\}_+$ is generally updated only every $\Delta_{overlap}{}^{\text{th}}$ sample for a reduction of required computing power (i.e. usually very important on a flight computer). Thus, the update of the quantity inside $IDFT\{...\}_+$ is additionally delayed by $\Delta_{overlap}$-1 samples in the worst case.

Therefore, the maximum feedback delay Δ (in addition to the one obligatory sample) is calculated as shown in Eq. (3-24):

$$\Delta = \Delta_{overlap} - 1 + \Delta_{\max} \tag{3-24}$$

Based on the assumption that DFT coefficients are approximately de-correlated, compare [83], the controller adaptation at a discrete frequency f_k is regarded as independent from the adaptation at all other frequencies in the following.

Thus, introducing Eq. (3-23) into Eq. (3-22), neglecting the $IDFT\{...\}_+$ operation, and substituting $H_n(f_k) = \Delta H_n(f_k) + H_{opt}(f_k)$ gives an approximate update equation for $\Delta H_n(f_k)$, i.e. the controller deviation from the optimum controller at the discrete frequency f_k:

$$\Delta H_n(f_k) \approx \Delta H_{n-1}(f_k) - c \cdot \tilde{S}_{\hat{r}r_n}(f_k)\Delta H_{n-\Delta-1}(f_k) - c \cdot \hat{R}_n^{*}(f_k)E_{opt_n}(f_k) \tag{3-25}$$

Thereby, the following definition for the *estimate* of the cross spectral density between the estimated filtered reference signal $\hat{r}$ and the sampled-time filtered reference signal r at the discrete frequency f_k at time step *n* has been applied:

$$\widetilde{S}_{\hat{r}r_n}(f_k) = \hat{R}_n^{\,*}(f_k) R_n(f_k) \tag{3-26}$$

The term $E_{opt_n}(f_k)$ is defined as the 2*N*-point DFT of the error signal that would be obtained with the optimum controller e_{opt}, evaluated for the discrete frequency f_k, i.e.:

$$E_{opt_n}(f_k) = D_n(f_k) + H_{opt}(f_k) R_n(f_k) \tag{3-27}$$

with $H_{opt}(f_k)$ denoting the evaluation of $H_{opt}\left(e^{j\omega T}\right)$ at the discrete frequency f_k. The signal e_{opt} is statistically independent from the filtered reference signal *r*, and also from its estimate $\hat{r}$, compare the definition of $H_{opt}\left(e^{j\omega T}\right)$ in Eq. (3-11).

Evaluating Eq. (3-21) at the discrete frequency f_k, taking the expectation value, and introducing Eq. (3-25) gives:

$$\begin{aligned}
&\left\langle \varepsilon_{excess_n}(f_k) \right\rangle = \left\langle \Delta H_n^{\,*}(f_k) S_{rr}(f_k) \Delta H_n(f_k) \right\rangle = \\
&= \left\langle \Delta H_{n-1}^{\,*}(f_k) S_{rr}(f_k) \Delta H_{n-1}(f_k) \right\rangle \\
&- c\left\langle \Delta H_{n-1}^{\,*}(f_k) S_{rr}(f_k) \widetilde{S}_{\hat{r}r_n}(f_k) \Delta H_{n-\Delta-1}(f_k) \right\rangle \\
&- c\left\langle \widetilde{S}_{\hat{r}r_n}^{\,*}(f_k) \Delta H_{n-\Delta-1}^{\,*}(f_k) S_{rr}(f_k) \Delta H_{n-1}(f_k) \right\rangle \\
&+ c^2 \left\langle \left| \widetilde{S}_{\hat{r}r_n}(f_k) \right|^2 \Delta H_{n-\Delta-1}^{\,*}(f_k) S_{rr}(f_k) \Delta H_{n-\Delta-1}(f_k) \right\rangle \\
&+ c^2 \left\langle \left(\hat{R}_n^{\,*}(f_k) E_{opt_n}(f_k) \right)^* \hat{R}_n^{\,*}(f_k) E_{opt_n}(f_k) \right\rangle \\
&- c\left\langle \Delta H_{n-1}^{\,*}(f_k) S_{rr}(f_k) \hat{R}_n^{\,*}(f_k) E_{opt_n}(f_k) \right\rangle \\
&+ c^2 \left\langle \widetilde{S}_{\hat{r}r_n}^{\,*}(f_k) \Delta H_{n-\Delta-1}^{\,*}(f_k) S_{rr}(f_k) \hat{R}_n^{\,*}(f_k) E_{opt_n}(f_k) \right\rangle \\
&- c\left\langle \left(\hat{R}_n^{\,*}(f_k) E_{opt_n}(f_k) \right)^* S_{rr}(f_k) \Delta H_{n-1}(f_k) \right\rangle \\
&+ c^2 \left\langle \left(\hat{R}_n^{\,*}(f_k) E_{opt_n}(f_k) \right)^* S_{rr}(f_k) \widetilde{S}_{\hat{r}r_n}^{\,*}(f_k) \Delta H_{n-\Delta-1}^{\,*}(f_k) \right\rangle
\end{aligned} \tag{3-28}$$

The last four terms in Eq. (3-28) are zero since e_{opt} is statistically independent from r, and from $\hat{r}$, as already mentioned above. Moreover, the following approximation is made for the fifth term on the right side of Eq. (3-28):

$$c^2\left\langle\left(\hat{R}_n^{\,*}(f_k)E_{opt_n}(f_k)\right)^*\hat{R}_n^{\,*}(f_k)E_{opt_n}(f_k)\right\rangle=$$

$$=c^2\left\langle\hat{R}_n(f_k)^*\hat{R}_n(f_k)\right\rangle\cdot\left\langle E_{opt_n}(f_k)^*E_{opt_n}(f_k)\right\rangle\approx c^2\cdot S_{ee_{\min}}(f_k)S_{\hat{r}\hat{r}}(f_k)$$

(3-29)

with $S_{ee_{\min}}(f_k)$ and $S_{\hat{r}\hat{r}}(f_k)$ denoting the power spectral densities of e_{opt} and of $\hat{r}$ evaluated at the discrete frequency f_k. Introducing Eq. (3-21) and Eq. (3-29) into Eq. (3-28) then makes:

$$\begin{aligned}&\left\langle\varepsilon_{excess_n}(f_k)\right\rangle\approx\left\langle\varepsilon_{excess_{n-1}}(f_k)\right\rangle-c\left\langle\widetilde{S}_{\hat{r}r_n}(f_k)a_{\Delta n-1}(f_k)\right\rangle-c\left\langle\widetilde{S}_{\hat{r}r_n}^{\,*}(f_k)a_{\Delta n-1}^{\,*}(f_k)\right\rangle\\&+c^2\left\langle\left|\widetilde{S}_{\hat{r}r_n}(f_k)\right|^2\varepsilon_{excess_{n-\Delta-1}}(f_k)\right\rangle+c^2\cdot S_{ee_{\min}}(f_k)S_{\hat{r}\hat{r}}(f_k)\\&=\left\langle\varepsilon_{excess_{n-1}}(f_k)\right\rangle-2c\left\langle\mathrm{Re}\left\{\widetilde{S}_{\hat{r}r_n}(f_k)a_{\Delta n-1}(f_k)\right\}\right\rangle\\&+c^2\left\langle\left|\widetilde{S}_{\hat{r}r_n}(f_k)\right|^2\varepsilon_{excess_{n-\Delta-1}}(f_k)\right\rangle+c^2\cdot S_{ee_{\min}}(f_k)S_{\hat{r}\hat{r}}(f_k)\end{aligned}$$

(3-30)

where $a_{\Delta n-1}(f_k)$ is defined as (the subscript Δ in the function $a_{\Delta n-1}(f_k)$ denotes that $\Delta H_{n-\Delta-1}(f_k)$ is Δ samples older than $\Delta H_{n-1}(f_k)$, and the sub-subscript n-1 denotes that $\Delta H_{n-1}(f_k)$ originates from one sample before n):

$$a_{\Delta n-1}(f_k)=\Delta H_{n-1}^{\,*}(f_k)S_{rr}(f_k)\Delta H_{n-\Delta-1}(f_k)\tag{3-31}$$

which, under the assumption that $\left|c\cdot\widetilde{S}_{\hat{r}r_n}(f_k)\right|<<1$ for all f_k in the controlled frequency range, may be expanded to (see *Appendix A*):

$$a_{\Delta n-1}(f_k)=\varepsilon_{excess\,n-\Delta-1}(f_k)-\Delta\cdot c\cdot\overline{S}_{\hat{r}r}^{\,*}(f_k)a_{1_{n-\Delta-1}}^{\,*}(f_k)+g_{\Delta n-1}(f_k)$$

(3-32)

with $g_{\Delta n-1}(f_k)$ denoting a dummy function with *zero ensemble average* defined in *Appendix A*, and with:

$$a_{1n-\Delta-1}(f_k) = \Delta H_{n-\Delta-1}{}^{*}(f_k) S_{rr}\left(f_{k_u}\right) \Delta H_{n-\Delta-2}(f_k) \tag{3-33}$$

The subscript 1 in the function $a_{1n-\Delta-1}(f_k)$ denotes that $\Delta H_{n-\Delta-2}(f_k)$ is 1 sample older than $\Delta H_{n-\Delta-1}(f_k)$, and the sub-subscript *n*-Δ-1 denotes that $\Delta H_{n-\Delta-1}(f_k)$ originates from Δ+1 samples before *n*. The term $\overline{S}_{\hat{r}r}{}^{*}(f_k)$ in Eq. (3-32) is defined as:

$$\overline{S}_{\hat{r}r}{}^{*}(f_k) = \frac{1}{\Delta} \sum_{m=1}^{\Delta} \left[\widetilde{S}_{\hat{r}r\,n-m}{}^{*}(f_k) \right] \tag{3-34}$$

Thereby, *m* denotes a counting variable. Assuming that the adaptation algorithm converges to a steady state, with $\langle \varepsilon_{excess_\infty}(f_k) \rangle$ denoting the ensemble average of the *steady-state* excess square control error, and with the assumption that $\left| c \cdot \widetilde{S}_{\hat{r}r_{n-m}}(f_k) \right| << 1$ for all f_k in the controlled frequency range, one can rewrite Eq. (3-30) for this converged steady state (see *Appendix B*):

$$\left\langle \varepsilon_{excess_\infty}(f_k) \cdot \left(2 \cdot c \cdot \mathrm{Re}\left\{ \widetilde{S}_{\hat{r}r_n}(f_k) \right\} - c^2 \cdot \left(2 \cdot \widetilde{S}_{\hat{r}r_n}(f_k) \overline{S}_{\hat{r}r}{}^{*}(f_k) \cdot \Delta + \left| \widetilde{S}_{\hat{r}r_n}(f_k) \right|^2 \right) \right) \right\rangle \approx$$

$$\approx c^2 \cdot S_{ee_{\min}}(f_k) S_{\hat{r}\hat{r}}(f_k) \tag{3-35}$$

If the multiplier of $\varepsilon_{excess_\infty}(f_k)$ equals zero in Eq. (3-35), then $\varepsilon_{excess_\infty}(f_k)$ tends to infinity, (since there is a finite value on the right side of the equation) and the adaptation algorithm becomes unstable. Thus, for the calculation of *necessary* boundaries for the convergence coefficient *c*, one can write:

$$2 \cdot c \cdot \mathrm{Re}\left\{ \widetilde{S}_{\hat{r}r_n}(f_k) \right\} - c^2 \cdot \left(2 \cdot \widetilde{S}_{\hat{r}r_n}(f_k) \overline{S}_{\hat{r}r}{}^{*}(f_k) \cdot \Delta + \left| \widetilde{S}_{\hat{r}r_n}(f_k) \right|^2 \right) = 0 \tag{3-36}$$

With $G(f_k)$ denoting the 2*N*-point DFT of the real plant's impulse response at the discrete frequency f_k, and with $\hat{G}(f_k)$ denoting the frequency response of the plant model at the discrete frequency f_k, $\widetilde{S}_{\hat{r}r_{n-m}}(f_k)$ is expanded to:

$$\widetilde{S}_{\hat{r}r_{n-m}}(f_k) = \widetilde{S}_{\hat{r}\hat{r}_{n-m}}(f_k)\frac{G(f_k)}{\hat{G}(f_k)} \tag{3-37}$$

Its real part $\mathrm{Re}\left\{\widetilde{S}_{\hat{r}r_{n-m}}(f_k)\right\}$ thus can be written as:

$$\mathrm{Re}\left\{\widetilde{S}_{\hat{r}r_{n-m}}(f_k)\right\} = \widetilde{S}_{\hat{r}\hat{r}_{n-m}}(f_k)\mathrm{Re}\left\{\frac{G(f_k)}{\hat{G}(f_k)}\right\} =$$

$$= \widetilde{S}_{\hat{r}\hat{r}_{n-m}}(f_k)\frac{\left|G(f_k)\right|}{\left|\hat{G}(f_k)\right|}\cos\left(\phi_G(f_k) - \phi_{\hat{G}}(f_k)\right) \tag{3-38}$$

Thereby, $\widetilde{S}_{\hat{r}\hat{r}_{n-m}}(f_k)$ denotes the estimate of the power spectral density of $\hat{r}$ over *N* samples at the *n*-*m*$^{\text{th}}$ time step, $\phi_G(f_k)$ and $\phi_{\hat{G}}(f_k)$ denote the phase angles of the transfer function $G(f_k)$, and its estimate $\hat{G}(f_k)$, (i.e. the plant model), $\left|G(f_k)\right|$ and $\left|\hat{G}(f_k)\right|$ are the correspondent magnitudes.

The key issue about $\widetilde{S}_{\hat{r}\hat{r}_{n-m}}(f_k)$ denoting an *estimate* of the power spectral density of the estimated filtered reference signal is that $\widetilde{S}_{\hat{r}\hat{r}_{n-m}}(f_k)$ can be calculated at each time step *n* anew which allows for continuous online calculation of the boundaries of the convergence coefficient *c*. The boundaries for the convergence coefficient *c* are obtained by introducing Eqs. (3-37) and (3-38) into Eq. (3-36) and taking the minimum over discrete frequencies f_k:

$$0 < c < \left[\frac{2}{2\cdot\Delta\cdot\overline{S}_{\hat{r}\hat{r}}(f_k) + \widetilde{S}_{\hat{r}\hat{r}_n}(f_k)}\cdot\frac{\left|\hat{G}(f_k)\right|}{\left|G(f_k)\right|}\cdot\cos\left(\phi_G(f_k) - \phi_{\hat{G}}(f_k)\right)\right]_{Minimum\ over\ f_k}$$

(3-39)

with:

$$\overline{S}_{\hat{r}\hat{r}}(f_k) = \frac{1}{\Delta}\sum_{m=1}^{\Delta}\left[\widetilde{S}_{\hat{r}\hat{r}n-m}(f_k)\right] \tag{3-40}$$

In principle also a frequency dependent convergence coefficient $c(f_k)$ could be used for updating the controller $H_n(f_k)$. However, using a frequency dependent $c(f_k)$ can cause the frequency domain controller $H_n(f_k)$ to update to values without causal time domain representation [29]. Thus, the same convergence coefficient was used for all frequencies here. Therefore, the upper boundary in Eq. (3-39) is the *minimum over* f_k of the quantity inside the brackets.

Since the quantity inside the brackets generally has a minimum at frequencies of modal peaks of the frequency responses $G(f_k)$, and $\hat{G}(f_k)$ respectively (i.e. here, at the frequency of the modal peak of first symmetric vertical wing bending vibration), taking the minimum over frequency in Eq. (3-39) is usually not too conservative.

Moreover, this procedure has the advantage, that outside the frequency range of first symmetric vertical wing bending vibration, where the coherence $\gamma_{\alpha d}{}^2\left(e^{j\omega T}\right)$ is usually bad, the adaptation is slowed down.

Eq. (3-39) must hold for all discrete frequencies f_k. Thus, the minimum value over f_k of the right side of Eq. (3-39) bounds the convergence coefficient *c*. Eq. (3-39) also illustrates that the phase error between the plant model $\hat{G}(f_k)$, and the real plant response $G(f_k)$ must be smaller than +/-90° to ensure stable adaptation. This is in accordance with the results in the literature [94], [114].

The convergence coefficient *c* that provides fastest adaptation of the structural controller in the frequency range of the first symmetric vertical wing bending vibration, the so-called optimum convergence coefficient c_{opt} is only about half the maximum possible convergence coefficient $c_{\max}$, see *Appendix C*.

$$c_{opt} \approx \frac{c_{\max}}{2} = \left[\frac{1}{2 \cdot \Delta \cdot \overline{S}_{\hat{r}\hat{r}}(f_k) + \widetilde{S}_{\hat{r}\hat{r}_n}(f_k)} \cdot \frac{\left|\hat{G}(f_k)\right|}{\left|G(f_k)\right|} \cdot \cos\left(\phi_G(f_k) - \phi_{\hat{G}}(f_k)\right) \right]_{Minimum\ over\ f_k} \tag{3-41}$$

Note, that using the optimum convergence coefficient c_{opt} makes the adaptation robust against e.g. a plant model phase error of +/- 60°, or to a plant model magnitude of only half of the $G(f_k)$ transfer function's magnitude (i.e. $\left|\hat{G}(f_k)\right| = 0.5 \cdot \left|G(f_k)\right|$.) For Δ=0, Eq. (3-39) provides the stability conditions for harmonic control without plant delay [8]. But one has to remember that Eq. (3-39) derivates from the assumption that $\left|c \cdot \widetilde{S}_{\hat{r}r_{n-m}}(f_k)\right| << 1$ for all f_k in the controlled frequency range. For Δ=0 however this assumption would not be quite justified.

For the four-engine example aircraft with proposed wing bending vibration control system $\Delta+1\approx100$ samples. Thus, for this thesis $\left|c\cdot\widetilde{S}_{\hat{r}r_{n-m}}(f_k)\right|\ll 1$ was sufficiently fulfilled.

Note, that with calm atmosphere $\widetilde{S}_{\hat{r}\hat{r}_{n-m}}(f_k)\approx 0$, and thus the upper bound of the convergence coefficient c tends to infinity according to Eq. (3-39). In this context it is recommended to introduce a threshold for $\widetilde{S}_{\hat{r}\hat{r}_{n-m}}(f_k)$ and to stop adaptation of the structural controller if $\widetilde{S}_{\hat{r}\hat{r}_{n-m}}(f_k)$ falls below this threshold.

The author believes that the above stability bounds are both *necessary* and *sufficient*, although a rigorous proof for their sufficiency could not be found. However, *sufficiency* can be shown *numerically* by solving the characteristic equation of Eq. (3-25) for different convergence coefficients c. With the approximation $\widetilde{S}_{\hat{r}r_n}(f_k)\approx S_{\hat{r}r}(f_k)=\textit{constant over } n$ for a sufficiently long DFT length $2N$ (which is a good approximation unless the power spectral density of $\hat{r}$ changes, e.g. when the atmospheric turbulence strength abruptly changes), the characteristic equation of Eq. (3-25) for the discrete frequency f_k makes:

$$1-z^{-1}+c\cdot S_{\hat{r}r}(f_k)\cdot z^{-\Delta-1}=0 \tag{3-42}$$

For the evaluation of Eq. (3-42), $S_{\hat{r}r}(f_k)$ is expanded to:

$$S_{\hat{r}r}(f_k)=\mathrm{Re}\{S_{\hat{r}r}(f_k)\}+j\cdot\mathrm{Im}\{S_{\hat{r}r}(f_k)\}=$$

$$=S_{\hat{r}\hat{r}}(f_k)\frac{\left|G(f_k)\right|}{\left|\hat{G}(f_k)\right|}\left[\cos\left(\phi_G(f_k)-\phi_{\hat{G}}(f_k)\right)+j\cdot\sin\left(\phi_G(f_k)-\phi_{\hat{G}}(f_k)\right)\right] \tag{3-43}$$

Introducing Eq. (3-43) and $c=\lambda\cdot c_{\max}$ with $c_{\max}$ from Eq. (3-39) into Eq. (3-42), and again approximating $\overline{S}_{\hat{r}\hat{r}}(f_k)\approx\widetilde{S}_{\hat{r}\hat{r}_n}(f_k)\approx S_{\hat{r}\hat{r}}(f_k)=\textit{constant over } n$ for a sufficiently long DFT length $2N$, it can be calculated numerically that for $0<\lambda<1$ all roots of Eq. (3-42) lie inside the unit circle, independently from the chosen value of Δ. Thus, the controller update algorithm in Eq. (3-25) is stable for $0<c<c_{\max}$.

Just to give an example, Figure 3-6 illustrates the roots of Eq. (3-42) depending on the convergence coefficient c for $\Delta = 5$ and a plant model phase error $\left(\phi_G(f_k)-\phi_{\hat{G}}(f_k)\right)=-\pi/3$. Then one finds Δ nearly axially symmetrical roots far inside the unit circle with increasing magnitude as the convergence coefficient is increased. These roots are not critical for the stability of the controller update algorithm. Only the $\Delta+1^{\text{th}}$ root is stability critical.

It converges to one at the convergence coefficient's lower boundary $c = 0$. For $c = c_{opt}$ the stability critical root approximately reaches its smallest magnitude. When the convergence coefficient is further increased, the stability critical root is again heading towards the unity circle, which it crosses, at about the convergence coefficient's upper boundary $c = c_{\max}$. For the sake of completeness it is alluded that for a plant model phase error close to zero there would be two such stability critical roots.

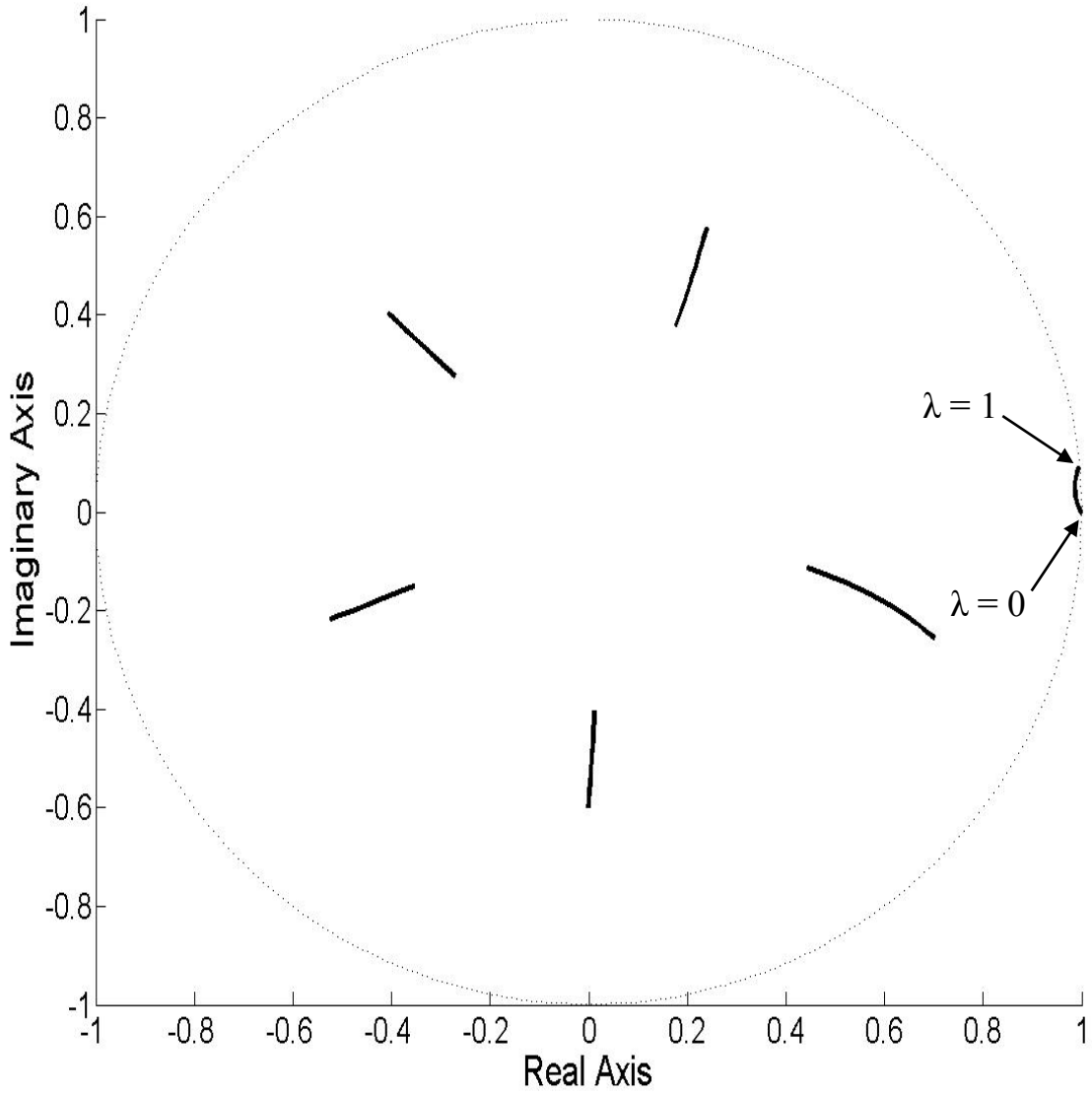

Figure 3-6. Root locus of the controller update algorithm's characteristic equation versus convergence coefficient *c* for Δ=5, and for $\left(\phi_G\left(e^{j\omega T}\right) - \phi_{\hat{G}}\left(e^{j\omega T}\right)\right) = -\pi/3$.

4 Numeric Simulations

In this chapter the behavior of the proposed adaptive wing bending vibration controller is investigated. The numeric simulations were carried out with state-space models of the symmetric dynamics of a large four-engine transport aircraft in steady state trimmed flight, compare Chapter 2.1. For the adaptive feed-forward controller an FIR length of $N = 64$ was chosen (N is chosen a power of two in order to be able to use the Fast Fourier Transform algorithm, compare [12].) This FIR length showed to be a good compromise between the demand for low computational load, and sufficient high frequency resolution.

For a good trade-off between low computational costs and high convergence speed, the quantity inside the $IDFT\{...\}_+$ brackets in Eq. (3-16) was updated only every $\Delta_{overlap} = 64^{th}$ sample.

The SCP delay $-\partial\phi_{G_c}(\omega)/\partial\omega$, measured from the plant transfer functions of all Mach and mass cases, plus a on sample delay reserved for the digital controller, converters, and anti-aliasing filters (AFs) is denoted $\Delta_G(\omega)$, and has been identified to be less than 36 samples, or rounded down to an integer value, $\Delta_{\max}$ makes 35 samples. Thus, the maximum feedback delay (in addition to the obligatory one sample delay considered in Eq. (3-23)) is $\Delta = 99$ samples for the time-domain simulations with the four-engine example aircraft. A sample time of $T = 40$ ms was used for the numeric simulations.

In Chapter 4.1 it is explained how the turbulence excitation and the reference measurement have been modeled. Chapter 4.2 shows the modal wing bending vibration reduction of the converged controller for mass case A at Mach 0.86, see Table 2-1. For this analysis a perfect plant model was used. The converged controller performance is about the same for all mass and Mach cases.

Chapter 4.3 shows the adaptation behavior with phase errors in the plant model. It is concluded that the feed-forward controller converges to a (slightly time-varying) estimate of a causal representation of $H_{opt}\left(e^{j\omega T}\right)$ after sufficient convergence time as long as the phase error in the plant model is smaller than +/- 90°, and the convergence coefficient c does not exceed the boundaries defined in Eq. (3-39). For the estimation of the performance of a non-adaptive feed-forward controller in the presence of phase and magnitude deviations from $H_{opt}\left(e^{j\omega T}\right)$ a rule of thumb formula is derived. In Chapter 4.4 it is shown that for the four-engine example aircraft used in this thesis one single mean plant model is sufficient for stable convergence of the wing bending vibration controller adaptation at all mass and Mach cases.

Finally, Chapter 4.5 shows the tracking capability of the adaptation algorithm. For this analysis the time variation of the plant was modeled by switching between state-space models of different mass cases and Mach numbers during the simulation. Moreover, in Chapter 4.6 it is shown for mass case A, Ma=0.86, that the converged feed-forward wing bending vibration controller can also compensate discrete gusts.

To sum up Chapter 4 shows that the proposed adaptation of the feed-forward wing bending vibration controller significantly improves the robustness of the control performance against modeling errors and also against variations in the plant dynamics compared to a non-adaptive feed-forward controller.

4.1 Modeling of the Turbulence and of the Reference Measurement

For the derivation of the adaptive feed-forward wing bending vibration control algorithm it has been assumed that the disturbance signal d is steady state in order to allow for a frequency domain representation. No assumption has been made about how atmospheric turbulence generates such a steady state disturbance signal d. The statistical properties of atmospheric turbulence were already investigated in the early 19th century by several authors (RIBNER [96], DRYDEN [24], and VON KÁRMÁN [112], [113]). Today the von Kármán turbulence formulation prevailed.

For an aircraft flying through turbulent atmosphere at transonic Mach numbers the validity of TAYLOR's *frozen field assumption* can be assumed (i.e. assumption that a turbulence field remains unchanged while passing the aircraft [107].) Then due to the geometry and dimensions of an aircraft the following approximations are obtained [109]:

- The aircraft's Eigen modes are mainly excited by vertical and lateral flow field variations.
- These variations are distributed stochastically in the horizontal plane (i.e. 2-dimensional turbulence), compare [21], [108], and [109].
- They are almost constant over the height of the aircraft due to the fact that the height of the aircraft is small compared to its length and its wingspan.
- The vertical flow field variations remain constant while moving from the front to the rear of the aircraft (i.e. Taylor's hypothesis, which is also supported by flight tests, see SLEEPER [105].)

In TEUFEL [109] the excitation of the symmetric and asymmetric Eigen modes of a large transport aircraft by 2-dimensional vertical and lateral turbulence is described. In this thesis however only the excitation of symmetric Eigen modes of the four-engine example aircraft by one-dimensional vertical turbulence is considered for the evaluation of the adaptive wing bending vibration controller.

This vertical turbulence excitation is modeled as span-wise constant angle of attack variation at the alpha probe mounting position α_w:

$$\alpha_w = \left(\alpha_{wind} + \alpha_v\right) \text{ [rad]} \tag{4-1}$$

The term α_w consists of a measurable share α_{wind}, and a non-measurable share α_v. Thereby, α_v considers the real time effect that the reference measurement of 2-dimensional vertical and lateral airflow at only one point of the span-wise distribution, and only in the vertical direction (i.e. measurement of only one-dimensional vertical turbulence) cannot provide a perfect reference for the real aircraft excitation. For high span-wise gradients of the turbulence (e.g. flight through a wake vortex) however this modeling is not valid, and the alpha probe does not provide a proper reference.

Considering small angles, $\alpha_{wind} = v_z / V_{TAS}$ in radians. Thereby, the vertical flow velocity v_z shall represent the one-dimensional von Kármán turbulence spectrum. For the time-domain simulations the von Kármán turbulence spectrum is generated by filtering a white noise signal. HOBLIT [56] proposes a 4th order filter in order to obtain a good approximation of the von Kármán turbulence spectrum. In this thesis this 4th order filter is further approximated by a 3rd order filter with the integral scale length chosen to L = 762m, as also recommended for the determination of gust loads, see HOBLIT [55].

In order to obtain a 75% coherence between the desired reference signal α_{wind}, and the aircraft excitation α_w, α_v must be von Kármán filtered white noise with $(1/3)^{1/2}$ magnitude of α_{wind}, but with *different initial seed*, see Figure 4-1. This follows from the definition of the coherence function in Eq. (3-13). Since the white noise signals for α_v, and for α_{wind} are completely de-correlated, the cross spectral density between the desired reference signal α_{wind} and the aircraft excitation α_w is equal to the power spectral density of α_{wind}, i.e.:

$$\gamma_{\alpha_{wind}\alpha_w}{}^2\left(e^{j\omega T}\right) = \frac{\left|S_{\alpha_{wind}\alpha_w}\left(e^{j\omega T}\right)\right|^2}{S_{\alpha_{wind}\alpha_{wind}}\left(e^{j\omega T}\right) S_{\alpha_w\alpha_w}\left(e^{j\omega T}\right)} = \frac{\left|S_{\alpha_{wind}\alpha_{wind}}\left(e^{j\omega T}\right)\right|^2}{S_{\alpha_{wind}\alpha_{wind}}\left(e^{j\omega T}\right) S_{\alpha_w\alpha_w}\left(e^{j\omega T}\right)} = \frac{S_{\alpha_{wind}\alpha_{wind}}\left(e^{j\omega T}\right)}{S_{\alpha_w\alpha_w}\left(e^{j\omega T}\right)} =$$

and with Eq. (4-1):

$$= \frac{S_{\alpha_{wind}\alpha_{wind}}\left(e^{j\omega T}\right)}{S_{\alpha_{wind}\alpha_{wind}}\left(e^{j\omega T}\right) + S_{\alpha_v\alpha_v}\left(e^{j\omega T}\right)} = 0.75 \tag{4-2}$$

From the second line of Eq. (4-3), it follows, that $S_{\alpha_v\alpha_v}\left(e^{j\omega T}\right)$ is 1/3 of $S_{\alpha_{wind}\alpha_{wind}}\left(e^{j\omega T}\right)$, and thus the magnitude of α_v is $(1/3)^{1/2}$ of the magnitude of α_{wind}, what was to be demonstrated.

In the time-domain simulations the reference signal α_{sim} is generated by adding α_{wind} to the aircraft state-space model's output α_{ground}. Note, that α_{ground} has been neglected in the derivation of the adaptive control algorithm and the stability analysis. However, α_{ground} was so small for the example aircraft without pilot inputs, that it did not affect the simulation results:

$$\alpha_{sim}(t) = \alpha_{wind}(t) + \alpha_{ground}(t) = \alpha_{air}(t) - \alpha_0(t) \text{ [rad]} \tag{4-3}$$

The reference signal used for the time-domain simulations α_{sim} is thus also equal to the measurable angle of attack at the alpha probe mounting position α_{air} minus the static angle of attack of the trimmed aircraft in a ground reference system α_0, i.e. the alternating share of the alpha probe signal. Any dynamic behavior of the alpha probe sensor has been neglected in this thesis.

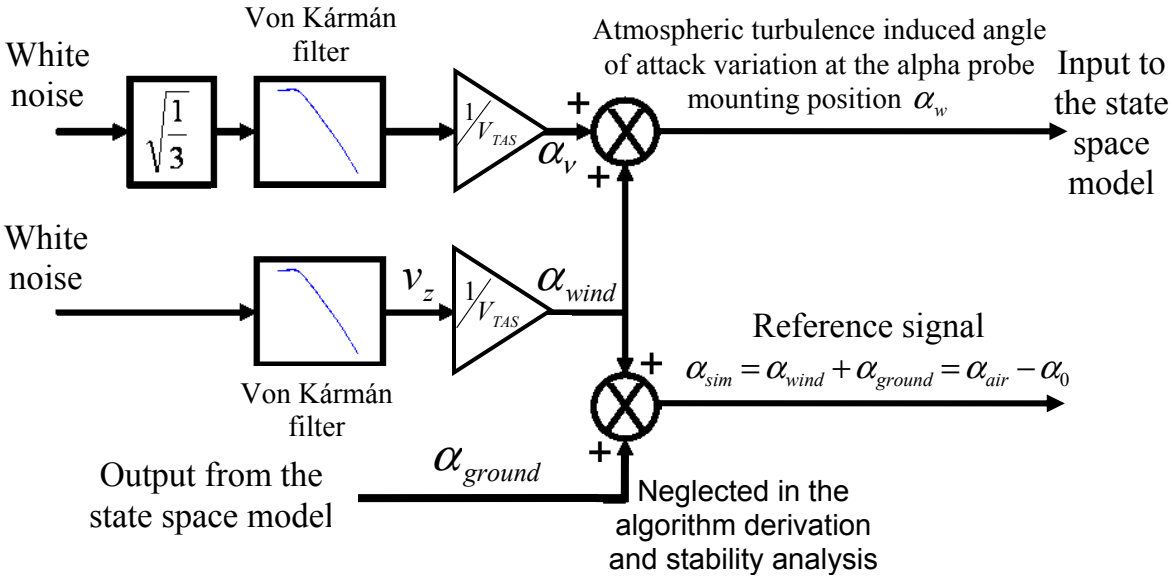

Figure 4-1. Modeling of the turbulence excitation with 75% coherence between the reference signal and the aircraft excitation.

4.2 Performance of the Converged Controller

In order to validate the performance of the converged controller, simulation runs with an approximately perfect plant model were performed (i.e. $\hat{G}(f_k) \approx G(f_k)$.) For convenience the estimated plant response $\hat{G}(f_k)$ thereby has been generated by evaluating the plant transfer function $G(s)$ for the discrete frequencies f_k, instead of evaluating the expectation value of the $2N$-point DFT of the real plant's impulse response at discrete frequencies f_k.

That means that the magnitude of the real plant response $G(f_k)$ has been slightly underestimated. This underestimation however is compensated by using c_{opt} for the adaptation, compare bottom of page 51.

So, one can write:

$$\frac{\left|\hat{G}(f_k)\right|}{\left|G(f_k)\right|}\cdot\cos\left(\phi_G(f_k)-\phi_{\hat{G}}(f_k)\right)\approx 1 \tag{4-4}$$

Introducing Eq. (4-4) into Eq. (3-41) the following computation algorithm for the convergence coefficient *c* at time step *n* (i.e. $c(n)$) is obtained:

$$c(n)=\left[\frac{1}{2\cdot\sum_{m=1}^{\Delta}\left[\widetilde{S}_{\hat{r}\hat{r}\,n-m}(f_k)\right]+\widetilde{S}_{\hat{r}\hat{r}_n}(f_k)}\right]_{Minimum\ over\ f_k} \tag{4-5}$$

This algorithm was used to continuously compute the convergence coefficient $c(n)$ used for controller update in the simulation. As a consequence of the results shown in Chapter 2-3 the quadratic coherence function between the disturbance signal and the reference signal was chosen to be $\gamma_{\alpha d}^{\,2}\left(e^{j\omega T}\right)=0.75$ for performance validation of the converged controller. The performance of the controller was measured after $1*10^4$ samples of convergence time starting from zero initialization of its coefficients (i.e. $h_0(n=0)=h_1(n=0)=h_2(n=0)=\ldots=h_{N-1}(n=0)=0$.)

Note, that for the implementation on a flying aircraft the controller coefficients would be initialized with the approximate optimum of the feed-forward wing bending vibration controller in order to reduce the convergence time.

Figure 4-2 illustrates the mean standardized magnitudes of the error signal output (i.e. average modal wing bending acceleration magnitude) over frequency for several cases. The *blue line* represents the uncontrolled aircraft whereas the *red line* represents the example aircraft with the robust band pass feedback wing bending vibration controller, designed in the European AWIATOR project [63].

An approximate 50% reduction of the modal wing bending acceleration magnitude was obtained at the first symmetric vertical wing bending frequency with this active wing bending damping system.

The *orange line* represents the example aircraft with the adaptive feed-forward wing bending vibration controller proposed in this thesis after $1*10^4$ samples of convergence time. As postulated by Eq. (2-17) an approximate 50% reduction of the mean standardized magnitude of the Fourier transform of the error signal, i.e. of $|\overline{E}|(e^{j\omega T})$ was obtained at the first symmetric vertical wing bending frequency. Since in the simulation $\gamma_{\alpha d}^{\ 2}(e^{j\omega T}) = 0.75$ is constant over frequency, the compensation of the higher modes (i.e. above 2.5 Hz) is overestimated. Note, that according to Chapter 2-3 the quadratic coherence function $\gamma_{\alpha d}^{\ 2}(e^{j\omega T})$ actually decreases with increasing frequency in the real atmosphere.

The *cyan line* illustrates the average modal wing bending acceleration magnitude with a combination between robust band pass feedback and converged adaptive feed-forward wing bending vibration control. This hybrid controller reduces the atmospheric turbulence excited first symmetric vertical wing bending vibration magnitude by more than 70%. The converged controller performance was about the same for all mass and Mach cases. For the performance plots for the other cases see *Appendix F*.

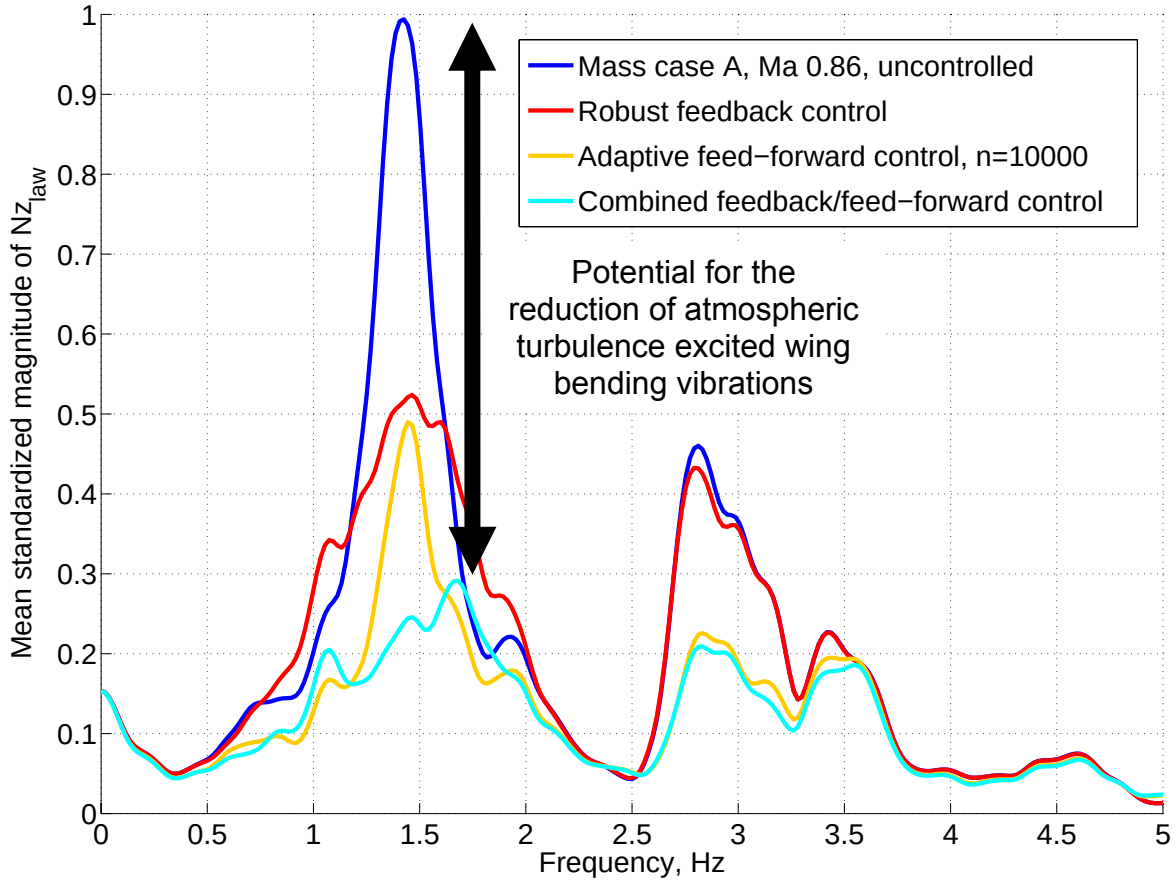

Figure 4-2. Performance of converged controller, mass case A, Ma=0.86, $\gamma_{\alpha d}^{\ 2}(e^{j\omega T}) = 0.75$.

4.3 Performance with Modeling Errors

The previous chapter showed that the proposed adaptive feed-forward wing bending vibration controller reaches the theoretic maximum attainable performance with a perfect plant model. In order to test the convergence behavior of the adaptation algorithm under more realistic conditions, numeric simulations were performed with phase errors in the plant model (i.e. $\hat{G}(f_k) \neq G(f_k)$.)

Note, that for demonstration purposes these simulations were carried out for plant model phase errors which, for the sake of a simple illustration, are constant over frequency f_k, well knowing that for such systems no physical representation exists. Furthermore a perfect coherence between the disturbance signal and the reference signal is assumed (i.e. $\gamma_{\alpha d}{}^2\left(e^{j\omega T}\right)=1$.) in order to separate the two performance degrading effects, namely the performance degradation due to modeling errors, and the performance degradation due to an imperfect coherence $\gamma_{\alpha d}{}^2\left(e^{j\omega T}\right)$.

Figure 4-3 shows the time behavior of the first 12 values of the *N*-point DFT of $\vec{h}(n)$ for three cases. The *blue lines* illustrate the adaptation with an approximately perfect plant model (i.e. $\hat{G}(f_k) \approx G(f_k)$.) The *red lines* illustrate the adaptation with +45° constant phase error for all f_k in the plant model $\hat{G}(f_k)$, and the *green lines* illustrate the adaptation with -45° constant phase error for all f_k. For the simulation runs with +/- 45° phase error one gets:

$$\frac{\left|\hat{G}(f_k)\right|}{\left|G(f_k)\right|} \cdot \cos\left(\phi_G(f_k) - \phi_{\hat{G}}(f_k)\right) \approx 0.71 \tag{4-6}$$

For the simulation runs with +/- 45° phase error the convergence coefficient computation algorithm thus makes:

$$c(n) = \left[\frac{0.71}{2 \cdot \sum_{m=1}^{\Delta} \left[\widetilde{S}_{\hat{r}\hat{r}\,n-m}(f_k)\right] + \widetilde{S}_{\hat{r}\hat{r}_n}(f_k)} \right]_{Minimum\ over\ f_k} \tag{4-7}$$

At the beginning of each run the controller coefficients were again initialized with zero (i.e. $h_0(n=0) = h_1(n=0) = h_2(n=0) = ... = h_{N-1}(n=0) = 0$.) The simulations were run for $1.25*10^5$ samples in order to test also the long-term behavior.

It has been observed that the discrete frequency domain controller coefficients move into different directions depending on the phase error at the beginning of the adaptation. But finally, the coefficients at high SCP gain frequencies (e.g. coefficients No. 4 and 5 for first symmetric vertical wing bending vibration control) converge to a (slightly time-varying) estimate of a causal representation of $H_{opt}\left(e^{j\omega T}\right)$ after about $6*10^3$ samples (with $N=\Delta_{overlap}=64$ and $T=40$ms.)

Thus, after sufficient convergence time the adaptive feed-forward wing bending vibration control system provides the optimum performance (already illustrated in Figure 4-2 for a perfect plant model) even with +/- 45° phase error in the plant model. According to Eq. (3-41), this is the case for any plant model phase error that is smaller than +/- 90°.

However, the upper boundary of the convergence coefficient decreases with the cosine function of the plant model phase errors. That means that the required convergence time goes to infinity, when the plant model phase errors goes to +/- 90°. For a plant model phase error of +/- 60° the upper boundary of the convergence coefficient is only halved, which still provides reasonably fast convergence of the adaptation algorithm.

Moreover, using the optimum convergence coefficient c_{opt} for the update of the controller coefficients already makes the adaptation algorithm robust against a plant model phase error of < +/- 60°. Thus, in order to provide a rule of thumb, one could say that plant model phase errors of up to +/- 60° will not affect the convergence speed severely.

Since in Eq. (3-16) the quantity inside the brackets $\{...\}_+$ represents an estimate of the gradient of the error surface by averaging over the last N samples the controller coefficients keep continuously slightly adapting within a certain area after $6*10^3$ samples. The way the controller tracks the estimated optimum depends on the phase error in the plant model, and has no notable influence on the wing bending vibration alleviation performance.

Note, that the controller converges much slower for frequencies with low SCP gain due to the small adaptation steps with a convergence coefficient which is constant over frequency. However, this has no influence on the performance of wing bending vibration control since there are no structural modes to control at low gain frequencies anyways.

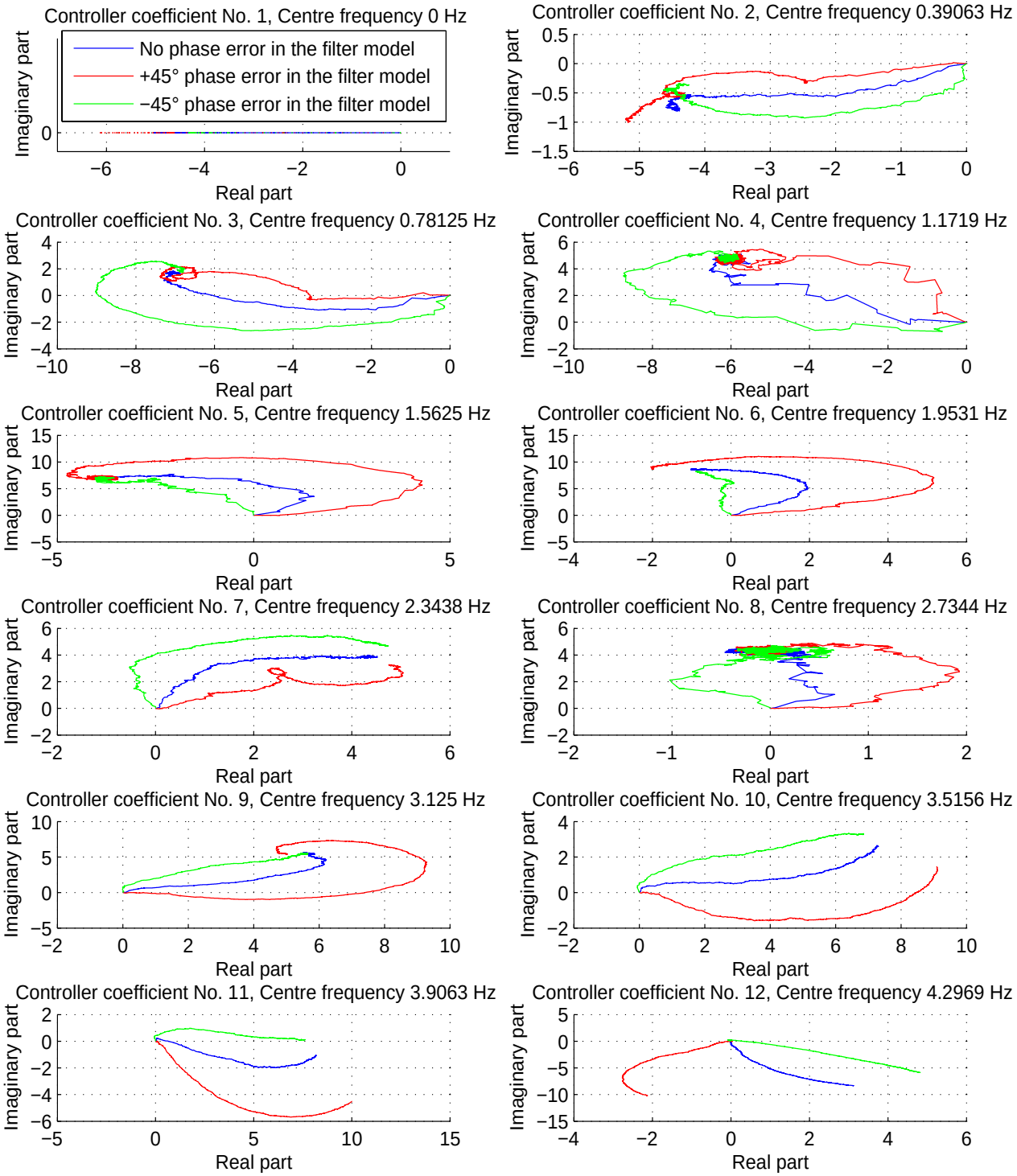

Figure 4-3. Convergence of the controller coefficients with phase errors in the plant model for mass case C, Ma=0.86, $\gamma_{\alpha d}{}^{2}\left(e^{j\omega T}\right)=1$.

In order to get a feeling for the performance of a *non-adaptive* feed-forward controller in the presence of modeling errors, the following admittedly simplistic calculations were performed. Thereby, a steady state excitation is assumed to allow for a frequency domain representation. Let the phase error of a *non-adaptive* feed-forward controller $H\left(e^{j\omega T}\right)$ be $\phi_{H\,opt}\left(e^{j\omega T}\right)-\phi_{H}\left(e^{j\omega T}\right)$ at a certain frequency ω, and let the multiplicative magnitude error $B\left(e^{j\omega T}\right)$ be defined as:

$$\left|H\left(e^{j\omega T}\right)\right|=\left(1+B\left(e^{j\omega T}\right)\right)\left|H_{opt}\left(e^{j\omega T}\right)\right| \tag{4-8}$$

The terms $\phi_{H\,opt}\left(e^{j\omega T}\right)$, and $\left|H_{opt}\left(e^{j\omega T}\right)\right|$ are the phase and magnitude of the optimum feed-forward controller $H_{opt}\left(e^{j\omega T}\right)$, whereas $\phi_{H}\left(e^{j\omega T}\right)$, and $\left|H\left(e^{j\omega T}\right)\right|$ are the phase and magnitude of the actually realized non-adaptive feed-forward controller $H\left(e^{j\omega T}\right)$.

For the further derivation some equations from Chapter 3 have to be reconsidered. Assuming ${\gamma_{\alpha d}}^{2}\left(e^{j\omega T}\right)=1$, Eq. (3-5) may be illustrated in the following vector graph, see Figure 4-4:

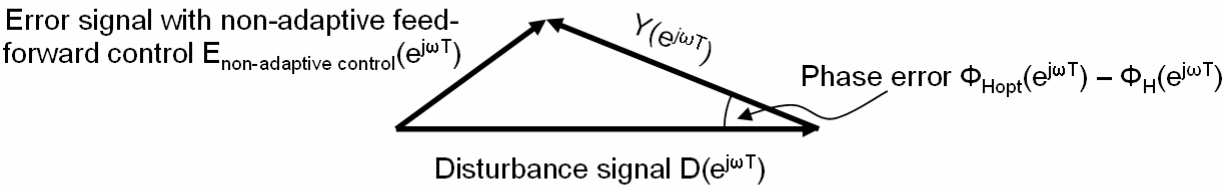

Figure 4-4. Vector graph for disturbance compensation with feed-forward control for a certain normalized angular frequency ωT.

Thereby, $E_{\text{non}-\text{adaptive control}}\left(e^{j\omega T}\right)$ is the Fourier transform of the error signal e with a non-adaptive feed-forward controller $H\left(e^{j\omega T}\right)$ commanding the symmetrically driven ailerons.

Introducing Eq. (3-5) into Eq. (3-6), makes:

$$S_{ee}\left(e^{j\omega T}\right)=S_{dd}\left(e^{j\omega T}\right)+S_{yy}\left(e^{j\omega T}\right)+2\cdot\mathrm{Re}\left\{S_{yd}\left(e^{j\omega T}\right)\right\} \tag{4-9}$$

with $S_{ee}\left(e^{j\omega T}\right)$, $S_{dd}\left(e^{j\omega T}\right)$, and $S_{yy}\left(e^{j\omega T}\right)$ denoting the power spectral densities of the error signal *e*, the disturbance signal *d*, and the share in the error signal due to feed-forward control *y*. Making use of Eq. (4-8) the term $S_{yy}\left(e^{j\omega T}\right)$ may be written as:

$$S_{yy}\left(e^{j\omega T}\right) = S_{rr}\left(e^{j\omega T}\right)\left|H\left(e^{j\omega T}\right)\right|^2 = S_{rr}\left(e^{j\omega T}\right)\left|H_{opt}\left(e^{j\omega T}\right)\right|^2\left(1+B\left(e^{j\omega T}\right)\right)^2 \tag{4-10}$$

Assuming that $\gamma_{rd}{}^2\left(e^{j\omega T}\right)=1$ and introducing Eq. (3-11)) one can rewrite $S_{yy}\left(e^{j\omega T}\right)$ to:

$$S_{yy}\left(e^{j\omega T}\right) = \frac{\left|S_{rd}\left(e^{j\omega T}\right)\right|^2}{S_{rr}\left(e^{j\omega T}\right)}\left(1+B\left(e^{j\omega T}\right)\right)^2 = S_{dd}\left(e^{j\omega T}\right)\left(1+B\left(e^{j\omega T}\right)\right)^2 \tag{4-11}$$

The term $\mathrm{Re}\left\{S_{yd}\left(e^{j\omega T}\right)\right\}$ is the real part of the cross spectral density between the share in the error signal due to feed-forward control *y*, and the disturbance signal *d*. Assuming that $\gamma_{rd}{}^2\left(e^{j\omega T}\right)=1$, $\mathrm{Re}\left\{S_{yd}\left(e^{j\omega T}\right)\right\}$ may be rewritten as:

$$\mathrm{Re}\left\{S_{yd}\left(e^{j\omega T}\right)\right\} = \mathrm{Re}\left\{\left\langle Y^*\left(e^{j\omega T}\right)D\left(e^{j\omega T}\right)\right\rangle\right\} =$$

$$= \left|S_{rd}\left(e^{j\omega T}\right)\right|\left|H\left(e^{j\omega T}\right)\right|\cos\left(\phi_D\left(e^{j\omega T}\right)-\phi_Y\left(e^{j\omega T}\right)\right) =$$

$$= \left|S_{rd}\left(e^{j\omega T}\right)\right|\left|H_{opt}\left(e^{j\omega T}\right)\right|\left(1+B\left(e^{j\omega T}\right)\right)\cos\left(\phi_D\left(e^{j\omega T}\right)-\phi_Y\left(e^{j\omega T}\right)\right) =$$

(again introducing Eq. (3-11))

$$= \frac{\left|S_{rd}\left(e^{j\omega T}\right)\right|^2}{S_{rr}\left(e^{j\omega T}\right)}\left(1+B\left(e^{j\omega T}\right)\right)$$

$$\cos\left(\left(\phi_A\left(e^{j\omega T}\right)+\phi_G\left(e^{j\omega T}\right)+\phi_{H_{opt}}\left(e^{j\omega T}\right)+180°\right)-\left(\phi_A\left(e^{j\omega T}\right)+\phi_G\left(e^{j\omega T}\right)+\phi_H\left(e^{j\omega T}\right)\right)\right) =$$

$$= -S_{dd}\left(e^{j\omega T}\right)\left(1+B\left(e^{j\omega T}\right)\right)\cos\left(\phi_{H_{opt}}\left(e^{j\omega T}\right)-\phi_H\left(e^{j\omega T}\right)\right) \tag{4-12}$$

The terms $\phi_D\left(e^{j\omega T}\right)$ and $\phi_Y\left(e^{j\omega T}\right)$ denote the phase angles of the Fourier transforms of the disturbance signal *d* and of the feed-forward share in the error signal *y*, whereas the term $\phi_A\left(e^{j\omega T}\right)$ denotes the phase angle of the Fourier transform of the reference signal α, and $\phi_G\left(e^{j\omega T}\right)$ is the phase angle of the plant transfer function $G\left(e^{j\omega T}\right)$.

Introducing Eq. (4-11) and Eq. (4-12) into Eq. (4-9) with $S_{ee}\left(e^{j\omega T}\right) = S_{ee_{non-adaptive\ control}}\left(e^{j\omega T}\right)$ finally gives the following performance index $\Xi\left(e^{j\omega T}\right)$ for $\gamma_{\alpha d}^{\ 2}\left(e^{j\omega T}\right) = 1$:

$$\Xi\left(e^{j\omega T}\right) = \frac{S_{dd}\left(e^{j\omega T}\right) - S_{ee_{\text{non-adaptive control}}}\left(e^{j\omega T}\right)}{S_{dd}\left(e^{j\omega T}\right)} =$$

$$= 2\cdot\left(1+B\left(e^{j\omega T}\right)\right)\cos\left(\phi_{H\,opt}\left(e^{j\omega T}\right) - \phi_H\left(e^{j\omega T}\right)\right) - \left(1+B\left(e^{j\omega T}\right)\right)^2 \qquad (4\text{-}13)$$

Thereby, $S_{dd}\left(e^{j\omega T}\right)$ denotes the power spectral density of the disturbance signal *d*, and $S_{ee_{\text{non-adaptive control}}}\left(e^{j\omega T}\right)$ is the power spectral density of the error signal *e* when a non-adaptive feed-forward controller $H\left(e^{j\omega T}\right)$ is used. As illustrated in Table 4-1, a performance index $\Xi\left(e^{j\omega T}\right)$ equal to one means perfect compensation of the disturbance signal, whereas $\Xi\left(e^{j\omega T}\right) = 0$ means no compensation.

Table 4-1. Significance of the performance index

Value of $\Xi\left(e^{j\omega T}\right)$	Impact on the control performance	Attainable $S_{ee_{\text{non-adaptive control}}}\left(e^{j\omega T}\right)$
0 %	no compensation of the disturbance signal	$S_{ee_{\text{non-adaptive control}}}\left(e^{j\omega T}\right) = S_{dd}\left(e^{j\omega T}\right)$
100 %	perfect compensation of disturbance signal	$S_{ee_{\text{non-adaptive control}}}\left(e^{j\omega T}\right) = 0$

In Figure 4-5 the performance index $\Xi\left(e^{j\omega T}\right)$ is plotted against the phase error and the multiplicative magnitude error for a certain normalized angular frequency ωT. It can be seen that, for steady state conditions and for $\gamma_{\alpha d}^{\ 2}\left(e^{j\omega T}\right) = 1$, a non-adaptive feed-forward controller with optimal magnitude (i.e. $B\left(e^{j\omega T}\right) = 0$), but with a phase error of $\phi_{H\,opt}\left(e^{j\omega T}\right) - \phi_H\left(e^{j\omega T}\right) =$ +/- 45° at said normalized angular frequency ωT provides a performance index $\Xi\left(e^{j\omega T}\right)$ of about 41% at this frequency. As shown before, an adaptive feed-forward controller provides a performance index $\Xi\left(e^{j\omega T}\right)$ of 100% for a plant model phase error of +/- 45°. In fact this simple example illustrates very clearly the advantage of the adaptation of feed-forward wing bending vibration control.

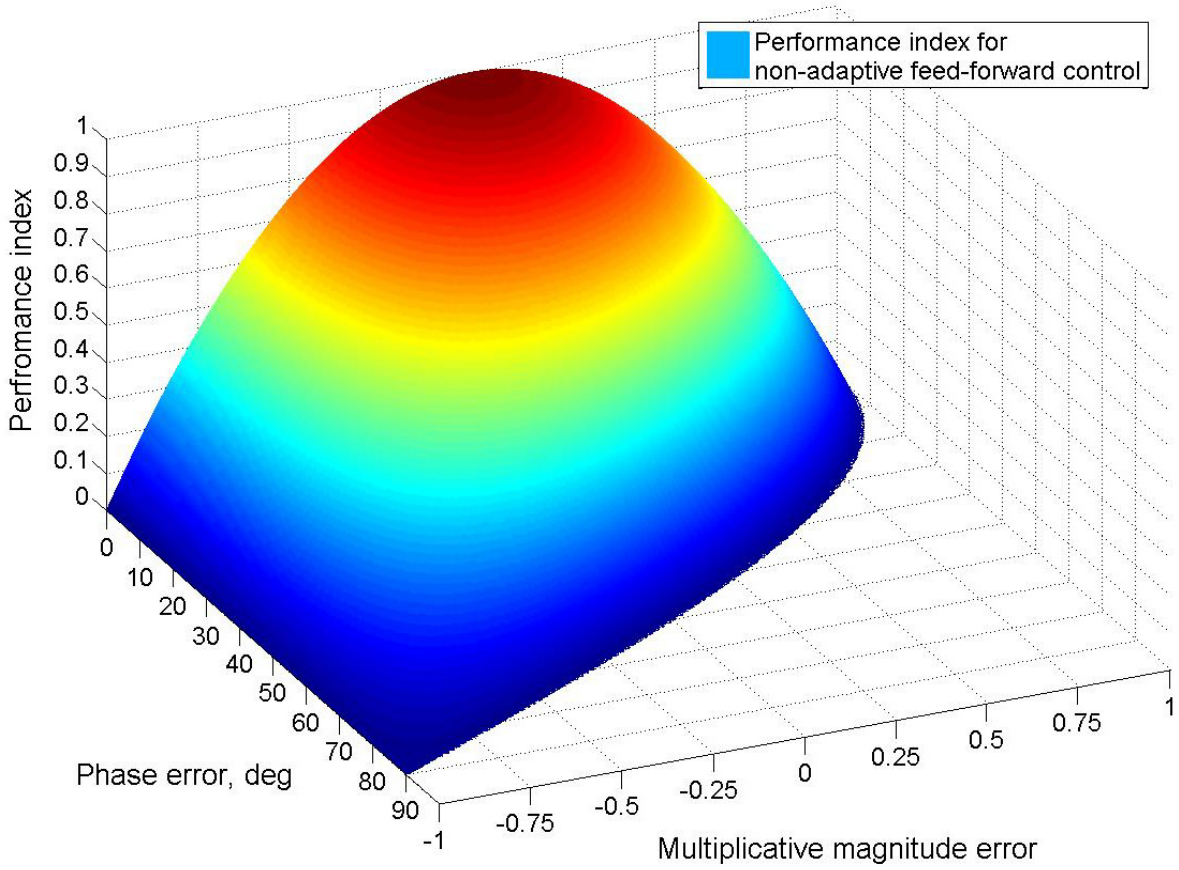

Figure 4-5. Performance index against phase error and magnitude error for a certain normalized angular frequency ωT, and perfect coherence $\gamma_{od}^{\,2}\left(e^{j\omega T}\right)=1$.

For $\gamma_{od}^{\,2}\left(e^{j\omega T}\right)\neq 1$ the power spectral density of the error signal $S_{ee}\left(e^{j\omega T}\right)$ makes:

$$S_{ee}\left(e^{j\omega T}\right)=S_{ee_{\text{non-adaptive control}}}\left(e^{j\omega T}\right)+S_{ee_{\min}}\left(e^{j\omega T}\right) \tag{4-14}$$

The non-adaptive controller can only compensate the share of the disturbance signal that is correlated with the reference signal, compare Figure 4-6 where the feed-forward compensation is illustrated in terms of power spectral densities of the related signals. The power spectral density of the correlated share of the disturbance signal is denoted $\left(S_{dd}\left(e^{j\omega T}\right)-S_{ee_{\min}}\left(e^{j\omega T}\right)\right)$.

However, for a non-adaptive feed-forward controller with phase and/or magnitude errors respectively this share cannot be fully compensated. An error due to imperfect compensation denoted $S_{ee_{\text{non-adaptive control}}}\left(e^{j\omega T}\right)$ remains in the secondary signal path.

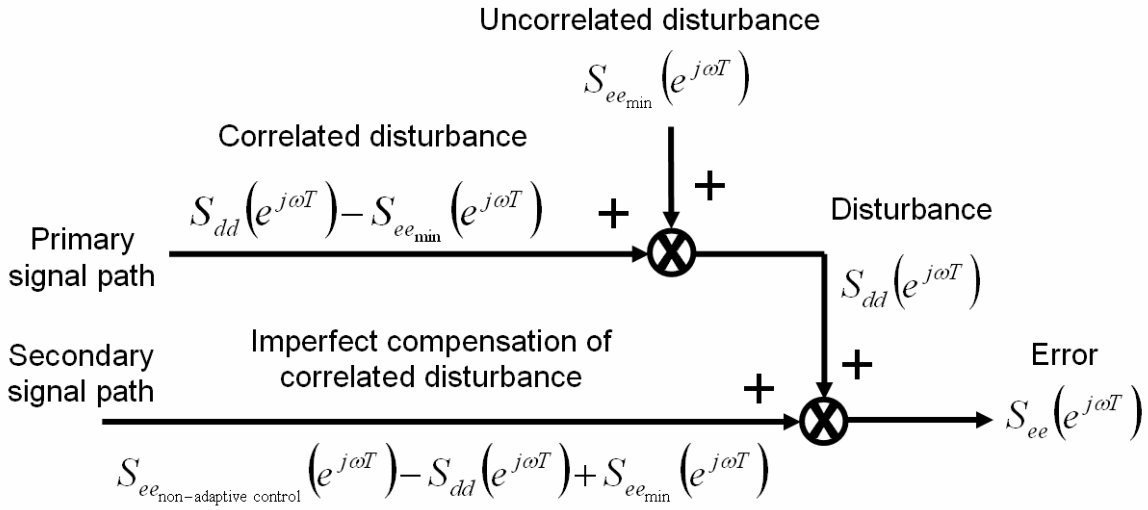

Figure 4-6. Illustration of feed-forward compensation in terms of signal powers.

Thus, substituting $S_{dd}\left(e^{j\omega T}\right)$ in Eq. (4-13) by $\left(S_{dd}\left(e^{j\omega T}\right)-S_{ee_{\min}}\left(e^{j\omega T}\right)\right)$ a more general form of the performance index can be defined for $\gamma_{\alpha d}{}^{2}\left(e^{j\omega T}\right)\neq 1$:

$$\Xi\left(e^{j\omega T}\right)=\frac{\left(S_{dd}\left(e^{j\omega T}\right)-S_{ee_{\min}}\left(e^{j\omega T}\right)\right)-S_{ee_{\text{non-adaptive control}}}\left(e^{j\omega T}\right)}{\left(S_{dd}\left(e^{j\omega T}\right)-S_{ee_{\min}}\left(e^{j\omega T}\right)\right)} \tag{4-15}$$

In addition Eq. (3-13) may be rewritten so that:

$$S_{ee_{\min}}\left(e^{j\omega T}\right)=\left(1-\gamma_{\alpha d}{}^{2}\left(e^{j\omega T}\right)\right)S_{dd}\left(e^{j\omega T}\right) \tag{4-16}$$

Substituting the term $S_{ee_{\text{non-adaptive control}}}\left(e^{j\omega T}\right)$ in Eq. (4-14) by the rearranged Eq. (4-15), and introducing Eq. (4-16), one finally obtains:

$$S_{ee}\left(e^{j\omega T}\right)=S_{dd}\left(1-\gamma_{\alpha d}{}^{2}\left(e^{j\omega T}\right)\Xi\left(e^{j\omega T}\right)\right) \tag{4-17}$$

which can easily be reordered in order to obtain the following equation for the estimation of the performance of a non-adaptive feed-forward controller with imperfect coherence between the reference, and the disturbance signal (i.e. $\gamma_{\alpha d}{}^2\left(e^{j\omega T}\right) \neq 1$):

$$\frac{S_{dd}\left(e^{j\omega T}\right) - S_{ee}\left(e^{j\omega T}\right)}{S_{dd}\left(e^{j\omega T}\right)} = \gamma_{\alpha d}{}^2\left(e^{j\omega T}\right) \Xi\left(e^{j\omega T}\right) \tag{4-18}$$

Remember, that the value for $\Xi\left(e^{j\omega T}\right)$ is calculated from the right side of Eq. (4-13).

4.4 Introduction of a Mean Plant Model

The previous chapter showed that unlike non-adaptive feed-forward control, the proposed adaptive feed-forward wing bending vibration controller converges to an estimate of a causal representation of $H_{opt}\left(e^{j\omega T}\right)$ as long as the plant model phase error is smaller than +/- 90°, and the convergence coefficient *c* remains within the boundaries defined in Eq. (3-39). The (mass case and Mach number dependent) variations of the SCP transfer function of the four-engine example aircraft used in this thesis turned out to be considerably smaller than +/- 90° in the controlled frequency range of up to 4 Hz. Thus, it was possible to use only one single mean plant model for the generation of the estimated filtered reference signal $\hat{r}$ required for controller update (review Eq. (3-15)) for all the mass cases and Mach numbers listed in Table 2-1.

Figure 4-7 shows magnitude and phase over frequency of the SCP transfer function of the four-engine example aircraft for different mass and Mach conditions evaluated at discrete frequencies f_k. In fact, $G(f_k)$ would have to be calculated by evaluating the expectation value of the 2*N*-point DFT of the SPC's impulse response at discrete frequencies f_k. The underestimation of the plant magnitude is compensated by using c_{opt} for the adaptation, as it was done in Chapter 4.2. The mean plant model $\hat{G}(f_k)$ (i.e. *red line*) has been calculated as mean value between maximum and minimum magnitude ($\left|\widetilde{G}_{\max}(f_k)\right|$ and $\left|\widetilde{G}_{\min}(f_k)\right|$), and mean value between maximum and minimum phase ($\phi_{\widetilde{G}\max}(f_k)$ and $\phi_{\widetilde{G}\min}(f_k)$) of the slightly biased estimates of $G(f_k)$, denoted with $\widetilde{G}(f_k)$, over all mass and Mach cases for all discrete frequencies f_k:

$$\left|\hat{G}(f_k)\right| = \frac{\left|\widetilde{G}_{\max}(f_k)\right| + \left|\widetilde{G}_{\min}(f_k)\right|}{2} \tag{4-19}$$

$$\phi_{\hat{G}}(f_k) = \frac{\phi_{\widetilde{G}\max}(f_k) + \phi_{\widetilde{G}\min}(f_k)}{2} \tag{4-20}$$

The calculation of the mean plant model's phase as described in Eq. (4-20) is only valid if the phases of the SCP transfer functions are illustrated in an unwrapped representation as it is done in the lower plot of Figure 4-7. The black dotted lines mark the corridor of +/-90° phase deviation from the mean plant transfer function. Using the red line transfer function for the generation of the estimated filtered reference signal $\hat{r}$, the proposed adaptation algorithm will converge to an estimate of a causal representation of the optimum controller $H_{opt}\left(e^{j\omega T}\right)$ as long as the actual phase of $G(f_k)$ remains inside this corridor, and the convergence coefficient c is chosen according to Eq. (3-39).

For all mass and Mach cases the phase of the plant response lies well inside this corridor. Thus, according to the theory one mean plant model is sufficient for the proposed adaptive algorithm to converge to an estimate of a causal representation of the optimum controller $H_{opt}\left(e^{j\omega T}\right)$ for all mass and Mach cases of the investigated aircraft model.

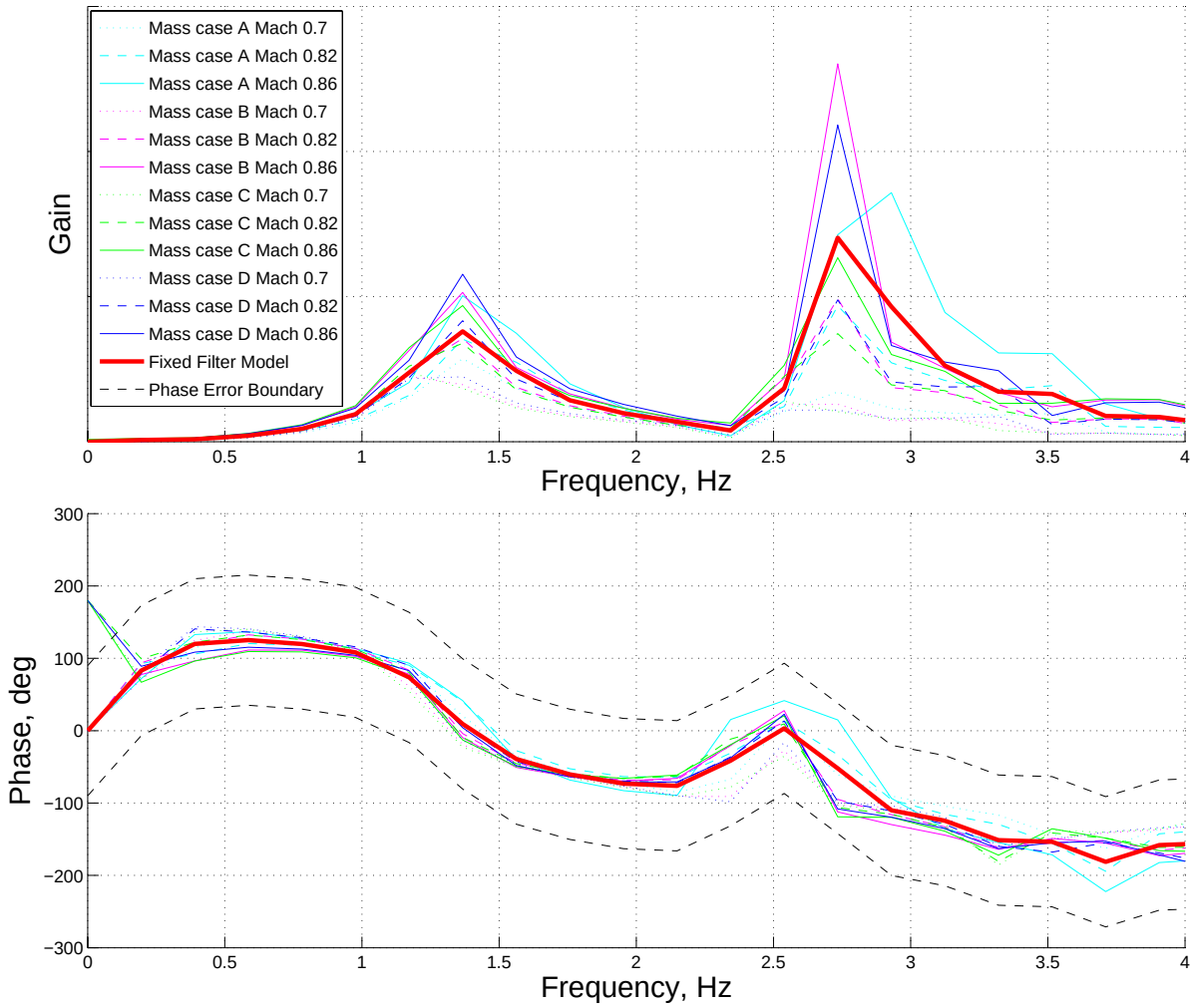

Figure 4-7. Mean plant model.

The static value of the plant model was chosen to be zero, see *red line* in Figure 4-7, because the static phase varies 180° between different mass and Mach cases. The plant model was also set to zero at frequencies above 4 Hz because of the huge phase variations between different mass and Mach cases. Setting the plant model to zero at frequencies where the phase is very uncertain or exposed to huge variations affects the causality of the plant model's time-domain representation. As long as the magnitude of the real SCP transfer function is very low at these frequencies compared to the magnitude at Eigen mode frequencies this effect is negligible. For convenience, no phase uncertainties of the SCP in addition to the phase variations due to flight and fuel mass condition are considered. Additional uncertainties can be caused by neglected higher structural modes, actuator uncertainties, etc.

A big challenge with respect to the maiden flight is the estimation of the magnitude of the SCP, which sometimes is evaluated too low at certain frequencies due to unexpected lightly damped modes. It is therefore recommended to use a conservative convergence coefficient *c* for a maiden flight. According to Eq. (3-39), if *c* is chosen 10 times smaller, the algorithm is safe against a SCP magnitude that is 10 times higher than estimated.

4.5 Transition Between Different Mass and Mach Cases

In the previous chapter it was shown that for the four-engine example aircraft used in this investigations one single mean plant model is sufficient for stable convergence of the wing bending vibration controller adaptation at all mass and Mach cases. For the analysis of the adaptive control algorithm with a mean plant model the time variation of the plant was modeled by switching between state-space models of different mass cases and Mach numbers during the simulation. This procedure takes into account that the feed-forward wing bending vibration controller has been adapted to a certain mass case before a flight phase in calm atmosphere, or landing and refueling respectively, i.e. before a phase, where the adaptation must be turned off due to following requirements:

- $\alpha_{wind} >> \alpha_{ground}$ in the frequency range of controlled structural modes, Eq. (2-20).
- $S_{rr}\left(e^{j\omega T}\right) \neq 0$ required for the existence of $H_{opt}\left(e^{j\omega T}\right)$, see Eq. (3-11).
- Finite upper boundary of the convergence coefficient *c*, see Eq. (3-39).

The mass case (as well as the Mach number) will probably change during this flight phase in calm atmosphere, or during ground time/refueling. When a flight phase in turbulent atmosphere is encountered thereafter, the adaptive feed-forward controller is turned on again, and has to adapt to the new mass case (and Mach number.) An open question thereby is, if a flight phase in turbulent atmosphere generally is long enough for proper controller adaptation. The answer can only be given through a detailed analysis of test flights, which goes beyond the scope of this thesis.

Looking at Figure 4-7 the following observations can be made for the SCP transfer functions of the four-engine example aircraft. Regarding phase and magnitude, the mass cases B and D are rather similar for equal Mach numbers. The SCP transfer function of mass case A at Ma = 0.86 is completely different from the transfer functions of all other cases. Naturally, there is also a huge magnitude difference between the transfer functions for low and high Mach numbers making the magnitude adaptation almost as important as the phase adaptation. Two worst cases have been identified:

- Switching from mass case A at Ma = 0.86 to any other mass case and back.
- Switching between Ma = 0.86 and Ma = 0.7.

Mainly these two worst cases are investigated in the following. At first the ability of the adaptive feed-forward wing bending vibration controller to track mass case variations is investigated. The (quadratic) coherence function between the disturbance signal and the reference signal was chosen to be $\gamma_{od}^{\,2}\left(e^{j\omega T}\right)=0.75$ for the performance validation of the adaptive controller with a mean plant model.

Moreover, the maximum deviation of the mean plant model's transfer function $\hat{G}(f_k)$ from any $\tilde{G}(f_k)$ transfer function was calculated for each frequency f_k and introduced into Eq. (3-41) in order to compute the optimum convergence coefficient c_{opt} used for the simulations with this mean plant model. The performance of the converged controller naturally was the same as for the adaptation with a perfect plant model, compare Figure 4-2.

In Figure 4-8 the time behavior of the frequency domain controller coefficients is illustrated for the following mass case variations. After $1*10^4$ samples (*blue line*) of adaptation to mass case A, Ma=0.86 starting from zero initialization, the controller is well adapted at least in the frequency range of the first symmetric vertical wing bending vibration (i.e. coefficients No. 4 and 5.) Then, the SCP transfer function is switched to mass case B for $5*10^3$ samples (*red line*). After that the SCP transfer function is switched to mass case C for $5*10^3$ samples (*green line*), then to mass case D again for $5*10^3$ samples (*cyan line*), and finally back to mass case A (*magenta line*). The simulation was stopped after $3*10^4$ samples.

Figure 4-9 shows the time behavior of the frequency domain controller coefficients for Mach number variations with an additional transition between mass case A and mass case B. Starting from zero initialization the feed-forward wing bending vibration controller is adapted to mass case B, Ma=0.86 for the first $1*10^4$ samples (*blue line*). Then, the SCP transfer function is switched to Ma=0.7 for $5*10^3$ samples (*red line*), still mass case B. After that, the SCP transfer function is switched to mass case A, Ma=0.86 for another $5*10^3$ samples (*green line*). Then, the Mach number is switched to Ma=0.7 again for $5*10^3$ samples (*cyan line*). Finally, the SCP transfer function is switched back to mass case B, Ma=0.86 (*magenta line*). The simulation was stopped after $3*10^4$ samples.

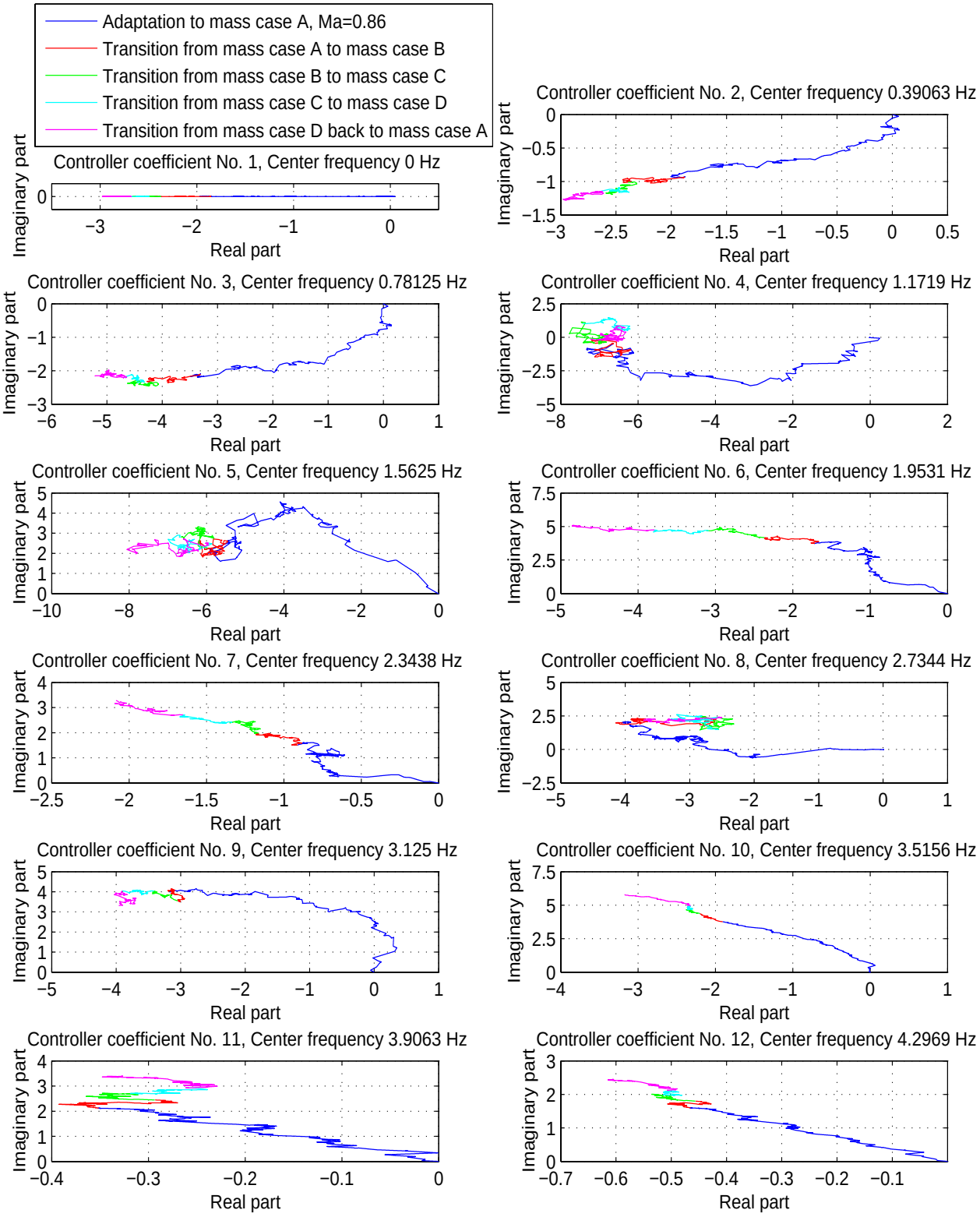

Figure 4-8. Tracking behaviour of the controller coefficients for mass case variations, $\gamma_{\alpha d}{}^{2}\left(e^{j\omega T}\right)=0.75$.

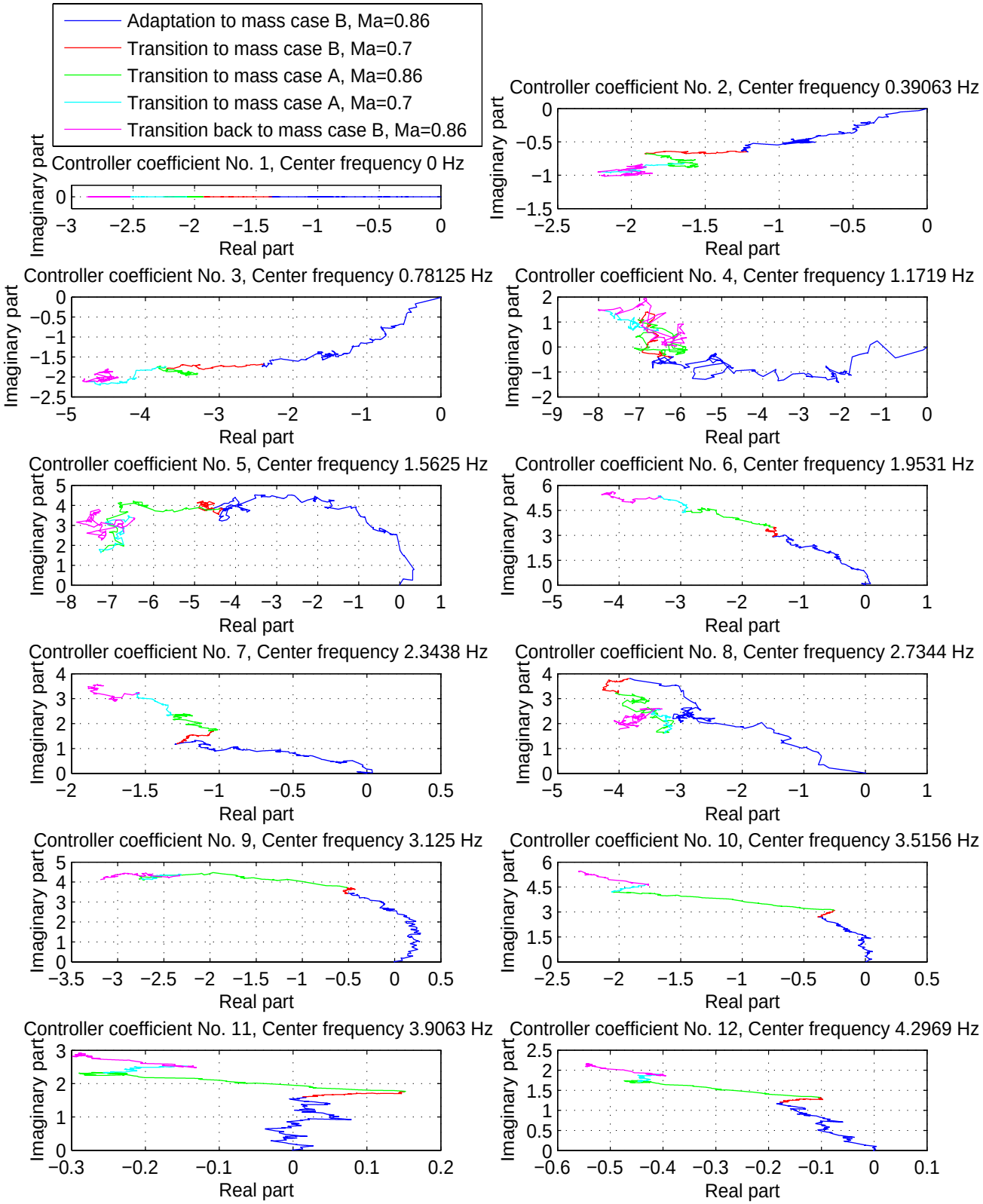

Figure 4-9. Mach number variations with transition between mass case A and mass case B, $\gamma_{\alpha d}{}^{2}\left(e^{j\omega T}\right)=0.75$.

It could be observed that at least the controller coefficient No. 4, which is apparently closest to the first symmetric vertical wing bending frequency, as well as the controller coefficient No. 8, which is in the frequency range of higher Eigen modes with high SCP gain track the mass case variations faster than within the $5*10^3$ samples and remain in a certain region until the mass case is changed again.

Note, that the coefficients at low SCP gain (i.e. low plant model gain) frequencies (i.e. coefficients No. 1, 2, 6, 10, 11) have not converged after the first $1*10^4$ samples, and remain converging into the same direction even when the mass case is switched. As already explained the slow convergence at frequencies with low SCP gain is due to the small adaptation steps at low SCP gain frequencies. This in turn is due to the convergence coefficient being chosen as minimum over allowed values over frequency, as described in Eq. (3-41). However, this does not affect the control performance. The coefficients at low SCP gain frequencies seem to result mainly from causality constraints for the time domain feed-forward controller $H(z)$.

Despite the switching between different mass and Mach cases no notable loss of wing bending vibration alleviation performance could be observed. The controller's tracking of plant variations seems to be fast enough to avoid any significant performance degradation due to plant variations.

4.6 Response of the Converged Controller to a Discrete Gust

In this chapter, it is demonstrated that the *converged* feed-forward wing bending vibration controller can also compensate *transient* atmospheric excitation. However, that does not necessarily mean that the adaptation works properly in the presence of a transient excitation. The influence of discrete gusts on the controller adaptation needs further investigations (e.g. on flight tests) going beyond the scope of this thesis.

In order to give a preliminary validation result of the influence of the *converged* feed-forward wing bending vibration controller (i.e. no additional robust feedback wing bending vibration control loop) on the time response of the four-engine example aircraft to a discrete gust, one case, namely mass case A, Ma = 0.86 is investigated in the following.

In these simulations no additional homogenous atmospheric turbulence is considered. The discrete gust is assumed to be one-dimensional, and to remain unchanged while passing the aircraft. The feed-forward controller is adapted with steady state atmospheric turbulence excitation (i.e. one-dimensional von Kármán turbulence spectrum) before the simulations with the discrete gust are performed.

The disturbance has been modelled as already described, i.e. $\alpha_{wind} = v_z / V_{TAS}$ in radians. with the vertical airflow $v_z(t)$ of the discrete gust being defined as:

$$v_z(t) = \frac{v_{z\max}}{2} \cdot \left(1 - \cos\left(2\pi \frac{V_{TAS} \cdot (t - t_0)}{L}\right)\right) \quad \text{for:} \quad t_0 \le t \le \frac{L}{V_{TAS}} + t_0 \qquad (4\text{-}21)$$

$$v_z(t) = 0 \quad \text{for:} \quad t < t_0 \quad \text{and for:} \quad t > \frac{L}{V_{TAS}} + t_0 \qquad (4\text{-}22)$$

Thereby, V_{TAS} denotes the true airspeed of the investigated aircraft model. The gust starts at t_0=0.5s. Three different scales of turbulence L have been investigated. Figure 4-10 shows the gust response for L = 100m, Figure 4-11 shows the gust response for L = 200m, and Figure 4-12 shows the gust response for L = 750m. The upper left plot in each figure illustrates the vertical airspeed of the discrete gust over time $v_z(t)$. The second plot from the top in the left column shows the according discrete feed-forward control input to the aileron actuators $u_{FF}(n)$. Thereby, the maximum vertical speed of the gust was chosen to $v_{z\max} = 1$ m/s for each simulation. For higher $v_{z\max}$ the control input partly exceeded the rate limit of the ailerons' actuators, especially for the gusts with L = 100m, and with L = 200m.

The third, and the 4th plot on the left side of each figure illustrate the pitch rate at the CG over time $q_{CG}(t)$, and the deviation of the wing bending moment on the left wing root $Mx_{WR}(t)$ from the static value in trimmed flight for the uncontrolled aircraft at mass case A, Ma = 0.86 (blue line), and for the aircraft with *converged* feed-forward wing bending vibration controller (red line.) In the right column of each figure from top to bottom the modal acceleration $Nz_{law}(t)$, as well as the vertical accelerations at the front fuselage $Nz_{front}(t)$, at the CG $Nz_{CG}(t)$, and at the rear fuselage $Nz_{rear}(t)$ are plotted over time.

All three figures feature the same scaling. It can thus be seen, that for the simulation with a scale of turbulence of L = 100m, the highest vertical accelerations at the front fuselage $Nz_{front}(t)$ are obtained, due to higher Eigen mode excitation. The highest wing root bending moment deviation from the static value, $Mx_{WR}(t)$ however is obtained with a scale of turbulence of L = 200m, where the excitation of the first symmetric vertical wing bending mode dominates.

The gust with a scale of turbulence of L = 750m excites mainly the alpha mode, and the modal wing bending acceleration excitation $Nz_{law}(t)$ therefore is very low. For all three scales of turbulence the converged feed-forward controller partly compensates the gust excitation of the pitch rate $q_{CG}(t)$, of the wing root bending moment deviation from the static value $Mx_{WR}(t)$, of the modal acceleration $Nz_{law}(t)$, as well as of the vertical accelerations $Nz_{front}(t)$, $Nz_{CG}(t)$, and $Nz_{rear}(t)$.

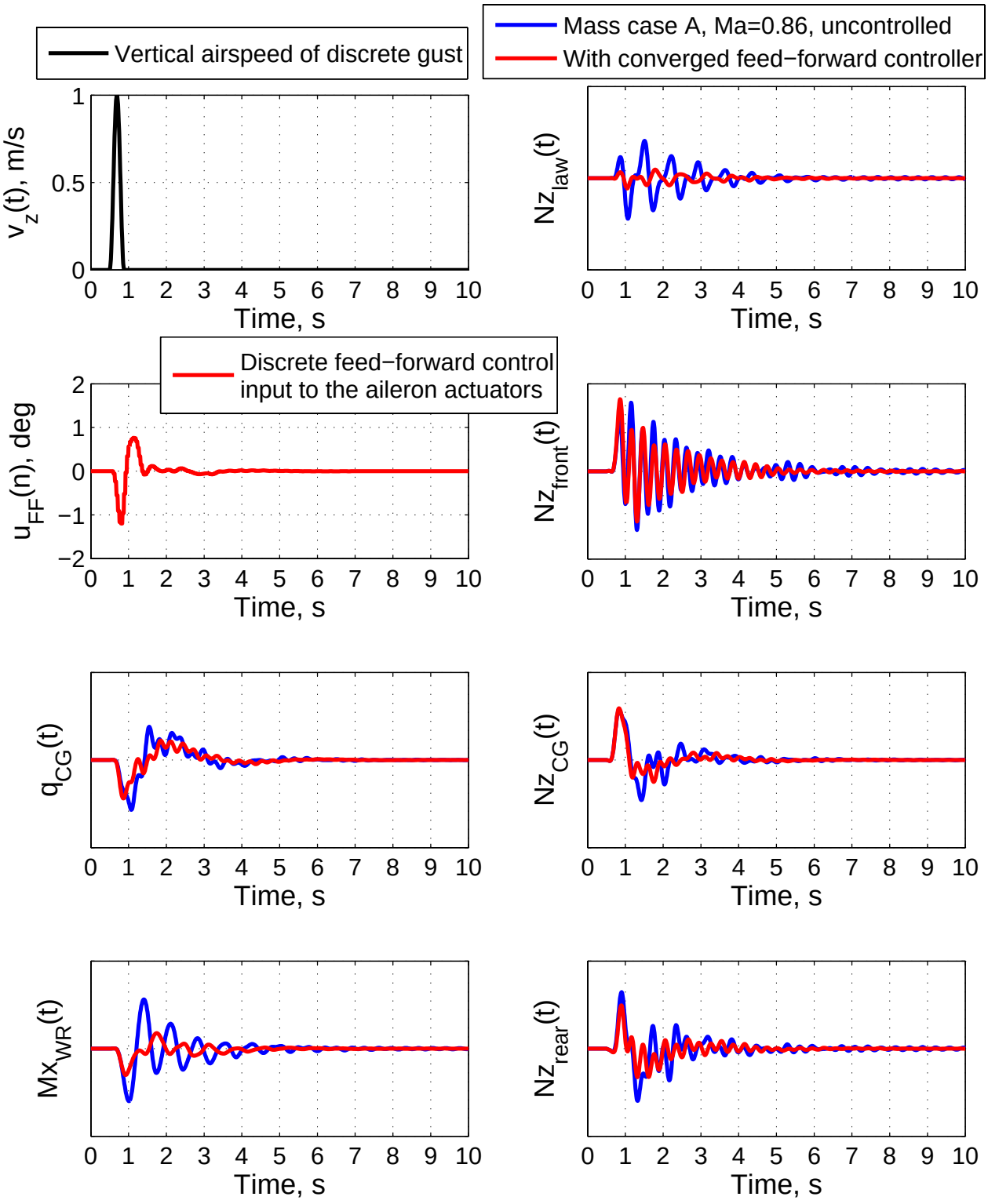

Figure 4-10. Time response of converged feed-forward controller to a discrete gust with *L*=100m.

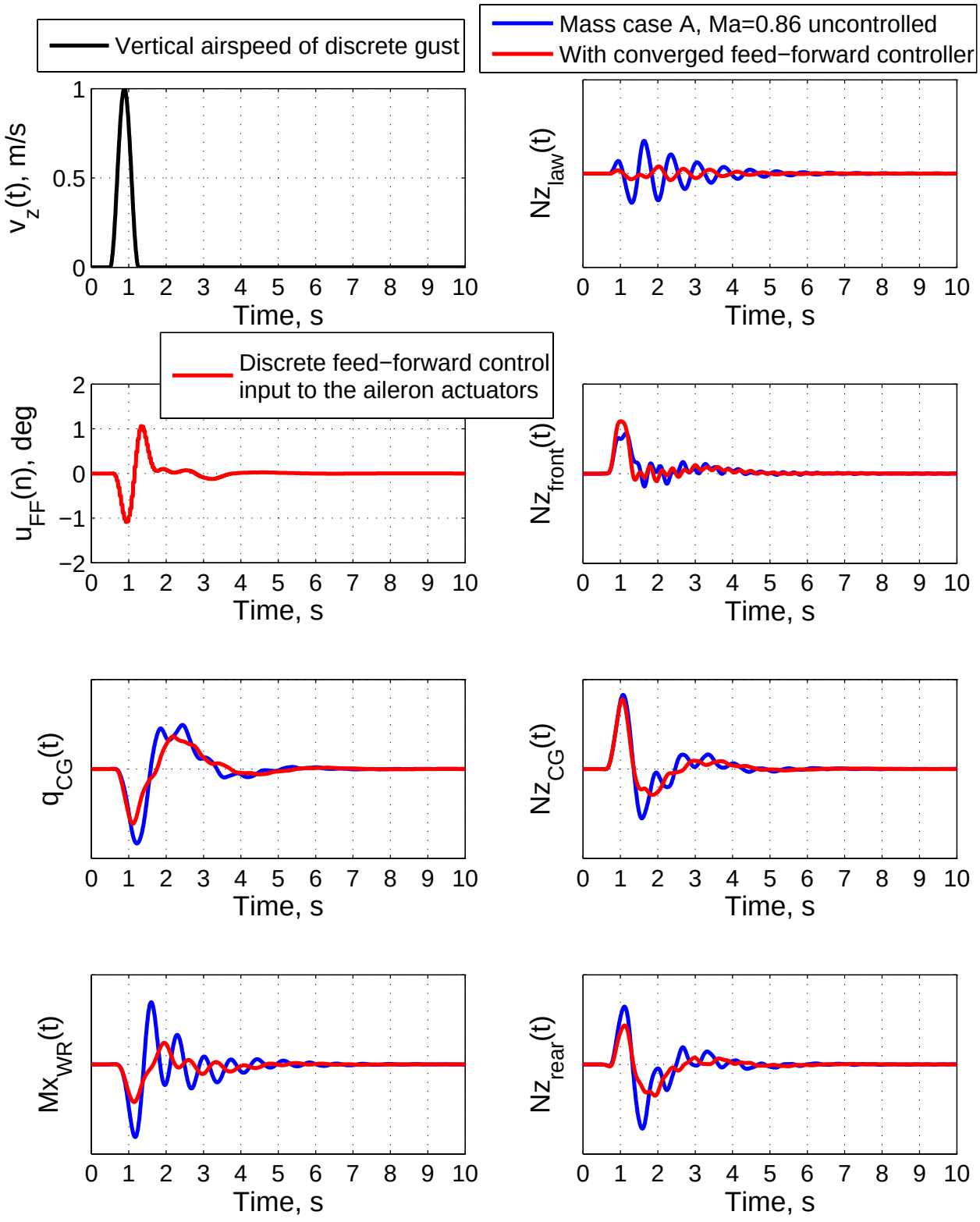

Figure 4-11. Time response of the aircraft with and without converged feed-forward controller to a discrete gust with *L*=200m.

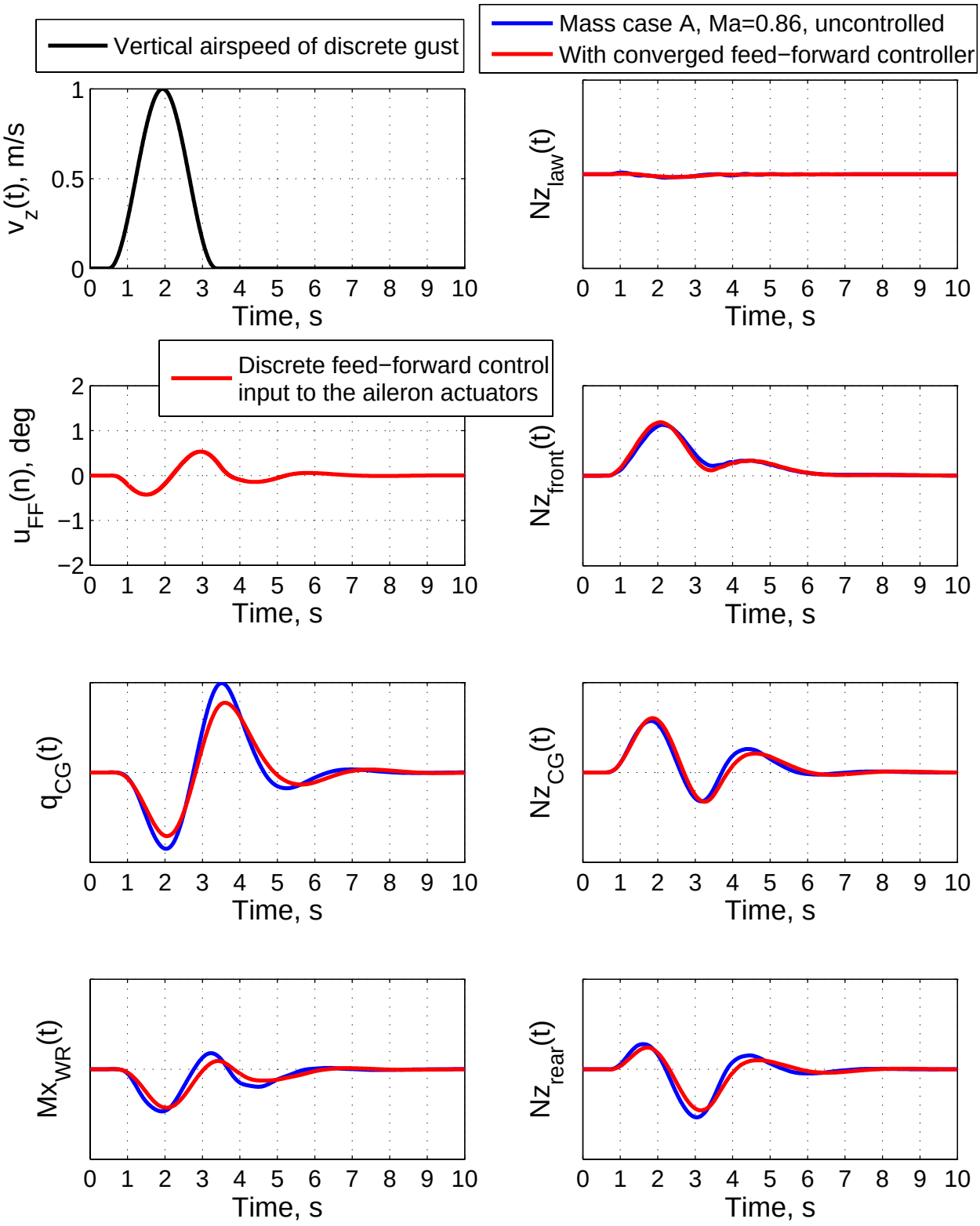

Figure 4-12. Time response of the aircraft with and without converged feed-forward controller to a discrete gust with *L*=750m.

5 Wind Tunnel Testing of the Adaptive Control System

In the previous chapters it has been shown by numeric simulations that adaptive feed-forward control is a very efficient means for the reduction of atmospheric turbulence excited wing bending vibrations on large transport aircraft. In order to investigate the real-time behavior of such an adaptive control system, a wind tunnel experiment has been performed with an elastic aircraft model. Thereby, the control objective was the active compensation of the first symmetric vertical wing bending mode excitation.

The testing of feed-forward vibration control in a wind tunnel poses many technical challenges. The most important of which is to generate locally correlated disturbances in order to provide a coherence between the disturbance signal and the reference measurement that is realistic for a flight in real atmosphere. This problem has been solved by designing a gust generator which was mounted right in front of the elastic wind tunnel model, while keeping wind tunnel turbulence low at the same time. Moreover, the signal that drives this gust generator was also used as reference signal.

In Chapter 5.1 the design of the experimental setup is explained whereas in Chapter 5.2 the wind tunnel test results are presented. These results from the real-time environment impressively support the validity of the previously derived theory and the numeric investigations. Said wind tunnel test partly has also been presented in [120].

5.1 The Experimental Setup

The wind tunnel test has been performed in the low speed wind tunnel facility A of the Institute of Aerodynamics at Technische Universität München. For investigations on the real-time behavior of the proposed adaptive wing bending vibration control system, subsonic wind tunnel tests at low Mach numbers are sufficient, regarding also costs of the experiments. Figure 5-1 illustrates the experimental setup. A gust generator consisting of a shaker motor which is able to continuously change the angle of attack of a wing segment is mounted in front of an elastic aircraft model. In order to obtain a 75% coherence between the reference signal and the disturbance signal in the frequency range of the first symmetric vertical wing bending mode (which would be realistic for a flight in real atmosphere, see Chapter 2.3), the signal x that drives the gust generator has been used as reference signal for feed-forward control at the same time.

The adaptive feed-forward controller then drives piezo-electric trailing edge flaps (i.e. one flap on each wing) in order to compensate the excitation of the first symmetric vertical wing bending mode. Piezo-electric drivers have the advantage that they can be

miniaturized at a reasonable prize, and offer control of phase and magnitude over a wide frequency range. The adaptive feed-forward control algorithm is implemented on a Digital Signal Processor (DSP), which is located outside the section of measurement.

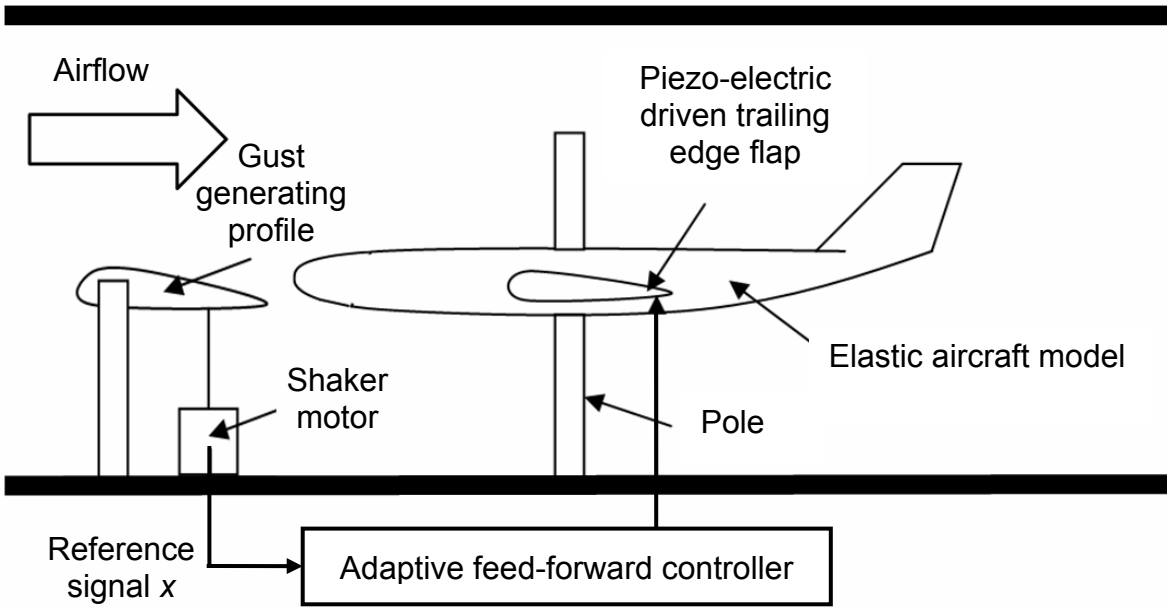

Figure 5-1. Layout of the experimental setup.

The elastic aircraft model is mounted on a vertical pole, see Figure 5-2 for details. The mounting allows roll, pitch, and yaw, but hinders vertical movements in order to prevent the model from exiting the narrow area of influence of the gust generator.

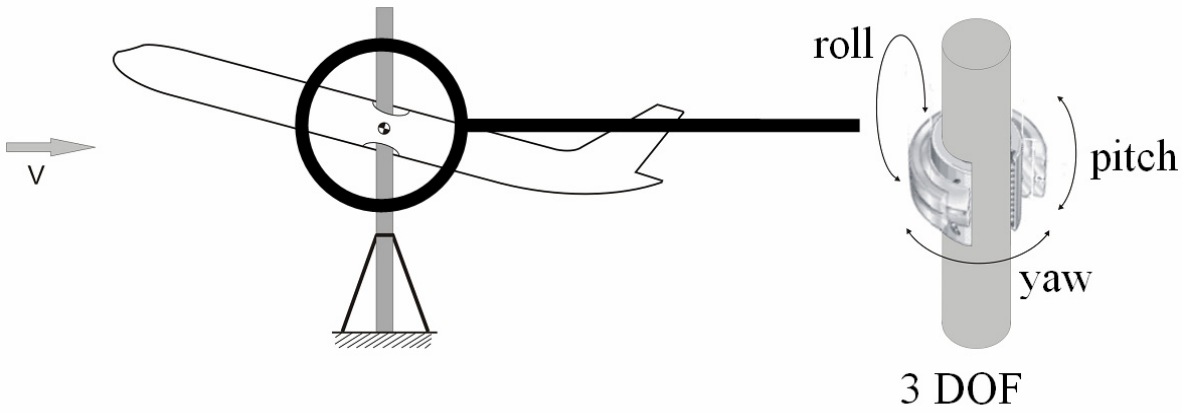

Figure 5-2. Mounting of the aircraft model.

The gust generator consists of a very stiff composite wing (i.e. part of a discarded helicopter blade) which is rotatably hinged in front of the aircraft model's nose in order to achieve maximum coherence (i.e. about 75%) between the gust excitation and the model's vibrations. The angle of attack of this wing is changed rapidly by a shaker motor, see Figure 5-3. This motor is driven with a white noise signal which is cut off at 25 Hz. This band pass white noise signal is generated by a separate signal generator. Due to the inertia, the gust generator naturally features a low pass behavior, but still excites the model's vibrations up to 25 Hz. Thus, it can be perfectly used for excitation of the first few Eigen modes of the aircraft model, especially for the excitation of the first symmetric vertical wing bending mode at about 10 Hz.

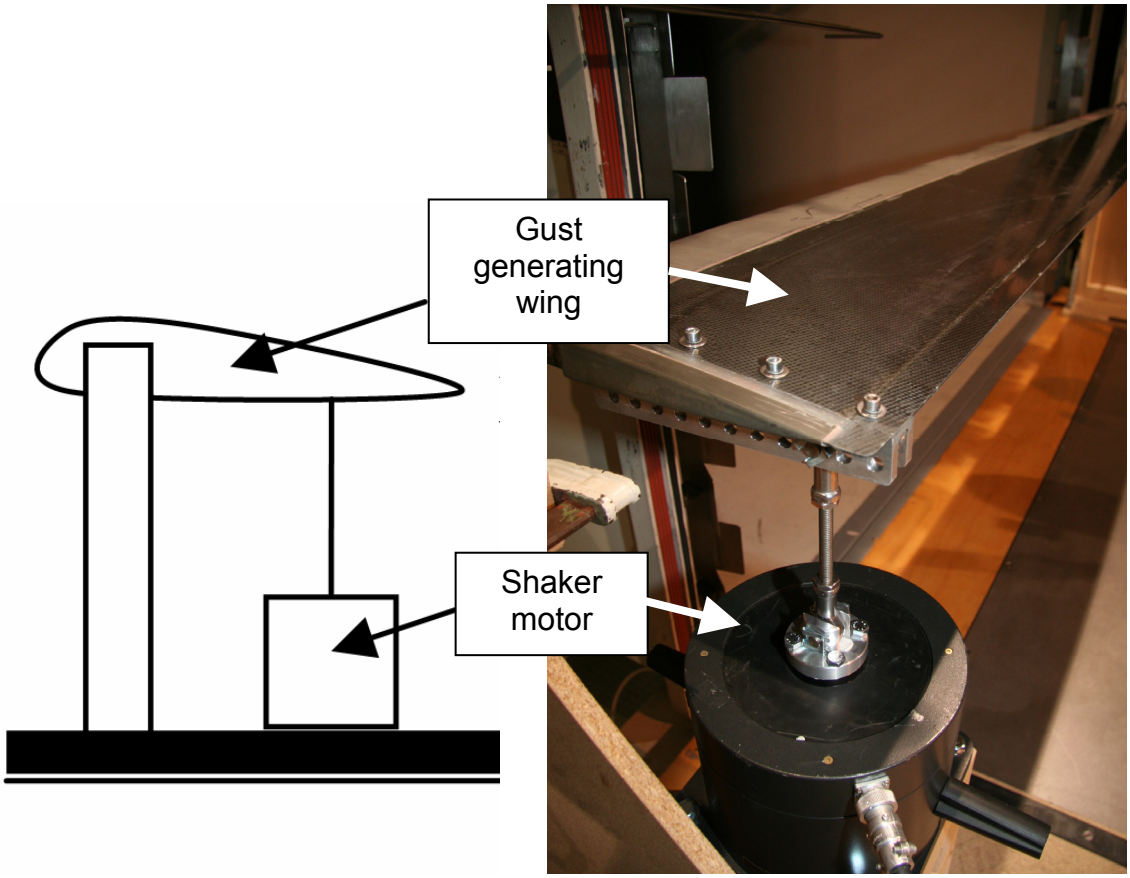

Figure 5-3. The gust generator.

For the wind tunnel tests an elastic model of a transport aircraft with similar structural Eigen mode distribution like the one that has been modeled for the numeric simulations in Chapter 4 has been designed. The design process of this elastic wind tunnel model is discussed in detail in [46]. Therefore only the most important features shall be mentioned here. The size of the elastic aircraft model was limited by the wind tunnel dimensions. The test section of wind tunnel A is 2.4m wide and 1.8m high. The model was built as large as possible in order to produce lowest possible Eigen frequencies and

to avoid actuators of very small size and with very high stiffness standards which are very costly. Figure 5-4 illustrates the dimensions of the wind tunnel model.

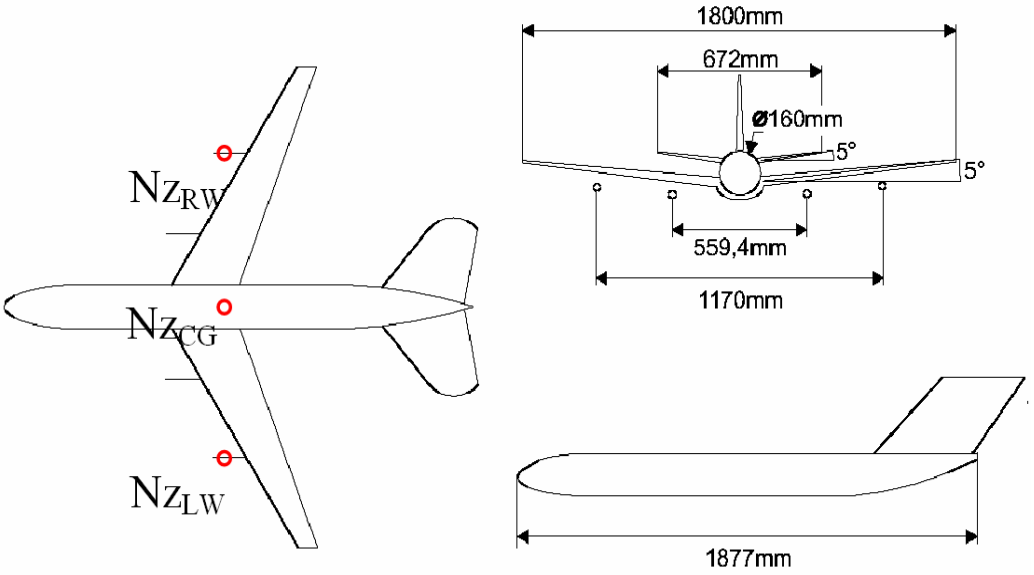

Figure 5-4. Dimensions of the elastic aircraft model and positions of the vertical acceleration sensors.

As discussed in detail in [46] the wind tunnel model's inner load carrying structure is made of aluminum, which is covered with foamed material to provide a suitable aerodynamic surface. The wings are additionally reinforced with GFRP ribs to ensure proper transmission of aerodynamic loads to the inner aluminum structure. Finally, a thin GFRP skin provides a smooth aerodynamic wing surface. The four aluminum engine masses are mounted on very stiff CFRP pylons, compare Figure 5-9.

The model has been designed with the first symmetric vertical wing bending frequency being at about 10 Hz, the first vertical fuselage bending frequency being at about 19 Hz, and the first symmetric planar wing bending frequency being at about 24 Hz. The second symmetric wing bending frequency resulted to be at about 30 Hz. Note, that in this thesis the control objective is the active compensation of only the first symmetric vertical wing bending mode excitation. If also the higher modes shall be controlled, stiffer, and thus more expensive actuators would be required.

Figures 5-5 through 5-8 illustrate the FEM derived first four symmetric Eigen modes of the inner load carrying aluminum structure, GFRP ribs, and rigidly connected masses of

the four engines and the tail unit of the elastic wind tunnel model. The foam material, as well as the thin GFRP skin have been neglected in the FEM simulations in order to save time. The shown FEM model consists of shell and beam elements, as well as of rigidly connected mass elements.

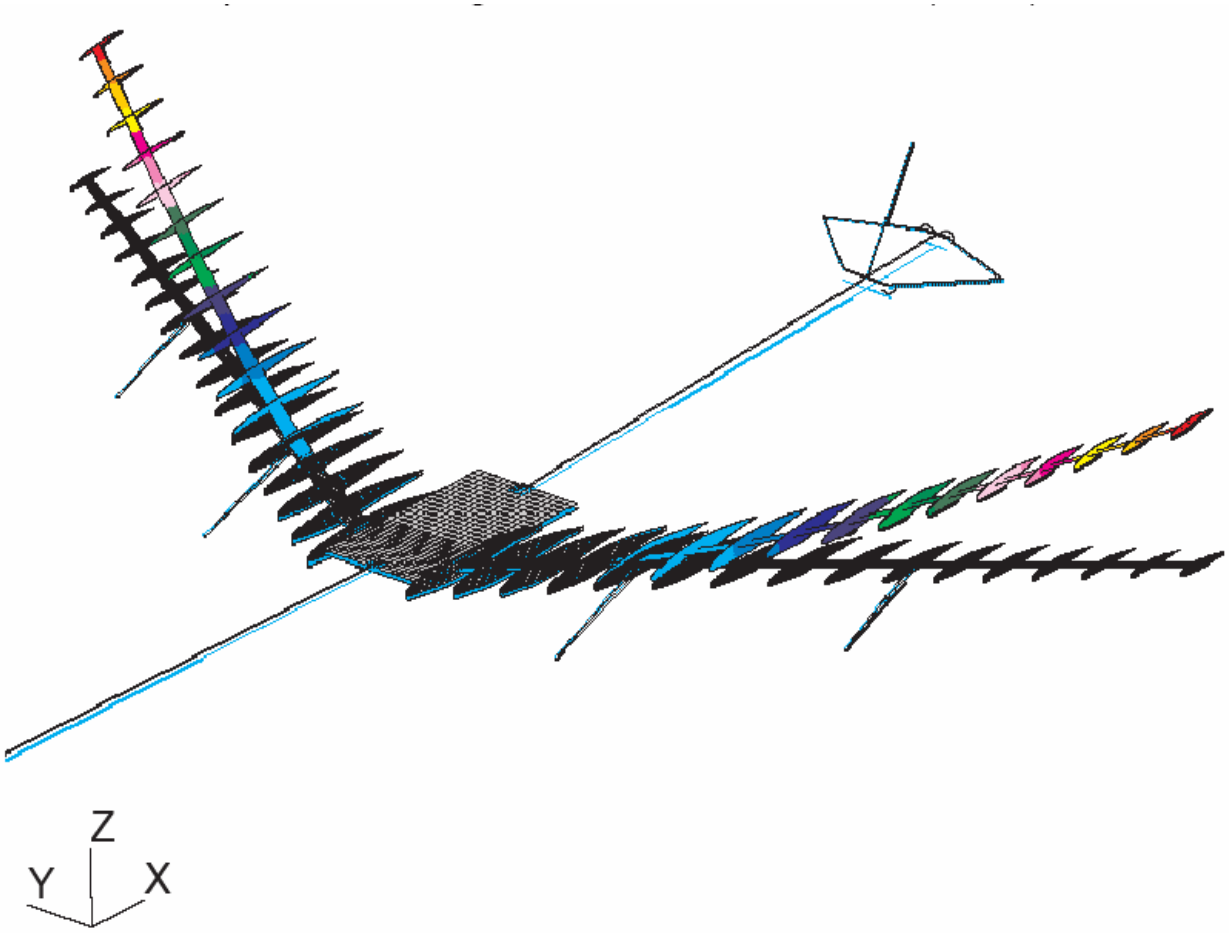

Figure 5-5. First symmetric wing bending mode of the wind tunnel model (~ 10 Hz).

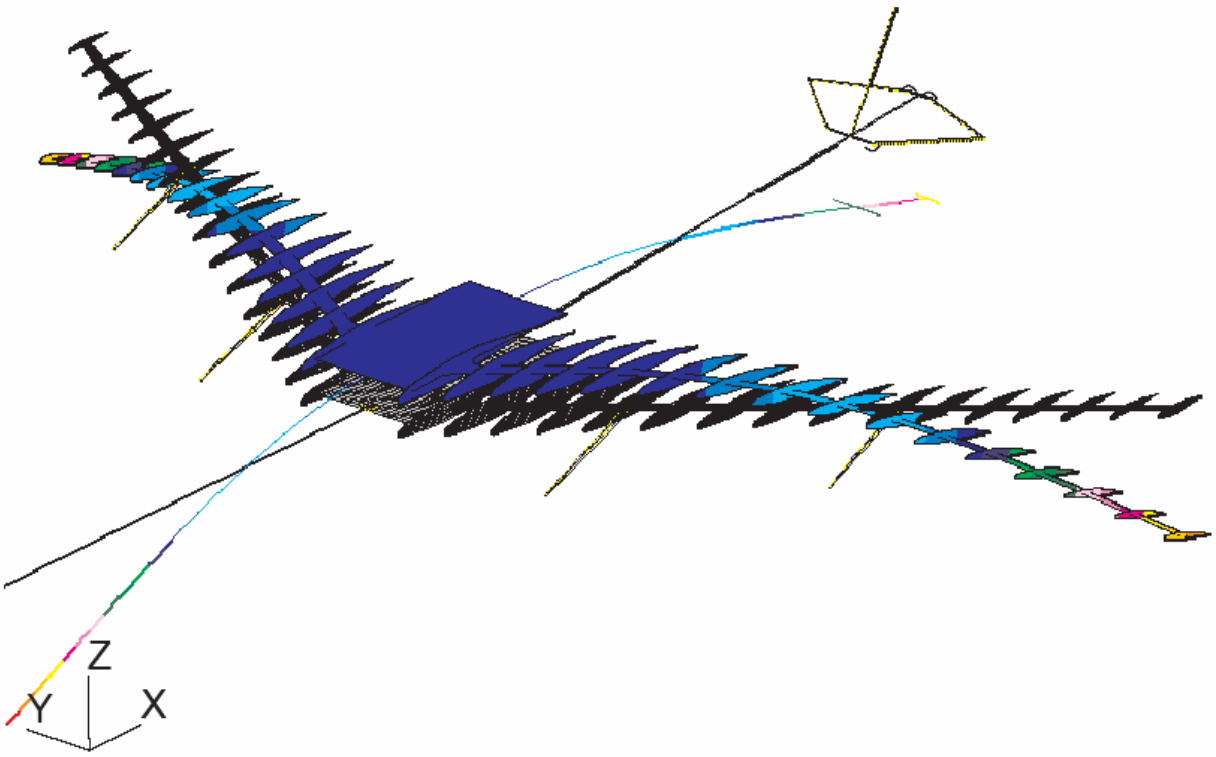

Figure 5-6. First fuselage bending mode of the wind tunnel model (~ 19 Hz).

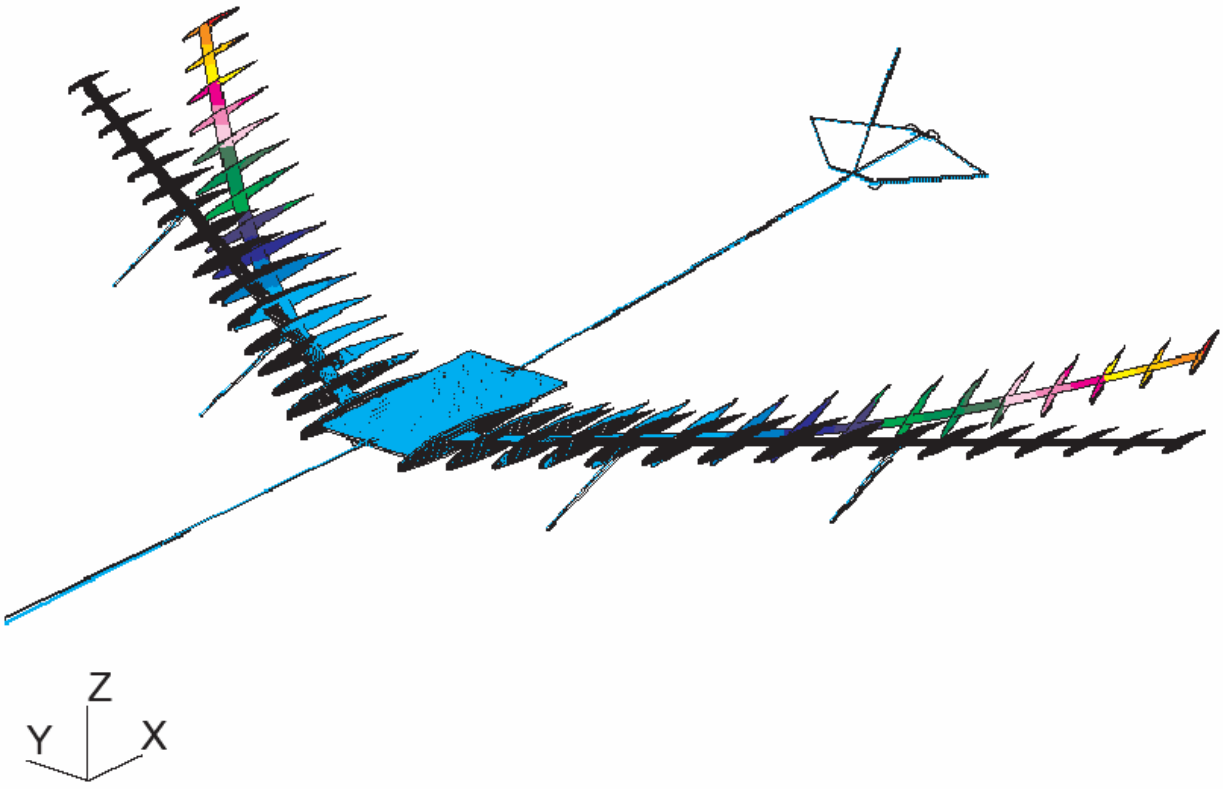

Figure 5-7. First in-plane wing mode of the wind tunnel model (~ 24 Hz).

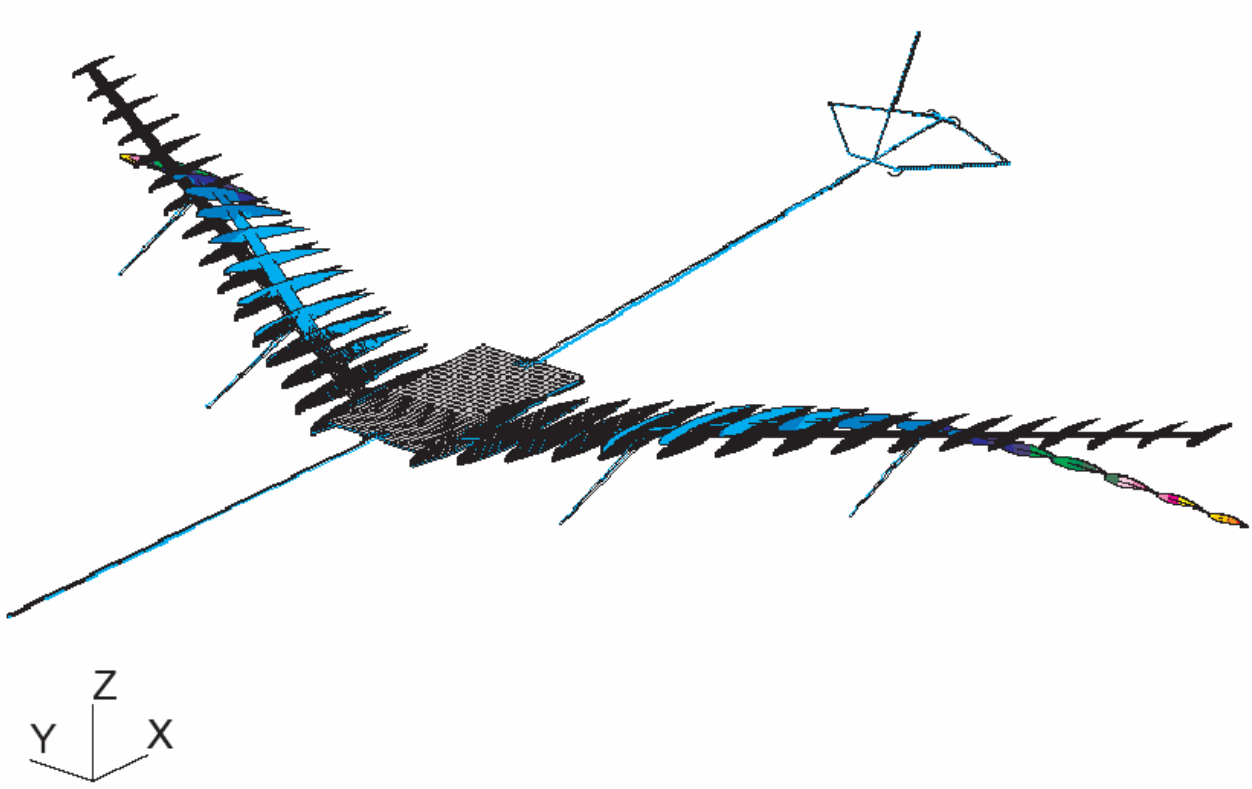

Figure 5-8. Second symmetric wing bending mode of the wind tunnel model (~ 30 Hz).

Comparing Figures 5-5 through 5-8 with Figure 2-1 through 2-6 one can see that the first four symmetric structural modes of the wind tunnel model do not contain any engine modes. This is due to the unrealistically high stiffness of the model's CFRP pylons (which have been modeled rigidly for the FEM analysis.) If the consideration of engine modes shall be introduced to the wind tunnel experiment an elastic design of the engine pylons would be required.

For the observation of the first symmetric vertical wing bending mode three vertical acceleration sensors have been mounted on the wind tunnel aircraft model, as proposed in Eq. (2-3), see red circles in Figure 5-4. Figure 5-9 shows the two aluminum engine masses and CFRP pylons of the right wing with a vertical acceleration sensor mounted on the outer engine mass.

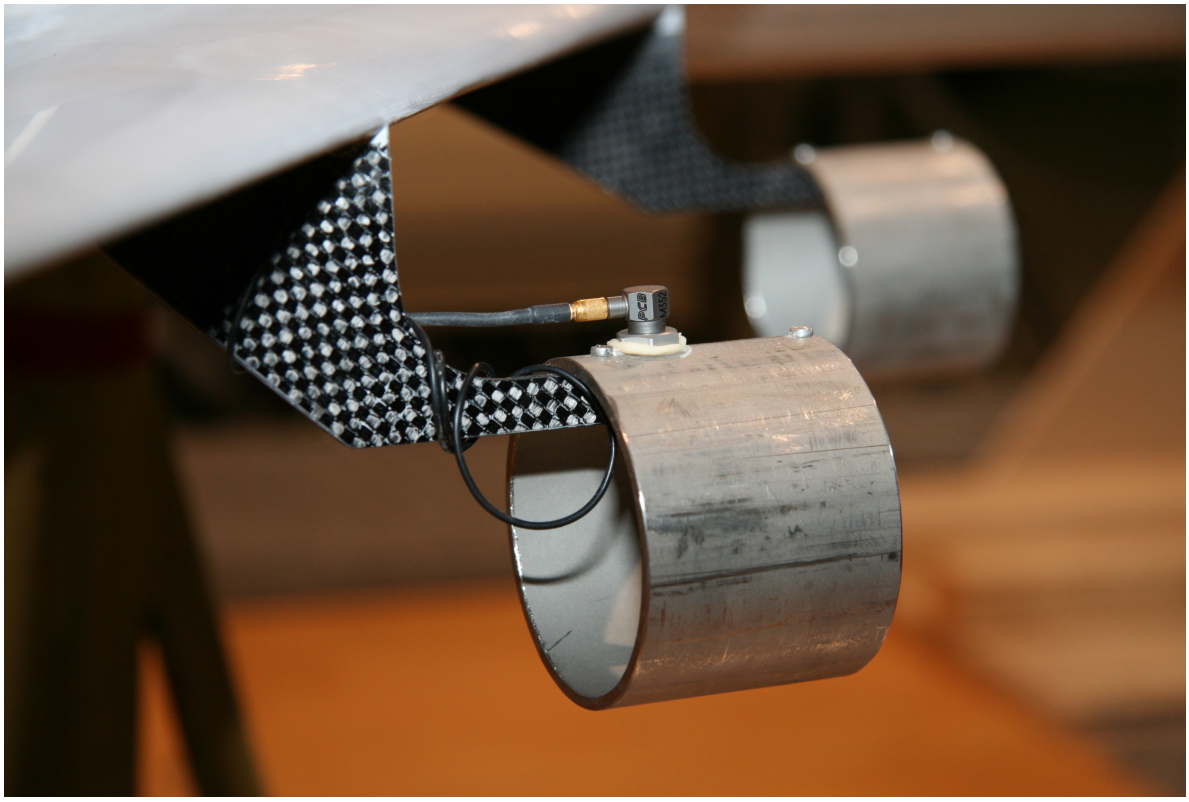

Figure 5-9. Vertical acceleration sensor mounted on the outer engine mass.

On each wing a piezo-electric driven trailing edge flap has been mounted for active wing bending vibration control. The trailing edge flaps consist of flat GFRP plates. Each of the two flaps are driven by two TH-7R THUNDER® piezo-actuators which are commercially available at the FACE® International Corporation. These actuators consist of a cambered metal plate with a piezo-electric layer on their upper side. Thereby, the camber of the metal plates serve as deflection amplifier.

The metal plates have been screwed to the wing arbors on one side. The GFRP flaps have been glued on the other plates' side, see Figure 5-10. The flaps are controlled via the voltage applied to the piezo-actuators, which is the simplest approach, but leads to a non-linear actuator behavior due to the piezo-material's hysteresis. The first bending frequency of the piezo-actuators with attached GFRP flap lies above 15 Hz, with as well as without current flow between the piezo-actuators' poles. The high voltages required for the piezo-electric flap drivers are generated by separate amplifiers outside the section of measurement, which are counted to the SCP in the following.

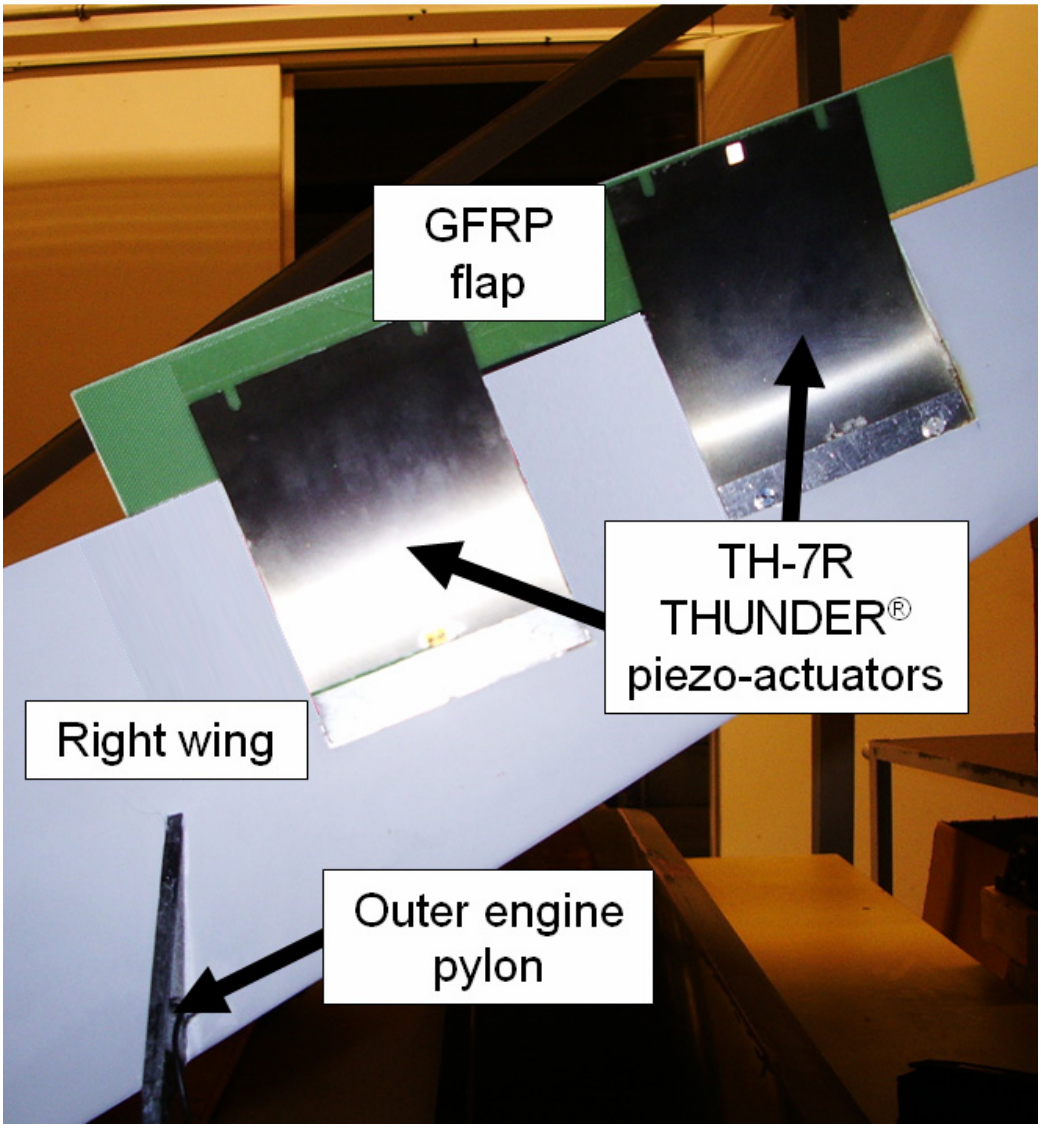

Figure 5-10. The piezo-electric driven trailing edge flap.

Finally, Figure 5-11 shows the elastic aircraft model mounted on the vertical support rod in the wind tunnel. The elastic aircraft model is trimmed by remotely controlled elevators (in red color.)

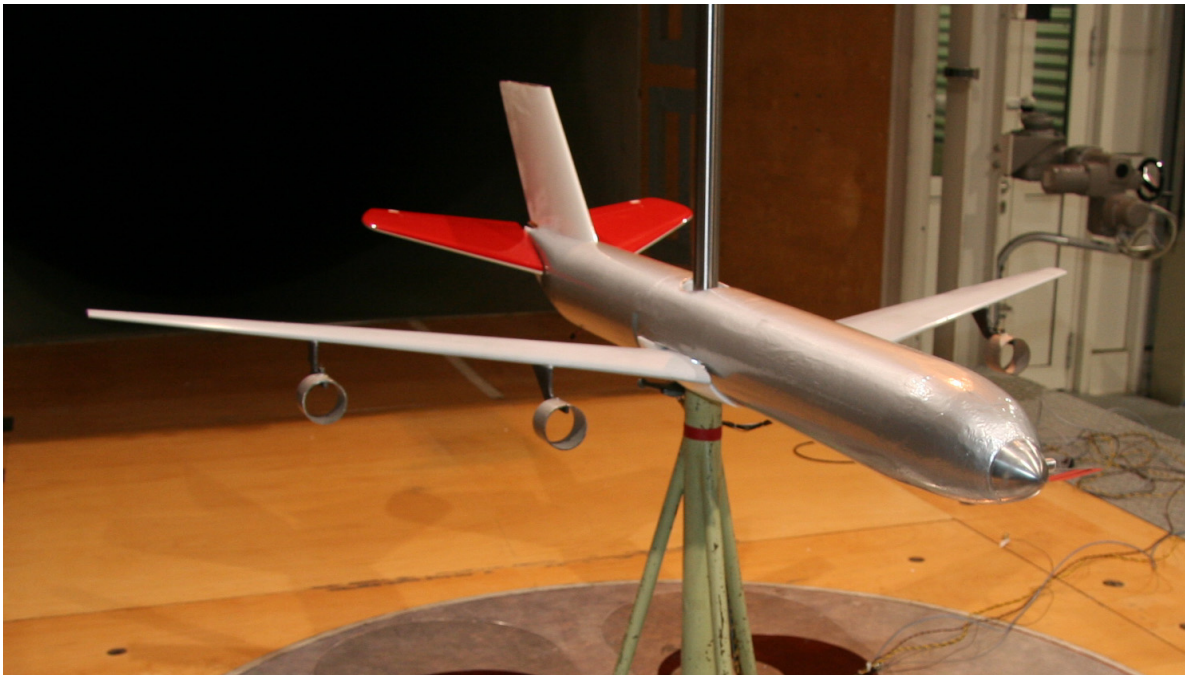

Figure 5-11. The complete elastic aircraft model in the wind tunnel.

5.2 Wind Tunnel Test Results

At first the discrete time plant transfer function $G(z)$ was identified offline at an airspeed of 30 m/s. For this system identification the gust generator was dismounted in order to keep the measurement noise as low as possible. In the literature various methods for system identification can be found, see [61], [62], [74].

Here, the DSP drives the plant with a linear chirp $x_{chirp}(n)$, defined in Eq. (5-1), in order to identify the plant transfer functions from the sampled-time symmetric trailing edge flap command to the sampled acceleration sensor signals $Nz_{LW}(n)$, $Nz_{CG}(n)$, and $Nz_{RW}(n)$. The identified plant transfer functions therefore also include the Digital to Analogue Converter (DAC) and the Reconstruction Filter (RF) required for the generation of a continuous-time control input that can be forwarded to the (continuous-time) plant, as well as the Anti-aliasing Filter (AF) and the Analogue to Digital Converter (ADC) required to obtain the sampled acceleration signals. The identified plant also includes the delay of the DSP, see Figure 5-12.

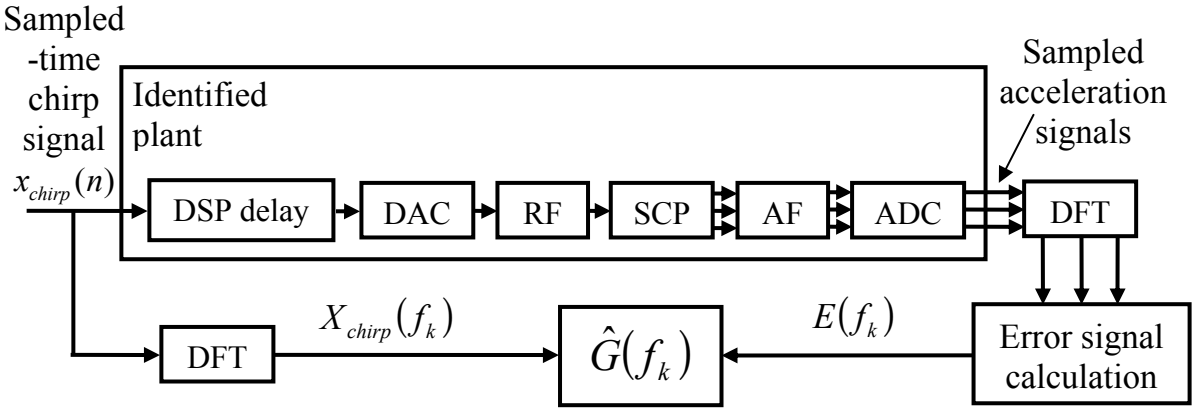

Figure 5-12. Offline system identification of the control plant.

The chirp signal $x_{chirp}(n)$ is a cosine signal with a temporally linear increasing frequency in the frequency range of the first symmetric vertical wing bending mode and the alpha mode.

$$x_{chirp}(n) = x_{\max} \cdot \cos\left(2\pi \left(f_{start} nT + \frac{f_{stop} - f_{start}}{2 \cdot N \cdot T} \cdot \frac{(nT)^2}{2} \right) \right), \; n = 0,1,2,...,2N-1 \quad (5\text{-}1)$$

Thereby, $t = nT$ denotes the time in seconds at the discrete time step n, with T denoting the sampling time. The sampling frequency $Fs = 1/T$ has been chosen to 250 Hz, and the DFT length for each identification run is $2 \cdot N = 2048$. The stop frequency has been chosen to $f_{stop} = 15.1$ Hz resulting in a start frequency of $f_{start} \approx 0.0367$ Hz, i.e. the start frequency is adjusted, so that when Eq. (5-1) is evaluated for $n = 2N$, the chirp's phase is an integer multiple of 2π.

This approach allows to string together several chirps, compare Eq. (5-3), without generating discontinuities at $n = 2N$, $n = 4N$, and so on. The chirp amplitude $x_{\max}$ has been adjusted so that the voltage limits of the piezo-electric trailing edge flaps are not exceeded.

The result of the plant identification with one single chirp is the 2N-point DFT of the chirp signal $X_{chirp}(f_k)$, as well as the according 2N-point DFT of the error signal $E(f_k)$, in which $E(f_k)$ is calculated from the sampled acceleration signals $Nz_{LW}(n)$, $Nz_{CG}(n)$, and $Nz_{RW}(n)$.

$$E(f_k) = 0.5 \cdot \left(DFT\left(Nz_{LW}(n)\right) + DFT\left(Nz_{RW}(n)\right) \right) - DFT\left(Nz_{CG}(n)\right) \quad (5\text{-}2)$$

The influence of measurement noise has been reduced by taking the mean value of the 2*N*-point DFTs of the error signals from *i*=5 continuously stringed together chirps. Considering, that the *i* stringed together chirps are identical, and with $E_i(f_k)$ denoting $E(f_k)$ identified with the i^{th} chirp, the Filter model $\hat{G}(f_k)$ is calculated as shown in Eq. (5-3):

$$\hat{G}(f_k) = \frac{\sum_{i=1}^{i=5} E_i(f_k)}{5 \cdot X_{chirp}(f_k)} \tag{5-3}$$

In Figure 5-13 the two upper plots illustrate the magnitude and the phase of the plant transfer function's estimate $\hat{G}(f_k)$ for discrete frequencies f_k as defined in Eq. (3-17) with $k = 2,3,4,...,123$.

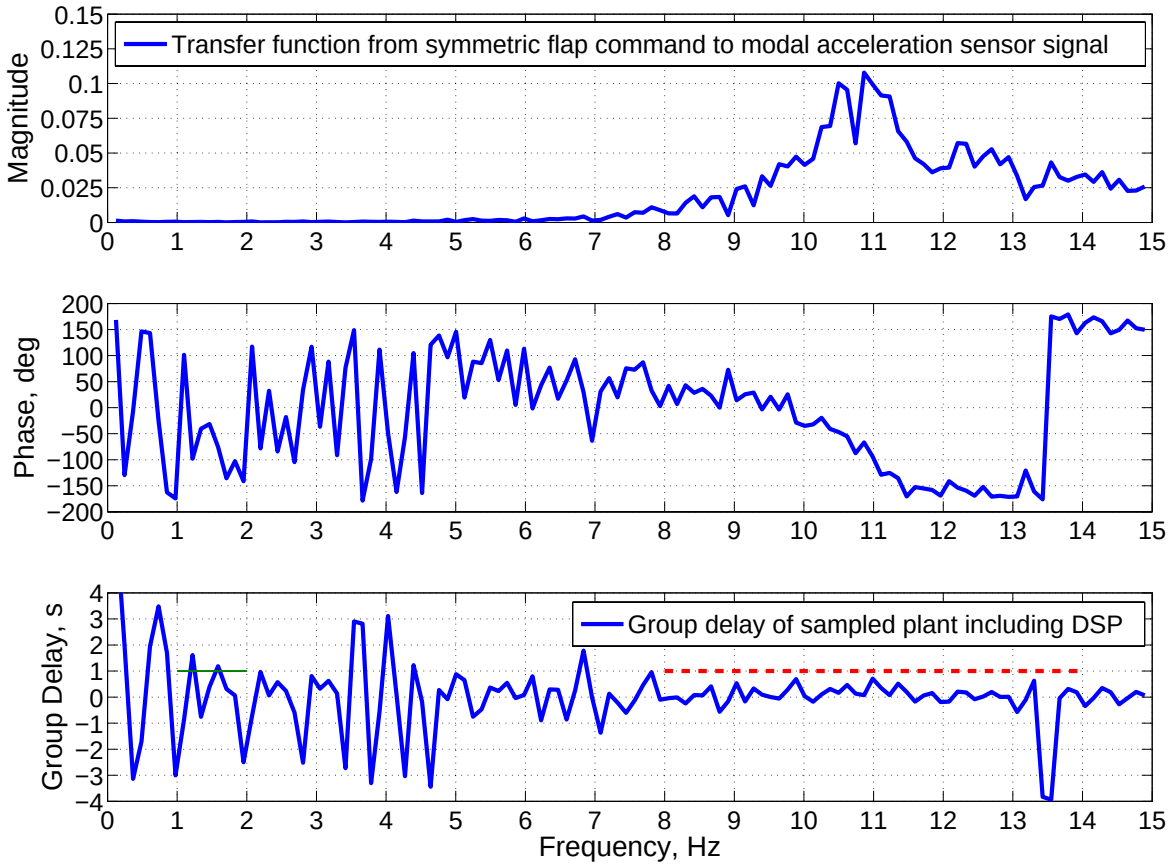

Figure 5-13. Magnitude and Phase of the transfer function $\hat{G}(f_k)$ of the offline identified plant, and according group delay $\Delta_{\hat{G}}(f_k)$ for discrete frequencies f_k.

The third plot shows the group delay $\Delta_{\hat{G}}(f_k)$ calculated from the plant transfer function's estimate $\hat{G}(f_k)$ (including the delay of the DSP) over discrete frequencies f_k in seconds. With $\phi_{\hat{G}}(f_k)$ denoting the phase angle of $\hat{G}(f_k)$ in radians, the group delay in seconds is approximated by numeric differentiation:

$$\Delta_G(f_k) \approx -\frac{N}{2\pi \cdot Fs} \cdot \phi_{\hat{G}}(f_{k+1}) - \phi_{\hat{G}}(f_{k-1}) \tag{5-4}$$

In the frequency range, where the plant transfer function's phase estimate is very uncertain (i.e. below about 4.7 Hz the phase uncertainty is > +/- 90°), the plant model $\hat{G}(f_k)$ has to be set to zero to avoid an incorrect controller adaptation. This means, that the computed non-causal frequency domain controller coefficients $H_n(f_k)$ will also be zero in this frequency range, whatever the value of the convergence coefficient *c* is. Thus, for the calculation of the convergence coefficient *c* the frequency range of $\hat{G}(f_k) = 0$ may be excluded.

Note, that strictly speaking setting the magnitude of $\hat{G}(f_k)$ to zero at certain frequencies must not generate magnitude steps in the transfer function of $\hat{G}(f_k)$, because this would affect the causality of the time domain controller $H_n(z)$.

At frequencies above about 15 Hz, $\hat{G}(f_k)$ was set to zero too in order to control only the first symmetric vertical wing bending mode. If also the compensation of the excitation of higher wind tunnel model's Eigen modes is aspired, stiffer actuators, or flaps deflection angle control instead of controlling the voltage applied to the piezo-actuators (i.e. using the actuators also in the frequency range of their Eigen modes) would be required. The plant model was introduced to the control algorithm implemented on the digital signal processor. Assuming that the identification uncertainty is a good quantitative measure of the estimation error, the following approximation has been made from the data illustrated in Figure 5-13:

$$\frac{\left|\hat{G}(f_k)\right|}{\left|G(f_k)\right|} \cdot \cos\left(\phi_G(f_k) - \phi_{\hat{G}}(f_k)\right) \approx 0.25 \quad \text{for:} \quad 4.7\ Hz < f_k < 15\ Hz \tag{5-5}$$

Thereby, it has been assumed that in the frequency range of the first symmetric vertical wing bending mode the maximum deviation of the plant model's phase $\phi_{\hat{G}}(f_k)$ from the true plant phase $\phi_G(f_k)$ is smaller than 60°, and that the plant model's magnitude $\left|\hat{G}(f_k)\right|$ is at least 0.5 times the true plant magnitude $\left|G(f_k)\right|$. Outside this frequency range the power spectral density of $\hat{r}$ is so small that the identification error has a minor influence on the convergence coefficients upper boundary, compare Eq. (3-41).

Since the power spectral density of $\hat{r}$ did hardly vary during the wind tunnel experiment (i.e. the plant was time-invariant, and the gust generator was driven with a steady state white noise signal *x*), the convergence coefficient's upper boundary $c_{\max}$ was regarded as almost time-invariant. Thus, in order to ease the implementation the delay of *m* samples (with $m = 1,2,\ldots,\Delta$) of the power spectral density estimate has been omitted in Eq. (3-41), i.e.:

$$\overline{S}_{\hat{r}\hat{r}}(f_k) = \frac{1}{\Delta}\sum_{m=1}^{\Delta}\left[\widetilde{S}_{\hat{r}\hat{r}_{\,n-m}}(f_k)\right] \approx \widetilde{S}_{\hat{r}\hat{r}_n}(f_k) \tag{5-6}$$

The highest group delays are usually experienced at the plant's Eigen frequencies. According to the offline system identification of the transfer function $G(z)$, the plant delay (including the delay of the DSP) is less than one second in the frequency range of the first symmetric vertical wing bending mode (compare the red dotted line in the third plot of Figure 5-13.) The sampling frequency of the DSP was adjusted to *Fs*=250 Hz for the wind tunnel experiment. A lower sampling rate would have done it too, but however, the used hardware was not designed for lower sampling rates. Thus, it can be seen that in the frequency range of the first symmetric vertical wing bending mode:

$$\Delta_{\hat{G}}(f_k) < 250 \; samples \tag{5-7}$$

The FIR length *N* was chosen to be 1024 in order to be on the safe side in regards to the frequency resolution. An FIR length of 512, or even less should have been sufficient too. In order to speed up controller convergence and minimize the required time for testing in the wind tunnel, $\Delta_{overlap}$ was set equal to one. Moreover, computation power was not a problem for the digital signal processor. Thus, according to Eq. (3-24), $\Delta+1$ was taken to be:

$$\Delta + 1 = 250 \; samples \tag{5-8}$$

Introducing Eqs. (5-5), (5-6), and (5-8) into Eq. (3-41), the convergence coefficient *c* can be computed online:

$$c(n) = \left[\frac{0.25}{2\cdot(\Delta+1)\cdot\widetilde{S}_{\hat{r}\hat{r}_n}(f_k)}\right]_{Minimum\ over\ f_k} = \left[\frac{1}{5\cdot 10^4\cdot\widetilde{S}_{\hat{r}\hat{r}_n}(f_k)}\right]_{Minimum\ over\ f_k} \tag{5-9}$$

As predicted by previous stability analysis and the numeric simulations the adaptive controller converged stable towards its optimum with the convergence coefficient computed as in Eq. (5-9).

Figure 5-14 shows the wind tunnel measurement of the coherence function between the reference signal *x* (i.e. also the gust generator driving signal), and the error signal *e*, (i.e. $\gamma_{xe}^{2}\left(e^{j\omega T}\right)$), without control (*blue line*), as well as with converged controller (*red line*). For the case without control (*blue line*), the error signal *e* is equal to the disturbance signal *d*. That means that the blue line represents also $\gamma_{xd}^{2}\left(e^{j\omega T}\right)$, and that the blue line's values can be used for attainable performance estimation according to Eq. (2-11).

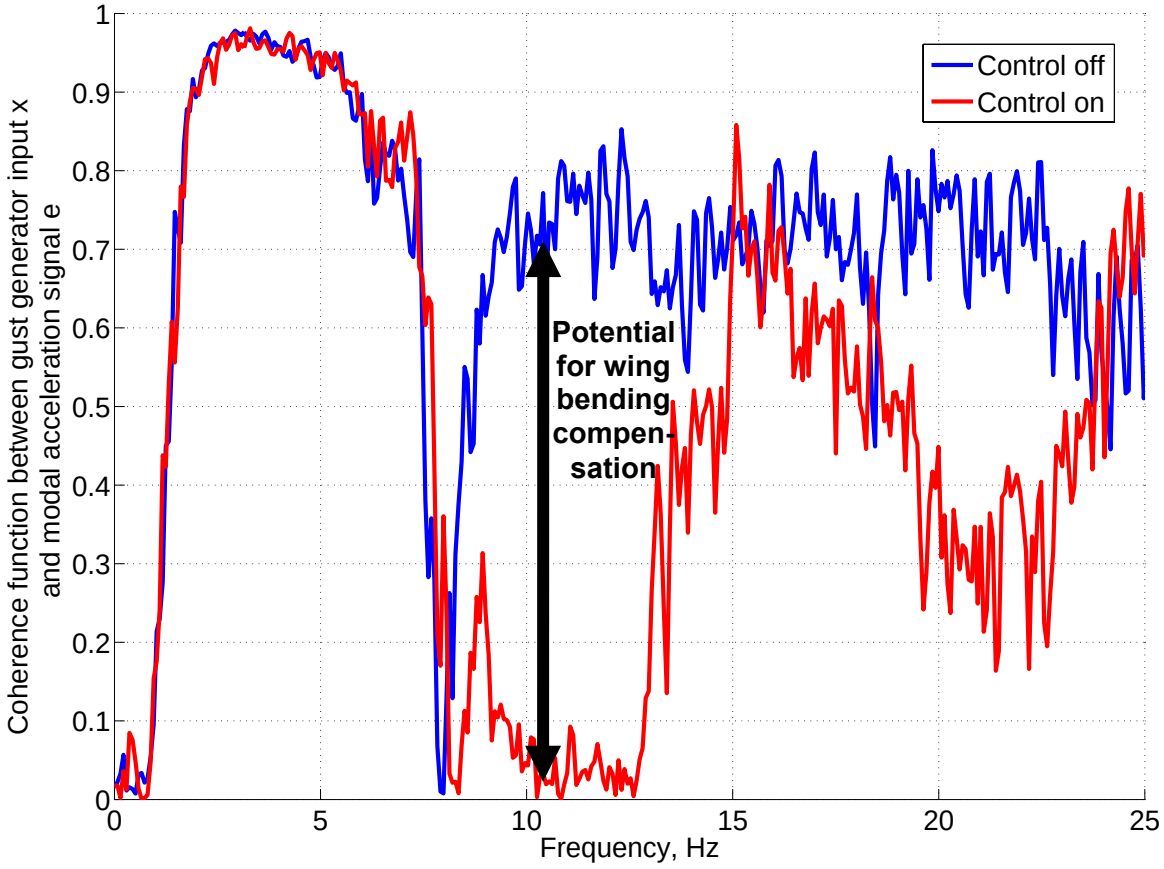

Figure 5-14. Coherence between reference signal and error signal.

The gust generator was driven with a steady state white noise signal *x* which was cut off at 25 Hz. The white noise magnitude was chosen so as to obtain about 75% measured coherence between the reference signal *x*, and the disturbance signal *d* (i.e. $\gamma_{xd}^2\left(e^{j\omega T}\right) \approx 0.75$) in the frequency range of the first vertical wing bending mode. The controller adapts until the share of the error signal *e*, which is correlated with the reference signal *x* is fully compensated by the feed-forward control system. This means that the coherence between the reference signal *x*, and the error signal *e*, $\gamma_{xe}^2\left(e^{j\omega T}\right)$ converges to zero in the frequency range of the first symmetric vertical wing bending mode, while the controller converges to a causal representation of an estimate of its optimum $H_{opt}\left(e^{j\omega T}\right)$.

Looking at Figure 5-14 the difference between the blue and the red line in the end made about 0.7 at the first symmetric vertical wing bending frequency (i.e. slightly above 10 Hz for a free stream velocity of 30 m/s, compare Figure 5-15), which corresponds to around 45% compensation of the error signal magnitude at this frequency, compare Eq. (2-11). The peak at about 4 Hz with almost perfect coherence between *x* and *e* (with as well as without control) represents the wind tunnel model's alpha mode. This mode is not controlled because the plant model is set to zero below about 4.7 Hz, preventing the controller from adaptation in this frequency range. The blue and the red line thus show almost the same coherence function up to 7 Hz.

Figure 5-15 shows the standardized average magnitude of the error signal *e* over frequency. The *blue line* represents the uncontrolled wind tunnel aircraft model, while the *red line* represents the model with converged feed-forward wing bending vibration controller (i.e. after about 250 seconds corresponding to ~$6.25*10^4$ samples of adaptation with a sample time *T* = 1/250 seconds starting from $h_0(n=0) = h_1(n=0) = ... = h_{N-1}(n=0) = 0$.) As shown in Figure 5-15 an average 45% reduction of modal accelerations of the first symmetric vertical wing bending mode has been obtained. This is in accordance with Eq. (2-11) for a coherence of $\gamma_{xd}^2\left(e^{j\omega T}\right) \approx 0.7$.

Note, that due to the piezo-electric driven trailing edge flaps' strong non-linear behavior, active control of the first symmetric vertical wing bending mode (i.e. controlled frequency range of about 4.7 Hz till 15 Hz) also excited the actuators Eigen frequencies (i.e. above 15 Hz.) In order to avoid this effect either a much stiffer actuator, or an actuator with linear behavior, or a compensation of the non-linearity (i.e. controlling the flaps' deflection angle instead of controlling the voltage applied to the piezo-actuators) would be required.

The handling of actuator non-linearities, especially at higher frequencies, is a general problem in active control technology. The objective of the wind tunnel experiment however, is to demonstrate the implementation of the proposed adaptive control algorithm, and investigate the real-time behavior of the adaptation. The optimization of the flap actuators is not an objective of this thesis.

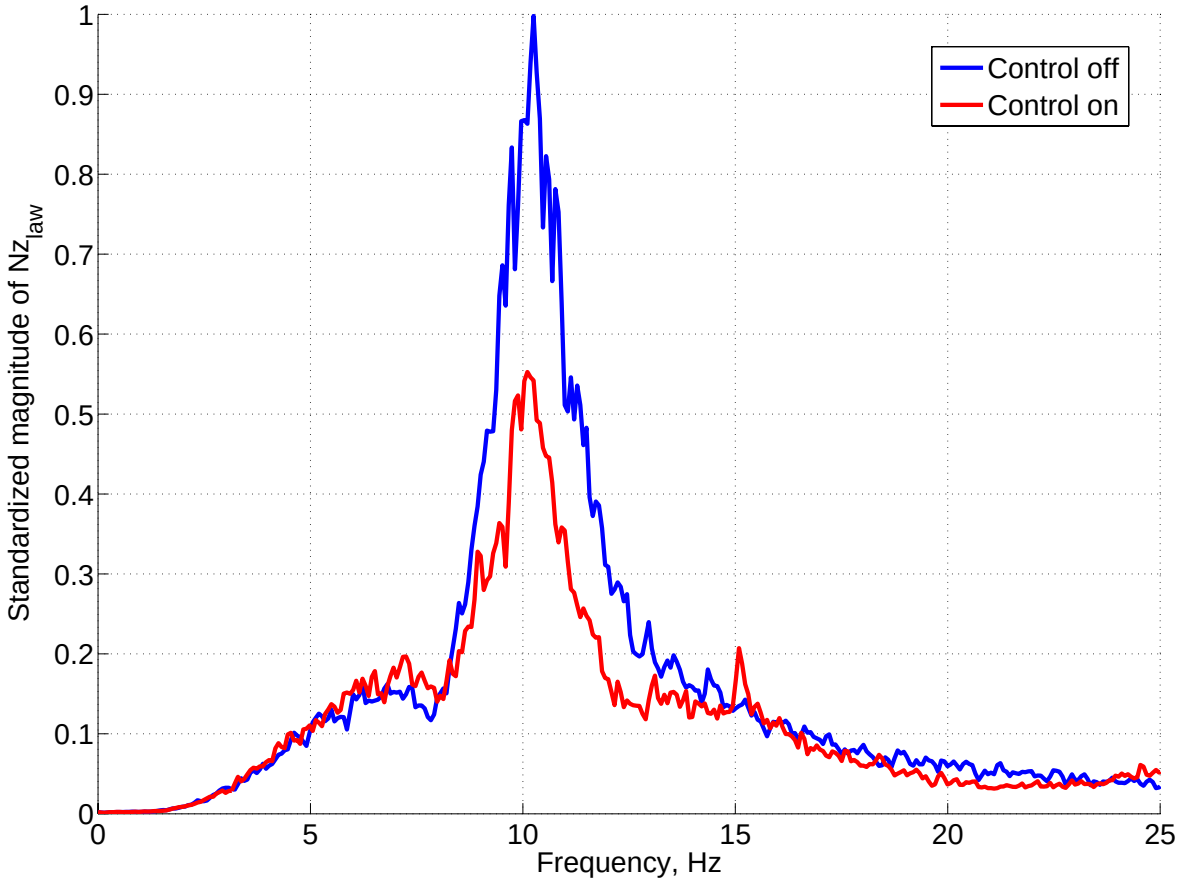

Figure 5-15. Reduction of the vertical wing bending acceleration magnitude.

Figure 5-16 shows the magnitude and phase of the feed-forward wing bending vibration controller after $1.5*10^5$ samples of adaptation (i.e. end of the test run.) The illustrated frequency response represents the DFT of the (causal) time domain controller $\vec{h}_{1.5\cdot10^5}(z)$.

Thus, although the plant model $\hat{G}(f_k)$ has been set to zero below about 4.7 Hz and above about 15 Hz, the magnitude does not have a step at those frequencies, but rather smoothly goes to zero below about 4.7 Hz and above about 15 Hz due to the constraint of causality of the feed-forward controller.

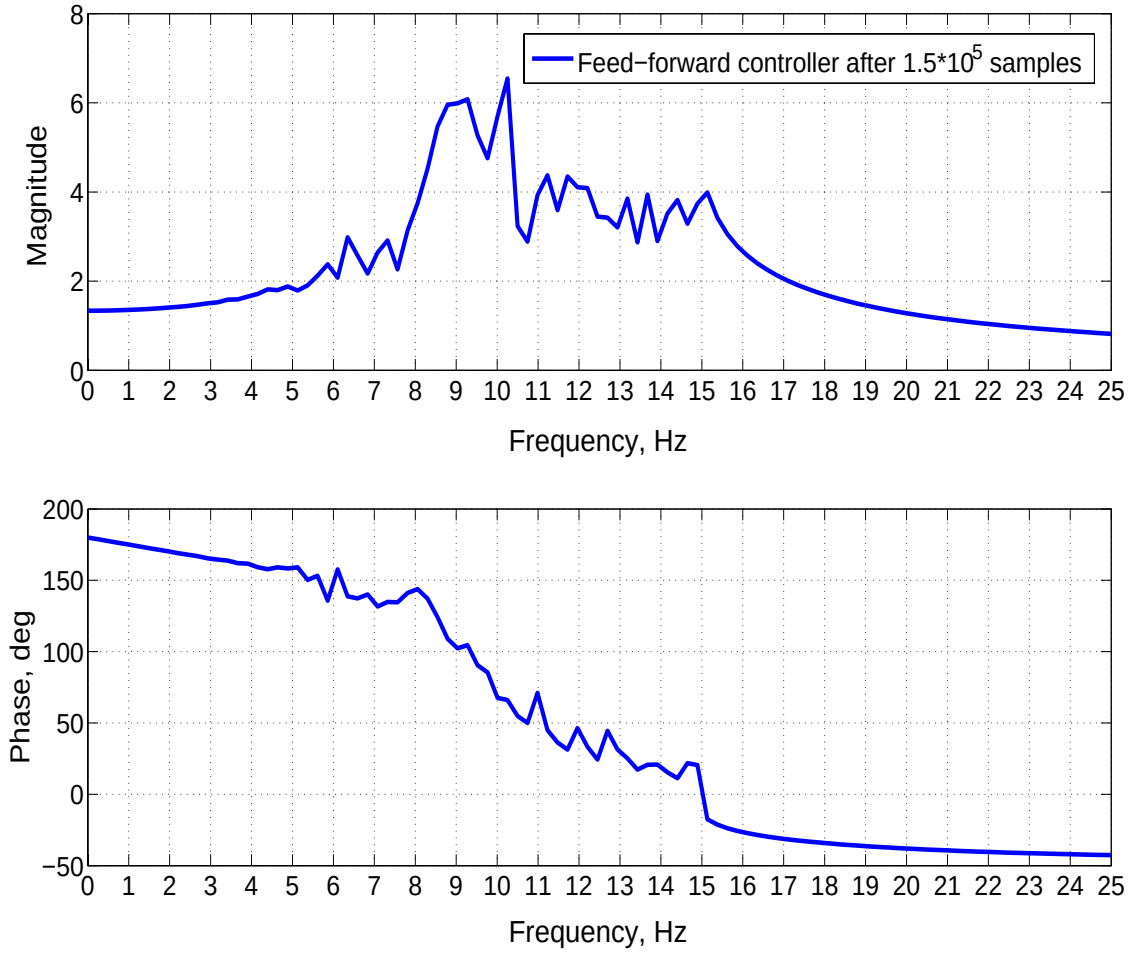

Figure 5-16. The feed-forward controller after $1.5*10^5$ samples of adaptation.

Finally, Figure 5-17 illustrates $1.5*10^5$ adaptation steps n of the frequency domain controller (i.e. N-point DFT of the (causal) time domain controller) coefficients number 36 through number 59 (corresponding to a frequency range of 8.5449 Hz to 14.1602 Hz) in the complex plane. All coefficients start from zero. At $n = 1.5*10^5$ the coefficients have already converged to a certain region around the theoretic optimum $H_{opt}\left(e^{j\omega T}\right)$ though. But, since in Eq. (3-16) the quantity inside the brackets $\{...\}_+$ represents an estimate of the gradient of the error surface by averaging over the last N samples the controller coefficients keep continuously slightly adapting. This oscillations of the controller around its theoretic optimum $H_{opt}\left(e^{j\omega T}\right)$ affects the performance only marginally. A smaller convergence coefficient c would reduce these oscillations, which can be seen from the term on the very right in Eq. (3-25), but would also increase the convergence time.

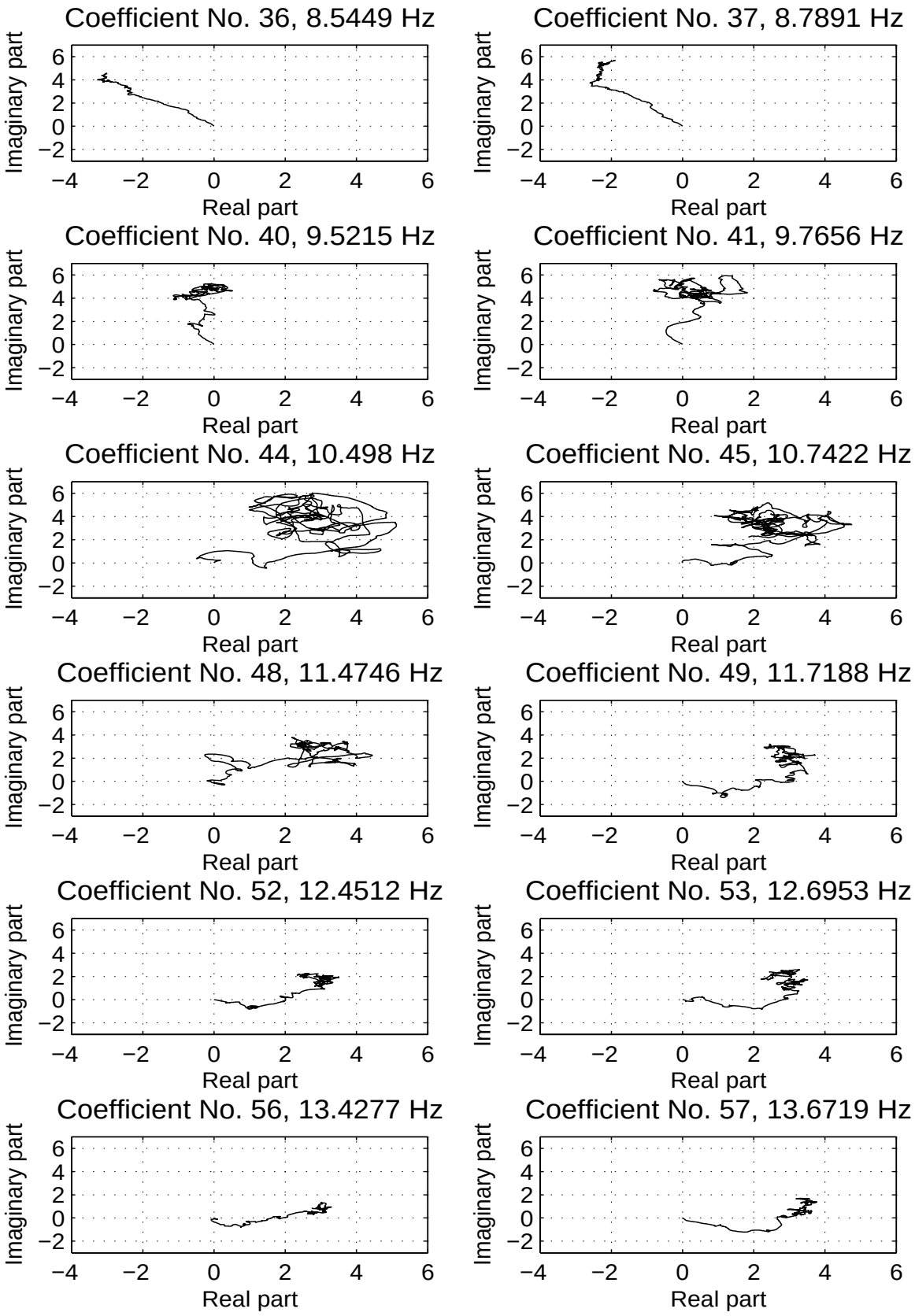

Figure 5-17. Convergence of the frequency domain controller

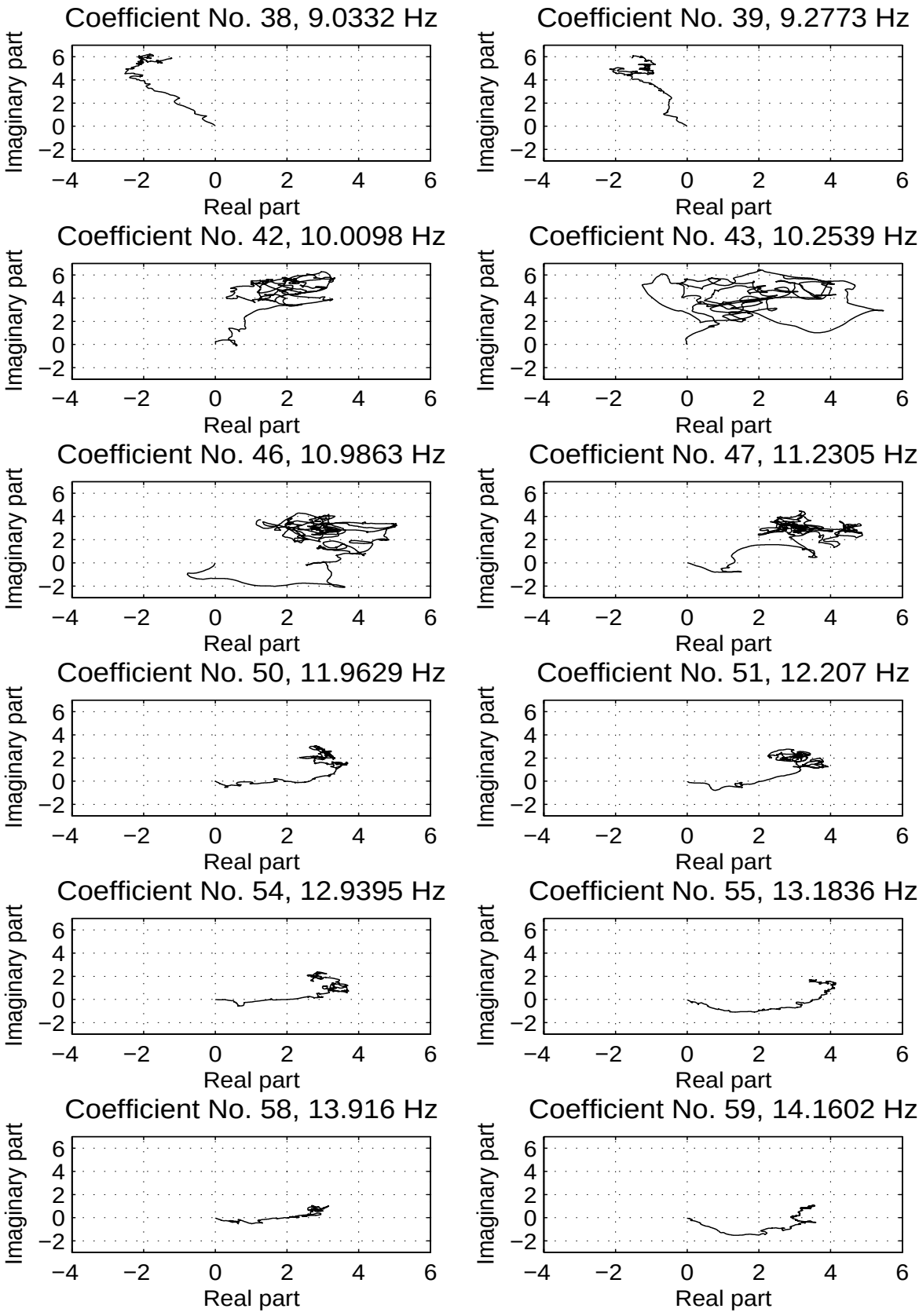

coefficients No. 36 through No. 59 during the wind tunnel experiment.

6 An Infinite Impulse Response Controller as a Perspective

It has been argued in the previous chapters that by supplementing state of the art feedback wing bending vibration control with an additional adaptive feed-forward controller the control performance can be maximized and dynamic loads excited by turbulence and maneuvers can be addressed at the same time. For the realization of the adaptive feed-forward controller mainly two approaches deem appropriate, use of an FIR feed-forward controller, and use of an Infinite Impulse Response (IIR) feed-forward controller. With the complex variable z, the according discrete transfer functions denote:

FIR controller:

$$H(z) = h_0(n) + h_1(n)z^{-1} + h_2(n)z^{-2} + \ldots + h_{N-1}(n)z^{-N+1} \tag{6-1}$$

IIR controller:

$$H(z) = \frac{A(z)}{B(z)} = \frac{a_0(n) + a_1(n)z^{-1} + a_2(n)z^{-2} + \ldots + a_I(n)z^{-I}}{1 + b_1(n)z^{-1} + b_2(n)z^{-2} + \ldots + b_K(n)z^{-K}} \text{ with } I \le K \tag{6-2}$$

Thereby, n denotes the time step, N is the filter length of the FIR controller, and I and K are the numbers of zeros, and poles of the IIR controller. The terms $A(z)$ and $B(z)$ are the numerator and the denominator of the discrete transfer function of the IIR controller, whereas a_i, and b_k are the according coefficients with $i = 0, 1, 2,\ldots,I$, and with $k = 1, 2,\ldots,K$.

As already mentioned the FIR controller has the advantage that it cannot converge to an unstable controller since only the zeros are adapted and all poles remain in the origin. Moreover, using an FIR controller the adaptation of the feed-forward path increases the robustness of the performance against modeling errors.

Note, that robust stability against modeling errors is much more difficult to prove for an adaptive IIR controller than for an adaptive FIR controller, and still would have to be investigated.

However, an IIR controller has the advantage that an infinite impulse response can be represented with a finite number of controller coefficients (i.e. I+K+2). Figure 6-1 shows that a 2nd order IIR controller is sufficient for proper feed-forward wing bending compensation on the four-engine example aircraft. Remember that according to the numeric simulations a filter length of N = 64 was required for wing bending compensation on the example aircraft with a controller sample time of T = 1/25.

In order to test the performance of such an adaptive IIR wing bending vibration control system, numeric simulation have been performed in WILDSCHEK ET AL. [119] with the state-space model of the symmetric dynamics of the previously described four-engine example aircraft for mass case A, Ma = 0.86, compare Table 2-1. An algorithm for feed-forward IIR controller adaptation that offers promising convergence behavior is the so-called filtered-U algorithm developed by ERIKSSON [37].

Using the filtered-U algorithm the time domain adaptation law for the IIR coefficients is:

$$a_i(n+1) = a_i(n) - c_1 \cdot e(n)\hat{r}(n-i) \tag{6-3}$$

$$b_k(n+1) = b_k(n) - c_2 \cdot e(n)\tilde{u}(n-k) \tag{6-4}$$

Thereby, $\hat{r}(n-i)$ is the n-i^{th} sample of the reference signal α filtered by the transfer function $\hat{G}(z)/B(z)$, and $\tilde{u}(n-k)$ is the n-k^{th} sample of the IIR controller's output u filtered by a transfer function $\hat{G}(z)/B(z)$. As an approximation the factor $1/B(z)$ may be removed for simplification of the adaptation algorithm, compare [37], and [115]. In both cases the controller converges to almost the same IIR approximation of $H_{opt}(e^{j\omega T})$, defined in Eq. (3-11), compare the green and the blue line Figure 6-2.

As already explained, the transfer function $\hat{G}(z)$ is an estimate of the control path from the sampled-time feed-forward control input $u_{FF}(n)$ to the sampled-time error sensor signal $e(n)$. This means that $\hat{G}(z)$ also includes the inner robust feedback loop. In WANG & REN [115] constraints on the accuracy of the estimate $\hat{G}(z)$ for stable convergence of the IIR adaptation are provided. The choice of the convergence coefficients c_1 and c_2 determine the convergence speed of the adaptive IIR controller towards the IIR approximation of $H_{opt}(e^{j\omega T})$, and thus also the stability of the adaptation.

Due to the lack of theoretic stability boundaries for c_1 and c_2, the convergence coefficients were chosen empirically. Moreover, a perfect representation of the four-engine example aircraft's SCP has been used for the filtering of the reference signal, i.e. $\hat{G}(z) = G(z)$.

Figure 6-1 shows the standardized power spectral density of the modal wing bending vibration acceleration Nz_{law} over frequency for the four-engine example aircraft with IIR feed-forward controllers of different orders after 7500 samples of adaptation time starting from $a_j(n=0)=b_k(n=0)=0$. The excitation is modeled as von Kármán turbulence with $\gamma_{\alpha d}{}^2\left(e^{j\omega T}\right)=1$. For convenience only IIR controllers with the same number of poles and zeros were considered (i.e. $I = K$.) One can see that a 2nd order IIR controller provides more than 90% reduction of $S_{ee}\left(e^{j\omega T}\right)$ for the example aircraft, which is almost the same as for a 3rd order IIR controller. A 1st order IIR controller however reduces $S_{ee}\left(e^{j\omega T}\right)$ by only 75%. Therefore, a 2nd order IIR controller was chosen for feed-forward wing bending vibration control with: $I = K = 2$.

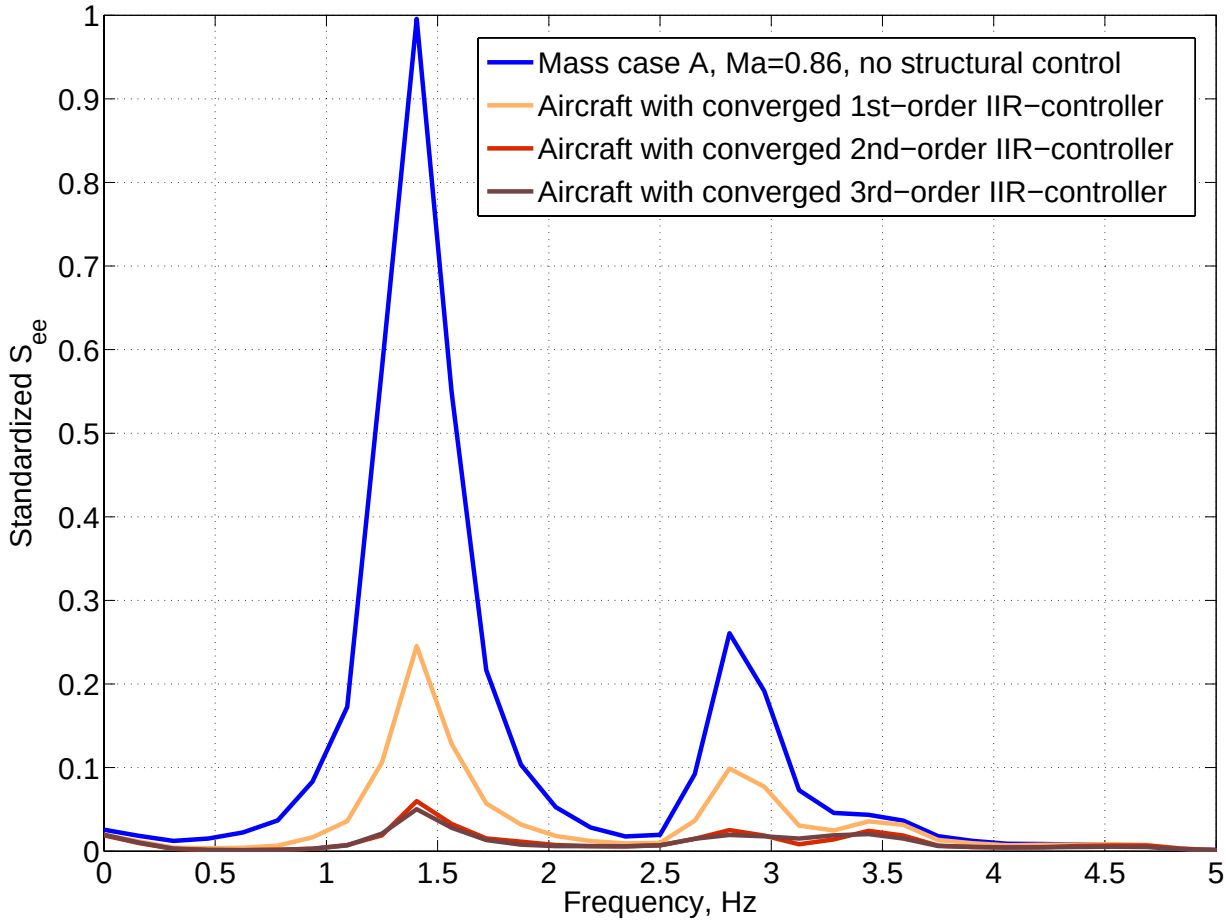

Figure 6-1. Performance with IIR feed-forward controllers of different orders for $\gamma_{\alpha d}{}^2\left(e^{j\omega T}\right)=1$ after 7500 samples of adaptation time.

Figure 6-2 shows the bode plots of the discrete-time transfer functions of 2nd order IIR controllers with $\hat{G}(z)/B(z)$ (i.e. *blue line*) and with $\hat{G}(z)$ (i.e. *green line*) filtering of the reference signal after 7500 samples convergence time. One can see that the simplification of the calculation of $\hat{r}(n-i)$ and $\tilde{u}(n-k)$ does not make any notably difference in the transfer function of the converged IIR controller.

For comparison the bode plot of the discrete-time transfer function of a converged FIR wing bending vibration controller with $N = 64$ is plotted in Figure 6-2 too. One can see that the phase and magnitude of IIR and FIR controller are almost the same at frequencies of high gains in the SCP transfer function, i.e. at frequencies of modal peaks. This explains the fact that for the example aircraft the 2nd order IIR controller provides the same wing bending vibration alleviation as the FIR controller, see Figure 6-3.

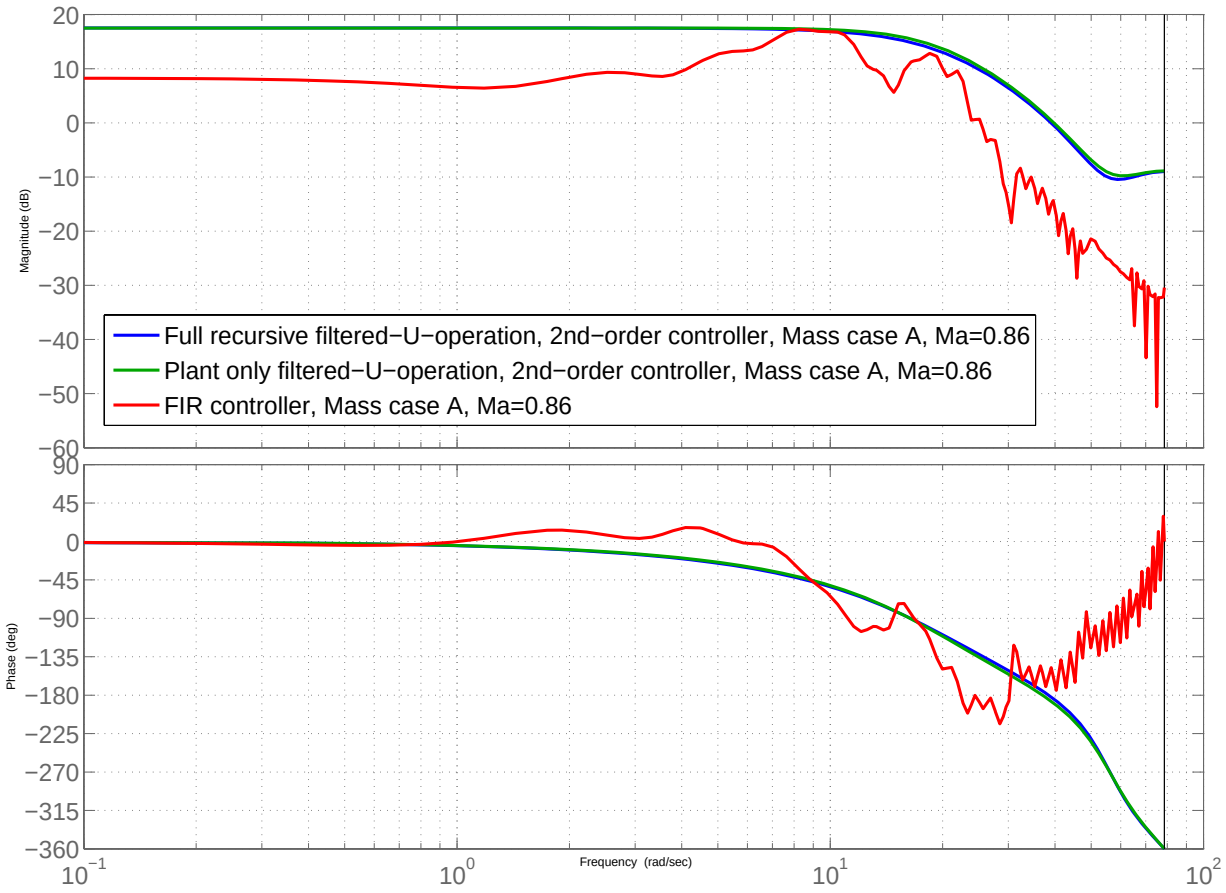

Figure 6-2. Converged 2nd order IIR controllers with $\hat{G}(z)/B(z)$ and $\hat{G}(z)$ filtered reference signal compared to a converged FIR controller with *N*=64, $\gamma_{\alpha d}{}^{2}\left(e^{j\omega T}\right)=1$.

Figure 6-3 illustrates the standardized magnitude of the modal acceleration Nz_{law} over frequency for the four-engine example aircraft for mass case A, Ma = 0.86. The *blue line* denotes the aircraft without structural control, and the *red line* is the standardized magnitude of Nz_{law} with a band pass feedback controller. The *violet* and the *green line* are for said robust feedback control with converged adaptive feed-forward augmentation using either an FIR or an IIR controller. The coherence between the reference signal α and the disturbance signal d was 75% in this simulation. The performance is almost the same for both, the FIR and the IIR feed-forward controller.

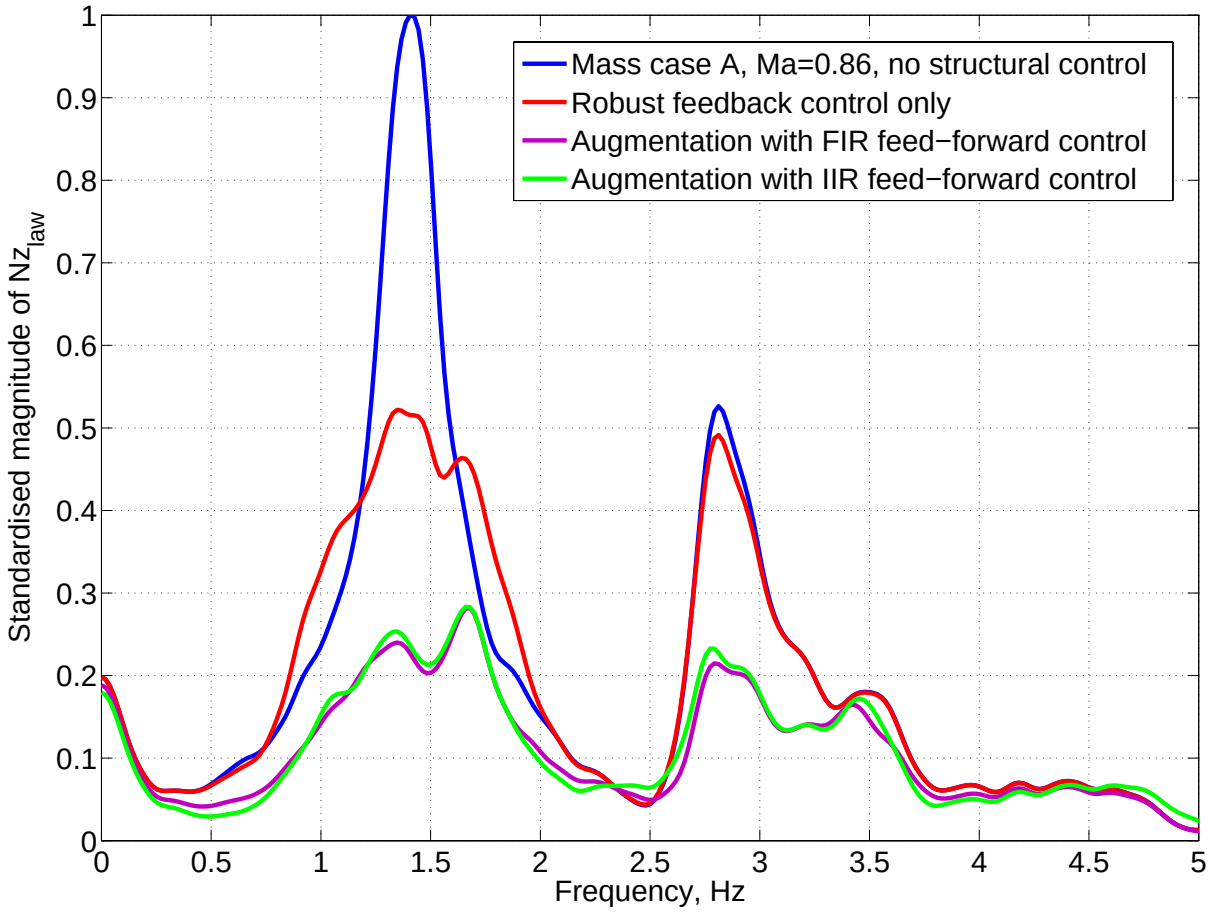

Figure 6-3. Comparison of hybrid controllers with FIR and with IIR feed-forward compensation, mass case A, Ma = 0.86, $\gamma_{\alpha d}^{\,2}\left(e^{j\omega T}\right) = 0.75$.

7 Conclusions and Outlook

In this thesis an adaptive feed-forward controller is proposed for the compensation of atmospheric turbulence excited wing bending vibrations on large transport aircraft (i.e. on aircraft with a first symmetric vertical wing bending frequency of about 1 Hz.) Investigations on the two-dimensional von Kármán turbulence spectrum show, that 50% reduction of the first symmetric vertical wing bending vibration magnitude can be obtained on a large four-engine example aircraft by pure feed-forward control if an alpha probe that responds quite directly to alpha variations up to 4 Hz is used as reference sensor. The problem with feed-forward compensation however, is that its performance is very sensitive to uncertainties in the plant.

In order to improve the robustness of the feed-forward wing bending vibration controller's performance against modeling errors, an adaptation loop is introduced. The performed robust stability analysis provides boundaries for the convergence coefficient and for the maximum allowable phase error. The controller update algorithm theoretically converges for phase errors in the Secondary Control Path (SCP) model below +/- 90° with the convergence time going to infinity for a +/- 90° phase error. The stable convergence of the controller adaptation has been exemplarily verified in numeric simulations for a phase error of +/- 45°.

As predicted the converged feed-forward controller provides a 50% reduction of the first symmetric vertical wing bending vibration magnitude with the coherence function modeled to be 75%. On the basis of the robust stability proof it is argued that the proposed adaptive feed-forward wing bending vibration controller can be implemented on a flying aircraft. Moreover, a formula is derived to demonstrate that the adaptation provides improved robustness of the performance against modeling errors compared to a non-adaptive feed-forward control system.

The design of a non-adaptive feed-forward control system would require accurate models of the Primary Control Path (PCP) and of the SCP. The SCPs (i.e. actuator to sensor transfer functions) of a new aircraft type are generally identified in flight tests in order to improve the quality of the SCP models for feedback control design. The flight test identification of the PCP however is not straightforward since flights through significant turbulence of several minutes duration would be required for the different Mach and mass cases, as well as for different flight levels. Without accurate knowledge of the PCP it is difficult to validate how optimal a non-adaptive feed-forward vibration control system is (i.e. to evaluate its performance.) Moreover, it has to be kept in mind, that the costs increase with increasing accuracy constraints on the plant model.

The proposed adaptive feed-forward wing bending vibration controller converges to the optimum with an approximate model of the SCP and without any knowledge of the PCP, and thus offers a fast and low cost method for feed-forward vibration control law optimization.

In addition an experimental wind tunnel setup for the investigation of the real-time behavior of the proposed adaptive wing bending vibration control system has been designed. In this context an elastic model of the four-engine transport aircraft has been built to serve as control plant. In order to provide a locally correlated disturbance a gust generator has been mounted upstream said elastic aircraft model. By using the gust generator driving signal as reference signal for feed-forward control, a coherence between the reference signal and the disturbance signal of 70% to 80% was obtained, which is comparable to the coherence estimate provided by the two-dimensional von Kármán turbulence model. Symmetrically driven piezo-electric trailing edge flaps were used as actuators. The SCP of the aircraft model was properly identified at 30 m/s airspeed with a chirp signal.

The adaptive control algorithm was implemented on a digital signal processor and then tested in the real-time wind tunnel environment at an airspeed of about 30 m/s. As predicted by previous stability analysis and numeric simulations the adaptive controller converged stable towards its optimum. So the theoretic boundaries for the convergence coefficient also proved to be valid in the wind tunnel experiment. With around 75% coherence between the reference signal and the disturbance signal, the converged controller reduced the average magnitude of the first symmetric vertical wing bending vibration by about 45% in the wind tunnel experiment. This is almost in accordance with the theoretical attainable vibration reduction.

Along with the results of this thesis however some further questions arose:

- One question is if the coherence between the disturbance signal and the reference signal can be increased by using other sensors than the alpha probe for the reference measurement. Research on improved reference sensors is being done e.g. at DLR [54], and at EADS [100].
- Another open question is whether the duration of flight phases with rough *steady state* turbulence excitation is generally long enough for proper controller adaptation (i.e. if for controller adaptation, real atmospheric turbulence excitation can be regarded as *steady state*.) It has been shown that the converged feed-forward controller can also compensate *transient* atmospheric excitation, compare Chapter 4.6. However, it has not been investigated yet in how far the superposition of the steady state turbulence with such transient excitation affects the adaptation of the controller. These questions can be answered best by excessive flight testing.
- The performance estimates provided in this thesis are based on the assumption that the quadratic coherence function between the alpha probe signal and the

excitation of the first symmetric vertical wing bending mode is about 75%. Said performance estimate should be validated in flight tests.

- Following such flight tests it should also be investigated if the convergence speed of the controller adaptation can be increased, and (if necessary) if the adaptation performance can be made robust in the presence of transient atmospheric excitation by developing an improved update algorithm. Note, that for example an LMS algorithm would provide a faster convergence speed than the frequency domain steepest descent algorithm used in this thesis. The LMS algorithm however, would also require more computational power.
- For simplification of the stability analysis of the proposed adaptive feed-forward controller, parasitic feedback from the actuators to the reference sensor has been neglected. For wing bending vibration compensation on the example aircraft it has been shown in numeric simulations that at least parasitic feedback due to structural coupling indeed is very small on the four-engine example aircraft. However, for a more general approach parasitic feedback should be considering in the stability proof in ongoing research.
- Moreover, the long-term influence of non-linearities in the plant has not been investigated yet. This should be done either in long-term numeric simulations or in flight tests. The introduction of a so-called leakage-term to the update algorithm might increase its robustness also in regards to non-linearities in the plant, compare [32], [40], and [44].
- In the previous chapter a recursive adaptive filter was introduced as feed-forward controller in order to reduce the required number of controller coefficients that have to be adapted. The derivation of proper conditions for robust stability of such an adaptive feed-forward control system would be an ambitious research project.
- In this thesis a SISO system has been sufficient for the compensation of symmetric wing bending vibrations on a transport aircraft of conventional configuration. If more than one error signal shall be considered in the cost function, and/or if more actuators have to be used (e.g. on unconventional aircraft configurations such as flying wing transport aircraft, and/or for simultaneous compensation of atmospheric turbulence excited rigid body motions and structural vibrations respectively), a MIMO system is required. Thus, it is proposed to investigate robust stability of an adaptive MIMO feed-forward controller too in the future.

Despite this open points the proposed adaptive wing bending vibration controller is valued to be a promising approach for the realization of feed-forward control of atmospheric turbulence excited structural vibrations with high performance robustness against modeling errors. The best vibration alleviation was obtained by a combination between robust feedback control and adaptive feed-forward compensation (i.e. hybrid control.) Such hybrid control offers a great potential for further reduction of dynamic loads (and thus a reduction of structural weight), as well as for the increase of passenger comfort and handling qualities on large airliners.

Appendix

Appendix A – Series Expansion of the Term a_{Δ}

In the style of another paper [75] the term $a_{\Delta n-i}(f_k)$ from Eq. (3-30) can be derived for Δ=1 and for time step *n-i* to:

$$
\begin{aligned}
&a_{1n-i}(f_k) = \Delta H_{n-i}{}^{*}(f_k) S_{rr}(f_k) \Delta H_{n-i-1}(f_k) \\
&= \Delta H_{n-i-1}{}^{*}(f_k) S_{rr}(f_k) \Delta H_{n-i-1}(f_k) - c \cdot \widetilde{S}_{\hat{r}r_{n-i}}{}^{*}(f_k) \cdot \Delta H_{n-i-2}{}^{*}(f_k) S_{rr}(f_k) \Delta H_{n-i-1}(f_k) \\
&- c \cdot \hat{R}_{n-i}(f_k) E_{opt_{n-i}}{}^{*}(f_k) S_{rr}(f_k) \Delta H_{n-i-1}(f_k) \\
&= \varepsilon_{excess\,n-i-1}(f_k) - b_{n-i}{}^{*}(f_k) \cdot a_{1\,n-i-1}{}^{*}(f_k) \\
&- c \cdot \hat{R}_{n-i}(f_k) E_{opt_{n-i}}{}^{*}(f_k) S_{rr}(f_k) \Delta H_{n-i-1}(f_k) \\
&= \varepsilon_{excess\,n-i-1}(f_k) - b_{n-i}{}^{*}(f_k) \cdot a_{1\,n-i-1}{}^{*}(f_k) + g_{1_{n-i}}(f_k)
\end{aligned}
\tag{A-1}
$$

with the definition $b_{n-i}(f_k) = c \cdot \widetilde{S}_{\hat{r}r_{n-i}}(f_k) = c \cdot \widetilde{S}_{\hat{r}\hat{r}_{n-i}}(f_k) G(f_k) / \hat{G}(f_k)$,

and with: $$g_{1_{n-i}}(f_k) = -c \cdot \hat{R}_{n-i}(f_k) E_{opt_{n-i}}{}^{*}(f_k) S_{rr}(f_k) \Delta H_{n-i-1}(f_k) \tag{A-2}$$

Note, that here $a_{1n-i}(f_k)$ denotes the auxiliary function $a_{\Delta n-i}(f_k)$ with Δ=1, and must not be mixed up with the coefficients of numerator of the IIR filter in Chapter 6.

Implementing the same approach with an arbitrary delay of Δ samples and assuming that generally $|b_{n-i}(f_k)| << 1$ for all f_k in the controlled frequency range gives for time step *n*-1:

$$
\begin{aligned}
&a_{\Delta n-1}(f_k) = \Delta H_{n-1}{}^*(f_k) S_{rr}(f_k) \Delta H_{n-\Delta-1}(f_k) \\
&= \Delta H_{n-2}{}^*(f_k) S_{rr}(f_k) \Delta H_{n-\Delta-1}(f_k) - b_{n-1}{}^*(f_k) \cdot \Delta H_{n-\Delta-2}{}^*(f_k) S_{rr}(f_k) \Delta H_{n-\Delta-1}(f_k) \\
&- c \cdot \hat{R}_{n-1}(f_k) E_{opt_{n-1}}{}^*(f_k) S_{rr}(f_k) \Delta H_{n-\Delta-1}(f_k) \\
&= a_{\Delta-1 n-2}(f_k) - b_{n-1}{}^*(f_k) \cdot a_{1 n-\Delta-1}{}^*(f_k) \\
&- c \cdot \hat{R}_{n-1}(f_k) E_{opt_{n-1}}{}^*(f_k) S_{rr}(f_k) \Delta H_{n-\Delta-1}(f_k) \\
&= a_{\Delta-2 n-3}(f_k) - b_{n-2}{}^*(f_k) \cdot a_{2 n-\Delta-1}{}^*(f_k) - b_{n-1}{}^* \cdot a_{1 n-\Delta-1}{}^*(f_k) \\
&- c \cdot \hat{R}_{n-2}(f_k) E_{opt_{n-2}}{}^*(f_k) S_{rr}(f_k) \Delta H_{n-\Delta-1}(f_k) \\
&- c \cdot \hat{R}_{n-1}(f_k) E_{opt_{n-1}}{}^*(f_k) S_{rr}(f_k) \Delta H_{n-\Delta-1}(f_k) \approx
\end{aligned}
$$

(neglecting higher order terms of $b_{n-i}(f_k)$)

$$
\begin{aligned}
&\approx a_{\Delta-2 n-3}(f_k) - b_{n-1}{}^*(f_k) \cdot a_{1 n-\Delta-1}{}^*(f_k) - b_{n-2}{}^* \cdot a_{1 n-\Delta-2}{}^*(f_k) \\
&- c \cdot \sum_{m=1}^{2} \left[\hat{R}_{n-m}(f_k) E_{opt_{n-m}}{}^*(f_k) S_{rr}(f_k) \Delta H_{n-\Delta-1}(f_k) \right] \\
&\approx \ldots \\
&\approx a_{1 n-\Delta}(f_k) - \sum_{m=1}^{\Delta-1} \left[b_{n-m}{}^*(f_k) \cdot a_{1 n-\Delta-m}{}^*(f_k) \right] \\
&- c \cdot \sum_{m=1}^{\Delta-1} \left[\hat{R}_{n-m}(f_k) E_{opt_{n-m}}{}^*(f_k) S_{rr}(f_k) \Delta H_{n-\Delta-1}(f_k) \right] \\
&\approx \varepsilon_{excess\, n-\Delta-1}(f_k) - \sum_{m=1}^{\Delta} \left[b_{n-m}{}^*(f_k) \cdot a_{1 n-\Delta-m}{}^*(f_k) \right] \\
&- c \cdot \sum_{m=1}^{\Delta} \left[\hat{R}_{n-m}(f_k) E_{opt_{n-m}}{}^*(f_k) S_{rr}(f_k) \Delta H_{n-\Delta-1}(f_k) \right] \\
&= \varepsilon_{excess\, n-\Delta-1}(f_k) - \sum_{m=1}^{\Delta} \left[b_{n-m}{}^*(f_k) \cdot a_{1 n-\Delta-m}{}^*(f_k) \right] + g_{\Delta n-1}(f_k)
\end{aligned}
\tag{A-3}
$$

with:

$$
g_{\Delta_{n-i}}(f_k) = -c \cdot \sum_{m=0}^{\Delta-1} \left[\hat{R}_{n-i-m}(f_k) E_{opt_{n-i-m}}{}^*(f_k) S_{rr}(f_k) \Delta H_{n-\Delta-i}(f_k) \right]
\tag{A-4}
$$

Appendix B – Stability Bounds for the Convergence Coefficient *c*

Rewriting Eq. (3-30) with $b_n(f_k)$ as defined in Appendix A gives:

$$\begin{aligned}
&\left\langle \varepsilon_{excess_n}(f_k)\right\rangle \approx \left\langle \varepsilon_{excess_{n-1}}(f_k)\right\rangle - \left\langle b_n(f_k)\cdot a_{\Delta n-1}(f_k)\right\rangle - \left\langle b_n{}^*(f_k)\cdot a_{\Delta n-1}{}^*(f_k)\right\rangle \\
&+\left\langle \left|b_n(f_k)\right|^2\cdot \varepsilon_{excess_{n-\Delta-1}}(f_k)\right\rangle + c^2\cdot S_{ee_{\min}}(f_k)S_{\hat{r}\hat{r}}(f_k) \\
&=\left\langle \varepsilon_{excess_{n-1}}(f_k)\right\rangle - 2\left\langle \mathrm{Re}\{b_n(f_k)\cdot a_{\Delta n-1}(f_k)\}\right\rangle + \left\langle \left|b_n(f_k)\right|^2\cdot \varepsilon_{excess_{n-\Delta-1}}(f_k)\right\rangle + c^2\cdot S_{ee_{\min}}(f_k)S_{\hat{r}\hat{r}}(f_k)
\end{aligned} \tag{B-1}$$

and introducing Eq. (A-3) into Eq. (B-1) gives:

$$\begin{aligned}
&\left\langle \varepsilon_{excess_n}(f_k)\right\rangle \approx \left\langle \varepsilon_{excess_{n-1}}(f_k)\right\rangle - 2\left\langle \mathrm{Re}\{b_n(f_k)\}\cdot \varepsilon_{excess\,n-\Delta-1}(f_k)\right\rangle \\
&+2\left\langle b_n(f_k)\cdot \sum_{m=1}^{\Delta}\left[b_{n-m}{}^*(f_k)\cdot \mathrm{Re}\left\{a_{1n-\Delta-m}{}^*(f_k)\right\}\right]\right\rangle + \left\langle \left|b_n(f_k)\right|^2\cdot \varepsilon_{excess_{n-\Delta-1}}(f_k)\right\rangle \\
&+c^2\cdot S_{ee_{\min}}(f_k)S_{\hat{r}\hat{r}}(f_k) - 2\left\langle \mathrm{Re}\left\{b_{n-\Delta-1}(f_k)\cdot g_{\Delta_{n-1}}(f_k)\right\}\right\rangle
\end{aligned} \tag{B-2}$$

Due to the fact that e_{opt} is statistically independent from *r*, and from $\hat{r}$, the expectation value of Eq. (A-4) is zero. Moreover, the last term in Eq. (B-2) is zero. Introducing Eq. (A-1) into Eq. (B-2) thus gives:

$$\begin{aligned}
&\left\langle \varepsilon_{excess_n}(f_k)\right\rangle \approx \left\langle \varepsilon_{excess_{n-1}}(f_k)\right\rangle - 2\left\langle \mathrm{Re}\{b_n(f_k)\}\cdot \varepsilon_{excess\,n-\Delta-1}(f_k)\right\rangle \\
&+2\left\langle b_n(f_k)\cdot \sum_{m=1}^{\Delta}\left[b_{n-m}{}^*(f_k)\cdot \varepsilon_{excess\,n-\Delta-m-1}(f_k)\right]\right\rangle \\
&-2\left\langle b_n(f_k)\cdot \sum_{m=1}^{\Delta}\left[b_{n-m}{}^*(f_k)\cdot \mathrm{Re}\{b_{n-\Delta-m}(f_k)\cdot a_{1n-\Delta-m-1}(f_k)\}\right]\right\rangle \\
&+\left\langle \left|b_n(f_k)\right|^2\cdot \varepsilon_{excess_{n-\Delta-1}}(f_k)\right\rangle + c^2\cdot S_{ee_{\min}}(f_k)S_{\hat{r}\hat{r}}(f_k) + 2\left\langle b_n(f_k)\cdot \sum_{m=1}^{\Delta}\left[b_{n-m}{}^*(f_k)\cdot \mathrm{Re}\left\{g_{1n-\Delta-m}{}^*(f_k)\right\}\right]\right\rangle
\end{aligned} \tag{B-3}$$

Now all higher than 2nd order terms of $b_{n-i}(f_k)$ are neglected since $|b_{n-i}(f_k)| << 1$. Moreover, the last term in Eq (B-3) is zero, because $e_{opt}(f_k)$ is statistically independent from r, and from $\hat{r}$,and the expectation value of Eq. (A-2) is zero.

$$\left\langle \varepsilon_{excess_n}(f_k) \right\rangle \approx \left\langle \varepsilon_{excess_{n-1}}(f_k) \right\rangle + \left\langle \left(\left| b_n(f_k) \right|^2 - 2\,\mathrm{Re}\{b_n(f_k)\} \right) \cdot \varepsilon_{excess\,n-\Delta-1}(f_k) \right\rangle$$
$$+ 2\left\langle b_n(f_k) \cdot \sum_{m=1}^{\Delta} \left[b_{n-m}{}^{*}(f_k) \cdot \varepsilon_{excess\,n-\Delta-m-1}(f_k) \right] \right\rangle + c^2 \cdot S_{ee_{\min}}(f_k) S_{\hat{r}\hat{r}}(f_k) \tag{B-4}$$

A *necessary* condition for stable adaptation of the structural controller is the existence of a finite steady-state of the ensemble average of the excess square control error $\left\langle \varepsilon_{excess_\infty}(f_k) \right\rangle$, for which the following applies:

$$\left\langle \varepsilon_{excess_n}(f_k) \right\rangle \approx \left\langle \varepsilon_{excess_{n-1}}(f_k) \right\rangle \approx \left\langle \varepsilon_{excess_{n-2}}(f_k) \right\rangle \approx \ldots \approx \left\langle \varepsilon_{excess_{n-\Delta-m-1}}(f_k) \right\rangle \approx \left\langle \varepsilon_{excess_\infty}(f_k) \right\rangle \tag{B-5}$$

A sufficient condition for Eq. (B-5) is that Eq. (B-5) also holds without expectation values:

$$\varepsilon_{excess_n}(f_k) \approx \varepsilon_{excess_{n-1}}(f_k) \approx \varepsilon_{excess_{n-2}}(f_k) \approx \ldots \approx \varepsilon_{excess_{n-\Delta-m-1}}(f_k) \approx \varepsilon_{excess_\infty}(f_k) \tag{B-6}$$

Thus, one can write:

$$c^2 \cdot S_{ee_{\min}}(f_k) S_{\hat{r}\hat{r}}(f_k) \approx \left\langle \varepsilon_{excess_\infty}(f_k) \cdot \left(2 \cdot \mathrm{Re}\{b_n(f_k)\} - 2 \cdot b_n(f_k) \cdot \overline{b}^{*}(f_k) \cdot \Delta - \left| b_n(f_k) \right|^2 \right) \right\rangle =$$
$$= \left\langle \varepsilon_{excess_\infty}(f_k) \cdot \left(2 \cdot c \cdot \mathrm{Re}\left\{ \widetilde{S}_{\hat{r}r_n}(f_k) \right\} - c^2 \cdot \left(2 \cdot \widetilde{S}_{\hat{r}r_n}(f_k) \cdot \overline{S}_{\hat{r}r}{}^{*}(f_k) \cdot \Delta + \left| \widetilde{S}_{\hat{r}r_n}(f_k) \right|^2 \right) \right) \right\rangle \tag{B-7}$$

with $\overline{b}^{*}(f_k)$ denoting:
$$\overline{b}^{*}(f_k) = \frac{1}{\Delta} \sum_{m=1}^{\Delta} \left[b_{n-m}{}^{*}(f_k) \right] \tag{B-8}$$

and with $\overline{S}_{\hat{r}r}{}^{*}(f_k)$ denoting:
$$\overline{S}_{\hat{r}r}{}^{*}(f_k) = \frac{1}{\Delta} \sum_{m=1}^{\Delta} \left[\widetilde{S}_{\hat{r}r\,n-m}{}^{*}(f_k) \right] \tag{B-9}$$

Setting the multiplier of $\varepsilon_{excess_\infty}(f_k)$ in Eq. (B-7) to zero gives the *necessary* boundaries for the convergence coefficient *c*.

Appendix C – Derivation of the Optimum Convergence Coefficient c_{opt}

For a rough estimate of the convergence coefficient c that provides the fastest adaptation of the structural controller in the frequency range of the first symmetric vertical wing bending mode, Eq. (B-4) is rewritten:

$$\left\langle \varepsilon_{excess_n}(f_k) \right\rangle \approx \left\langle \varepsilon_{excess_{n-1}}(f_k) \right\rangle + \left\langle \left(c^2 \cdot \left| \widetilde{S}_{\hat{r}r\,n}(f_k) \right|^2 - 2 \cdot c \cdot \mathrm{Re}\left\{ \widetilde{S}_{\hat{r}r\,n}(f_k) \right\} \right) \cdot \varepsilon_{excess\,n-\Delta-1}(f_k) \right\rangle$$
$$+ 2c^2 \left\langle \widetilde{S}_{\hat{r}r\,n}(f_k) \cdot \sum_{m=1}^{\Delta} \left[\widetilde{S}_{\hat{r}r\,n-m}{}^{*}(f_k) \cdot \varepsilon_{excess\,n-\Delta-m-1}(f_k) \right] \right\rangle + c^2 \cdot S_{ee_{\min}}(f_k) S_{\hat{r}\hat{r}}(f_k)$$

(C-1)

When the controller is still far from its optimum, the first three terms in Eq. (C-1) are assumed to be much bigger than $c^2 \cdot S_{ee_{\min}}(f_k) S_{\hat{r}\hat{r}}(f_k)$. Thus, the term $c^2 \cdot S_{ee_{\min}}(f_k) S_{\hat{r}\hat{r}}(f_k)$ is neglected. For derivation of the optimum convergence coefficient $c_{opt}(f_k)$ (i.e. convergence coefficient that provides fastest adaptation) Eq. (C-1) is differentiated with respect to c, and it is assumed, that for the first adaptation step n=1 it applies that:

$$\left\langle \varepsilon_{excess_{n-1}}(f_k) \right\rangle = \left\langle \varepsilon_{excess_{n-2}}(f_k) \right\rangle = \ldots = \left\langle \varepsilon_{excess_{n-\Delta-m-1}}(f_k) \right\rangle \tag{C-2}$$

Thus, one gets:

$$\frac{\partial \left\langle \varepsilon_{excess_n}(f_k) \right\rangle}{\partial c} \approx 2 \cdot \left\langle \varepsilon_{excess_{n-1}}(f_k) \cdot \left(-\mathrm{Re}\left\{ \widetilde{S}_{\hat{r}r_n}(f_k) \right\} + c \cdot \left(2 \cdot \widetilde{S}_{\hat{r}r_n}(f_k) \cdot \overline{S}_{\hat{r}r}{}^{*}(f_k) \cdot \Delta + \left| \widetilde{S}_{\hat{r}r_n}(f_k) \right|^2 \right) \right) \right\rangle$$

(C-3)

For setting the right side of Eq. (C-3) to zero, a sufficient solution would be:

$$c_{opt} \approx \frac{\mathrm{Re}\left\{ \widetilde{S}_{\hat{r}r_n}(f_k) \right\}}{2 \cdot \widetilde{S}_{\hat{r}r_n}(f_k) \cdot \overline{S}_{\hat{r}r}{}^{*}(f_k) \cdot \Delta + \left| \widetilde{S}_{\hat{r}r_n}(f_k) \right|^2} = \frac{c_{\max}}{2} \tag{C-4}$$

Thus, the convergence coefficient with shortest possible convergence time c_{opt} is about half the maximum convergence coefficient $c_{\max}$.

Appendix D – Assumption of a Quasi-Steady State Feed-Forward Controller

In Chapter 3 it has been assumed, that the adaptive feed-forward controller may be regarded as quasi-steady state, in order to be able to rearrange the controller $H(z)$ and the plant $G(z)$. This procedure (which is commonly used in the literature [30]) is necessary for the computation of the complex gradient of $S_{ee}\left(e^{j\omega T}\right)$ required for the derivation of the update algorithm for controller adaptation, and for the computation of the global optimum of the FIR controller respectively. In order to be able to illustrate the error that is made by this rearrangement, the share of feed-forward control in the error signal for rearranged $H(z)$ and $G(z)$, namely the signal $\tilde{y}(n)$ has been monitored throughout a time-domain simulation, see Figure D-1.

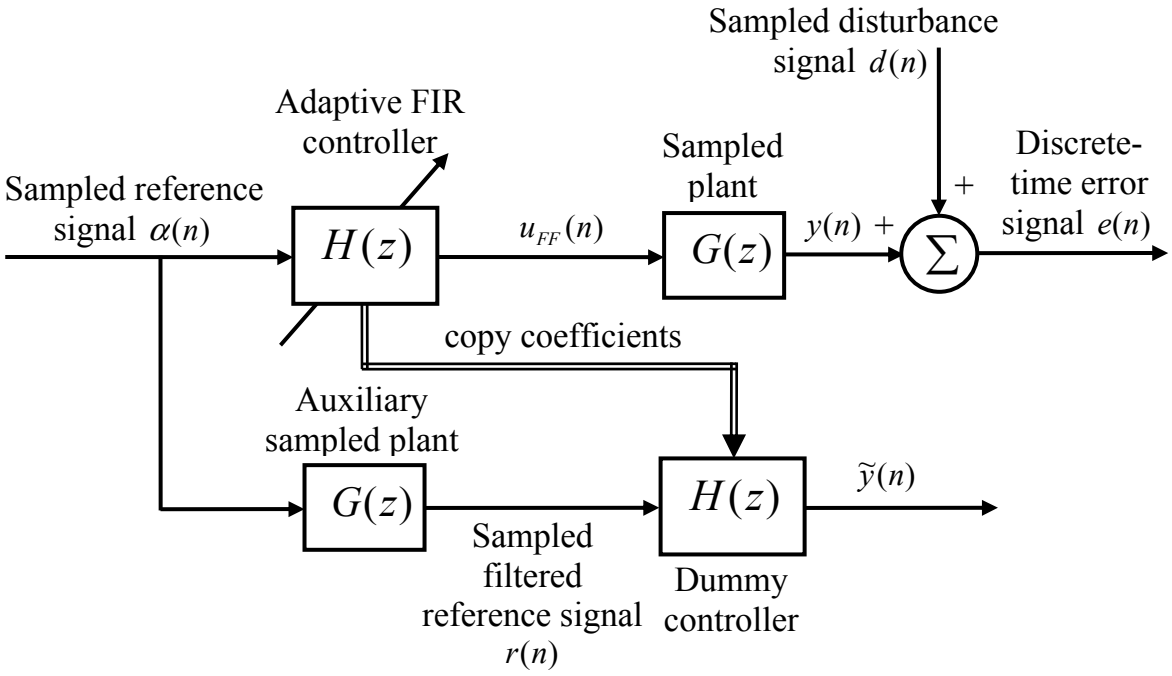

Figure D-1. Rearranged controller $H(z)$ and plant $G(z)$.

The feed-forward controller thereby is adapted with a convergence coefficient chosen according to Eq. (C-4). The coefficients of the adaptive FIR controller are copied to a second dummy controller. The input to this dummy controller is the sampled filtered reference signal $r(n)$ generated by an auxiliary sampled plant, whereas the output of the dummy controller is the signal $\tilde{y}(n)$. The simulation was run with the four-engine example aircraft for mass case A, Ma=0.86 for $1.25*10^4$ samples starting from zero initialization, i.e. $h_0(n=0)=h_1(n=0)=...=h_{N-1}(n=0)=0$.

Generating the quotient of the cross spectral density $\langle Y^*(e^{j\omega T})\tilde{Y}(e^{j\omega T})\rangle$ and the power spectral density $\langle Y^*(e^{j\omega T})Y(e^{j\omega T})\rangle$ from the monitored signals $y(n)$, and $\tilde{y}(n)$, finally provides an estimate of the error which is made by rearranging the controller $H(z)$ and the plant $G(z)$. Figure D-2 illustrates the magnitude and the phase of $\langle Y^*(e^{j\omega T})\tilde{Y}(e^{j\omega T})\rangle / \langle Y^*(e^{j\omega T})Y(e^{j\omega T})\rangle$ over frequency, which would represent an estimate of the transfer function from $y(n)$ to $\tilde{y}(n)$ if $y(n)$, and $\tilde{y}(n)$ were steady state. For $\tilde{y}(n) = y(n)$ the quotient of the cross spectral density $\langle Y^*(e^{j\omega T})\tilde{Y}(e^{j\omega T})\rangle$ and the power spectral density $\langle Y^*(e^{j\omega T})Y(e^{j\omega T})\rangle$ would be equal to one, i.e. no error. One can see, that in the controlled frequency range (i.e. zero till 4 Hz) the deviations from one in fact are marginally, i.e. < 1% in magnitude, and < 1° in phase. With increasing frequency the error increases, which however should not affect the controller adaptation and performance.

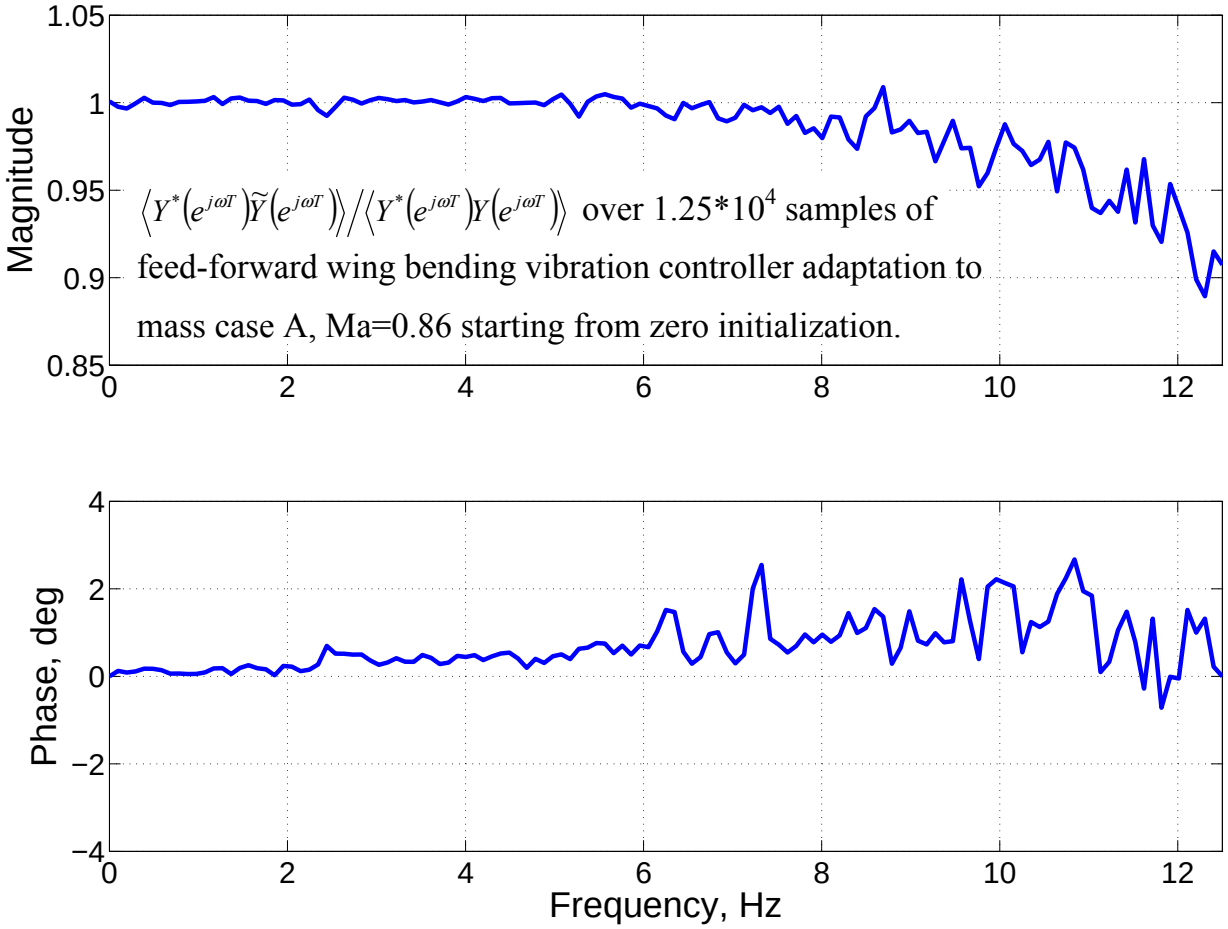

Figure D-2. Quotient of the cross spectral density $\langle Y^*(e^{j\omega T})\tilde{Y}(e^{j\omega T})\rangle$ and the power spectral density $\langle Y^*(e^{j\omega T})Y(e^{j\omega T})\rangle$ for controller adaptation to mass case A, Ma=0.86.

Appendix E – Justification of Neglecting Parasitic Feedback

The derivation of the adaptive structural control algorithm did not take *parasitic feedback* from the feed-forward control input u_{FF} to the alpha probe measurement into account. In order to check the share of parasitic feedback in the alpha probe signal due to feed-forward control input induced aircraft movements and vibrations, u_{FF} is fed through a second auxiliary aircraft model during the numeric simulations.

The output of this second aircraft model represents the parasitic feedback share in the alpha probe signal, and is compared with the alpha probe signal $\alpha_{sim} = \alpha_{air} - \alpha_0$, see Figure E-1. As already mentioned, any feed-forward control input induced local aerodynamic effects on α_{air} have been neglected in this thesis.

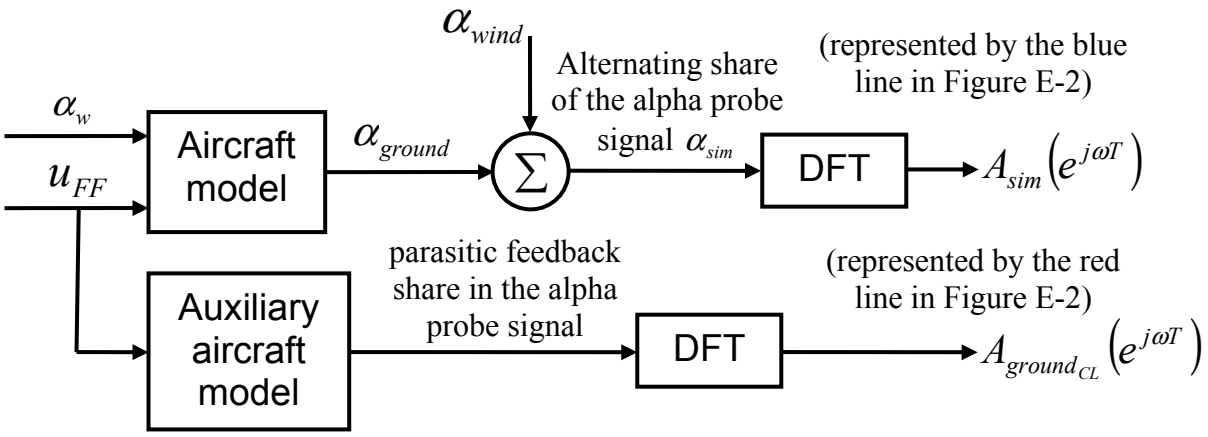

Figure E-1. Modeling of the parasitic feedback measurement.

The *blue line* in Figure E-2 represents the standardized magnitude of the Fourier transform of the alpha probe signal $A_{sim}\left(e^{j\omega T}\right)$ over frequency, whereas the *red line* represents the standardized magnitude of the Fourier transform of the parasitic feedback share in the alpha probe signal $A_{ground_{CL}}\left(e^{j\omega T}\right)$. For the example aircraft model parasitic feedback makes less than 1% of the alpha probe signal's magnitude in the frequency range of controlled structural modes (i.e. > ~ 0.7 Hz). Parasitic feedback due to feed-forward control input induced local aerodynamic effects on α_{air} has not been investigated, but is expected to be even smaller. Thus, neglecting parasitic feedback in the stability analysis seems to be justified, which is also approved by results of numeric simulations.

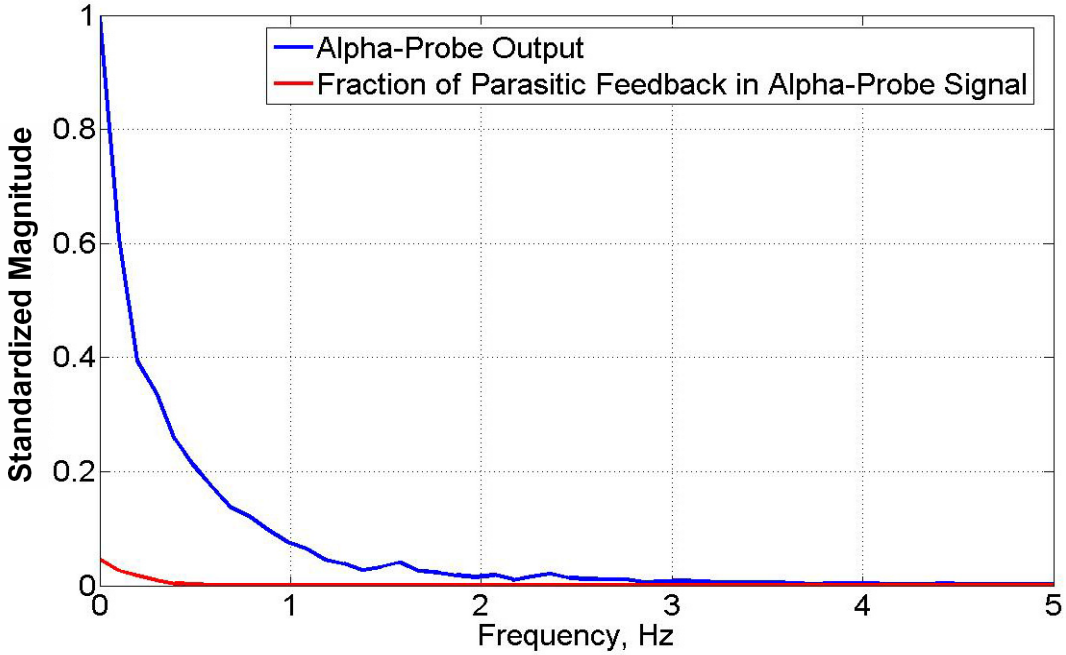

Figure E-2. Parasitic feedback in the alpha probe signal.

It was tested numerically, that if the parasitic feedback's magnitude is twice as high, the performance of the controller convergence is already decreased with the convergence coefficient chosen as in Eq. (C-4). By choosing a smaller convergence coefficient a stable controller adaptation has been obtained for even higher magnitudes of parasitic feedback. However, the stability analysis introduced in this thesis then would not be valid any more. Note, that in the frequency range of rigid body modes parasitic feedback is much higher (i.e. > 5%.), but did not affect the performance of the adaptive wing bending vibration controller.

Appendix F – Performance of the Converged Controller for Different Cases

In the following the mean standardized magnitudes of the DFTs of the following example aircraft state-space model outputs are plotted over frequency:

- Modal acceleration sensor Nz_{law} (i.e. error signal e.)
- Pitch rate q at the CG q_{CG}.
- Vertical wing bending moment deviation at the left wing root $M_{x_{WR}}$.
- Vertical acceleration at the cockpit Nz_{front}.
- Vertical acceleration at the CG Nz_{CG}.
- Vertical acceleration at the rear fuselage Nz_{rear}.

The Figures F-1 through F-12 represent the simulation results with a mean plant model for the following cases, compare also Table 2-1.

Table F-1. Assignment of the Figures F-1 through F-12.

Mach number	Mass case A	Mass case B	Mass case C	Mass case D
0.7	F-9	F-10	F-11	F-12
0.82	F-5	F-6	F-7	F-8
0.86	F-1	F-2	F-3	F-4

Thereby, the *blue line* represents the uncontrolled aircraft, whereas the *red line* represents the example aircraft with a robust band pass feedback wing bending vibration controller optimized for high Mach numbers [63]. An approximate 50% reduction of the first symmetric vertical wing bending vibration magnitude is achieved with this active wing bending damping system for all mass cases at Ma = 0.86. At lower Mach numbers the performance of the robust feedback controller decreases.

The *orange line* represents the example aircraft with the proposed adaptive feed-forward wing bending vibration controller after $1*10^4$ samples of convergence time. As postulated by Eq. (2-13) an approximate 50% reduction of the first symmetric vertical wing bending vibration magnitude is obtained for all mass and Mach cases. Since in the simulation $\gamma_{\alpha d}{}^2\left(e^{j\omega T}\right)=0.75$ is constant over frequency (which is actually not true for the real atmosphere, compare Chapter 2-3), the compensation of higher modes (i.e. above 2.5 Hz) is overestimated. Note, that according to the two-dimensional von Kármán turbulence model, the quadratic coherence function $\gamma_{\alpha d}{}^2\left(e^{j\omega T}\right)$ actually decreases with increasing frequency in the real atmosphere, and so does the performance of the feed-forward compensation of turbulence excited vibrations.

The *cyan line* illustrates the average modal wing bending acceleration magnitude with a combination between robust band pass feedback and converged adaptive feed-forward wing bending vibration control. This hybrid controller reduces the magnitude of the atmospheric turbulence excited first symmetric vertical wing bending vibration by more than 70% for all mass cases at Ma = 0.86.

Due to the reduced performance of the robust feedback controller at lower Mach numbers the performance of the hybrid controller naturally is also decreased. Since the control objective was to reduce the quadratic cost function of only the error signal *e*, the other state-space model outputs are slightly excited in some cases, particularly in the frequency range of rigid body motions. In order to avoid this effect, the according quantities would have to be considered in the control optimization criteria.

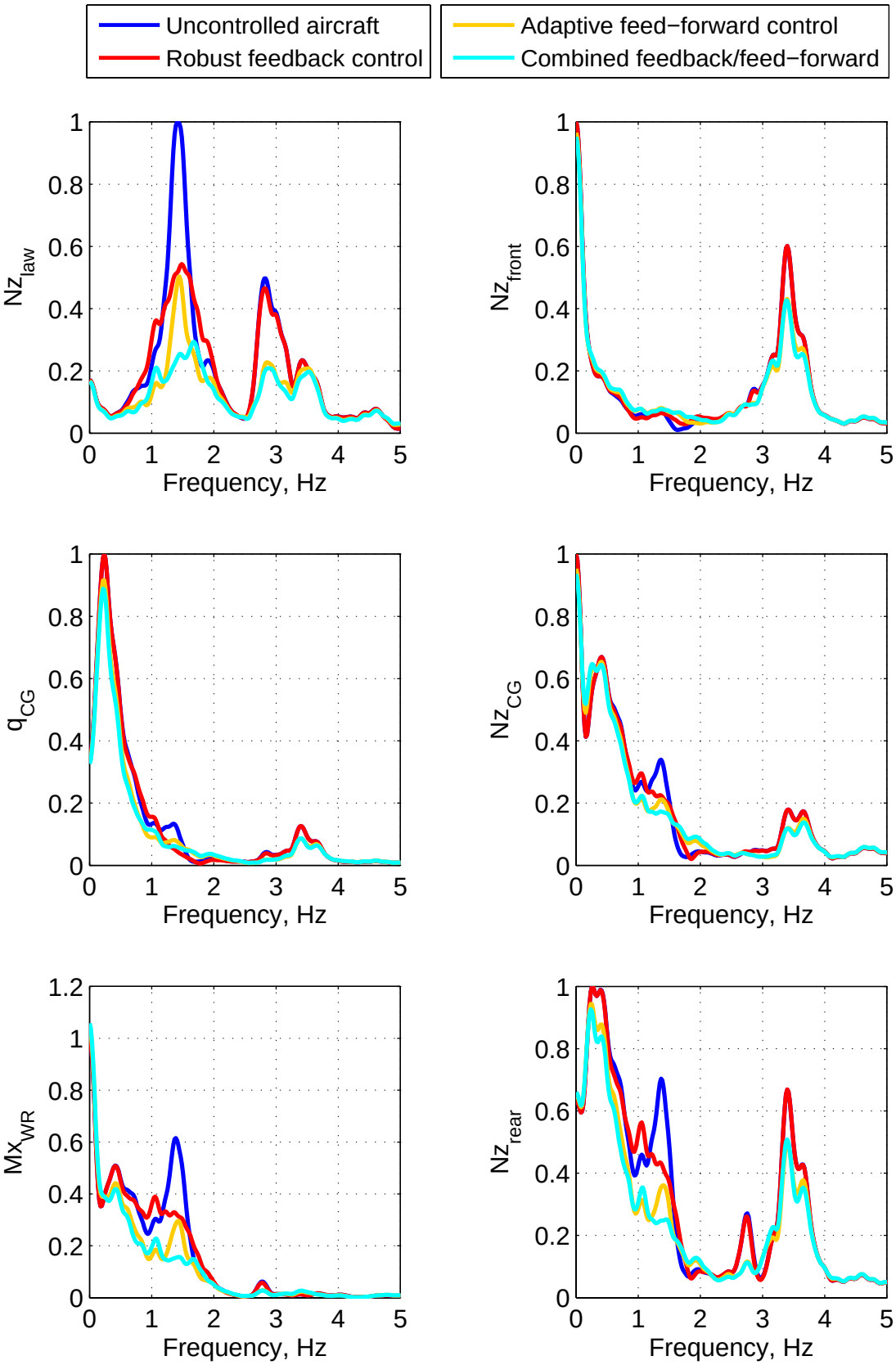

Figure F-1. Performance comparison of different controllers with a mean plant model, mass case A, Ma=0.86, $\gamma_{od}{}^{2}\left(e^{j\omega T}\right)=0.75$.

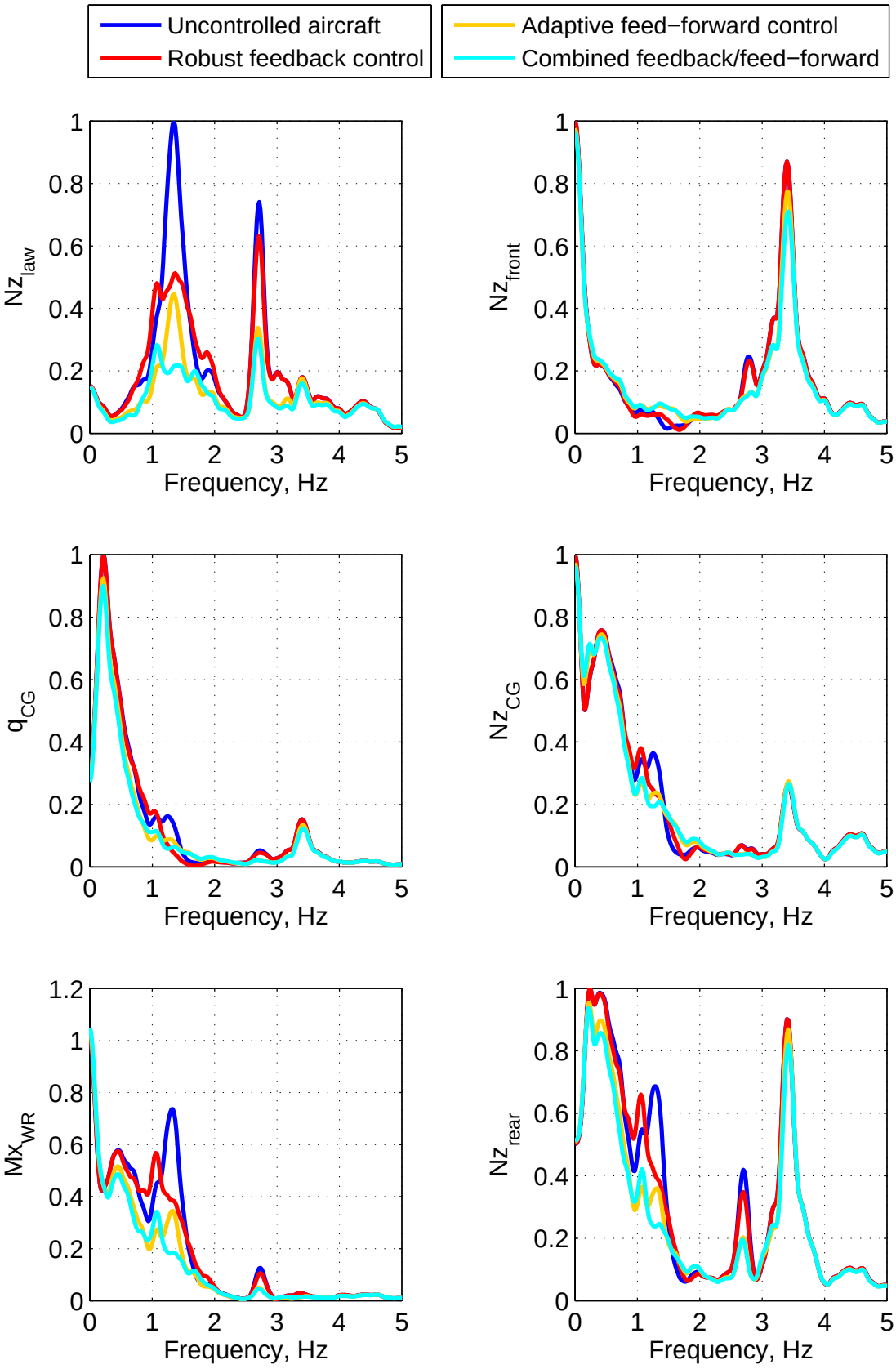

Figure F-2. Performance comparison of different controllers with a mean plant model, mass case B, Ma=0.86, $\gamma_{\alpha d}{}^{2}\left(e^{j\omega T}\right)=0.75$.

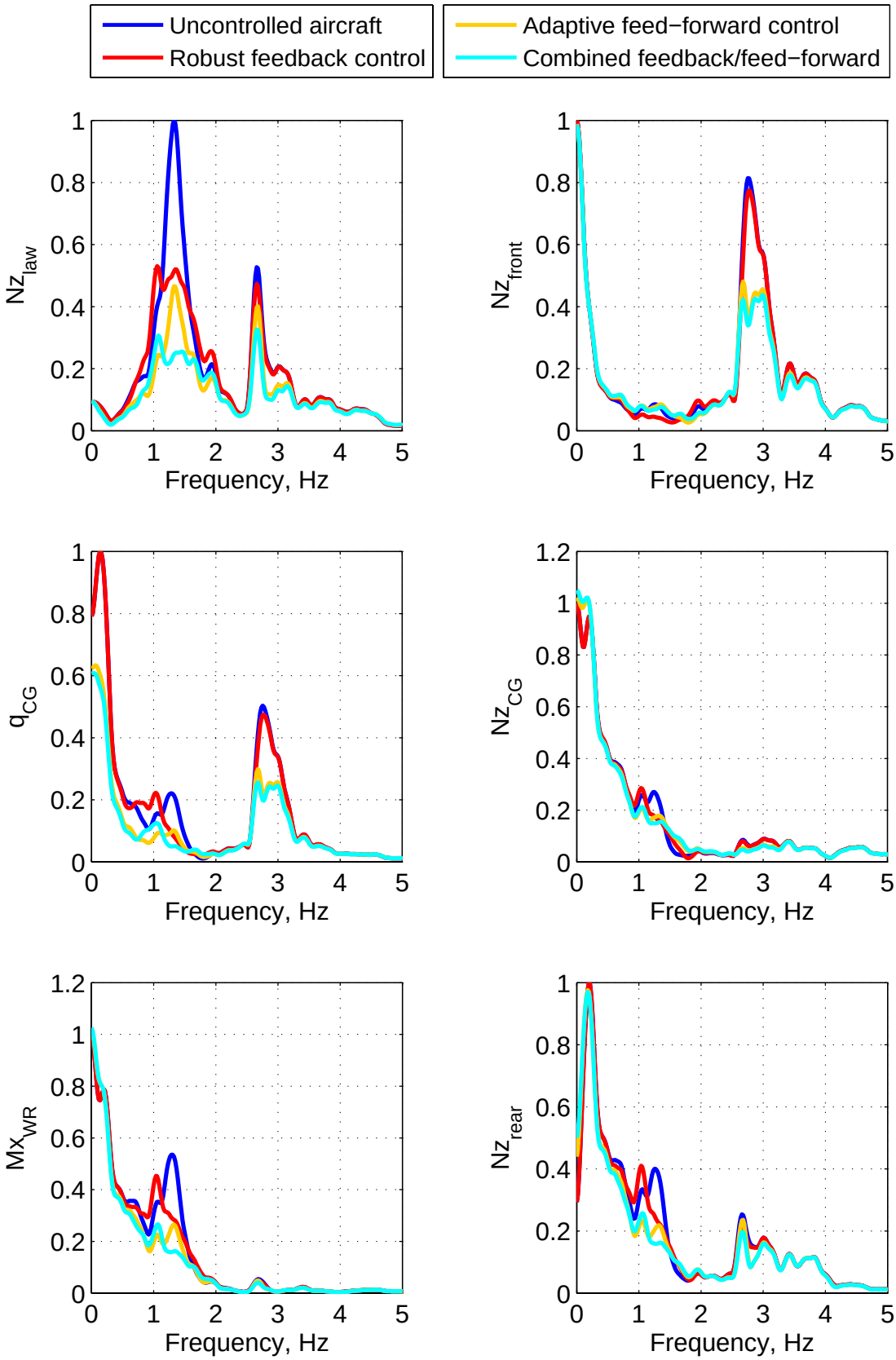

Figure F-3. Performance comparison of different controllers with a mean plant model, mass case C, Ma=0.86, $\gamma_{\alpha d}{}^{2}\left(e^{j\omega T}\right)=0.75$.

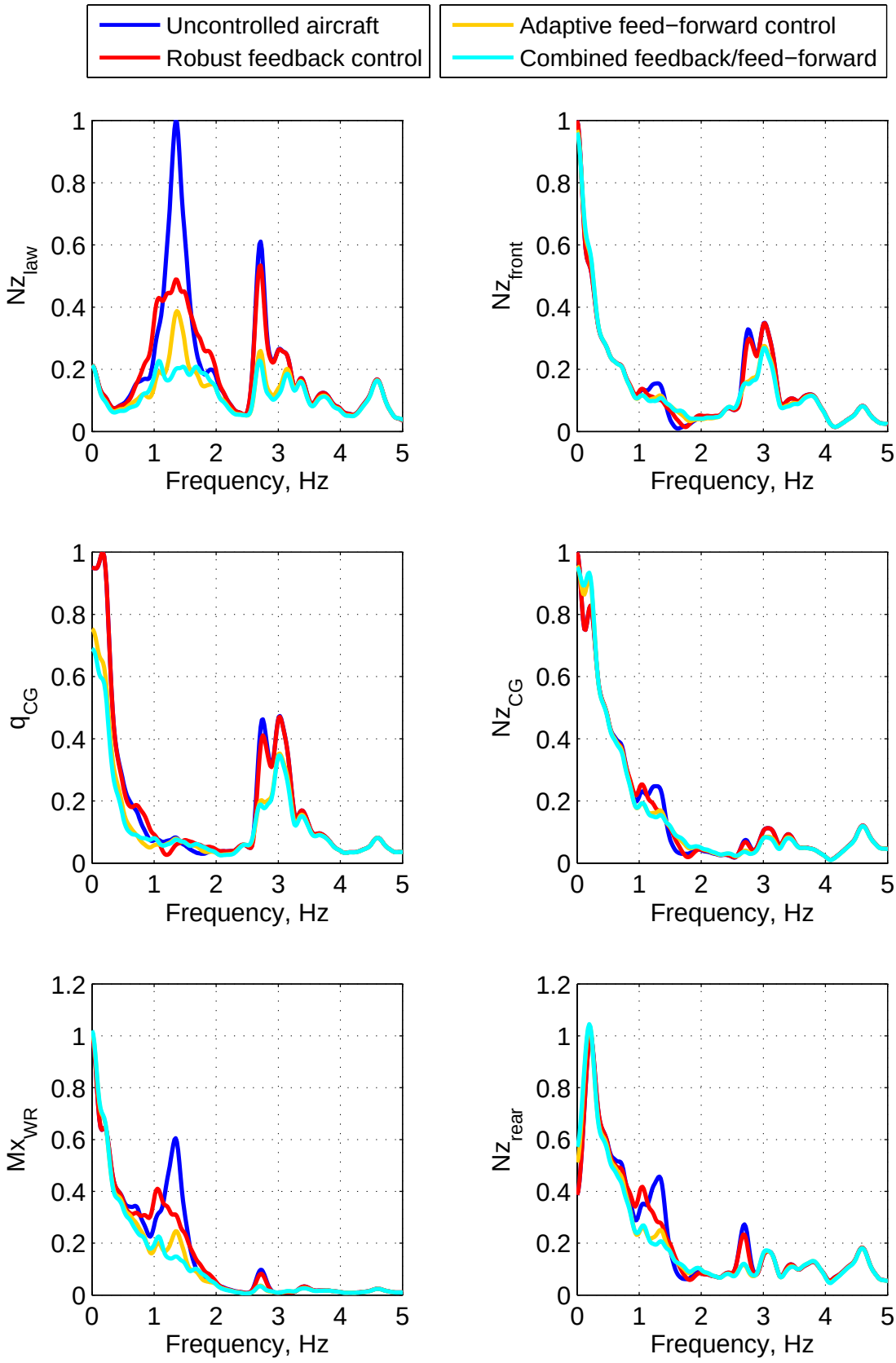

Figure F-4. Performance comparison of different controllers with a mean plant model, mass case D, Ma=0.86, $\gamma_{\alpha d}{}^{2}\left(e^{j\omega T}\right)=0.75$.

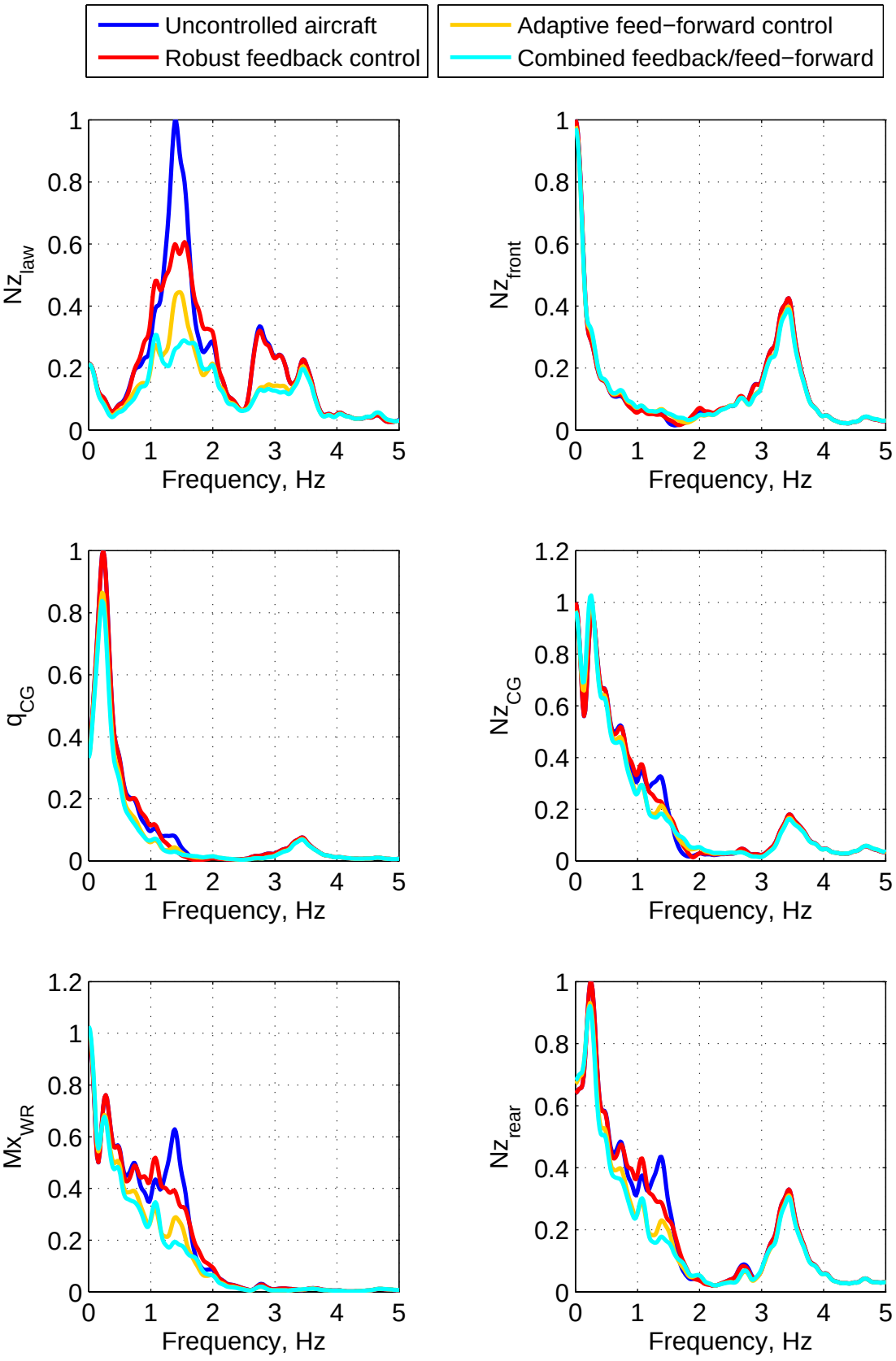

Figure F-5. Performance comparison of different controllers with a mean plant model, mass case A, Ma=0.82, $\gamma_{\alpha d}{}^{2}\left(e^{j\omega T}\right)=0.75$.

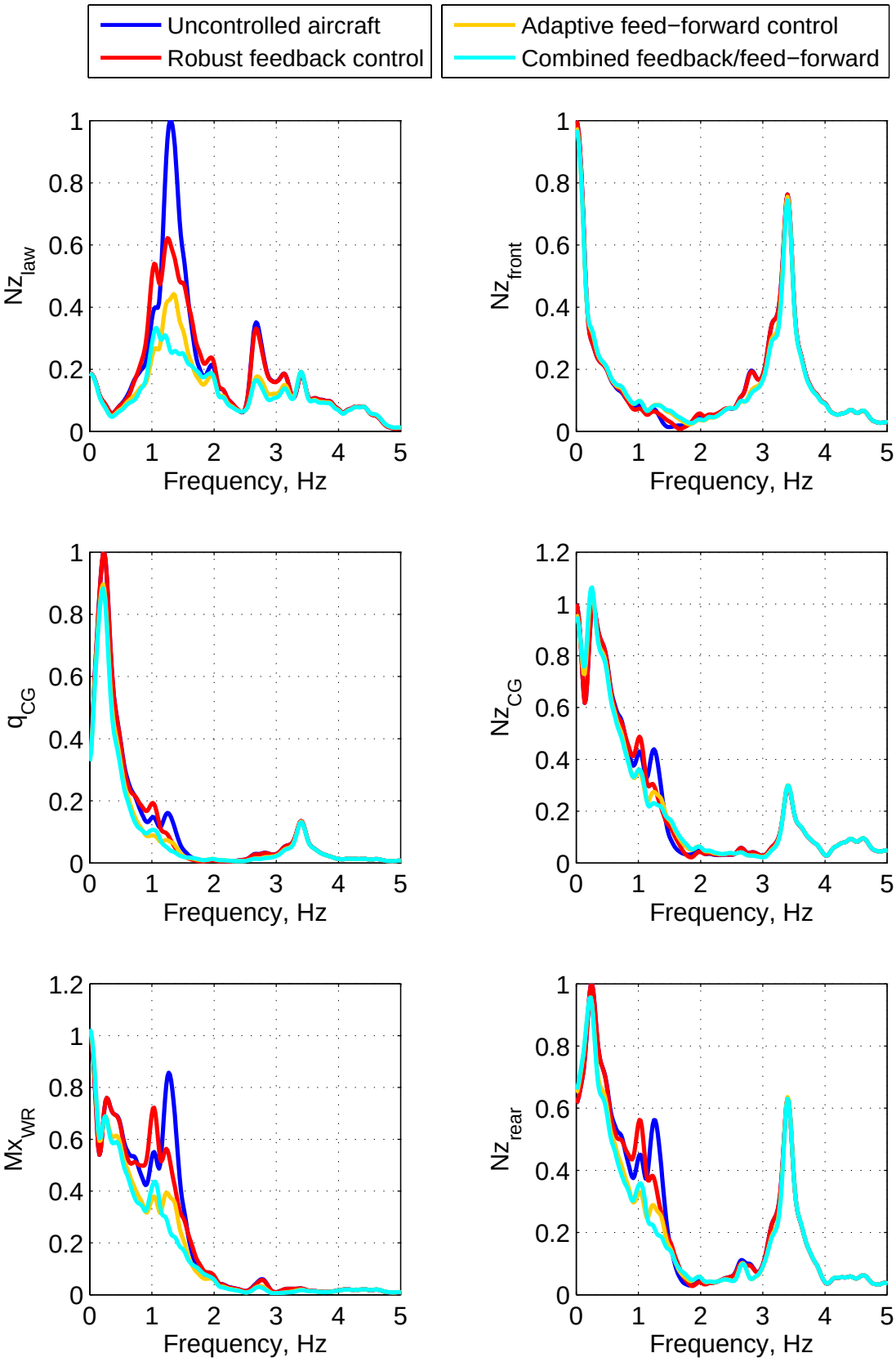

Figure F-6. Performance comparison of different controllers with a mean plant model, mass case B, Ma=0.82, $\gamma_{\alpha d}{}^{2}\left(e^{j\omega T}\right)=0.75$.

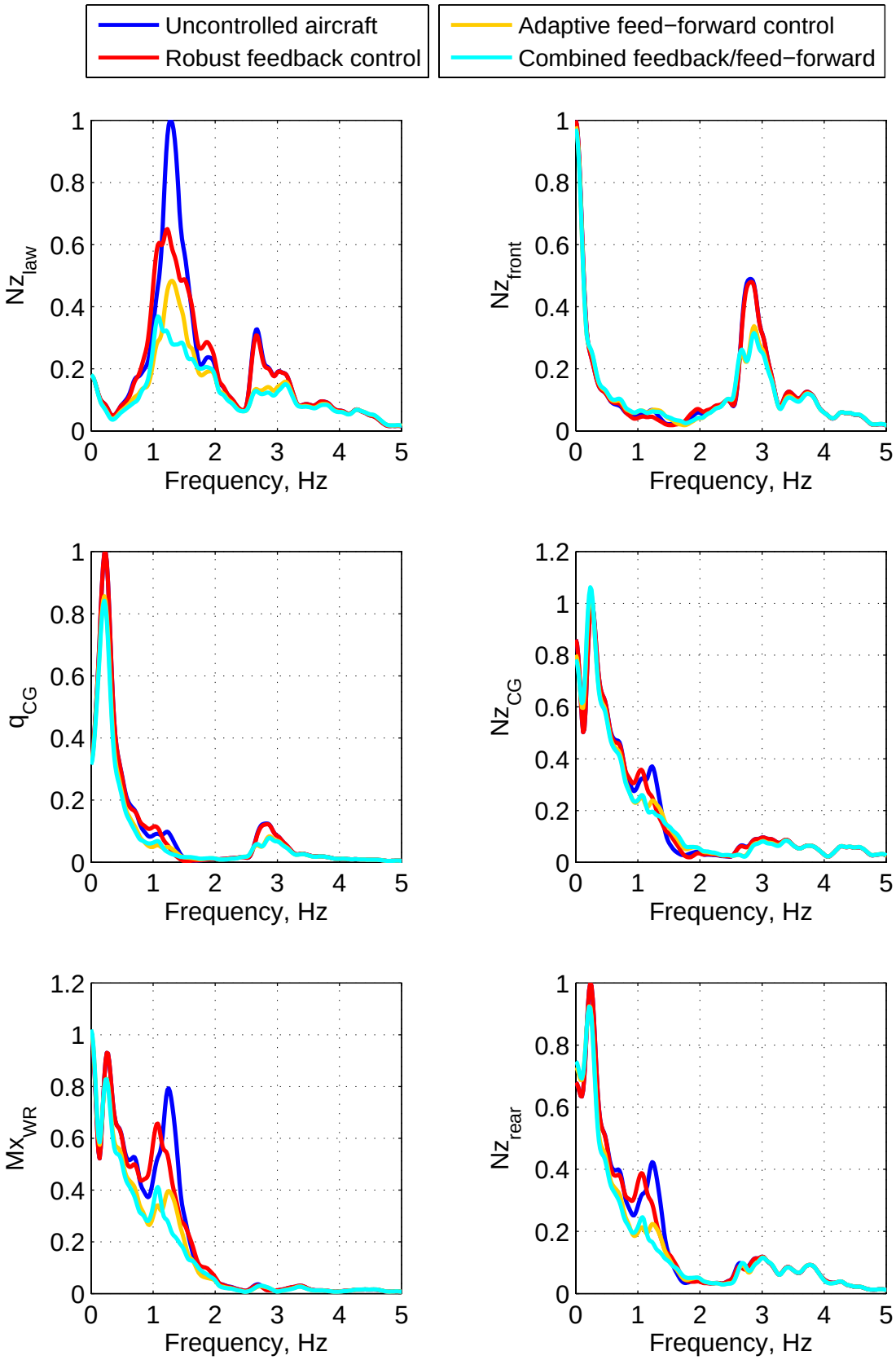

Figure F-7. Performance comparison of different controllers with a mean plant model, mass case C, Ma=0.82, $\gamma_{\alpha d}{}^{2}\left(e^{j\omega T}\right)=0.75$.

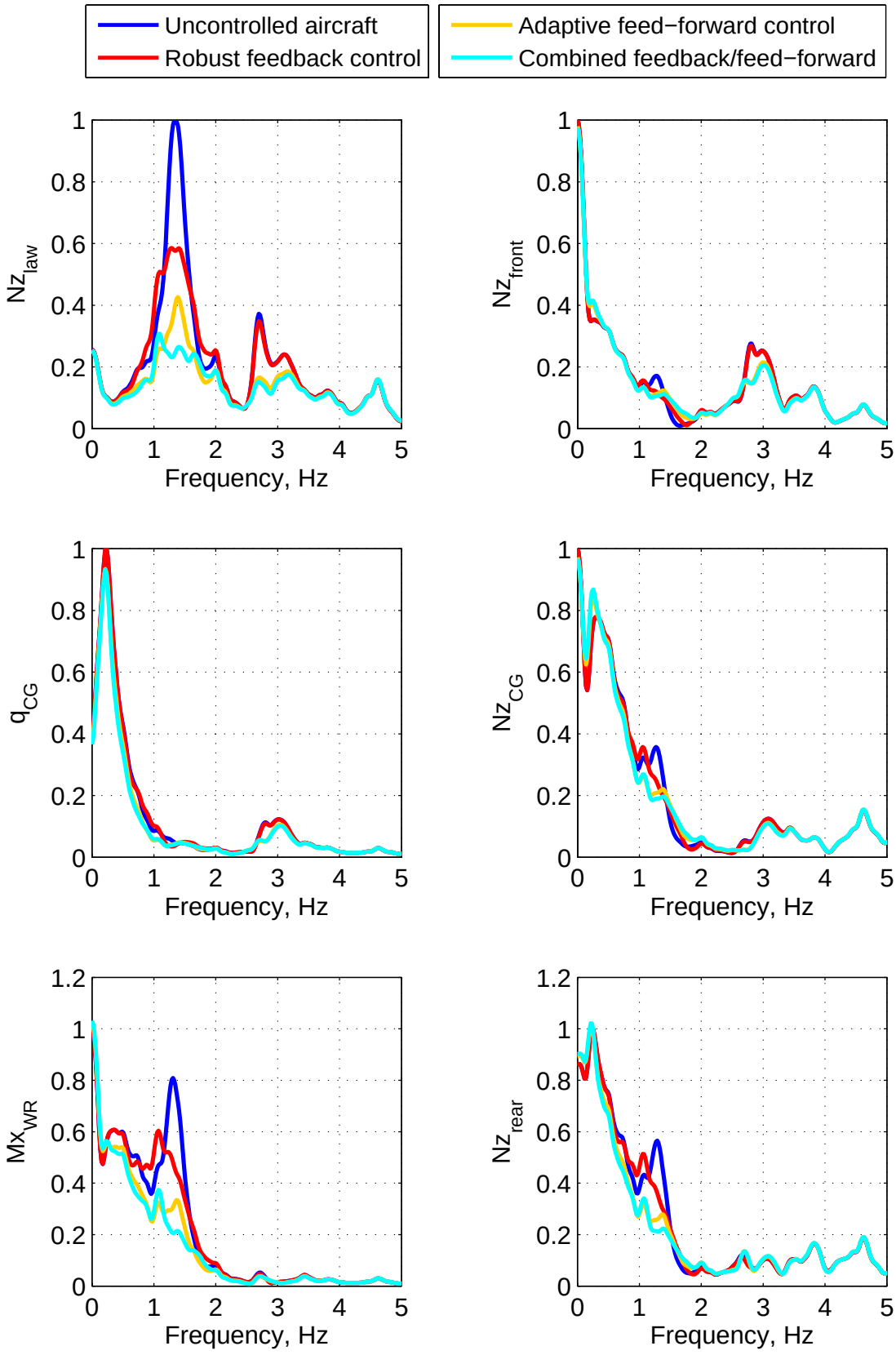

Figure F-8. Performance comparison of different controllers with a mean plant model, mass case D, Ma=0.82, $\gamma_{\alpha d}{}^{2}\left(e^{j\omega T}\right)=0.75$.

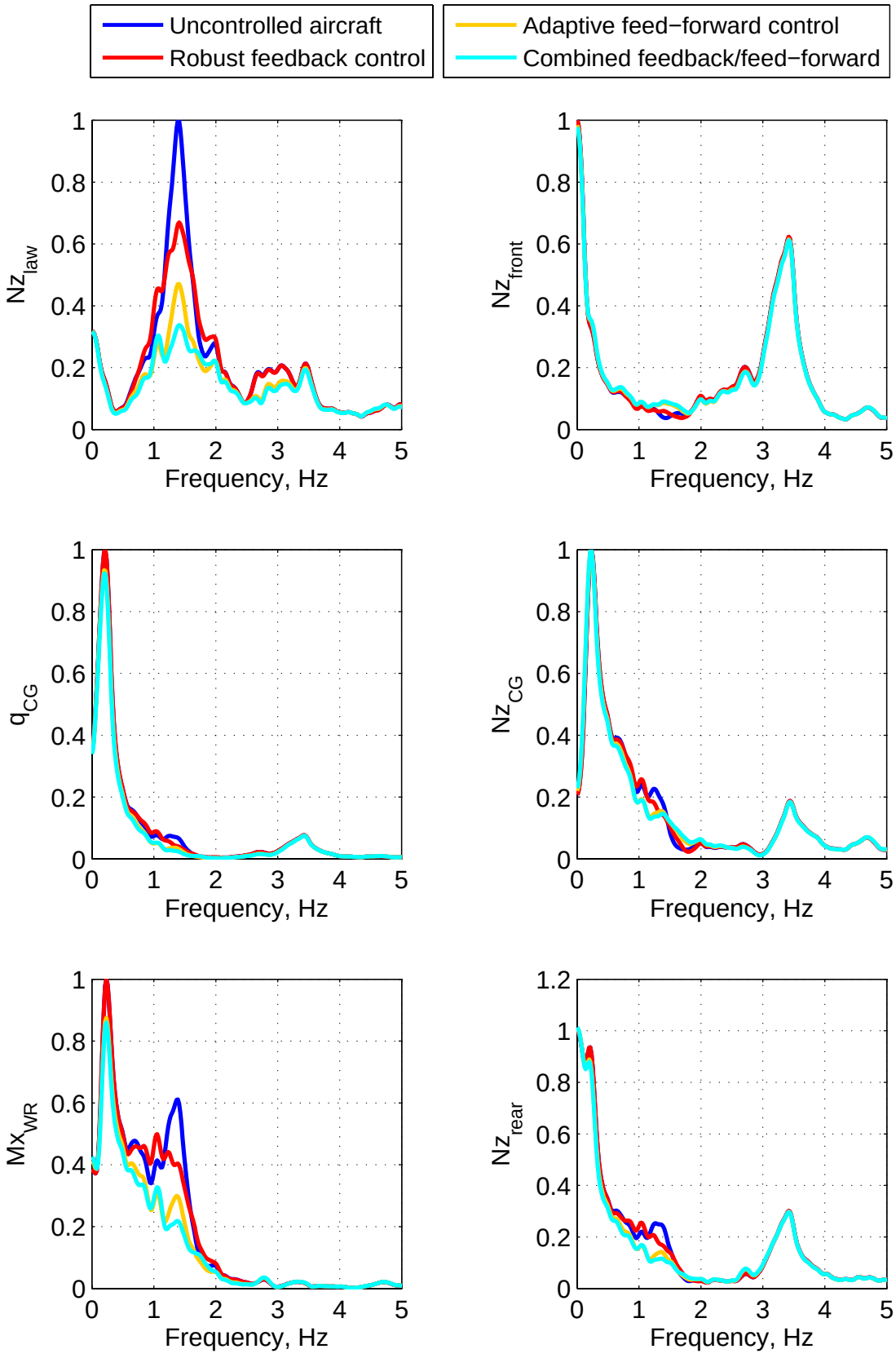

Figure F-9. Performance comparison of different controllers with a mean plant model, mass case A, Ma=0.7, $\gamma_{\alpha d}{}^{2}\left(e^{j\omega T}\right)=0.75$.

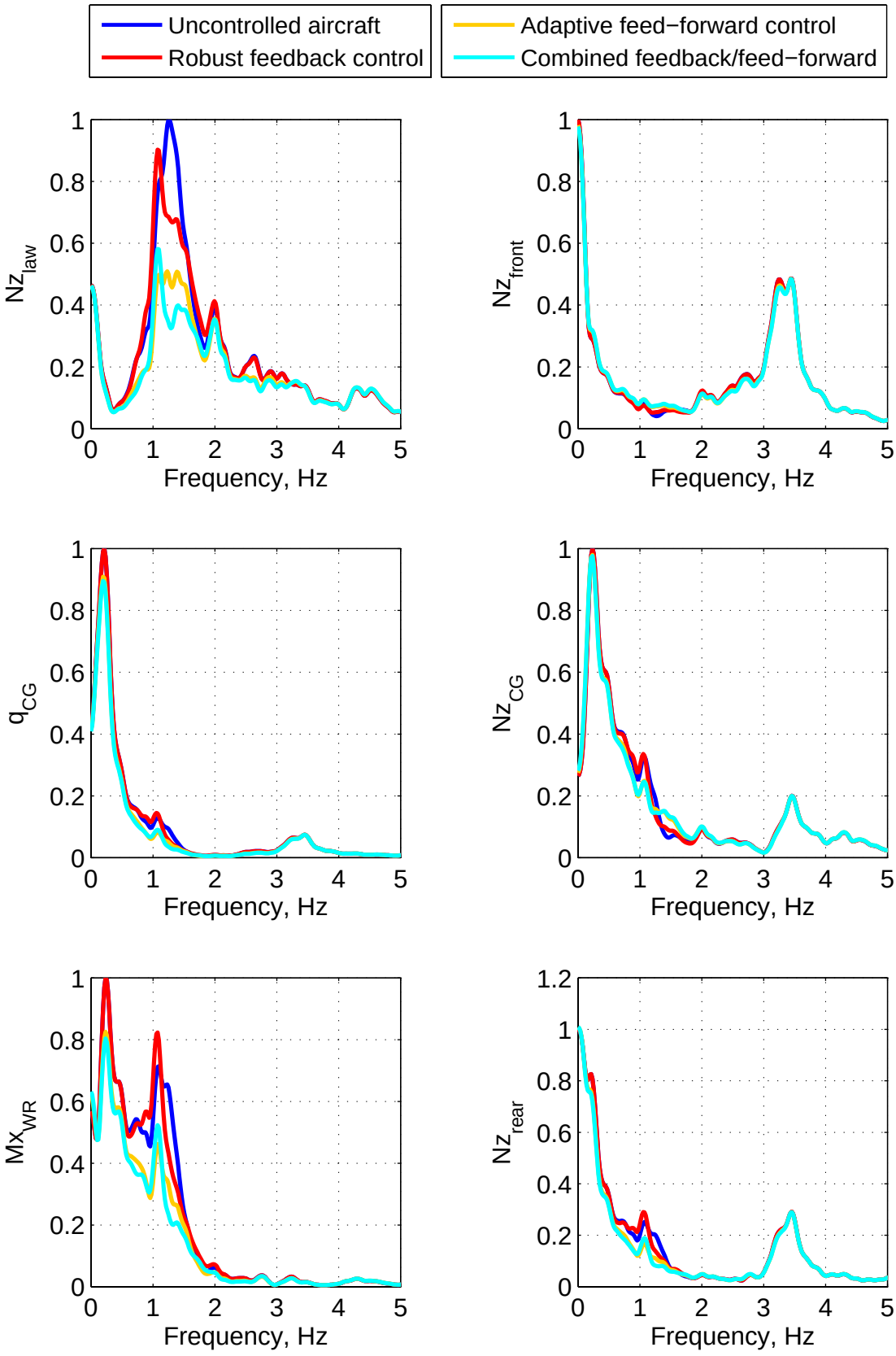

Figure F-10. Performance comparison of different controllers with a mean plant model, mass case B, Ma=0.7, $\gamma_{\alpha d}{}^{2}\left(e^{j\omega T}\right)=0.75$.

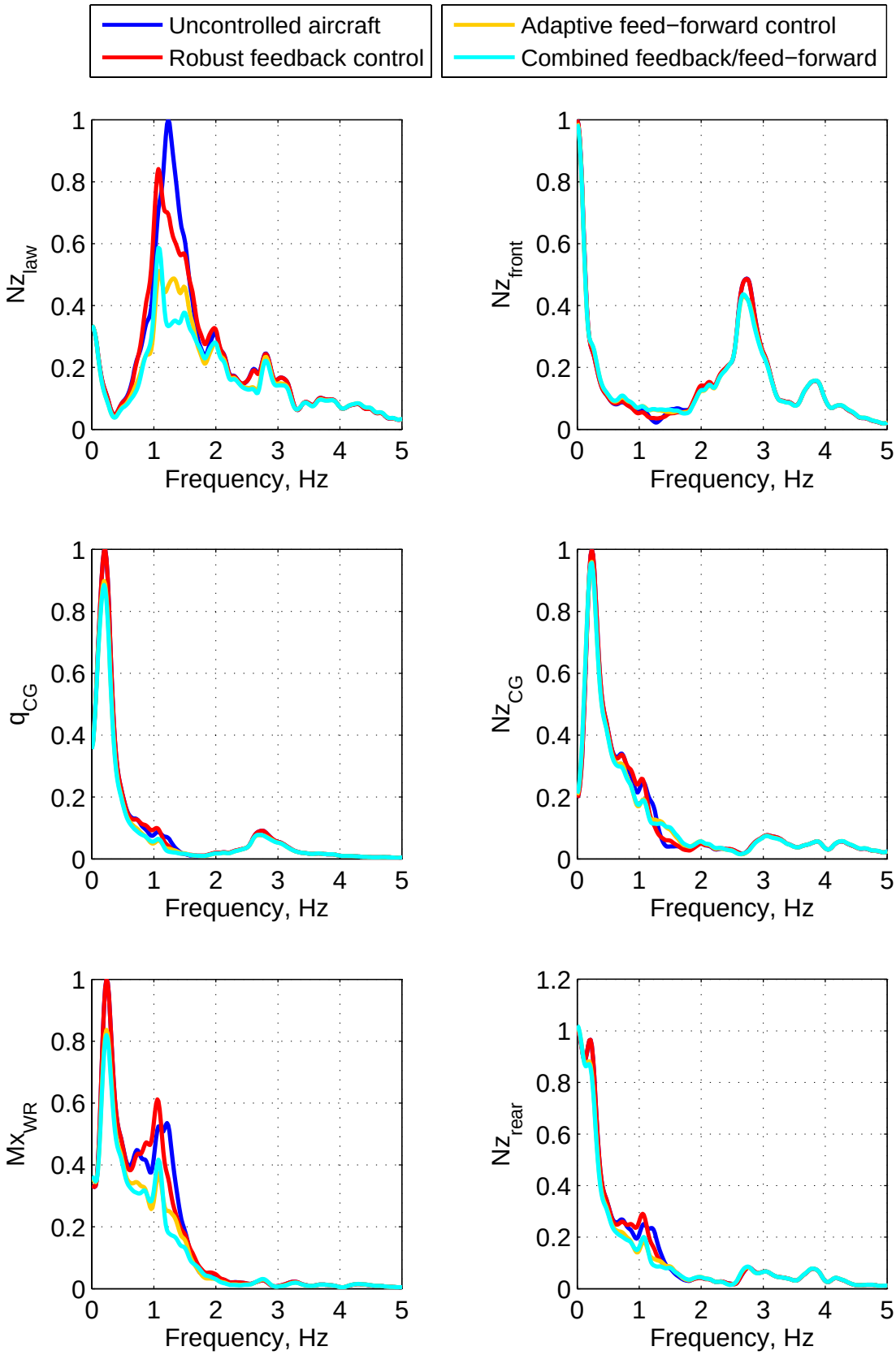

Figure F-11. Performance comparison of different controllers with a mean plant model, mass case C, Ma=0.7, $\gamma_{\alpha d}{}^{2}\left(e^{j\omega T}\right)=0.75$.

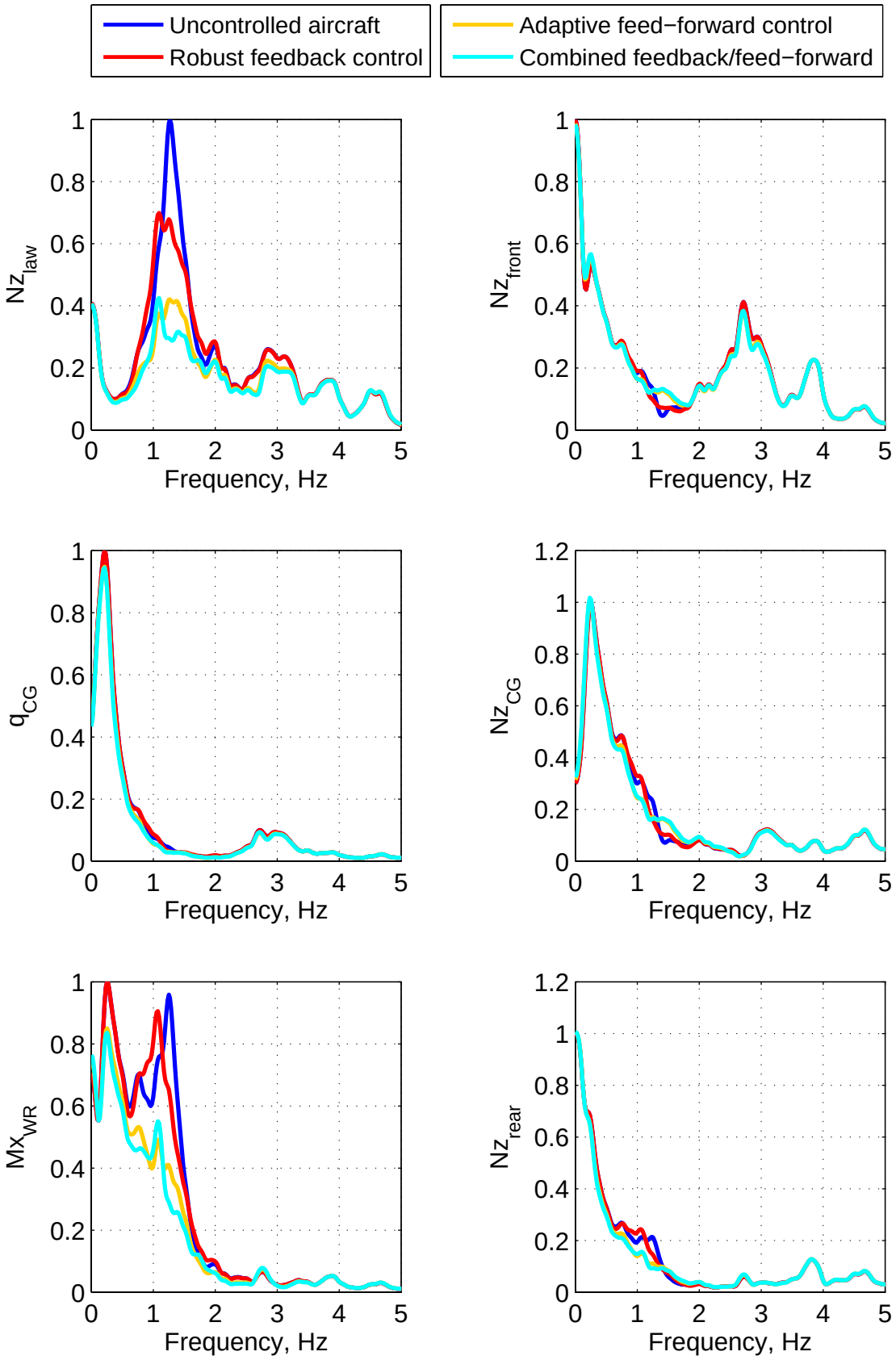

Figure F-12. Performance comparison of different controllers with a mean plant model, mass case D, Ma=0.7, $\gamma_{\alpha d}{}^{2}\left(e^{j\omega T}\right)=0.75$.

Appendix G – Definition of Transforms Used in this Thesis

The Laplace transform of a function $x(t)$ (in this thesis t is the time in seconds) is given by the one-sided integral transformation:

$$X(s) = \mathcal{L}\{x(t)\} = \int_0^\infty e^{-st} x(t) dt \tag{G-1}$$

With angular frequency ω, the Fourier transform of a function $x(t)$ is obtained by setting the Laplace variable $s = j\omega$, and integration also over negative time:

$$X(j\omega) = \mathcal{F}\{x(t)\} = \int_{-\infty}^\infty e^{-j\omega t} x(t) dt \tag{G-2}$$

Then the Inverse Fourier Transform (IFT) is given by:

$$x(t) = IFT\{X(j\omega)\} = \frac{1}{2\pi} \int_{-\infty}^\infty X(j\omega) e^{j\omega t} d\omega \tag{G-3}$$

The z transform of a sequence $x(n)$, e.g. of a sampled-time signal is defined as:

$$X(z) = \sum_{n=-\infty}^{\infty} x(n) z^{-n} \tag{G-4}$$

The Fourier transform of a sampled-time signal $x(n)$ is obtained by setting the z-transform variable $z = e^{j\omega T}$, compare [27], with T denoting the sample time in seconds:

$$X(e^{j\omega T}) = \mathcal{F}\{x(n)\} = \sum_{n=-\infty}^{\infty} x(n) e^{-j\omega nT} \tag{G-5}$$

Thereby, ωT denotes the (non-dimensional) normalized angular frequency, and n is the discrete time step. Thus, the time $t = nT$.

In this thesis also the Inverse Fourier Transform (IFT) for sampled signals is required, which is given by:

$$x(n) = IFT\{X(j\omega)\} = \frac{1}{2\pi}\int_{0}^{2\pi} X(e^{j\omega T})e^{j\omega nT}d\omega T \tag{G-6}$$

The Discrete Fourier Transform (DFT) over N samples of a sampled-time signal $x(n)$ with n=0,1,2,…,N-1 is defined by:

$$X(f_k) = DFT\{x(n)\} = \sum_{n=0}^{N-1} x(n)e^{-j2\pi f_k nT} \tag{G-7}$$

with discrete frequencies f_k (in Hertz) defined for the discrete frequency variable k=1,2,…,N by the following equation:

$$f_k = \frac{Fs(k-1)}{N} \tag{G-8}$$

Thereby, $Fs = 1/T$ denotes the sampling frequency in Hertz of the sampled-time signal $x(n)$. The Inverse Discrete Fourier Transform (IDFT) is given by:

$$x(n) = IDFT\{X(f_k)\} = \frac{1}{N}\sum_{f_k=0}^{\frac{N-1}{N\cdot T}} X(f_k)e^{j2\pi f_k nT} \tag{G-9}$$

The Fast Fourier Transform and its inverse are efficient implementations of the DFT and the IDFT which can be applied for $N = 2^m$, when m is an arbitrary integer value.

Appendix H – Measured Coherence for the ATTAS Aircraft

In Chapter 2.3 the two-dimensional von Kármán turbulence spectrum was used to estimate the performance that can be expected of feed-forward compensation of turbulence-excited wing bending vibrations. The theoretically obtainable performance depends on the quadratic coherence function between the reference signal α, and the disturbance signal d, denoted $\gamma_{\alpha d}{}^{2}\left(e^{j\omega T}\right)$. In order to validate the approach used in Chapter 2.3, flight test data from the DLR Advanced Technologies Testing Aircraft System (ATTAS, see [48], [69]), was evaluated. For this coherence analysis, data from a flight in rough atmosphere was used.

The first structural Eigen mode of the ATTAS aircraft is a symmetric pylon bending mode at about 3.5 Hz, compare Figure H-1. The first symmetric vertical wing bending mode has an Eigen frequency of about 5 Hz.

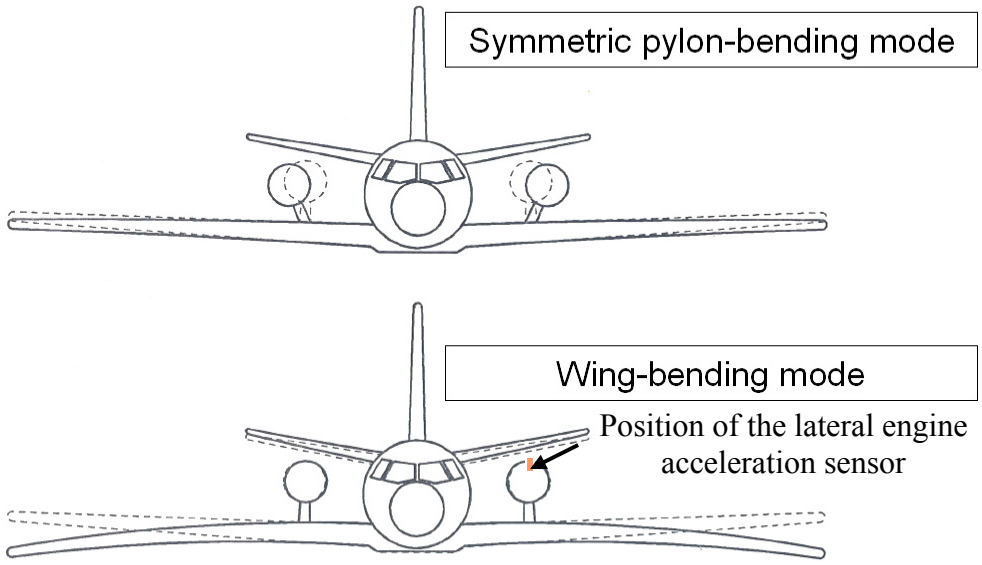

Figure H-1. Eigen modes of the ATTAS research aircraft.

The first structural Eigen mode can be observed at high signal to noise ratio by a *lateral* acceleration sensor mounted on top of the left engine (unfortunately no proper modal acceleration sensor signal as described in Eq. (2-3) was available for the observation of first symmetric vertical wing bending). This *lateral* acceleration sensor does not measure any disturbing longitudinal rigid body motions, which is very advantageous for the coherence analysis since the rigid body motions then do not have to be compensated in the acceleration signal.

The aerodynamic center of the ATTAS aircraft has an Y-coordinate of +/-4m to +/-5m, and the Y-coordinate of the nose boom mounted alpha probe is zero, i.e. the relevant span-wise separation between reference measurement and wing excitation is between $\overline{ab} = 4\,\text{m}$, and $\overline{ab} = 5\,\text{m}$. As already illustrated in Chapter 2.3 for the four-engine example aircraft, an estimate of the quadratic coherence function between reference measurement and excitation of the first structural Eigen modes can be read from plotting Eq (2-14) for a reasonable cruise speed, and for various span-wise separation distances $\overline{ab}$, see Figure H-2 for such a plot for the ATTAS aircraft.

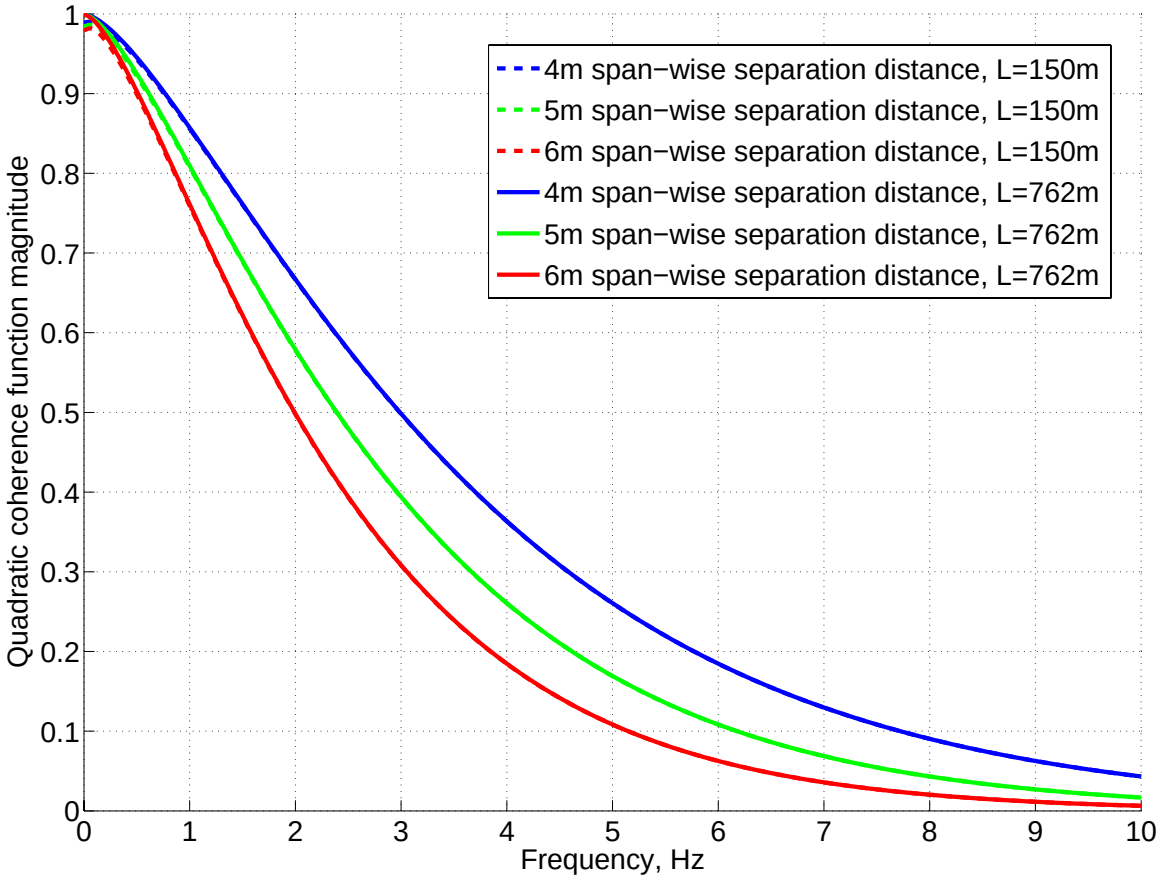

Figure H-2. Von Kármán turbulence model computed quadratic coherence function between two span-wise separated points “a” and “b” for the ATTAS.

According to Figure H-2 the quadratic coherence function between nose boom mounted alpha probe and *lateral* engine acceleration for the ATTAS makes almost 40% at 3.5 Hz, i.e. at the frequency of the first structural Eigen mode of the ATTAS.

In order to confirm the coherence estimate obtained by evaluating Eq (2-14) for the Y-distance between the alpha probe and the aerodynamic center of the wing, data of a ATTAS test flight in rough atmosphere has been evaluated, see Figure H-3.

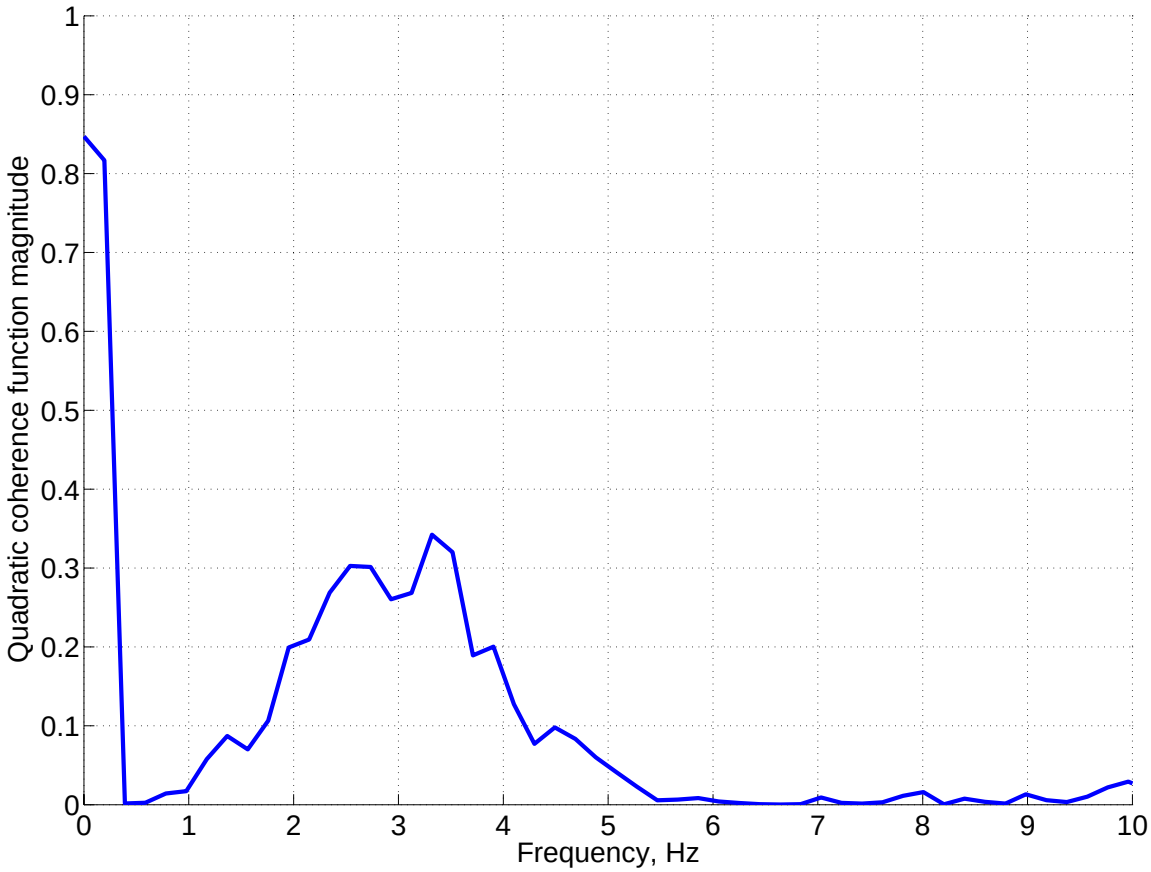

Figure H-3. Quadratic coherence function between nose boom mounted alpha probe and lateral engine acceleration for the ATTAS.

The flight test measured quadratic coherence function between nose boom mounted alpha probe signal and lateral engine acceleration signal indeed is at least 30% at 3.5 Hz. Thus, according to Eq. (2-17) the modal acceleration of the first structural Eigen mode of the ATTAS theoretically can be reduced by 15-20% by feed-forward compensation.

This is far less than the estimated reduction of modal wing bending accelerations for the large four-engine example aircraft. As indicated by the title of this thesis, the proposed adaptive feed-forward controller is a proper means for the compensation of turbulence excited vibrations only on large aircraft, where the first structural Eigen modes (such as the first symmetric vertical wing bending mode) are at rather low frequencies (~1 Hz).

Bibliography

[1] ABEL, I., AND SANDFORD, M., "Status of two studies on Active Control of Aeroelastic Response," NASA Technical Memorandum X-2909, Washington 1973.

[2] ABEL, I., PERRY, B., AND NEWSOM, J., "Comparison of Analytical and Wind-Tunnel Results for Flutter and Gust Response of a Transport Wing with Active Controls," NASA Technical Paper 2010, 1982.

[3] ABDELMOULA, F., "Design of an Open-Loop Gust Alleviation Control System for Airborne Gravimetry," *Aerospace Science and Technology*, No. 6, 1999, pp. 379-389.

[4] ACKERMANN, J., *Robuste Regelung - Analyse und Entwurf von linearen Regelungssystemen mit unsicheren physikalischen Parametern*, Springer, Berlin, 1993.

[5] ADCOCK, I., "Lotus adaptive engine mounts – the sound of silence," *Motor Trend*, May 1992, pp. 72-73.

[6] ASTRÖM, K., "Adaptive Feedback Control," *Proceedings of the IEEE*, Vol. 75, No. 2, February 1987, pp. 185-217.

[7] AYACHE, A., GHIAPPA, C., AND PUYOU, G., "Gain Scheduling using Multimodel Eigenstructure Assignment: A new Application," *5th IFAC Symposium on Robust Control Design*, Toulouse, France, 05.-07. July, 2006.

[8] BOUCHER, C., ELLIOT, S., NELSON, P., "Effect of Errors in the Plant Model on the Performance of Algorithms for Adaptive Feed-forward Control," *IEE, Proceedings-F*, Vol. 138, No. 4, August 1991, pp. 315.

[9] BOUCHER, C., ELLIOT, S., AND BAEK, K-H., "Active Control of Helicopter Rotor Tones," *Internoise 96 - 25th Anniversary Congress*, Liverpool, 1996.

[10] BREITSAMTER, C., "Aerodynamic Active Vibration Alleviation For Buffet Excited Vertical Tails," *RTO-AVT Symposium on Vortex Flow and High Angle of Attack*, Loen, Norwegen, 07.-11. May, 2001.

[11] BREITSAMTER, C., "Aerodynamic Active Control of Fin-Buffet Load Alleviation," *AIAA Journal of Aircraft*, Vol. 42, No. 5, 2005, pp. 1252-1263.

[12] BRIGHAM, O., "*FFT – Schnelle Fourier-Transformation*," R.Oldenbourg, München, 1989.

[13] BRITT, R., JACOBSON, S., AND ARTHURS, T., "Aero-servo-elastic Analysis of the B-2 Bomber," *Journal of Aircraft*, Vol. 37, No. 5, September/October 2000.

[14] BROCKHAUS, R., "*Flugregelung, 2. Auflage*, **"** Springer, Berlin, 2001, pp. 119 & 209.

[15] BURDISSO, R., VIPPERMANN, J., AND FULLER C., "Causality analysis of feed-forward controlled systems with broadband inputs," *Journal of Acoustical Society of America*, Vol. 94, No. 1, 1993, pp. 234-242.

[16] CALISE, A., KIM, N., AND BUFFINGTON, J., "Adaptive Compensation for Flexible Dynamics," *AIAA Guidance, Navigation, and Control Conference and Exhibit*, Monterey, California, 2002.

[17] CALISE, A., SHIN, Y., AND JOHNSON, M., "Comparison Study of Conventional and Neural Network Based Adaptive Control of Wing Rock," *AIAA Guidance, Navigation, and Control Conference and Exhibit*, Providence, Rhode Island, 16.-19. August, 2004.

[18] CLARK, R., AND BERNSTEIN, D., "Hybrid Control: Separation in Design," *Journal of Sound and Vibration*, Vol. 214, No. 4, 1998, pp. 784-791.

[19] CORTELLESSA, V., CUKIC, B., DEL GOBBO, D., MILI, A., NAPOLITANO, M., SHERESHEVSKY, M., AND SANDHU, H., "Certifying Adaptive Flight Control Software," Department of Computer Science and Electrical Engineering & Department of Mechanical and Aerospace Engineering, Morgantown, West Virginia University 2004.

[20] COUCHE, J., CHARETTE, F., AND FULLER, C., "Active Control of Automobile Cabin Noise with Advanced Speakers," *136th Acoustical Society of America Meeting*, Norfolk, Virginia, 13. October, 1998.

[21] CRIMALDI, J., BRITT, R., AND RODDEN, W., "Response of B-2 Aircraft to Nonuniform Spanwise Turbulence," *Journal of Aircraft*, Vol. 30, No. 5, September-October 1993, pp. 652-659.

[22] DORNHEIM, M., "Manufacturers See Evolutionary Change To Handle Turbulence," *Aviation Week & Space Technology*, 27. July, 1998, pp. 76-79.

[23] DORNHEIM, M., "B-2 Tackles Tough Turbulence," *Aviation Week & Space Technology*, 27. July, 1998, pp. 79-80.

[24] DRYDEN, H., "A Review of the Statistical Theory of Turbulence," *Turbulence – Classical Papers on Statistical Theory*, S.K. Friedlander and Leonard Topper, Interscience Publishers, Inc., New York, 1961 pp. 115-150.

[25] EDWARDS, J., "Flight Test Results of an Active Flutter Suppression System," *Journal of Aircraft*, Vol. 20, No. 3, March 1983.

[26] ELLIOT, S., NELSON, P., STOTHERS, I., AND BOUCHER, C., "In-flight experiments on the active control of propeller-induced cabin noise," *Journal of Sound and Vibration*, Vol. 140, No. 2, 1990, pp. 219-238.

[27] ELLIOTT, S., *Signal Processing for Active Control*, Academic Press, London, 2001, pp. 51-61.

[28] ELLIOTT, S., *Signal Processing for Active Control*, Academic Press, London, 2001, pp. 77-78 & 151-152.

[29] ELLIOTT, S., *Signal Processing for Active Control*, Academic Press, London, 2001, pp. 89-91 & 152-154.

[30] ELLIOTT, S., *Signal Processing for Active Control*, Academic Press, London, 2001, pp. 124-126.

[31] ELLIOTT, S., *Signal Processing for Active Control*, Academic Press, London, 2001, pp. 105-106 & 132-133.

[32] ELLIOTT, S., *Signal Processing for Active Control*, Academic Press, London, 2001, pp. 144-149.

[33] ELLIOTT, S., *Signal Processing for Active Control*, Academic Press, London, 2001, pp. 319-327.

[34] ELLIOTT, S., *Signal Processing for Active Control*, Academic Press, London, 2001, pp. 357-366.

[35] ELLIOTT, S., *Signal Processing for Active Control*, Academic Press, London, 2001, pp. 341-344.

[36] ELLIOTT, S., *Signal Processing for Active Control*, Academic Press, London, 2001, pp. 478-479.

[37] ERIKSSON, L., "Development of the filtered-U algorithm for active noise control," *Journal of the Acoustical Society of America*, Vol. 89, 1991, pp. 257-265.

[38] FERRERES, G., AND PUYOU, G., "Feasibility of H_∞ design Specifications: an Interpolation Method," *American Control Conference (ACC)*, Portland, Oregon, 08.-10. June, 2005.

[39] FERRERES, G., AND PUYOU, G., "Flight Control Law Design for a Flexible Aircraft: Limits of Performance," *AIAA Journal of Guidance, Control, and Dynamics*, Vol. 29, No. 4, 2006, pp. 870-878.

[40] FRAANJE, R., VERHAEGEN, M., AND DOELMAN, N., "Increasing the Robustness of a Preconditioned Filtered-X LMS Algorithm," *Signal Processing Letters, IEEE*, Vol. 11, Issue 2, February 2004, pp. 285–288.

[41] FREYMANN, R., "Active Flutter Suppression on a Delta Wing Model Structure," Göttingen DFVLR, Institut für Aeroelastik 1985.

[42] FULLER, C., ELLIOTT, S., AND NELSON, P., *Active Control of Vibration*, Academic Press, London, 1996, pp. 91-92.

[43] FULLER, C., ELLIOTT, S., AND NELSON, P., *Active Control of Vibration*, Academic Press, London, 1996, pp. 95-97.

[44] FULLER, C., ELLIOTT, S., AND NELSON, P., *Active Control of Vibration*, Academic Press, London, 1996, pp. 106-107.

[45] GARDNER, W., "Learning Characteristics of Stochastic-Gradient-Descent Algorithms: A general Study, Analysis, and Critique," *Journal of Signal Processing*, Vol. 6, 1984, pp. 113-133.

[46] GIANNOPOULOS, T., "Structural design of a full-flexible aircraft wind-tunnel model for validation of control systems for active suppression of wing-/fuselage-vibrations using piezoelectric trailing edge flaps," Diploma thesis, RWTH Aachen, Department of Aerospace and Lightweight Structures, Aachen (Germany), 13. January 2006.

[47] GLOVER, J., "Adaptive Noise Cancelling Applied to Sinusoidal Interferences," *IEEE Transactions on Acoustics, Speech, and Signal Processing*, Vol. ASSP-25, No. 6, December 1977, pp. 484-491.

[48] HAHN, K.-U., AND KÖNIG, R., "ATTAS flight test and simulation results of the advanced gust management system LARS," *AIAA Atmospheric Flight Mechanics Conference*, Hilton Head Island, SC, 10.-12. August, 1992.

[49] HALSEY, S., AND GOODALL, M., "Kalman Filtering for Structural Coupling," Department of Electronic and Electrical Engineering, Loughborough University, UK, 2003.

[50] HANEL, M., "Robust Integrated Flight and Aeroelastic Control System Design for a Large Transport Aircraft," Dissertation, Fortschritt-Bericht VDI, Reihe 11, Nr. 297, VDI-Verlag, Düsseldorf, 2001.

[51] HANSEN, C., "Current research in active control of noise," *International Sound & Vibration Digest*, Vol. 1, No. 2, 12. November, 1994.

[52] HANSEN, C., "Overview of active noise control systems," *International Sound & Vibration Digest*, Vol. 1, No. 3, 26. January, 1995.

[53] HARRIS R., RICKARD, W., "Active Control Transport Design Criteria," *Journal of Aircraft*, Vol. 16, No. 11, November 1979.

[54] HECKER S., AND HAHN, K.-U., "Advanced Gust Load Alleviation System for Large Flexible Aircraft," *1st CEAS European Air & Space Conference*, Berlin, Germany, 10.-13. September, 2007.

[55] HOBLIT, F., "*Gust Loads on Aircraft: Concepts and Applications*," AIAA Education Series, Washington 1988, pp. 42-50.

[56] HOBLIT, F., "*Gust Loads on Aircraft: Concepts and Applications*," AIAA Education Series, Washington 1988, pp. 171.

[57] HOFFMANN, F., MAIER, R., JÄNKER, P., HERMLE, F., AND BERTHE, A., "Helicopter Interior Noise Reduction by using Active Gearbox Struts," *12th AIAA/CEAS Aeroacoustics Conference*, Cambridge, Massachusetts, 08.-10. May, 2006.

[58] HÖNLINGER, H., ZIMMERMANN, H., SENSBURG, O., AND BECKER, J., "Structural Aspects of Active Control Technology," *Flight Mechanics Panel Symposium*, Turin, Italy, 09.-13. May, 1994.

[59] IMBERT, N., MOUYON, PH., AND MONTSENY, G., "State Representation and Simulation of 2D Turbulent Wind," *AIAA Modeling and Simulation Technologies Conference and Exhibit*, Denver, CO, 14.-17. August, 2000.

[60] ISERMANN, R., AND LACHMANN, K.-H., „Parameter-adaptive Control with Configuration Aids and Supervision Functions," *Automatica*, Vol. 21, No. 6, 1985, pp. 625-638.

[61] ISERMANN, R., *Identifikation dynamischer Systeme 1 – Grundlegende Methoden*, Springer, Berlin, 1992.

[62] ISERMANN, R., *Identifikation dynamischer Systeme 2 – Besondere Methoden, Anwendungen*, Springer, Berlin, 1992.

[63] JEANNEAU, M., AVERSA, N., DELANNOY, S., AND HOCKENHULL, M., "Awiator's study of a Wing Load Control: Design and Flight-test Results," *16th IFAC Symposium on Automatic Control in Aerospace*, St. Petersburg (RUSSIA), 14.-18. June, 2004.

[64] JEANNEAU, M., LAMOLIE, J., PUYOU, G., AND AVERSA, N., "Awiator's design of Multi-objective Control Laws," *16th IFAC World Congress*, Prague, 04.-08. July, 2005.

[65] JOHNSON, E., AND CALISE, A., "Pseudo-control hedging: a new method for Adaptive Control," Advances in Navigation Guidance and Control Technology Workshop, Redstone Arsenal, Alabama, 01.-02. November, 2000.

[66] JOHNSTON, J., ET AL., "Accelerated Development and Flight Evaluation of Active Controls Concepts for Subsonic Transport Aircraft Volume 1 – Load Alleviation/Extended Span Development and Flight Test," NASA CR-159097, 1979, pp. 02-11.

[67] KAUFMAN, H., BARKANA, I., AND SOBEL, K., *Direct Adaptive Control Algorithms – Theory and Applications*, Springer, New York, 1998.

[68] KEWLEY, D., CLARK, R., AND SOUTHWARD, S., "Feed-forward control using the higher-harmonic, time-averaged gradient descent algorithm," *Journal of the Acoustical Society of America*, Vol. 97, 1995, pp. 2892-2905.

[69] KÖNIG, R., HAHN, K.-U., AND WINTER, J., "Advanced Gust Management System, " *Flight Mechanics Panel Symposium*, Turin, Italy, 09.-13. May, 1994.

[70] KRAG, B., "Manöverlaststeuerung und Böenabminderung," *Flugtechnik I – Einige moderne Aspekte der Kampfflugzeugentwicklung, Teil 2*, Mannheim, 04.-05. October, 1976, pp. 15 & B12.

[71] KROGMANN, U., "Beitrag zur Anwendung neuronaler Netze in der Flugregelung," Dissertation, Universität Braunschweig, 1995.

[72] LANDAU, Y., *Adaptive Control: The Model Reference Approach*, Dekker, New York, 1979.

[73] LEE, H., KROO, I., AND BIENIAWSKI, S., "Flutter Suppression for High Aspect Ratio Flexible Wings using Micro-flaps," *43. AIAA/ASME/ASCE/AHS/ASC Structures, Structural Dynamics, and Material Conference*, Denver, Colorado, 22.-25. April 2002.

[74] LJUNG, L., *System Identification, Theory For The User*, Prentice Hall, New Jersey, 1999.

[75] LONG, G., LING, F., AND PROAKIS, J., "The LMS Algorithm with Delayed Coefficient Adaptation," *IEEE Transactions on Acoustics, Speech, and Signal Processing*, Vol. 37, No. 9, September 1989.

[76] LUEG, P., "Verfahren zur Dämpfung von Schallschwingungen," Austrian Patent No. 141998, Filed: Feb. 2, 1933, Patented: Jan. 15, 1935.

[77] LUEG, P., "Process of silencing sound oscillations," US Patent No. 2,043,416, 1936.

[78] MAEDA, Y., AND YOSHIDA, T., "An active noise control without estimation of secondary-path – ANC using simultaneous perturbation," *Proceedings of ACTIVE99*, Fort Lauderdale, FL., 1999, pp. 985-994.

[79] MAIER, R., ZILLMANN, J., ROURE, A., WINNINGER, M., ENGHARDT, L., TAPKEN, U., NEISE, W., ANTOINE, H., AND BOUTY, E., "Active Control of Fan Tone Noise from Aircraft Engines," *7th AIAA/CEAS Aeroacoustics Conference*, Maastricht, Netherlands, 28.-30. May, 2001.

[80] MILLOTT, T., WELSH, W., AND YOERKIE, C., "Flight Test of Active Gear-Mesh Noise Control on the S-76 Aircraft," *American Helicopter Society 54th Annual Forum,* Washington, DC, 20.-22. May, 1998.

[81] MIYAZAWA, Y., "Flight Control Law and Structural Filter Design for a flexible Aerospace Vehicle," *AIAA Guidance, Navigation, and Control Conference and Exhibit*, Denver, Colorado, 14.-17. August 2000.

[82] MORGAN, D., "An Analysis of Multiple Correlation Cancellation Loops with a Filter in the Auxiliary Path", *IEEE Transactions on Acoustics, Speech, and Signal Processing*, Vol. ASSP-28, No. 4, August, 1980.

[83] MOSCHYTZ, G., AND HOFBAUER, M., *Adaptive Filter*, Springer, Berlin, 2000.

[84] MUKHOPADHYAY, V., NEWSOM, J., AND ABEL, I., "A Direct Method for Synthesizing Low-Order Optimal Feedback Control Laws with Application to Flutter Suppression," *AIAA Atmospheric Flight Mechanics Conference*, Danvers, Massachusetts, 11.-13. August, 1980.

[85] MUKHOPADHYAY, V., "Transonic Flutter Suppression Control Law Design, Analysis and Wind-Tunnel Results," *International Forum on Aeroelasticity and Structural Dynamics*, Williamsburg, Virginia, 22.-25. June, 1999.

[86] NARENDRA, K., AND ANNASWAMY, A., *Stable Adaptive Systems*, Prentice-Hall, New Jersey, 1989.

[87] NEWTON, G., GOULD, L., AND KAISER, J., "*Analytical design of linear feedback controls*," Wiley, New York, 1957.

[88] PAGE, A., MELONEY, E., AND MONACO J., "Flight Testing of a Retrofit Reconfigurable Control Law Architecture Using an F/A-18C," *AIAA Guidance, Navigation, and Control Conference and Exhibit*, Keystone, Colorado, 21.-24. August, 2006.

[89] PALUMBO, D., CABELL, R., CLINE, J., AND SULLIVAN, B., "Flight test of ASAC Aircraft Interior Noise Control," *5th AIAA/CEAS Aeroacoustics Conference and Exhibit*, Vol. 2, Bellevue, WA, 10.-12. May, 1999.

[90] PALUMBO, D., CABELL, R., CLINE, J., AND SULLIVAN, B., "Active Structural Acoustic Control of Interior Noise on a Raytheon 1900D," NASA/TM-2000-209846, 2000.

[91] PRASAD, J., CALISE, A., PEI, Y., AND CORBAN, J., "Adaptive Nonlinear Controller Synthesis and Flight Test Evaluation," *Proceedings of the 1999 IEEE International Conference on Control Applications*, Kohala Coast-Island of Hawai'i, 22.-27. August, 1999.

[92] PUYOU, G., FERRERES, G., CHIAPPA, C., AND MENARD, P., "A Multi-objective Method for Flight Control Law Design," *AIAA Guidance, Navigation, and Control Conference and Exhibit*, Providence, Rhode Island, 16.-19. August, 2004.

[93] RANEY, D., JACKSON, B., BUTTRILL C., AND ADAMS W., "The Impact of Structural Vibration on Flying Qualities of a Supersonic Transport," *AIAA Atmospheric Flight Mechanics Conference*, Montreal, Canada, 06.-09. August, 2001.

[94] REN W., AND KUMAR P. R., "Adaptive Active Noise Control Structures, Algorithms and Convergence Analysis," *Proc. InterNoise*, 1989, pp. 435-440.

[95] REW K-H., HAN J-H., AND LEE, I., "Multi-Modal Vibration Control Using Adaptive Positive Position Feedback," *Journal of Intelligent Material Systems and Structures*, Vol. 13, 2002, pp. 13-22.

[96] RIBNER, H., "Spectral Theory of Buffeting and Gust Response; Unification and Extension," *Journal of the Aeronautical Science*, Vol. 23, No. 12, 1956

[97] ROBINSON P., "The Use of Predictive Lidar Measurements in Alleviating Turbulence Induced Disturbances of Aircraft in Flight," *SPIE - Society of Photo-Optical Instrumentation Engineers*, Vol. 2737, pp. 86-97.

[98] RYNASKI, E., ANDRISANI, D., AND EULRICH, B., "Gust alleviation using direct turbulence measurements", AIAA-1979-1674, 1979.

[99] SCANLAN, R., AND ROSENBAUM, R., *Introduction to the Study of Aircraft Vibration and Flutter*, The Macmillan Company, New York, 1951.

[100] SCHMITT, N., REHM, W., PISTNER, T., ZELLER, P., DIEHL, H., AND NAVÉ, P., "Airborne direct detection UV LIDAR," *23rd International Laser Radar Conference ILRC*, Nara, Japan, 24.-28. July, 2006.

[101] SCHULER, J., Flugregelung und aktive Schwingungsdämpfung für flexible Großraumflugzeuge, Dissertation, Fortschrittbericht VDI Reihe 8 Nr. 688, Düsseldorf: VDI-Verlag 1998.

[102] SCHWANE, U., "Datenbasierte Generierung von Adaptionsregeln und Anwendung zur Erhöhung der Bahngenauigkeit eines Industrieroboters," Dissertation, Fortschritt-Bericht VDI Reihe 8 Nr. 748, Düsseldorf: VDI-Verlag 1999.

[103] SHETA, E., MOSES, R., HUTTSELL, L., AND HARRAND, V., "An Active Smart Material Control System for F/A-18 Buffet Alleviation," *International Forum on Aeroelasticity and Structural Dynamics*, Amsterdam, Netherlands, 04.-06. Juni, 2003.

[104] SHIFRIN, C., HILL, B., AND DONINGTON, C., "Saab 340Bs get active antinoise system," *Aviation Week & Space Technology*, May 9, 1994, pp. 55-56.

[105] SLEEPER, R., "Spanwise Measurement of Vertical Components of Atmospheric Turbulence," NASA TP-2963, Washington 1990.

[106] SOREIDE, D., BOGUE, R., EHERNBERGER, L., AND BAGLEY, H., "Coherent Lidar Measurement for Gust Load Alleviation," NASA Technical Memorandum TM-104318, Washington 1996.

[107] TAYLOR, G., "Statistical theory of turbulence," *Proceedings of the Royal Society London*, A164, 1938, pp. 478.

[108] TEUFEL, P., HANEL, M., AND K. WELL., "Integrated Flight Mechanic and Aeroelastic Modelling and Control of a flexible Aircraft considering Multidimensional Gust Input," *RTO AVT Specialists' Meeting on Structural Aspects of Flexible Aircraft Control*, Ottawa, Canada, 18.-20. October 1999.

[109] TEUFEL, P., "Böenmodellierung und Lastabminderung für ein flexibles Flugzeug," Dissertation, Universität Stuttgart, 2003.

[110] TEWES, S., "Active Trim Panel Attachments for Control of Sound Transmission through Aircraft Structures," Dissertation, Technische Universität München, 2006.

[111] URIE, M., ET AL., "Accelerated Development and Flight Evaluation of Active Controls Concepts for Subsonic Transport Aircraft Volume 2 – AFT C.G. simulation and analysis," NASA CR-159098, 1979.

[112] VON KÁRMÁN, T., AND HOWARTH, L., "On the Statistical Theory of Isotropic Turbulence," *Turbulence – Classical Papers on Statistical Theory*, S.K. Friedlander and Leonard Topper, Interscience Publishers, Inc., New York, 1961, pp. 76-99.

[113] VON KÁRMÁN, T., "Progress in the Statistical Theory of Turbulence," *Turbulence – Classical Papers on Statistical Theory*, S.K. Friedlander and Leonard Topper, Interscience Publishers, Inc., New York, 1961, pp. 162-174.

[114] WANG, K., AND REN, W., "Convergence Analysis of the Multi-Variable Filtered-X LMS Algorithm with Application to Active Noise Control," *IEEE, Transactions on Signal Processing*, Vol. 47, 1999, pp. 1166-1169.

[115] WANG, K., AND REN, W., "Convergence analysis of the filtered-U algorithm for active noise control," *Journal of Signal Processing,* Vol. 73, 1999, pp. 255-266.

[116] WIDROW, B., AND STEARNS, S., *Adaptive Signal Processing*, Prentice-Hall, New Jersey, 1985.

[117] WIDROW, B., AND WALACH, E., *Adaptive Inverse Control*, Prentice Hall, New Jersey, 1996.

[118] WILDSCHEK, A., MAIER, R., HOFFMANN, F., JEANNEAU, M., AND BAIER, H., "Active Wing Load Alleviation with an Adaptive Feed-forward Control Algorithm," *AIAA Guidance, Navigation, and Control Conference and Exhibit*, Keystone, CO, 21.-24. August, 2006.

[119] WILDSCHEK, A., MAIER, R., JATEGAONKAR, R., AND BAIER, H., "Augmentation of active wing bending control with a supplementary adaptive feed-forward control algorithm," *EUCASS 2007 - 2nd European Conference For Aerospace Sciences*, Brussels, Belgium, 01.-06. July, 2007.

[120] WILDSCHEK, A., MAIER, R., HOFFMANN, F., STEIGENBERGER, J., KAULFUSS, K.-H., BREITSAMTER, C., ALLEN, A., ADAMS, N., BAIER, H., GIANNOPOULOS, T., AND DAFNIS, A., "Wind Tunnel Testing of an Adaptive Control System for Vibration Suppression on Aircraft," *AIAA Guidance, Navigation, and Control Conference and Exhibit*, Hilton Head Island, SC, 20.-24. August, 2007.